

University of Wollongong - Research Online

Thesis Collection

Title: The impact of detector volume on penumbral dose prediction in a 6 MV radiation therapy X-ray beam

Author: Johnson Yuen

Year: 2009

Repository DOI:

Copyright Warning

You may print or download ONE copy of this document for the purpose of your own research or study. The University does not authorise you to copy, communicate or otherwise make available electronically to any other person any copyright material contained on this site.

You are reminded of the following: This work is copyright. Apart from any use permitted under the Copyright Act 1968, no part of this work may be reproduced by any process, nor may any other exclusive right be exercised, without the permission of the author. Copyright owners are entitled to take legal action against persons who infringe their copyright. A reproduction of material that is protected by copyright may be a copyright infringement. A court may impose penalties and award damages in relation to offences and infringements relating to copyright material.

Higher penalties may apply, and higher damages may be awarded, for offences and infringements involving the conversion of material into digital or electronic form.

Unless otherwise indicated, the views expressed in this thesis are those of the author and do not necessarily represent the views of the University of Wollongong.

Research Online is the open access repository for the University of Wollongong. For further information contact the UOW Library: research-pubs@uow.edu.au

University of Wollongong Thesis Collections

University of Wollongong Thesis Collection

University of Wollongong

Year 2009

The impact of detector volume on
penumbral dose prediction in a 6 MV
radiation therapy X-ray beam

Johnson Yuen
University of Wollongong

Yuen, Johnson, The impact of detector volume on penumbral dose prediction in a 6 MV radiation therapy X-ray beam, MSc thesis, School of Engineering Physics, University of Wollongong, 2009. <http://ro.uow.edu.au/theses/851>

This paper is posted at Research Online.
<http://ro.uow.edu.au/theses/851>

NOTE

This online version of the thesis may have different page formatting and pagination from the paper copy held in the University of Wollongong Library.

UNIVERSITY OF WOLLONGONG

COPYRIGHT WARNING

You may print or download ONE copy of this document for the purpose of your own research or study. The University does not authorise you to copy, communicate or otherwise make available electronically to any other person any copyright material contained on this site. You are reminded of the following:

Copyright owners are entitled to take legal action against persons who infringe their copyright. A reproduction of material that is protected by copyright may be a copyright infringement. A court may impose penalties and award damages in relation to offences and infringements relating to copyright material. Higher penalties may apply, and higher damages may be awarded, for offences and infringements involving the conversion of material into digital or electronic form.

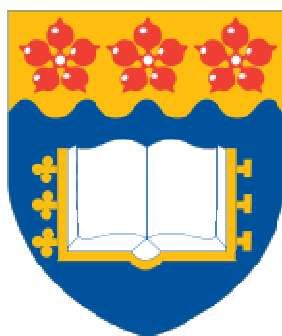
**The impact of detector volume on penumbral dose prediction
in a 6 MV radiation therapy X-ray beam**

A thesis submitted in partial fulfilment of the requirements for the award of the degree

MASTER OF SCIENCE - RESEARCH

From

THE UNIVERSITY OF WOLLONGONG



By

Johnson Yuen, BSc (Hon Class 1)

School of Engineering Physics

2009

Thesis Certification

CERTIFICATION

I, Johnson Yuen, declare that this thesis, submitted in fulfilment of the requirements for the award of Masters of Research in Medical Physics, in the Department of Engineering, University of Wollongong, is wholly my own work unless otherwise referenced or acknowledged. The document has not been submitted for qualifications at any other academic institution

Signed

Johnson Yuen

3rd March 2009

TABLE OF CONTENTS

CHAPTER 1: INTRODUCTION	1
1.0 INTRODUCTION TO THE THESIS	1
1.1 WHY IS RADIOTHERAPY IMPORTANT?	2
1.2 HOW IS MEDICAL RADIATION DELIVERED IN RADIOTHERAPY?	6
1.3 MODERN ADVANCES IN LINAC RADIOTHERAPY	14
CHAPTER 2: LITERATURE REVIEW	20
2.1 INTRODUCTION TO SCOPE OF STUDY	20
2.2 PHYSICS IN THE PENUMBRAL REGION	24
2.3 REVIEW OF DETECTORS	29
2.4 REVIEW OF THE DIAMOND DETECTOR	37
2.5 REVIEW OF THE MULTILEAF COLLIMATOR (MLC)	44
CHAPTER 3: EXPERIMENTAL METHOD	54
3.1 EQUIPMENT USED FOR DATA COLLECTION	54
3.2 METHOD OF DATA COLLECTION	64
3.3 DATA ANALYSIS AND PROCESSING	74
3.4 RADIOTHERAPY TREATMENT PLANNING SYSTEM MODELLING	76
3.5 RADIOTHERAPY TREATMENT PLANNING SYSTEM PLANNING	83
3.6 DISCUSSION OF BEAM PARAMETERS USED	87
CHAPTER 4: ANALYSIS OF THE CURVE PROPERTIES OF THE DOSE PROFILES MEASURED WITH DIFFERENT DETECTORS	91
4.1 OVERVIEW	91
4.2 SENSITIVE DETECTOR DIAMETER DATA	92
4.3 INFLECTION POINT OF PROFILES	94
4.4 INTERSECTION POINT OF DETECTORS	101
4.4 DISCUSSION OF INTERSECTION AND INFLECTION POINTS	106
4.5 CONCLUSIONS OF INTERSECTION AND INFLECTION POINTS	107
CHAPTER 5: DERIVING VIRTUAL ZERO DETECTOR VOLUME PROFILES BASED ON EXTRAPOLATION OF DATA FROM MULTIPLE DETECTOR DIAMETERS	110
5.1 THEORY	110
5.2 METHOD	111
5.3 RESULTS	112
5.4 VALIDATION OF METHOD	116
5.5 DISCUSSION	124
5.6 CONCLUSIONS	129
CHAPTER 6: DERIVING VIRTUAL ZERO DETECTOR VOLUME PROFILES BY DECONVOLUTION BASED ON DETECTOR DATA	131

6.1	THEORY	131
6.2	METHOD	134
6.3	RESULTS	139
6.4	DISCUSSION	144
6.5	CONCLUSIONS	147
CHAPTER 7: ANALYSIS OF THE EFFECT OF DETECTOR VOLUME ON SMEARING OF DOSE PROFILES		150
7.1	PENUMBRA ANALYSIS	150
7.2	FIELD SIZE ANALYSIS.....	153
7.3	DOSE ANALYSIS	156
7.4	DISCUSSION OF PROFILE PARAMETERS.....	164
7.5	CONCLUSION	167
CHAPTER 8: A NON-LINEAR EXTRAPOLATION EQUATION USING PENUMBRA DATA TO CALCULATE VIRTUAL ZERO DETECTOR VOLUME PENUMBRAS.....		174
8.1	THEORY	174
8.2	METHOD	177
8.3	RESULTS	182
8.4	DISCUSSION	188
8.4	CONCLUSIONS	191
CHAPTER 9: THE PINNACLE SOURCE SIZE MODEL WITH RESPECT TO THE DETECTOR EFFECT		194
9.1	INTRODUCTION	194
9.2	METHOD	195
9.3	RESULTS.....	196
9.4	DISCUSSION	206
9.5	CONCLUSIONS	208
CHAPTER 10: EFFECT OF DETECTOR VOLUME ON ISODOSE DISTRIBUTIONS		214
10.1	OVERVIEW	214
10.2	METHOD	214
10.3	RESULTS: PLAN 4FS1	217
	RESULTS: 4 FIELD 10×10 CM2 PLAN.....	226
	RESULTS: 4 FIELD PROSTATE PLAN	231
	DISCUSSION	235
	CONCLUSION	237
CHAPTER 11: CONCLUSION AND FUTURE WORK.....		241
11.1	CONCLUSIONS	241
11.2	POTENTIAL CLINICAL SIGNIFICANCE	244
11.3	FUTURE WORK	246

APPENDIX A: THE EFFECT OF JAW POSITION FOR MLC FIELDS IN THE CENTRAL AXIS	252
APPENDIX B: PROFILE MEASUREMENTS ALONG LEAF-END JUNCTION.....	256
APPENDIX C: INVESTIGATION INTO THE EFFECT OF END-LEAF OFFSET	260
APPENDIX D: EFFECT OF LATERAL ELECTRON EQUILIBRIUM AND BEAM QUALITY ESTIMATES WITH FIELD SIZE	268
APPENDIX E: BASIC MATHEMATICAL MODELLING OF THE CENTRAL AXIS DOSE VERSUS THE OUT OF FIELD DOSE	273
APPENDIX F: MCC FILE FORMAT.....	279
APPENDIX G: BEAM QUALITY ACROSS THE PROFILE	284
APPENDIX H: RESULTS OF SOURCE SIZE SURVEY	289
APPENDIX I: CODE FOR DECONVOLUTION	295
APPENDIX J: CODE FOR PLANAR DOSE.....	298
REFERENCES.....	300

LIST OF FIGURES

FIGURE 1.1: CAUSES OF DEATH FOR MALES, 2005 DATA FROM (AIHW 2005). THE LEADING CAUSE OF DEATH FOR FEMALES FOLLOWS A SIMILAR CURVE, AND DATA FOR THIS CAN BE FOUND IN THE LITERATURE.	3
FIGURE 1.2: COMPARISON OF DATA FROM DEPTH DOSE CURVES OF 100 kV PHOTONS (KOCH & STERZEL THERAPIX C100) AND 6MV PHOTONS (CLINAC 600C) AT ST. GEORGE HOSPITAL	8
FIGURE 1.3: FIGURE OF A TYPICAL LINEAR ACCELERATOR, ADAPTED FROM (VAN-DYK 1999)	9
FIGURE 1.4: ILLUSTRATION OF THE DIFFERENCE BETWEEN CONVENTIONAL AND CONFORMAL THERAPY (WEBB 1993)	14
FIGURE 1.5: DIAGRAM SHOWING FIVE INTENSITY MODULATED PROFILES TO TREAT THE TARGET VOLUME (HATCHED), ILLUSTRATION FROM (BRAHME 1988)	15
FIGURE 1.6: AN ISODOSE CURVE FROM A HEAD AND NECK PLAN WITH IMRT THAT ILLUSTRATES THE SPARING OF THE PAROTID GLANDS, ILLUSTRATION FROM (IMRT-CWG 2001)	16
FIGURE 1.7: DOSE-RESPONSE CURVE FOR TUMOUR CONTROL AND NORMAL TISSUE RESPONSE. SMALL ARROW INDICATES THE EFFECT ON DOSE RESPONSE WITH 5% CHANGE IN DOSE. ILLUSTRATION FROM (VAN-DYK 1999)	17
FIGURE 1.8: FIGURE SHOWING THE TUMOUR CELL AND ILLUSTRATING THE GTV (A), CTV (B), AND THE PTV (C). DIAGRAM FROM (VAN-DYK 1999).	18
FIGURE 2.1: SCHEMATIC DIAGRAM OF THE COLLIMATOR GEOMETRY ILLUSTRATING THE VARIABLES FOR THE CALCULATION OF GEOMETRIC PENUMBRA, FROM (AAPM 2008). NOTE THAT THE SCD FOR VARIAN MACHINES IS 38.0 CM FOR THE X JAW AND 48.3 CM FOR THE Y JAW	26
FIGURE 2.2: FOR (A), THE FIELD SIZE CORRESPONDS TO CHARGED PARTICLE EQUILIBRIUM AND FWHM CORRESPONDS TO 50% DOSE LEVEL OF CPE. FOR (B), THE FIELD SIZE IS OF THE SAME ORDER AS CPE AND THE PENUMBRA FROM THE OPPOSING FIELD OVERLAPS TO CAUSE A SMALL ERROR. FOR (C), FWHM IS OVERESTIMATED WITH RESPECT TO 50% DOSE LEVELS OF CPE SINCE THE RESULTING CURVE HAS A LOWER MAXIMUM VALUE. ADAPTED FROM (DAS, DING ET AL. 2007)	28
FIGURE 2.3: THE 80-20% PENUMBRA PLOTTED AGAINST THE DETECTOR SIZE A FOR A 6 MV BEAM. IT WAS FOUND (PAPPAS, MARIS ET AL. 2006) THAT THE USE OF A DETECTOR LESS THAN 0.5 MM WOULD MINIMISE THE VOLUME EFFECT FROM A DETECTOR.	31
FIGURE 2.4: MEASURED RESPONSE OF THE DIAMOND DETECTOR AT PHOTON ENERGIES FROM 4-25 MV WITH THE STOPPING POWER RATIO OF WATER/CARBON AND OF WATER/AIR FROM (LAUB, KAULICH ET AL. 1997)	40
FIGURE 2.5: LOGIC DIAGRAM HIGHLIGHTING THE RELATIONSHIP OF RECOMBINATION TIME, CONDUCTIVITY, DOSE RATE, AND THE NUMBER OF HOLES IN THE DIAMOND DETECTOR	42
FIGURE 2.6: ILLUSTRATION OF A GENERAL LEAF FROM A MLC WITH A CURVED END, ADAPTED FROM (AAPM_TG_50 2001)	46
FIGURE 2.7: CROSS-SECTIONAL VIEWS OF THE VARIAN 120-LEAF MLC WITH THE (A) END VIEW AND THE (B) SIDE VIEW (KIM, SIEBERS ET AL. 2001)	48
FIGURE 2.8: FOR ROUNDED LEAF END MLCs, THE ACTUAL FIELD SIZE CALIBRATION DIFFERS FOR LIGHT (X_{LIGHT}) AND RADIATION FIELD (X_{RAD}) EDGES, AND DEPENDS IN A COMPLEX WAY ON THE MOTION OF THE LEAVES (X_{MLC}) (GRAVES, THOMPSON ET AL. 2001)	50

FIGURE 2.9: RADIATION FIELD MEASUREMENTS OF ORIGINAL AND CORRECTED AVERAGES (RIGHT)	
BETWEEN MEASURED AND READOUT (GRAVES, THOMPSON ET AL. 2001)	52
FIGURE 3.1: MLC SHAPER OPTIONS.....	55
FIGURE 3.2: PTW WATER TANK.....	56
FIGURE 3.3: MP3 ELECTROMETER (ABOVE) AND MP3 CONTROL UNIT (BELOW)	56
FIGURE 3.4: COMPARISON BETWEEN PDD DATA FOR DIAMOND DETECTOR AND 0.125 CC IONISATION	
CHAMBER FOR JAW DEFINED 10x10 CM ² FIELD	61
FIGURE 3.5: DERIVATION OF DIAMOND DETECTOR DOSE RATE DEPENDENCE WITH LOG OF DIAMOND PDD	
AND LOG OF IC PDD	62
FIGURE 3.6: PROFILE SHOWING THE RAW DIAMOND DETECTOR PROFILE AND THE PROFILE WITH DOSE-RATE	
CORRECTION APPLIED (TOPOLNJAK, HEIDE ET AL.) WITH THE DOSE DIFFERENCE (BOTTOM)	63
FIGURE 3.7: DIAGRAM SHOWING THE DIRECTION OF THE POSITION OF THE MLC LEAF MOTION WITH	
RESPECT TO THE JAW POSITIONS. NOTE THAT THIS DIAGRAM IS NOT THE VARIAN 120 LEAF MLC	
SYSTEM USED IN THE STUDY.	65
FIGURE 3.8: THE END-LEAF OFFSET CONTRIBUTES SIGNIFICANT DOSE IN THE PERPENDICULAR PROFILE	
(LEFT) IF MEASURED WITHOUT ANY OFFSET. THE DETECTOR CAN BE OFFSET SO THAT IT MEASURES	
THE PERPENDICULAR PROFILE AWAY FROM THE CENTRAL AXIS, SO THAT THE OUT-OF-FIELD	
PERPENDICULAR PROFILE DOES NOT MEASURE THE END-LEAF JUNCTION DOSE.	67
FIGURE 3.9: THE END-LEAF OFFSET CONTRIBUTES SIGNIFICANT DOSE IN THE PERPENDICULAR PROFILE	
(LEFT) IF MEASURED WITHOUT ANY OFFSET. THE END-LEAF JUNCTION CAN BE OFFSET (RIGHT) SO	
THAT THE OUT-OF-FIELD PERPENDICULAR PROFILE DOES NOT MEASURE THE END-LEAF JUNCTION	
DOSE.	67
FIGURE 3.10: <i>CENTRECHECK</i> SOFTWARE INDICATING THAT THE CHAMBER POSITION REQUIRES NO SHIFT TO	
BE IN THE CENTRE WITH THE RADIATION FIELD.	70
FIGURE 3.11: FIRST GROUP OF SETTINGS REQUIRED IN TBAScan	71
FIGURE 3.12: SECOND GROUP OF SETTINGS IN TBAScan	72
FIGURE 3.13: STEP SETTINGS FOR PDD.....	72
FIGURE 3.14: STEP SETTINGS FOR PROFILES	73
FIGURE 3.15: SPEED SETTINGS FOR CHAMBER MOVEMENT	73
FIGURE 3.16: DELAY TIMES FOR CHAMBER POSITIONS (ZERO WAS SET FOR ALL POSITIONS).....	74
FIGURE 3.17: PROCESSING FUNCTIONS, SHOWING THE SYMMETRISE AND SMOOTH FUNCTION ON THE LEFT	
HAND SIDE OF THE SCREEN	74
FIGURE 3.18: THE DEPTH DOSE TAB FOR BEAM MODELLING IN PINNACLE ³	77
FIGURE 3.19: ACTUAL ENERGY SPECTRA USED IN THE STUDY.....	77
FIGURE 3.20: COMPARISON BETWEEN COMPUTED AND MEASURED PDD IN PINNACLE ³	78
FIGURE 3.21: THE BUILD-UP TAB IN THE BEAM MODELLING SECTION IN PINNACLE ³	79
FIGURE 3.22: THE INFELD TAB IN BEAM MODELLING IN PINNACLE ³	80
FIGURE 3.23: THE OUT-OF-FIELD TAB IN THE BEAM MODELLING SECTION IN PINNACLE ³	80
FIGURE 3.24: COMPARISON OF MEASURED AND COMPUTED PROFILES IN PINNACLE ³	82
FIGURE 3.25: THE PHANTOM TAB IN THE BEAM MODELLING SECTION IN PINNACLE ³	82
FIGURE 3.26: THE DVH IN THE PLAN EVALUATION MENU IN PINNACLE ³	86

FIGURE 3.27: ILLUSTRATION OF THE PENUMBRA WIDTH, WHICH IS THE DISTANCE SUBTENDED FROM NORMALISED DOSE VALUES OF 20% AND 80%	87
FIGURE 3.28: AN ILLUSTRATION OF THE PERCENTAGE DEPTH DOSE, WITH THE SURFACE DOSE D_s BEING THE SURFACE DOSE, D_{MAX} BEING THE DOSE CORRESPONDING TO MAXIMUM DOSE, AND D_{EX} BEING THE EXIT DOSE. THE REGION BEFORE D_{MAX} IS REFERRED TO AS THE BUILD-UP REGION. FIGURE ADAPTED FROM (IAEA 2005).....	88
FIGURE 3.29: ILLUSTRATION OF THE PROGRAM STRUCTURE USED TO CALCULATE TMR.....	89
FIGURE 4.1: DIAGRAM ILLUSTRATING THE DIMENSIONS OF THE 0.125 CC IONISATION CHAMBER FROM THE MANUFACTURER (PTW-FRIEBURG 2008)	93
FIGURE 4.2: DIAGRAM ILLUSTRATING THE DIMENSIONS OF THE PINPOINT DETECTOR FROM THE MANUFACTURER (PTW-FRIEBURG 2008)	93
FIGURE 4.3: DIAGRAM ILLUSTRATING THE DIMENSIONS OF THE DIAMOND DETECTOR FROM THE MANUFACTURER (PTW-FRIEBURG 2008).	94
FIGURE 4.4: FIGURE SHOWING THE FIRST DERIVATIVE OF A $1 \times 1 \text{ cm}^2$ FIELD AT 10 CM DEPTH	95
FIGURE 4.5: FIGURE SHOWING THE FIRST DERIVATIVE OF A $10 \times 10 \text{ cm}^2$ FIELD AT 10 CM DEPTH	96
FIGURE 4.6: FIGURE SHOWING THE SECOND DERIVATIVE OF A $1 \times 1 \text{ cm}^2$ FIELD AT 10 CM DEPTH	97
FIGURE 4.7: FIGURE SHOWING THE SECOND DERIVATIVE OF A $10 \times 10 \text{ cm}^2$ FIELD AT 10 CM DEPTH	97
FIGURE 4.8: PLOT OF THE RATIO OF THE SPATIAL POSITION OF INFLECTION POINT OVER FIELD EDGE WITH SQUARE FIELD SIZE AT 10 CM DEPTH	99
FIGURE 4.9: PLOT OF THE NORMALISED DOSE AT INFLECTION POINT FOR EACH SET OF DATA WITH SQUARE FIELD SIZE AT 10 CM DEPTH	100
FIGURE 4.10: ENLARGED REGION SHOWING THE INTERSECTION OF THE PROFILES RELATING TO THE IC, PP, AND DD PROFILES.....	101
FIGURE 4.11: FIGURE SHOWING THE DEPENDENCE OF INTERSECTION POINT ON FIELD SIZE	102
FIGURE 4.12: PLOT HIGHLIGHTING THE UNDERESTIMATE AREA AND THE OVERESTIMATE AREA IN A PROFILE WITH RELATION TO THE INTERSECTION POINT.	104
FIGURE 5.1: ILLUSTRATING THE EXTRAPOLATION PROCEDURE FOR MLC CROSSPLANE $1 \times 1 \text{ cm}^2$ SQUARE FIELD AT 10 CM DEPTH.	111
FIGURE 5.2: PLOT OF THE RESULTS OF THE EXTRAPOLATION PROFILE MLC CROSSPLANE $1 \times 1 \text{ cm}^2$ SQUARE FIELD AT 10 CM DEPTH.	113
FIGURE 5.3: EXTRAPOLATION PROFILE WITH R^2 (DOTTED), COMPARED WITH DATA FROM PROFILES AT A DEPTH OF 10 CM AND FIELD SIZE $1 \times 1 \text{ cm}^2$ (JAW CROSSPLANE DATA).....	114
FIGURE 5.4: EXTRAPOLATION PROFILE WITH R^2 (DOTTED), COMPARED WITH DATA FROM PROFILES AT A DEPTH OF 10 CM AND FIELD SIZE $2 \times 2 \text{ cm}^2$ (JAW CROSSPLANE DATA).....	114
FIGURE 5.5: EXTRAPOLATION PROFILE WITH R^2 (DOTTED), COMPARED WITH DATA FROM PROFILES AT A DEPTH OF 10 CM AND FIELD SIZE $5 \times 5 \text{ cm}^2$ (JAW CROSSPLANE DATA).....	115
FIGURE 5.6: EXTRAPOLATION PROFILE WITH R^2 (DOTTED), COMPARED WITH DATA FROM PROFILES AT A DEPTH OF 10 CM AND FIELD SIZE $10 \times 10 \text{ cm}^2$ (JAW CROSSPLANE DATA).....	115
FIGURE 5.7: DOSE DIFFERENCE OF EXTRAPOLATION PROFILE WITH IC (DOTTED), COMPARED WITH DATA AT A DEPTH OF 10 CM AND FIELD SIZE $1 \times 1 \text{ cm}^2$ (JAW CROSSPLANE DATA).....	116
FIGURE 5.8: PLOT OF R^2 VERSUS DOSE DIFFERENCE FOR CROSSPLANE JAWS, $1 \times 1 \text{ cm}^2$ AT 10 CM DEPTH ..	117
FIGURE 5.9: PLOT OF R^2 VERSUS DOSE DIFFERENCE FOR INPLANE JAWS, $1 \times 1 \text{ cm}^2$ AT 10 CM DEPTH.	118

FIGURE 5.10: PLOT OF R^2 VERSUS DOSE DIFFERENCE FOR CROSSPLANE MLC, $1 \times 1 \text{ cm}^2$ AT 10 CM DEPTH.	118
FIGURE 5.11: PLOT OF R^2 VERSUS DOSE DIFFERENCE FOR INPLANE MLC, $1 \times 1 \text{ cm}^2$ AT 10 CM DEPTH.	119
FIGURE 5.12: SHOWING THE PLOT OF THE COST FUNCTIONS (RHS) WITH THE ZE AND IC PROFILES (LHS) FOR $1 \times 1 \text{ cm}^2$ FIELD DEFINED BY JAW AT A DEPTH OF 10 CM. THE COST FUNCTION IS CALCULATED WITH EQ. 5.1.	120
FIGURE 5.13: AVERAGED COST FUNCTION FOR THE IC FOR DOSE POINTS MORE THAN 10% AT A DEPTH OF 10 CM.	122
FIGURE 5.14: ZE PROFILE IN THE INPLANE DIRECTION FOR A $1 \times 1 \text{ cm}^2$ FIELD AT A DEPTH OF 10 CM	123
FIGURE 5.15: PROFILE ILLUSTRATING THE EFFECT OF EXTRAPOLATING PENUMBRA WITH DETECTOR DIAMETER WITH THE INCLUSION OF A DOSE POINT MEASURED WITH A DETECTOR DIAMETER LESS THAN 1.5 MM (THE DOTTED LINE WAS ADDED TO HIGHLIGHT THE EFFECT OF THE INCLUSION) ADAPTED FROM (PAPPAS, MARIS ET AL. 2006)	127
FIGURE 6.1 A DIAGRAM ILLUSTRATING THE CONCEPTS OF THE DETECTOR RESPONSE FUNCTION, THE TRUE PROFILE, AND THE MEASURED PROFILE (CHANG, YIN ET AL. 1996)	132
FIGURE 6.2: FIGURE SHOWING THE DECONVOLUTION OF RAW IC DATA AND THE DECONVOLUTION OF A GAUSSIAN FIT OF IC DATA	135
FIGURE 6.3: GAUSSIAN CURVE FIT FOR $1 \times 1 \text{ cm}^2$ AT 10 CM DEPTH	137
FIGURE 6.4: GAUSSIAN CURVE FIT FOR $2 \times 2 \text{ cm}^2$ CURVE AT 10 CM DEPTH	137
FIGURE 6.5: GAUSSIAN CURVE FIT FOR $5 \times 5 \text{ cm}^2$ CURVE AT 10 CM DEPTH	138
FIGURE 6.6: FIGURE SHOWING THE PLOT OF THE KERNEL FUNCTIONS	139
FIGURE 6.7: DECONVOLUTION OF IC WITH VARIOUS KERNELS COMPARED WITH ZE FOR A $1 \times 1 \text{ cm}^2$ FIELD AT 10 CM DEPTH (JAW CROSSPLANE)	141
FIGURE 6.8: DECONVOLUTION OF PP WITH VARIOUS KERNELS COMPARED WITH ZE FOR A $1 \times 1 \text{ cm}^2$ FIELD AT 10 CM DEPTH (JAW CROSSPLANE)	142
FIGURE 6.9: DECONVOLUTION OF DD WITH VARIOUS KERNELS COMPARED WITH ZE FOR A $1 \times 1 \text{ cm}^2$ FIELD AT 10 CM DEPTH (JAW CROSSPLANE)	143
FIGURE 7.1: PLOT OF PENUMBRAL VARIATION OVER FIELD SIZES (10 CM DEPTH)	151
FIGURE 7.2: MEASURED FIELD SIZE VARIATION OVER SET FIELD SIZE (OVER DEPTHS 1.5 TO 20 CM AND SET FIELD SIZE 1×1 TO $10 \times 10 \text{ cm}^2$)	154
FIGURE 7.3: MEASURED FIELD SIZE VARIATION OVER DEPTH ($1 \times 1 \text{ cm}^2$ FIELD SIZE)	155
FIGURE 7.4: DOSE DIFFERENCE VARIATION OVER FIELD SIZE (10 CM DEPTH); PLOT OF THE MAXIMUM DOSE DIFFERENCE AS A PERCENTAGE OVER FIELD SIZES. THE Y-AXIS IS CALCULATED USING EQUATION 7.1.	158
FIGURE 7.5: DOSE DIFFERENCE VARIATION OVER DEPTH ($1 \times 1 \text{ cm}^2$ FIELD SIZE); PLOT OF THE MAXIMUM DOSE DIFFERENCE AS A PERCENTAGE OVER DEPTH.	159
FIGURE 7.6: PLOT OF THE SUMMED OF THE OVERESTIMATE AND UNDERESTIMATE AS A PERCENTAGE OF THE TOTAL SUMMED DOSE IN THE PROFILE WITH FIELD SIZE. THE SUMMED(OVERESTIMATE) IS CALCULATED USING EQ. 7.5, SUMMED(UNDERESTIMATE) USES EQ. 7.6, AND OVERALL CHANGE USES EQ. 7.7.	160
FIGURE 7.7: PLOT OF THE SUMMED OF THE OVERESTIMATE AND UNDERESTIMATE AS A PERCENTAGE OF THE TOTAL SUMMED DOSE IN THE PROFILE WITH DEPTH. THE SUMMED(OVERESTIMATE) IS CALCULATED USING EQ. 7.5, SUMMED(UNDERESTIMATE) USES EQ. 7.6, AND OVERALL CHANGE USES EQ. 7.7. ..	162

FIGURE 7.8: PLOT OF THE RATIO OF THE SUMMED OVERESTIMATE AND UNDERESTIMATE IN THE PROFILE WITH FIELD SIZE.	163
FIGURE 8.1: FIGURE ILLUSTRATING A PLOT WHICH INCLUDES BOTH THE EFFECTS OF PENUMBRAL INCREASE DUE TO FIELD SIZE (ILLUSTRATED WITH CLOSED CIRCLES $1 \times 1 \text{ cm}^2$, OPEN CIRCLES $2 \times 2 \text{ cm}^2$, TRIANGLES $5 \times 5 \text{ cm}^2$, AND STARS $10 \times 10 \text{ cm}^2$) AND DEPTH (ILLUSTRATED WITH RED FOR DEPTH 1.5 CM, BLACK FOR DEPTH 5.0 CM, GREEN FOR DEPTH 10.0 CM, AND BLUE FOR DEPTH 20.0 CM).....	175
FIGURE 8.2: PLOT SHOWING THE RELATIONSHIP BETWEEN THE CHANGE IN PENUMBRA SIZE DUE TO DETECTOR DIAMETER AND THE MEASURED ZE PENUMBRA FOR THE JAW CROSSPLANE DATA.....	176
FIGURE 8.3 PLOT SHOWING THE RELATIONSHIP BETWEEN THE CHANGE IN PENUMBRA SIZE DUE TO DETECTOR DIAMETER AND THE MEASURED ZE PENUMBRA FOR THE MLC CROSSPLANE	177
FIGURE 8.4: DIAGRAM ILLUSTRATING THE CORRELATION BETWEEN THE INCREASE IN MEASURED PENUMBRA FROM ZE PENUMBRA WITH DETECTOR DIAMETER (SEE EQUATION 8.1)	178
FIGURE 8.5: PLOT OF THE RELATIONSHIP BETWEEN THE LINEAR COEFFICIENT M1 AND THE ZE PENUMBRA FOR THE JAW CROSSPLANE DATA	179
FIGURE 8.6: PLOT OF THE RELATIONSHIP BETWEEN THE LINEAR COEFFICIENT M1 AND THE ZE PENUMBRA FOR THE MLC CROSSPLANE DATA	179
FIGURE 8.7: PLOT OF THE SIMULATED ZE PENUMBRA CALCULATED BY THE NON-LINEAR ZE PENUMBRA EQUATION FOR AN ARBITRARY DETECTOR DIAMETER	182
FIGURE 8.8: PLOT SHOWING THE DEVIATION FROM THE ZE PENUMBRA WITH THE IC DATA WITH AND WITHOUT THE CORRECTION MADE WITH THE NON-LINEAR PENUMBRA EQUATION WITH THE JAW CROSSPLANE DATA	183
FIGURE 8.9: PLOT SHOWING THE DEVIATION FROM THE ZE PENUMBRA WITH THE PP DATA WITH AND WITHOUT THE CORRECTION MADE WITH THE NON-LINEAR PENUMBRA EQUATION WITH THE JAW CROSSPLANE DATA	183
FIGURE 8.10: PLOT SHOWING THE DEVIATION FROM THE ZE PENUMBRA WITH THE DD DATA WITH AND WITHOUT THE CORRECTION MADE WITH THE NON-LINEAR PENUMBRA EQUATION WITH THE JAW CROSSPLANE DATA	184
FIGURE 8.11: PLOT SHOWING THE DEVIATION FROM THE ZE PENUMBRA WITH THE IC DATA WITH AND WITHOUT THE CORRECTION MADE WITH THE NON-LINEAR PENUMBRA EQUATION WITH THE MLC CROSSPLANE DATA	186
FIGURE 8.12: PLOT SHOWING THE DEVIATION FROM THE ZE PENUMBRA WITH THE PP DATA WITH AND WITHOUT THE CORRECTION MADE WITH THE NON-LINEAR PENUMBRA EQUATION WITH THE MLC CROSSPLANE DATA	187
FIGURE 8.13: PLOT SHOWING THE DEVIATION FROM THE ZE PENUMBRA WITH THE DD DATA WITH AND WITHOUT THE CORRECTION MADE WITH THE NON-LINEAR PENUMBRA EQUATION WITH THE MLC CROSSPLANE DATA	187
FIGURE 8.14: THE EFFECT OF VARIOUS IC15 LINE SPREAD FUNCTIONS ON THE BROADENING OF 20%-80% PENUMBRA AS MODELLED BY THE DECONVOLUTION MODEL INVOLVING THE ELLIPTIC AND GAUSSIAN KERNEL FUNCTION (VAN'T.VELD, LUJIK ET AL. 2001).....	190
FIGURE 9.1: PLOT ILLUSTRATING THE RELIABILITY OF THE RELATIONSHIP BETWEEN THE PINNACLE MODELLED PENUMBRA AND THE PINNACLE SOURCE SIZE.	197

FIGURE 9.2: THE CALCULATED PINNACLE SOURCE SIZE (MM) WITH VARIOUS DATASETS OVER DEPTH AT A FIELD SIZE OF $1 \times 1 \text{ cm}^2$	199
FIGURE 9.3: THE CALCULATED PINNACLE SOURCE SIZE (MM) WITH VARIOUS DATASETS OVER VARIOUS FIELD SIZES AT A DEPTH OF 1.5 CM.	201
FIGURE 9.4: FIGURE ILLUSTRATING THE RELATIONSHIP BETWEEN THE ZE PENUMBRA FOR THE ZE AND THE MEASURED DETECTOR DATASET.	202
FIGURE 9.5: FIGURE ILLUSTRATING THE RELATIONSHIP BETWEEN THE ZE PENUMBRA FOR THE ZE AND THE NON-LINEAR PENUMBRA CORRECTED DETECTOR DATASET.	203
FIGURE 9.6: FIGURE SHOWING THE DIFFERENCE BETWEEN THE CALCULATED PINNACLE SOURCE SIZE USING FINITE DETECTORS AND THE ZE CALCULATED PINNACLE SOURCE SIZE MODELLED TO MATCH ZE PENUMBRA PROFILES.	204
FIGURE 9.7: COMPARISON OF CALCULATED SOURCE SIZE BASED ON GEOMETRIC PENUMBRA AND MODELLED SOURCE SIZE BASED ON RTPS MODEL OF PENUMBRA	205
FIGURE 10.1: PINNACLE ISODOSE DISTRIBUTION SHOWING THE BEAM GEOMETRY USED IN THE PLAN 4FS1	217
FIGURE 10.2: PLOT SHOWING THE DIFFERENCE IN ISODOSE DISTRIBUTION FOR ONE $1 \times 1 \text{ cm}^2$ FIELD BETWEEN THE 0.4 MM SOURCE SIZE MODEL (TOP) AND THE 2.4 MM SOURCE SIZE MODEL (BOTTOM) USED IN THE PLAN 4FS10.....	218
FIGURE 10.3 PLOT SHOWING THE ISODOSE DIFFERENCE PLOT FOR A SINGLE FIELD (GANTRY 0), WHERE EACH POINT WAS CALCULATED BY ISODOSE POINT (2.4 MM MODEL) MINUS ISODOSE POINT (0.8 MM MODEL)	219
FIGURE 10.4: PLOT SHOWING THE DIFFERENCE IN ISODOSE DISTRIBUTION FOR 4 $1 \times 1 \text{ cm}^2$ FIELDS BETWEEN THE 0.4 MM SOURCE SIZE MODEL (TOP) AND THE 2.4 MM SOURCE SIZE MODEL (BOTTOM) USED IN THE PLAN 4FS10.....	219
FIGURE 10.5: PLOT SHOWING THE ISODOSE DIFFERENCE PLOT FOR COMBINED 4 FIELDS, WHERE EACH POINT WAS CALCULATED BY ISODOSE POINT (2.4 MM MODEL) MINUS ISODOSE POINT (0.8 MM MODEL)	220
FIGURE 10.6: PROFILE ACROSS THE ROWS IN FIGURE 10.5 AT $Y=0$ FOR COMBINED BEAMS.....	220
FIGURE 10.7: DOSE ANALYSIS IN TERMS OF SUMMATION OF 2D DOSE IN A SINGLE $1 \times 1 \text{ cm}^2$ FIELD	221
FIGURE 10.8: DOSE ANALYSIS IN TERMS OF SUMMATION OF 2D DOSE IN A FOUR $1 \times 1 \text{ cm}^2$ FIELD ARRANGEMENT.....	222
FIGURE 10.9: PINNACLE ISODOSE DISTRIBUTION SHOWING THE BEAM GEOMETRY USED IN THE PLAN 2FS1A	223
FIGURE 10.10: PLOT SHOWING THE ISODOSE DIFFERENCE PLOT, AT GANTRY 0 FOR TWO SINGLE FIELDS (GANTRY 0), WHERE EACH POINT WAS CALCULATED BY ISODOSE POINT (2.4 MM MODEL) MINUS ISODOSE POINT (0.8 MM MODEL).....	224
FIGURE 10.11: PLOT SHOWING THE DIFFERENCE IN ISODOSE DISTRIBUTION FOR ONE 2×1 (ABUTTED) cm^2 FIELD BETWEEN THE 0.4 MM SOURCE SIZE MODEL (TOP) AND THE 2.4 MM SOURCE SIZE MODEL (BOTTOM)	224
FIGURE 10.12 ISODOSE DIFFERENCE. NORMALISED ISODOSES 24 MINUS NORMALIZED ISODOSES 08, COMBINED FIELDS.....	225
FIGURE 10.13 PROFILE WITH DATA FROM ROWS ALONG $Y=2.45 \text{ cm}$ (HIGHEST DOSE REGION) SHOWING DIFFERENT SOURCE SIZE FOR COMBINED BEAMS.....	225

FIGURE 10.14: PINNACLE ISODOSE DISTRIBUTION SHOWING THE BEAM GEOMETRY USED IN THE PLAN 4FS10	226
FIGURE 10.15: PLOT SHOWING THE DIFFERENCE IN ISODOSE DISTRIBUTION FOR ONE 10×10 CM ² FIELD BETWEEN THE 0.4 MM SOURCE SIZE MODEL (TOP) AND THE 2.4 MM SOURCE SIZE MODEL (BOTTOM) USED IN THE PLAN 4FS10	227
FIGURE 10.16: PLOT SHOWING THE ISODOSE DIFFERENCE PLOT, AT GANTRY 0 FOR TWO SINGLE FIELDS (GANTRY 0), WHERE EACH POINT WAS CALCULATED BY ISODOSE POINT (2.4 MM MODEL) MINUS ISODOSE POINT (0.8 MM MODEL)	228
FIGURE 10.17: PLOT SHOWING THE ISODOSE DIFFERENCE PLOT, AT GANTRY 0 FOR FOUR SINGLE FIELD THAT ARE 10×10 CM ² , WHERE EACH POINT WAS CALCULATED BY ISODOSE POINT (2.4 MM MODEL) MINUS ISODOSE POINT (0.8 MM MODEL)	228
FIGURE 10.18: PLOT SHOWING THE ISODOSE DIFFERENCE PLOT, AT GANTRY 0 FOR FOUR SINGLE FIELDS THAT ARE 10×10 CM ² (GANTRY 0), WHERE EACH POINT WAS CALCULATED BY ISODOSE POINT (2.4 MM MODEL) MINUS ISODOSE POINT (0.8 MM MODEL)	229
FIGURE 10.19: PROFILE FROM ROW DATA ALONG Y=0 (CENTRAL REGION) SHOWING DIFFERENT SOURCE SIZE FOR COMBINED BEAMS	229
FIGURE 10.20: DOSE ANALYSIS IN TERMS OF SUMMATION OF 2D DOSE IN A SINGLE 10×10 CM ² FIELD	230
FIGURE 10.21: DOSE ANALYSIS IN TERMS OF SUMMATION OF 2D DOSE IN A FOUR 10×10 CM ² FIELD ARRANGEMENT	230
FIGURE 10.22: PINNACLE ISODOSE DISTRIBUTION SHOWING THE BEAM GEOMETRY USED IN THE PLAN PROST	231
FIGURE 10.23: PLOT SHOWING THE DIFFERENCE IN ISODOSE DISTRIBUTION FOR AN OBLIQUE 10×10 CM ² FIELD BETWEEN THE 0.4 MM SOURCE SIZE MODEL (TOP) AND THE 2.4 MM SOURCE SIZE MODEL (BOTTOM) USED IN THE PLAN 4FS10	232
FIGURE 10.24: PLOT SHOWING THE ISODOSE DIFFERENCE PLOT, AT GANTRY 0 FOR THE OBLIQUE FIELD, WHERE EACH POINT WAS CALCULATED BY ISODOSE POINT (2.4 MM MODEL) MINUS ISODOSE POINT (0.8 MM MODEL)	233
FIGURE 10.25: PLOT SHOWING THE CONTOUR PLOTS FOR THE TWO SOURCE SIZE SETTING IN THE PROSTATE PLAN, WHERE EACH POINT WAS CALCULATED BY ISODOSE POINT (2.4 MM MODEL) MINUS ISODOSE POINT (0.8 MM MODEL)	233
FIGURE 10.26: PLOT SHOWING THE ISODOSE DIFFERENCE PLOT, FOR FOUR IN THE PROSTATE PLAN, WHERE EACH POINT WAS CALCULATED BY ISODOSE POINT (2.4 MM MODEL) MINUS ISODOSE POINT (0.8 MM MODEL)	234
FIGURE 10.27: PLOT OF THE DEPENDENCE OF CHANGE OF THE MEAN DOSE AS A PERCENTAGE OF THE MEAN DOSE OF THE SOURCE SIZE 0.8 MM WITH SOURCE SIZE	235
FIGURE C.1: THE END-LEAF OFFSET CONTRIBUTES SIGNIFICANT DOSE IN THE PERPENDICULAR PROFILE (LEFT) IF MEASURED WITHOUT ANY OFFSET. THE END-LEAF JUNCTION CAN BE OFFSET (RIGHT) SO THAT THE OUT-OF-FIELD PERPENDICULAR PROFILE DOES NOT MEASURE THE END-LEAF JUNCTION DOSE.	261
FIGURE C.2: CONSIDERATION OF THE EFFECTIVE DISTANCE OF THE CENTRAL AXIS TO THE CLOSEST DOSE POINT IN THE LEAF-END DOSE REGION WITH REGARDS TO PHANTOM SCATTER AT 100 CM SAD. THE MLC LEAF-END OFFSET IS ALSO SHOWN HERE.	261

FIGURE C.3: EFFECT OF END-LEAF OFFSET ON THE DOSE AT DMAX. THE READING ASSOCIATED WITH AN END-LEAF OFFSET OF 0 CM WAS THE HIGHEST AND WAS USED TO COMPARE WITH THE OTHER READINGS.	262
FIGURE C.4: A NORMALISED PERPENDICULAR PROFILE SHOWING THE EFFECT OF THE LEAF-END OFFSET ON THE OUT OF FIELD DOSE, THE FIELD EDGE, AND THE PENUMBRA.....	263
FIGURE C.5: PLOT OF THE LEAF END JUNCTION PROFILE AT A DEPTH OF 1.5 CM FOR A CLOSED MLC FIELD WITH VARIOUS LEAF END OFFSETS	264
FIGURE D.1: PLOT OF TPR (20,10) WITH SQUARE FIELD SIZE DEFINED BY THE JAW AND MLC AND MEASURED WITH IC, PP, AND DD.	269
FIGURE D.2: VARIATION OF THE DIAMETER ASSOCIATED WITH LATERAL ELECTRON EQUILIBRIUM AS CALCULATED FROM $TPR_{(20,10)}$ COMPARED WITH THE INCREASE OF SQUARE FIELD SIZE (RED). THE INTERSECTION SHOWS THE MINIMUM FIELD SIZE WHERE THERE IS LEE FOR THE CASE OF JAWS AND MLCS.....	270
FIGURE E.1: FIGURE SHOWING THE DIMENSIONS OF THE MODEL USED.....	274
FIGURE E.2: ILLUSTRATION OF THE OUT OF FIELD RELATIVE TO THE CENTRAL AXIS READING AS A % WITH INCREASING SQUARE FIELD SIZE FOR THE CASE OF MLC AND JAW WITH DIFFERENT DETECTOR READINGS. DATA ANALYSED WITH A DEPTH OF 10 CM.	275
FIGURE E.3: RESULTS OF MODELLED NORMAL DOSE OVER TUMOUR DOSE FOR JAW SETTINGS. SP1 CONSIDERS A NORMAL TISSUE VOLUME 1 CM AROUND THE TUMOUR VOLUME.	276
FIGURE E.4: RESULTS OF MODELLED NORMAL DOSE OVER TUMOUR DOSE FOR MLC SETTINGS. SP1 CONSIDERS A NORMAL TISSUE VOLUME 1 CM AROUND THE TUMOUR VOLUME.	276
FIGURE G.1: VARIATION OF BEAM QUALITY ACROSS THE PROFILE FOR A $1 \times 1 \text{ cm}^2$ FIELD.....	284
FIGURE G.2: VARIATION OF BEAM QUALITY ACROSS THE PROFILE FOR A $5 \times 5 \text{ cm}^2$ FIELD	285
FIGURE G.3: VARIATION OF BEAM QUALITY ACROSS THE PROFILE FOR A $10 \times 10 \text{ cm}^2$ FIELD.....	286
FIGURE G.4: THE BEAM QUALITY VARIATION WITH FIELD SIZE (BLACK). THE CHANGE IN BEAM QUALITY ACROSS THE PROFILE IS ALSO PLOTTED (RED) WITH FIELD SIZE.	286

LIST OF TABLES

TABLE 2.1: DATA ILLUSTRATING THE MINIMUM BEAM DIAMETER CORRESPONDING TO LATERAL ELECTRON EQUILIBRIUM (LEE) FOR DIFFERENT LINAC BEAM ENERGIES, ADAPTED FROM (LI, SOUBRA ET AL. 1995)	23
TABLE 2.2: A COMPARISON OF SELECTED FEATURES OF A SAMPLE OF DETECTORS.....	35
TABLE 3.1: SPECIFICATIONS FOR THE 0.125 CC IONISATION CHAMBER USED IN THIS STUDY (PTW-FRIEBURG 2008)	58
TABLE 3.2: SPECIFICATIONS FOR THE PINPOINT CHAMBER USED IN THIS STUDY (PTW-FRIEBURG 2008) ...	59
TABLE 3.3: SPECIFICATIONS FOR THE DIAMOND DETECTOR USED IN THIS STUDY (PTW-FRIEBURG 2008) .	60
TABLE 3.4: ORIENTATION OF LINEAR ACCELERATOR TO ILLUSTRATE THE DIFFERENT IN NAMING CONVENTIONS AS WELL AS COMMONLY USED TERMS.....	64
TABLE 3.5: SETTINGS USED FOR JAW DATA ACQUISITION.....	68
TABLE 3.6: SETTINGS USED FOR MLC DATA ACQUISITION	69
TABLE 3.7: ILLUSTRATION OF THE DATA FORMAT REQUIRED BY PINNACLE ³	75
TABLE 3.8: INFELD TAB PARAMETERS USED	79
TABLE 3.9: OUT-OF-FIELD PARAMETERS USED	81
TABLE 3.10: THE PINNACLE ³ DOSE MAP FORMAT REQUIRED. THE FILE ENDS WITH “PTS”.	84
TABLE 3.11: THE FILE FORMAT OF THE EXPORTED PINNACLE ³ PLANAR DOSE DISTRIBUTION.....	85
TABLE 3.12 TABULATED DATA OF PARAMETERS USED IN EXAMPLE CALCULATION OF TPR FROM PDD AND PSF.....	89
TABLE 4.1: TABULATED VOLUME, ACTIVE SIZE, AND PHYSICAL SIZE FOR DETECTORS USED (PTW-FRIEBURG 2008)	92
TABLE 4.2: TABULATED DATA SHOWING THE SPATIAL POSITION OF THE INFLECTION POINT, THE FIELD EDGE, AND THE RATIO OF THE TWO VALUES	98
TABLE 4.3: TABULATED DATA SHOWING THE AVERAGE DOSE AT THE INTERSECTION POINT AND THE DEVIATION FROM EXPECTED INFLECTION POINT <i>THE DATA IS DERIVED FROM A DEPTH OF 10 CM AT VARIOUS FIELD SIZES.</i>	103
TABLE 4.4: TABULATED DATA SHOWING THE EFFECT OF DETECTOR VOLUME ON DOSE WITH RESPECT TO THE REGIONS IN THE PROFILE.	105
TABLE 6.1: A SELECTION OF MODELS OF KERNELS USED FOR DECONVOLUTION.	133
TABLE 6.2: EQUATIONS RELATING TO THE DIFFERENT ORDERS OF GAUSSIAN FUNCTION, AND MAXIMUM DIFFERENCES FROM MEASURED DATA.	136
TABLE 6.3: NOTATION USED IN FIGURES 6.7, 6.8, 6.9.	140
TABLE 7.1: OVERESTIMATE OF THE PENUMBRA FROM ZE PENUMBRA IN MM WITH VARIATION WITH FIELD SIZE.....	151
TABLE 7.2: PENUMBRAL VARIATION OVER DEPTHS (1x1 cm ² FIELD SIZE); PLOT SHOWING THE DEPENDENCE OF THE DIFFERENCE IN PENUMBRA MEASUREMENT FROM ZE PENUMBRA WITH DEPTH.	152
TABLE 7.3: OVERESTIMATE OF THE PENUMBRA FROM ZE PENUMBRA IN MM WITH VARIATION WITH DEPTH.	153
TABLE 7.4: OVERESTIMATE OF THE FIELD SIZE FROM ZE FIELD SIZE IN MM WITH FIELD SIZE (SEE FIG. 7.2)	155

TABLE 7.5: OVERESTIMATE OF THE FIELD SIZE FROM ZE FIELD SIZE IN MM WITH DEPTH (SEE FIG. 7.3)	156
TABLE 7.6: MAXIMUM DOSE DIFFERENCE ALONG THE PROFILE OVER FIELD SIZE (SEE FIG. 7.4)	159
TABLE 7.7: MAXIMUM DOSE DIFFERENCE ACROSS THE PROFILE WITH DEPTH (SEE FIG. 7.5)	160
TABLE 7.8: TABULATED DATA OF OVERESTIMATES AND UNDERESTIMATES OF PROFILE WITH FIELD SIZE (SEE FIG. 7.6)	161
TABLE 7.9: TABULATED DATA OF OVERESTIMATES AND UNDERESTIMATES OF PROFILE WITH DEPTH (SEE FIG. 7.7)	162
TABLE 7.10: TABULATED DATA OF THE RATIO OF OVERESTIMATES AND UNDERESTIMATES OF PROFILE WITH FIELD SIZE. THE FIELD SIZE OF $2.3 \times 2.3 \text{ cm}^2$ WAS INTERPOLATED FROM THE GRAPH IN FIGURE 7.8. .	163
TABLE 7.11: SUMMARY OF THE DOSE ANALYSIS WITH COMMENTS ON THE CLINICAL IMPLICATIONS OVER FIELD SIZES.	169
TABLE 8.1: EXPERIMENTALLY DETERMINED COEFFICIENTS FOR THE NON-LINEAR ZE PENUMBRA EQUATION	181
TABLE 8.2: TABULATED DATA SHOWING A SUMMARY OF THE CHANGE IN ERRORS IN TERMS OF VARIATION OF PENUMBRA FROM THE ZE PENUMBRA DUE TO THE APPLICATION OF THE NON-LINEAR PENUMBRA EQUATION FOR THE JAW CROSSPLANE DATA	185
TABLE 8.3: TABULATED DATA SHOWING A SUMMARY OF THE CHANGE IN ERRORS IN TERMS OF VARIATION OF PENUMBRA FROM THE ZE PENUMBRA DUE TO THE APPLICATION OF THE NON-LINEAR PENUMBRA EQUATION FOR THE MLC CROSSPLANE DATA	188
TABLE 9.1: THE VARIATION OF THE PINNACLE SOURCE SIZE AND THE PINNACLE MODELLED PENUMBRA IN MM	196
TABLE 9.2: COEFFICIENTS OF THE POLYNOMIAL RELATIONSHIP BETWEEN THE PINNACLE SOURCE SIZE AND PINNACLE MODELLED PENUMBRA AT VARIOUS FIELD SIZES AND DEPTHS (FOR JAW CROSSPLANE DATA)	198
TABLE 9.3: AVERAGED PINNACLE SOURCE SIZES, VARIATION OF SOURCE SIZE WITH DEPTH, AND DEVIATION FROM THE ZE SOURCE SIZE FOR VARIOUS DATASETS OVER DEPTHS AT A FIELD SIZE OF 1×1 cm^2 (SEE FIGURE 9.2)	200
TABLE 9.4: AVERAGED PINNACLE SOURCE SIZES, VARIATION OF SOURCE SIZE WITH DEPTH, AND DEVIATION FROM THE ZE SOURCE SIZE FOR VARIOUS DATASETS OVER VARIOUS FIELD SIZES AT A DEPTH OF 1.5 CM (SEE FIGURE 9.3)	201
TABLE 9.5: TABULATED DATA SHOWING THE AVERAGE DIFFERENCE FROM CALCULATED SOURCE SIZE WITH THE ZE CALCULATED SOURCE SIZE OVER FIELD SIZE OF $1 \times 1 \text{ cm}^2$ AND DEPTH 1.5 CM. THE ZE SOURCE SIZE WAS 0.9 MM.	206
TABLE 9.6: MODELLING OF THE SENSITIVE DIAMETER OF PTW DETECTORS WITH MEASURED PENUMBRA IN COLUMN 3 (SEE EQUATION 8.5) AND THE PINNACLE RTPS SOURCE SIZE IN COLUMN 4(SEE EQUATION 9.1) AT A FIELD SIZE OF $1 \times 1 \text{ cm}^2$ AND DEPTH 1.5 CM.	210
TABLE 10.1: PINNACLE PARAMETERS USED IN THE PLAN 4 FIELD $1 \times 1 \text{ cm}^2$ (4FS1)	215
TABLE 10.2: PINNACLE PARAMETERS USED IN THE PLAN 2 FIELD $1 \times 1 \text{ cm}^2$ ABUTTED (2FSA)	215
TABLE 10.3: PINNACLE PARAMETERS USED IN THE PLAN 4 FIELD $10 \times 10 \text{ cm}^2$ (4FS10)	216
TABLE 10.4: PINNACLE PARAMETERS USED IN THE PLAN PROSTATE	216
TABLE 10.5: DOSE VOLUME HISTOGRAM DATA SHOWING THE MEAN DOSE OF VARIOUS STRUCTURES AS A FUNCTION OF SOURCE SIZE	234

TABLE 10.6: TABULATED RESULTS DETAILING THE MAXIMUM POINT DIFFERENCES AND SUMMED OVERALL CHANGE FOR THE $1 \times 1 \text{ cm}^2$ AND $10 \times 10 \text{ cm}^2$ FIELD SIZE BEAMS OVER A SINGLE FIELD AND FOUR FIELD ARRANGEMENT BETWEEN THE ZE MODEL AND THE IC MODEL	238
TABLE A.1: SETTINGS USED FOR THE INVESTIGATION OF JAW-MLC SEPARATION	253
TABLE C.1: TABLE SHOWING THE FWHM (FIELD SIZE) IN CM WITH VARIATION WITH DEPTH AND LEAF-END OFFSET FOR A MLC FIELD SIZE OF $1 \times 1 \text{ cm}^2$, JAW SETTING OF $30 \times 30 \text{ cm}^2$	263
TABLE F.1: FILE FORMAT OF THE MCC FORMAT USED WITH MEPHYSTO MC ² (PART 1/2)	280
TABLE F.2 FORMAT OF THE MCC FORMAT USED WITH MEPHYSTO MC ² (PART 2/2)	281
TABLE H.1: ANONYMOUS RESULTS FROM THE SOURCE SIZE SURVEY FOR THE PINNACLE RTPS (PTO)	289
TABLE I.1: DECONVOLUTION CODE USED IN MATLAB FOR THE THESIS (PTO)	295
TABLE J.1: CODE FOR CREATION OF THE PLANAR DOSE FILE FOR THE PINNACLE RTPS	298

LIST OF ABBREVIATIONS

Abbreviation	Meaning
3DCRT	Three-dimensional conformal radiation therapy
CPE	Charged particle equilibrium
d(DD)	Deconvolved DD data
d(IC)	Deconvolved IC data
d(PP)	Deconvolved PP data
DD	Diamond Detector
DDC	DD penumbra with non-linear penumbral correction (see Chapter 8)
DVH	Dose volume histogram
IC	0.125 cc Ionisation Chamber
ICC	IC penumbra with non-linear penumbral correction (see Chapter 8)
IMRT	Intensity modulated radiation therapy
LEE	Lateral electron equilibrium
MLC	Multi-leaf collimator
PDD	Percentage depth dose
PP	Pinpoint Chamber
PPC	PP penumbra with non-linear penumbral correction (see Chapter 8)
PTV	Planning target volume
QA	Quality assurance
RTPS	Radiotherapy treatment planning system
TPR	Tissue phantom ratio
ZE	Virtual zero extrapolated volume data

Abstract

Introduction With the adoption of technologies such as stereotactic radiosurgery in the treatment of cancer, there is an increasing trend towards smaller field sizes where the importance of accurate penumbral measurements is critical. Small segments are also common in intensity modulated radiation therapy deliveries; hence accurate dose assessment at the edge of multi-leaf collimated segmented fields is also paramount.

Clinically used detectors have significant detector volumes that contribute to measurement of wider penumbral dose profiles than the beam produces. This overestimate of penumbral width in turn has an impact on the radiotherapy treatment planning modelled dose distributions used for patient treatment. This is because the penumbra broadening in the dose profile affects the source size parameter used in radiotherapy treatment planning system. In this thesis, the extent of penumbral broadening was quantified and methods to produce data with effectively zero detector volumes were investigated. This data was used to calculate a source size for the computer model to best match the measured data.

Methods Data was measured for a 6 MV beam (Varian Clinac 600C) using a diamond detector, a pinpoint detector, and a 0.125 cc ionisation chamber. Extrapolation and deconvolution techniques were used to calculate zero detector volume data. The extrapolation technique was studied in detail and a new verification technique, which involved R^2 and dose differences, was developed to calculate the fit and errors associated with the extrapolation method. The amount of penumbral broadening and source size overestimation in Pinnacle decreased with decreasing detector diameter.

Results In this study, penumbral broadening of up to +1.8 mm (80%-20% penumbra) due to the detector volume effect was found to occur across both large and small field sizes and this resulted in overestimations in the source size parameter in the Pinnacle radiotherapy treatment planning system by +1.2 mm for the 0.125cc ionisation chamber (from the zero detector source size of 0.9 mm).

The effect of source size overestimation in Pinnacle was studied by the calculation of dose distributions with the virtual zero detector dataset and the 0.125 cc ionisation chamber dataset.

The point in the middle of the field had minimal change but there were changes in the dose distribution which were due to a summation of penumbral perturbations of each beam. It was found that for large field sizes ($\sim 10 \times 10 \text{ cm}^2$) the summed doses in the treatment region were underestimated by approximately 0.5%. For small field sizes

($1 \times 1 \text{ cm}^2$) summed dose in the treatment region was overestimated by approximately 3.5% while over the whole region there was an overestimation of approximately 11%. For the case of a 3DCRT prostate plan, changes in dose were underestimated by to 1% for volumes typical of the PTV and overestimated by up to +1.5% for volumes typical of organs at risk.

Equations were derived that produced agreeable links between the detector volume and the penumbral width as well as the penumbral width and the source size parameter in Pinnacle. The coefficients required in these equations were calculated from datasets obtained from the measurement of dose profiles by physical detectors and the calculation of dose profiles in the treatment planning system respectively. The use of these equations could be used to estimate and/or correct for the detector volume effect on the source size parameter in the treatment planning system with a minimum of beam measurement time. However, further investigations are required to verify this over a wide range of conditions such as beam energy and collimator design.

The 1D dose profiles measured with different detectors were analysed in terms of intersection point and inflection point. The results indicated that there were significant deviations of both these points from a normalised dose of 50% with small field sizes. There was an overestimate of the radiation field size (50%) by 0.8 mm measured with the 0.125cc ionisation chamber at the field size of $1 \times 1 \text{ cm}^2$ but at other field sizes measured the radiation field size was within $\pm 0.2 \text{ mm}$. The intersection point determined the spatial location of overestimation and underestimation of point and summed dose. The overall summed dose was found to be unaffected by the detector volume effect at a field size of $2.3 \times 2.3 \text{ cm}^2$, which was similar to the minimum field size for lateral electron equilibrium ($2.6 \times 2.6 \text{ cm}^2$).

Conclusions- The results of a survey of different radiotherapy institutions indicated that approximately half of measurements done for use in modelling the Pinnacle radiation treatment planning system involved the use of ionisation chambers (approximately 0.1 cm^3). In this study, it was demonstrated that (1) the detector volume effect is significant as matching the model to broad penumbra overestimates the virtual source size parameter by the order of +1 mm in Pinnacle; (2) that the effect on dose distributions for single fields in the penumbra the dose may be different by 1-10% compared with zero detector profile matched data (3) that corrections to the detector volume can be made with a new single detector technique combined with a predictive equation. This makes the correction more feasible with consideration to time constraints

Acknowledgements

In the course of my research, the length of time used was proportionate to my appreciation in the importance of scientific investigation in the extension of life, which the author concluded was important.

My largest source of appreciation goes to my supervisor, Professor Peter Metcalfe from the University of Wollongong. My memories of him as a model Medical Physicist are most aptly described in this enduring word, “stoic”: *a philosopher holding virtue to the highest good and teaching indifference to pleasure and pain, one of great self control*. His advice was given in areas that included beam modelling, lateral thinking and scientific writing. That discussions were often made over coffee or tea, and occasionally over a biscuit, made research accessible and satisfying.

At the inevitable risk of unintentionally excluding people who have helped me or underestimating the value in the importance of the help afforded to me, I will attempt to write, in no order of importance, my acknowledgements in a concise manner to:

- Anatoly Rozenfield, for his extensive knowledge in physics he shared to me
- Rashmi Gupta (St. George Hospital), for providing me with guidance in Pinnacle
- Wen Chuan Dong (Royal Hobart Hospital), for providing me with scientific discussions
- Robin Hill (Royal Prince Alfred Hospital), for the loan of the diamond detector
- Jim Boehm (St. George Hospital), for approval and discussion of my research and studies
- Bradley Oborn (St. George Hospital), for help with MATLAB and for useful discussions
- Nick Hardcastle (University of Wollongong), for his help with Pinnacle and Monte Carlo

A survey was made in the Pinnacle users email list which was instrumental to the study and many thanks extend to those who replied to me. Many thanks to my colleagues at the St. George Hospital for their role in training me as a Medical Physicist, with special mention to my former supervisors Ms. Feng Qin Chen and Ms. Gwi Ae Cho.

To those from whom I have received support from during my thesis, thank you. My family, extended family and close friends acted for my well-being. In particular, to those I have neglected when doing my research I would like to express my gratitude with the following: *I do not regret the things I've done, but those I did not do* (R. Cochrane).

Chapter 1: Introduction

1.0 INTRODUCTION TO THE THESIS

The impact of accurate small field dosimetry extends from limitations in small radiosurgery beams to small segments in Intensity-modulated Radiotherapy (IMRT-CWG). Due to small multiple segments used in IMRT, IMRT involves an increased amount of commissioning and QA of the dosimetric, mechanical, and treatment planning properties (Carlson 2001; Saw, Ayyangar et al. 2001; Saw, Siochi et al. 2001; Venencia and Besa 2004) before clinical use. The potential inaccuracies and uncertainties in IMRT include the accuracy of the measurement and modelling of small fields, which are superpositioned in IMRT as multiple segments are used to modulate the intensity of the beam.

The detector volume effects the dose measurement in regions where there is a dose gradient, most notably in the penumbra region of a dose profile. Small detectors such as diamond detectors have been studied (Azcona, Siochi et al. 2002) to investigate local difference of doses in the PTV due to this effect (Laub and Wong 2003). Techniques to minimise the detector volume effect by calculating the profiles associated with an effective detector size of zero were studied and compared.

The effect of detector size on the modelling of dose distributions from a radiotherapy treatment planning system (Pinnacle RTPS) is studied. The effect of detector size was found to influence the optimal source size parameter best employed in treatment planning to establish the best penumbral match. This in turn affects the dose distribution and consequently the dose to the PTV. The clinical significance of the detector volume errors are then compared to other dosimetric and mechanical errors associated with modern radiotherapy machines.

1.1 WHY IS RADIOTHERAPY IMPORTANT?

1.1.1 What are the leading causes of death?

A basic principle of modern civilisation and, in particular, of the healthcare sector, is the improvement of the quality of life of society through the use of medical technology to cure or to reduce the severity of disease.

In Australia, the most prevalent causes of mortality today are no longer from starvation nor from a lack of shelter. The major causes of death in the 1900s were infectious and parasitic diseases, respiratory disease, circulatory disease and cancer (AIHW 2008). Major strides were made in the form of advances in sanitation, nutrition, and medical knowledge which reduced the incidence of infection dramatically (Wiki 2008). The major causes are now due to cancer, injuries and poisoning, nervous system diseases, and cardiovascular disease (AIHW 2005), with the relative risk of these causes in causing the death of a member of our society depends on the age group (see Figure 1.1). Cancer is a significant contributor to current causes of death, with ~15% of deaths in males aged 1-44 years old, ~40% of deaths in males aged 45-84 years old, and ~20% of deaths in males older than 84 years (AIHW 2005). Radiotherapy is one of the major accepted treatments for cancer often in combination with other modalities (surgery and chemotherapy). For those people diagnosed with cancer most patients are suitable for referral for radiotherapy as the primary, adjuvant, or as the palliative treatment (Hansen and Roach 2007).

Please see print copy for image

Figure 1.1: causes of death for males, 2005 data from (AIHW 2005). The leading cause of death for females follows a similar curve, and data for this can be found in the literature.

**Digestive disorders (25-64 years age group), endocrine (65-84 years age group), and Genitourinary diseases (85+ year age group).*

1.1.2 An introduction to cancer and common cancers in Australia

Cancer refers to cells that undergo an uncontrolled, abnormal cell growth. They are the result of mutations in the DNA that cause a block in a set of rules in the cell, signalling a halt in cell growth.

Eventually, a single cancer cell will double, and continue to propagate until there is some form of diagnosis. This of course can either be made through self examination or via a medical professional – utilising imaging, detection using x-rays, other biochemical means, or until symptoms such as pain or bleeding start to occur in the patient.

There are also benign tumour cells, which do not generally cause major problems for their host, and malignant cancer cells, that have no clear borders and spread directly to surrounding tissues. In addition, malignant cancer cells can even

spread to other parts of the body and commence division –this is known as metastasis (Dollinger, Rosenbaum et al. 2002).

Data for 2005 (Tracey, Baker et al. 2005), regarding the most common cancers in NSW, Australia, are the cancers of the prostate (17%), bowel (13%), breast (12%), melanoma (10%), and lung cancer (ICRU29). The median age of diagnosis for cancer in men was 68 years and the median age in women was 66 years. The incidence rate for all cancers over all ages was 570 new cases per 100,000 for males (0.57%) and 390 new cases per 100,000 for females (0.39%). Cancer incidence rates have not changed significantly over the last 10 years in males while increasing by 7% for females. More significant is the trend towards increases in life-expectancy, which will increase the number of cancer treatments in Australia.

1.1.3 Trends in cancer incidence, risk factors for cancer, and cancer survival rates

Current life expectancies (AIHW 2008) are 78.5 years for males and 83.3 years for females in Australia (2005), in comparison with 71.2 years for males and 78.3 years for females in the 1980s, 67.9 years for males and 74.2 years for females in the 1960s, and 66.1 years for males and 70.6 years for females in the 1940s. The cohort life expectancies, based on calculations taking into account the decreasing future death rates, estimate life expectancies of 87.1 years for males and 90.4 years for females in Australia in 2050 (Babel, Bomsdorf et al. 2007).

In 1800, the worldwide life expectancy did not exceed 30 years (Riley 2001). Research into the discovery of genes relating to diseases and the ability to manipulate genes may increase the upper limit of survival to 150 years (Olshansky, Carnes et al. 1990). Increases in life expectancy is a sign of positive development in society, however as the population ages and cancer incidence follows, improvements in cancer treatment will become more important in maintaining the life quality of the population diagnosed with cancer.

Lifestyle factors may also play a role in the possibility of reducing the risk of cancer to improve life expectancy, as the major cancer risk factors estimated by (Dollinger, Rosenbaum et al. 2002) were diet (30-35%), tobacco (30-32%), viruses and infection (10%), sexual factors (7%), and alcohol (3-4%). The cancer risk factor for radiation (environmental, medical, and diagnostic dose) is 1%, for sunlight (ultraviolet) is 1%.

A diet high in fat involves an increased risk of cancers of the colon, uterus, and prostate and may be prevented with a diet rich in fruits and vegetables for a healthy dose of fibre, vitamins, and minerals. Use of tobacco increases the chances of cancers of the lung, larynx, mouth, esophageus, bladder, kidney, throat, stomach, pancreas, or cervix, and incidence is reduced by the avoidance or reduced intake of tobacco (including smokeless tobacco products). Infection with certain viruses can increase the risk of cancer, e.g. years of infection with the Hepatitis B and hepatitis C viruses can cause liver cancer, and the incidence of viruses may be controlled with vaccinations (NCI 2008).

The risk of cancer from radiation is stochastic, based on probability, with doses above 100 millisieverts received in a short time increasing the risk of developing cancer linearly with dose. The risk, averaged over all ages and cancer types is about 1 in 100 for every 100 millisieverts of dose (ARPANSA 2008). In terms of developing a guideline for radiation safety, the ICRP (International Commission on Radiation Protection) has set a limit on members of the public of 1 mSv in a year. The annual average radiation dose to the Australian population from natural background was surveyed to be 2.3 mSv per year (ARPANSA 1990), which when compared with other cancer risk factors may explain the low probability of cancer incidence from radiation when compared with larger risk factors such as diet, tobacco, and viruses.

The current five-year survival after diagnosis for all types of cancer was 63%, with a five year survival for 88% for breast and prostate cancer, 65% for bowel cancer, 90% for melanoma, and 14% for lung cancer (Tracey, Baker et al. 2005). In terms of treatment of cancer, the trend in the data quality index related to radiotherapy is the ratio of mortality to incidence (M/I). This ratio may be due to a variety of factors, which may include a combination of improved diagnosis or treatment. The M/I for various cancers have improved through the years (Tracey, Baker et al. 2005), in particular prostate cancer (59% in 1972, 16% in 2005), bowel cancer (61% in 1972, 36% in 2005), breast cancer (38% in 1972, 22% in 2005), and melanoma (20% in 1972, 11% in 2005). Improvements of the M/I ratio have been achieved through research and development into new modalities and techniques in cancer treatment.

1.1.4 The use of radiotherapy in cancer treatment and how radiation kills tumour cells

Various cancer treatment options are available depending on the site of the cancer in the body. For example, with prostate cancer, surgery and radiotherapy are the primary

modalities with hormonal manipulation and chemotherapy as other options (Kaisary 1999); for bowel cancer, surgery is the primary option with radiotherapy and chemotherapy for the management of metastasis; for breast cancer, surgery and radiotherapy are primary modalities with chemotherapy as an optional adjuvant (Hansen and Roach 2007). Radiation therapy has been used in approximately half of all treatments of cancer, both as the primary treatment method or concurrently with other modalities such as surgery and chemotherapy (Hendry, Jeremic et al. 2006).

Radiation can kill both normal and tumour cells by direct or indirect action. Direct action involves radiation ionizing molecules in the DNA to cause strands to break. Indirect action involves the production of free radicals, with the predominant reaction being the production of hydroxyl radicals when water is ionised by radiation. In addition, the range of indirect damage is within 10^{-10} m of the site of interaction, with damage there is short time for repair of the DNA, but this repair is becomes less likely with extra DNA breaks within four base pairs of the first (Metcalfe, Kron et al. 2007).

Cell death by radiation involves probability, with an increasing dose providing an increase in the tumour control probability (TCP) –and also an increasing normal tissue complication probability (NTCP). The primary aim is to maximise the radiation dose to the tumour to irradiate the cancer cells while minimising the dose to normal cells. Radiation to cells in normal tissue can cause two types of reactions: early tissue reactions refer to the damage of renewing cells (such as the bone marrow) which results in decrease or a complete obstruction of the production of mature cells in such a cell line (Hendry, Jeremic et al. 2006); late tissue reactions refer to damages to infrequently dividing cells that may be clinically expressed 3 months or later (Tannock, Hill et al. 2005), and cause different types of cell death, e.g. radiation-induced apoptosis (cell suicide).

1.2 HOW IS MEDICAL RADIATION DELIVERED IN RADIOTHERAPY?

1.2.1 Historical advances leading to the modern radiotherapy treatment

Radiotherapy has been in limited use of for over 100 years since the discovery of x-rays, but has only been in widespread use for about 40 years since the development of the Cobalt-60 machine which was followed by the medical linear accelerator. A short

timeline of important discoveries in radiotherapy are outlined below (Van-Dyk 1999), with a brief note on the significance of each discovery.

- i. 1895, Wilhelm Conrad Roentgen discovers x-rays.
The use of x-rays for diagnosis was quickly realised.
- ii. 1899, First radiotherapy patient treated.
Cancer cured but there was recurrence and normal tissue injury.
- iii. 1910, First Brachytherapy patient with radium needles
The use of needles for brachytherapy (close range radiation) is still used today.
- iv. 1911, The field of radiobiology is born.
Fractionization, involving splitting a single treatment over various fractions, was investigated.
- v. 1913, X-ray tube with a peak of 140 kV
The peak of 140 kV allowed treatment of superficial tumours.
- vi. 1951, Co60 gamma ray developed
The average energy of the Co60 of 1.25 MeV allowed treatment of deeper tumours with skin sparing.
- vii. 1960s, Linear accelerator developed
Development of the modern linear accelerator design was achieved.
- viii. 1970s, CT introduced in radiotherapy physics
The use of CT imaging in radiotherapy allowed 3D treatment planning to eventually become routine.

Please see print copy for image

Figure 1.2: Comparison of data from depth dose curves of 100 kV photons (Koch & Sterzel Therapix C100) and 6MV photons (Clinac 600C) at St. George Hospital

The major significance of the development of linear accelerators can be illustrated in an analysis of the depth dose curves (see figure 1.2). Low energy photons deposit most of their dose at the surface and are limited in treating deep-seated tumours as the surface dose would cause major problems such as erythema or delayed-cell necrosis. However, low-energy photons are still widely used but mainly for treatment of surface tumours (e.g. skin cancers).

For deep-seated tumours in areas such as the breast and the prostate, radiation dose at a length of several cm inside the body is required. The ability of photon energies from the linear accelerator to deposit a significant amount of their energy at a clinical depth (e.g. ~66% at 10 cm deep for 6 MV photons), in addition to the ability to deliver very low doses at the surface has made the medical linear accelerator the most popular device for radiotherapy currently (Metcalf, Kron et al. 2007). It should be noted that skin sparing was first introduced with the Co-60 beam (nominal energy at 1.25 MV), but was superseded by medical linear accelerators which were capable of multiple higher energies and a higher dose rate.

1.2.3 How the linear accelerator produces a clinical photon beam

To achieve electron energies in the megavoltage range (10^6 eV), modern linear accelerators apply microwave power to further accelerate the electrons after their initial acceleration in a strong electric field (see figure 1.3). The basic concept involves the following steps (Karzmark and Morton 1997; Van-Dyk 1999; Metcalfe, Kron et al.

Please

se
see
prin
cop
y fo
ima
ge

Please see print copy for image

Please see print copy for image

gun.

- a. This is powered by a *modulator*, which supplies high power pulses, and a *control unit*, which provides the timing for the modulator.
 - b. Initial acceleration of the electrons is made through the voltage difference between the cathode and anode.
2. Electrons enter the accelerating waveguide with the speed from the initial acceleration
 - a. Energy is transferred from high power RF (radiofrequency) fields to accelerate the electrons using microwave in phase with electrons from the gun.
 - b. The RF power is derived from either a *klystron* or a *magnetron*, with the *pulsed modulator* supplying the high voltage, high current, short duration pulses to the RF power.

- i. Magnetrons are a source of RF power with an array of resonant cavities that accelerate and decelerate electrons into bunches to produce RF power output that is transported using an aerial. They tend to be used on lower energy linacs (4-8 MeV)
 - ii. Klystrons is a RF power amplifier that amplifies an input RF from a RF driver. Electrons are emitted from the cathode and they pass through a buncher cavity, and are accelerated or decelerated in the oscillating RF field and are bunched into a velocity determined by the resonant frequency of the buncher cavity. The electrons will transfer their energy to the RF field of the catcher cavity if the catcher cavity has the same resonant frequency as the buncher cavity.
 - c. A *circulator* is installed between the RF generator and the accelerating waveguide to prevent reflected radiation from moving back to the generator –instead, the circulator absorbs energy from reflected radiation and dissipates the heat through water cooling.
3. Electrons are steered and focused from the accelerating guide towards the target
- a. *Steering coils* in the accelerating waveguide maintain the beam position to within the centre of the waveguide and towards the desired track.
 - b. *Focusing coils* in the accelerating waveguide minimises the beam divergence in the cross section, which may be due to electron repulsion in the pencil beam and a variation in the radial component of the electric field.
 - c. *Bending magnets* are employed in some linear accelerators as part of the steering of electron beam transport systems for linacs above 6 MeV as the accelerator waveguides are too long to be mounted vertically. Bending magnets serve to guide the electrons exiting the accelerator waveguide into the target, usually at 90° or 270° .
4. Electrons are incident on the target to produce photons which are then shaped
- a. Electrons are incident on the target after the bending magnet and generate *bremsstrahlung photons*, as well as collisional losses and scattered electrons.
 - b. After the target is the *primary fixed collimator*, a divergent cone structure composed of tungsten designed to prevent head leakage, by absorbing

photons not directed towards a 50 cm diameter circular beam at 100 cm SSD.

- c. Clinical treatment plans aim towards a homogenous dose distribution in the tumour volume, and the *flattening filter* aims to attenuate the forward peaked photon output from the target into a flatter beam. The desired flatness is refers to a profile measured at 10 cm depth with a field of 40 x 40 cm². The flattening filter is shaped like a cone with the cone facing a target so that the higher fluence region of the photon beam (centre) is attenuated more than the outer regions.
 - i. The flattening filter has to be sufficiently thick as a large proportion of transmitted electrons through a thin target will then become incident on the flattening filter to act as an addition source of photons.
 - ii. The flattening filter is usually made of copper, with varying thicknesses depending on energy.
- d. Two sets of *secondary collimators* (also called *jaws*) are positioned below and are driven by motors to conform tho the field size required. They are designed so that the face of the jaw is parallel to the beam divergence.

1.2.4 How the linear accelerator maintains beam output and symmetry

Two sets of *monitor unit ionisation chambers* are mounted under the flattening filter in order to monitor the beam output and shape. The first set consists of four sections of parallel plate ionisation chambers to measure the symmetry, flatness, and beam output in the transverse direction of the beam. The second set consists of a similar configuration but measures the radial direction of the beam (Metcalf, Kron et al. 2007).

These monitor unit ionisation chambers record dose in *monitor units (MU)*, which are the monitors of the beam dose output. The institution will need to follow international protocols, e.g. the procedure as specified in TRS-398 (Andreo, Burns et al. 2004), to calibrate the linear accelerator, with an example of this being the calibration of 1 MU to 1 cGy at 100 cm SSD with a field size of 10 x 10 cm² at d_{\max} in water. The machine is able to use a feedback system to maintain a constant dose rate, considered in terms of MU/second, and to deliver a precise amount of radiation dose by terminating the beam once the desired amount of MU as monitored is delivered.

In addition to adjustment of the beam output, the monitor unit ionisation chambers are also able to detect and measure symmetry of the beam. If the electron beam is incident at an angle to the target, the angular steering of the incident electron beam by the current adjustment to the bending magnet is required and if the electron beam is not incident at the centre of the target, positional steering is required. The *electronic beam steering control circuit* in the bending magnet is also able to use a feedback system from the external MU chamber segments to maintain beam symmetry (Metcalf, Kron et al. 2007).

1.2.5 How the linear accelerator directs the beam towards the patient

In clinical use, the linear accelerator has a complex network of calibrated light, radiation, and mechanical positioning aids for precise radiotherapy treatment delivery to patients. The linac has three degrees of movement: the couch, the collimator, and the gantry. Any combination of these three motions is able to provide a beam at any angle to the patient (Metcalf, Kron et al. 2007). To be more specific, the gantry and the collimator can rotate along its axis while the couch can move, by rotation, vertically, longitudinally, and laterally.

1.2.6 Quality Assurance Tests for linear accelerators

As the linacs involve potentially dangerous radiation doses, any fault conditions and inaccuracies are to be avoided. Inherent faults may sometimes be detected by the internal checks, which trigger *interlocks* that disable the beaming of the machine temporarily. The quality assurance of the linac is the responsibility of the medical physicists, and this represents a substantial workload in the verification and the maintenance of the machine. The machine, if found to be out of tolerance in a particular subsystem, can be recalibrated to an improved level of performance or precision.

The manufacturers of linacs have design specifications, which are included in tender documents. However, guidelines exist for test selection, protocol, and tolerances from organisations and are given in documents such as IPEM report 81 (IPEM 1999), the report from AAPM TG40 (AAPM 1994), and the ACPSEM position paper (Millar, J et al. 1997).

There are different types of checks, with selected examples of tests and tolerances:

- i. Electromechanical tests: these check that the mechanical parts have linear movement, reproducible movement, accurate movement, and that indicators are accurate.

Light and radiation field coincidence: Check that the light field corresponds to the radiation field, tolerance 2 mm or 1%.

- ii. Radiation tests: these check that the beam has the correct shape and is providing the correct output accurately and linearly.

X-ray output constancy: Measure the beam output independently and check that the output is constant and consistent, tolerance 2%.

- iii. Safety tests: these check that interlocks are triggered with machine malfunction and that in an emergency the machine will stop beaming

Door interlock: Check that if the door interlock inhibits and stops beaming, tolerance met if functional.

1.3 MODERN ADVANCES IN LINAC RADIOTHERAPY

1.3.1 Development of MLCs with 3DCRT as a major improvement in radiotherapy

Physical strategies tend to focus on the improvement of dose distribution in the patient by optimising the shape of beams with respect to shaping the beam edges, modulating the shape of the beam, the intensity of the beam, and the angular directions of multiple beams. Early radiotherapy treatments involved shaping the beam in rectangular shapes to the target volumes in the *beam's eye view* (BEV). It was observed in the 1960s that tumour volumes were irregular in shape and that this required a shaping of the radiation beam. This was a basic but important improvement in the field of radiotherapy that served to reduce the volume of normal tissue irradiated and to reduce the dose to critical structures close to the boundaries of the tumour volumes (Mayles, Nahum et al. 2007).



Figure 1.4: Illustration of the difference between conventional and conformal therapy (Webb 1993)

The shaping of the beam (see figure 1.4) was initially performed with customised lead blocks, which were manufactured to project a shadow to match the area being shielded. Issues with this method involved practical issues such as the weight of the blocks, the time required to manufacture the blocks, and the issues of attaching the blocks to the shadow tray of the linear accelerator in a non-horizontal position. The physical issue was that most blocks were constructed with parallel sides, which compromised the beam penumbra as the sides of the blocks didn't match the divergent beam lines (Webb 1993). A superior solution was found with development of the multileaf collimator

(MLC), which involve motor-driven leaves that are individually driven to allow flexible beam shaping (Metcalf, Kron et al. 2007). This modulation of the beam shape to conform to the tumour volume is known as 3D conformal radiotherapy (3DCRT).

1.3.2 Use of small segments with IMRT to avoid critical organs

The next advance was by IMRT, developed into a clinical role in the 1990s, which involved further modulating the field in terms of intensity within the field and the optimisation of radiation fields with the specification of dose objectives. The intensities of rays that go through sensitive normal tissues can be decreased and the intensities that go through tumour volumes can be increased. The treatment planning procedure changed into specifying clinical objectives and constraints and allowing inverse planning algorithms to find an optimal solution iteratively, with most solutions converging on less than 10 intensity-modulated beams (Bortfield 2006). IMRT enhances the difference in dose between the tumour volume and critical organs and allows for the choice of better local control with reduced morbidity or the same cure with fewer acute side effects (Webb 1993).

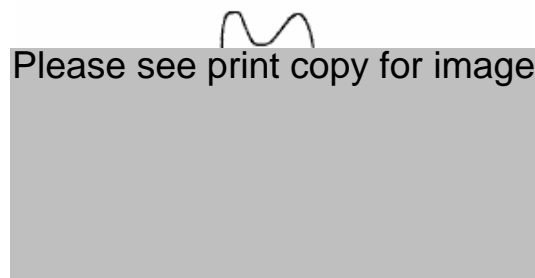


Figure 1.5: Diagram showing five intensity modulated profiles to treat the target volume (hatched), illustration from (Brahme 1988)

3DCRT delivered conformal radiation profiles that were shaped to the tumour shape (see figure 1.5). IMRT also delivers a radiation profile that conforms to the tumour shape but in addition modulates the intensity- this modulation of intensity in IMRT was achieved with a series of different leaf configurations (each known as a *segment*) for the MLCs (Azcona, Siochi et al. 2002), and the superposition of doses from all segments creates the required non-homogenous profile. This is illustrated as one of the intensity modulated profiles in figure 1.6. The superposition of a combination of these profiles incident towards the patient creates superior patient plans, allowing the sparing of critical organs.

Please see print copy for image

Figure 1.6: An isodose curve from a head and neck plan with IMRT that illustrates the sparing of the parotid glands, illustration from (IMRT-CWG 2001)

1.3.3 The importance of accuracy and precision in radiotherapy treatments

Accuracy and precision are crucial in radiotherapy, and the effectiveness of the radiotherapy treatment relies on the dose distribution in the tumour and the surrounding tissues. The concept of accuracy and precision, especially in radiotherapy, may require further elaboration:

Accuracy refers to errors that are of a systematic nature. Repeated measurements do not improve the accuracy of the measured result. Precision, however, refers to errors that are related to the reproducibility of measurement under the same conditions (Metcalf, Kron et al. 2007). Repeated measurements or averages of measurements improve the variation as the average approaches the true mean.

In clinical practice, accuracy refers to how accurate the dose distribution planned conforms to the actual tumour volume. In the real world, due to the physical characteristics of megavoltage photon beams, there are significant doses around the tumour volume. 3DCRT was the first major step towards improvement of precision in radiotherapy, with IMRT being the next major step.

Precision refers to the uncertainty of the delivered dose distribution with respect to the planned dose distribution. This may include the error involved with inter-fraction and intra-fraction variations during treatment.

Delivering dose accurately is important. From clinical observation, a difference in patient dose of 10% is detectable for tumours and a difference in dose of 7% is

observable for normal tissue reactions (IPEM 1999; Van-Dyk 1999). Due to patient variability other groups have alternative views on dose tolerances. A difference of 5% in dose is considered to make a clinically significant difference in TCP and NTCP (Brahme 1984). In terms of radiobiology, the tolerance values for accuracies for normal cells and tumour cells are similar because both TCP and NTCP have a high sensitivity with radiation dose at a similar region of interest on the dose response curves(see figure 1.7).



Figure 1.7: Dose-response curve for tumour control and normal tissue response. Small arrow indicates the effect on dose response with 5% change in dose. Illustration from (Van-Dyk 1999)

1.3.4 Challenges in IMRT segment dosimetry

IMRT is inherently more complicated than 3DCRT and many issues have arisen in IMRT that have the potential to compromise accuracy. The technique of IMRT itself involves dose inhomogeneity, and verification of IMRT doses involves increased uncertainty due to sharper dose gradients (Sanchez-doblado, Hartmann et al. 2007). In addition, segments in IMRT can become as small as $1 \times 1 \text{ cm}^2$ and the use of small fields involves a lack of electronic equilibrium (Lydon 2005).

Factors affecting dosimetry that may compromise accuracy in IMRT also include the technique used for modulating the fluence, the dose calculation algorithm and other aspects of the planning system, and mechanical limitations of the MLC hardware (Arnfield, Wu et al. 2001). There are also a larger amount of small segments with inaccuracies due to the volume effect of dosimeters with the penumbral dose becoming another factor (Kron, Elliot et al. 1993; Chang, Yin et al. 1996; Laub and Wong 2003).

1.3.5 IMRT and the link between precision, accuracy, therapeutic ratio, and margins

In radiotherapy, improved accuracy refers to improved dose distributions around the tumour volumes. This improves the *therapeutic ratio*, which is considered to refer to the ratio of tumour control and normal tissue complication probabilities at a specified dose level (Van-Dyk 1999). A combination of increased tumour control and reduced normal tissue complications is possible. A discussion of precision and uncertainty in radiotherapy should also include the issue of margins in radiotherapy. ICRU report 50 (ICRU 1993) outlines a clinical protocol recognised internationally:

- GTV: the gross tumour volume refers to the demonstrated size and location of malignant tumour.
- CTV: the clinical tumour volume refers to the GTV with a margin to include microscopic subclinical tumour cells.
- PTV: the planning target volume refers to a margin to include patient repositioning and uncertainties. This also includes the net effect of all geometrical variations.
- Treated volume: this refers to the volume that receives a high dose close to the planning volume.
- Irradiated volume: this refers to the volume that receives a significant amount of dose.

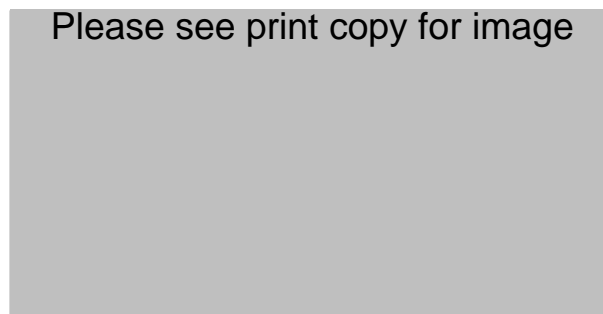


Figure 1.8: Figure showing the tumour cell and illustrating the GTV (A), CTV (B), and the PTV (C). Diagram from (Van-Dyk 1999).

IMRT has a benefit of increased accuracy and better conformity of the dose distribution to the tumour volume. However, as the conformity of IMRT plans is better, the correct definition of PTV is more critical to prevent increased dose out of field to prevent tumour recurrence. Research into individual components of IMRT can decrease the degree of uncertainty in the modelling, measurement, and delivery of IMRT and improve treatment outcomes in the future.

Chapter 2: Literature Review

2.1 INTRODUCTION TO SCOPE OF STUDY

2.1.1 Small field

The term *small field* relates to specific criteria in the scientific literature. One set of criteria relates to the consideration of the exposed parts of the beam source with the projection of the detector through the beam aperture that involves the source size, together with considerations of the detector size utilised in measurement, and the lateral electron range in the medium (Das, Ding et al. 2007).

In terms of actual field sizes with respect to lateral electron equilibrium, for a beam energy of 6 MV, a small field was defined, conservatively, to be 2-3 cm beam diameter (Björngård, Tsai et al. 1990; Li, Soubra et al. 1995; Crop, Reynaert et al. 2007). In terms of field sizes with respect to the relative exposure of the detector to the entirety of the source distribution in the linear accelerator head, it has been established that there exists some field size where further reductions will effectively block the detector from the beam source (Das, Ding et al. 2007), since the beam source is not an effective point source (this will be discussed in later chapters). The first effect will come into consideration in this study, where a minimum field size of $1 \times 1 \text{ cm}^2$ was studied. The second effect is likely to occur at field sizes in the range of source sizes ($\sim 2 \text{ mm}$), and will not be studied in our investigations.

The beam conditions of the small field are different to typical clinical fields characterised by electron equilibrium across most of the beam inter-umbra (fields greater than $3 \times 3 \text{ cm}^2$). Due to a hardening effect with the flattening filter, small field sizes are characterised by a harder photon beam spectrum, with an increased average photon energy spectra (Heydarian, Hoban et al. 1996; Crop, Reynaert et al. 2007; Das, Ding et al. 2007). This is due to the attenuation and beam hardening from the flattening filter –photons collimated by small fields undergo an increased amount of attenuation predominantly from the thickest central region of the flattening filter which effectively filters out low energy incident photons. In addition, there is a decreased scatter contribution from small fields compared to large fields, which contributes to a decreasing variation of photon energy spectra with depth as well (Heydarian, Hoban et al. 1996).

Small field dosimetry is a challenging area of research because of physical reasons such as electron disequilibria, and also because of technical reasons. Due to technological limitations in the manufacture of an ideal detector, there are significant discrepancies (up to 10%) in essential dose measurements in small photon beams between various radiation detectors, even for detectors specifically designed for the purpose. (Zhu and Bjarngard 1994; Cheung, Choi et al. 1999; Kubo, Wilder et al. 1999; Zhu, Allen et al. 2000; Tsai, Rivard et al. 2003; Ding, Duggan et al. 2006). Even in terms of experimental techniques, imperfections in the alignment of the detector in the beam axis and field size variations have a sensitive effect on depth dose curves in small field dosimetry (Vlamynck, Palmans et al. 1999). In short, challenges in dose measurements in small fields introduce a greater probability of significant error (Das, Ding et al. 2007) as compared to field sizes exhibiting electron equilibria.

2.1.2 Radiotherapy involving small fields: IMRT and stereotactic irradiation

Various forms of radiotherapy involve small fields. The delivery of IMRT often requires segments as small as 2 cm or less in at least one dimension (Laub and Wong 2003; Arnfield, Otto et al. 2005), while stereotactic irradiation involves the treatment of lesions 3-4 cm in diameter (Heydarian, Hoban et al. 1996; Clark, Teke et al. 2006) with typical volumes as small as 1 cm³ (Van-Dyk 1999). Although the focus of this thesis is aimed at clinical applications of 3DCRT and IMRT, the application of improved accuracy in small field dosimetry will involve similar techniques and advantages with reference to stereotactic irradiation.

In defining the scope of clinical treatments in terms of small fields, the measurement of small field sizes is not discrete but quantised because the field size in IMRT is defined by the MLC. Smaller field sizes than 1 cm can be achieved in the direction of the MLC leaf motion but no further decreases from 0.5 cm (Varian) in field sizes can be made in the direction perpendicular to the direction of MLC leaf motion (Varian have recently marked a 2.5 mm MLC in 2009). This is because scaling to lower treatment diameter comes to a limit due to the mechanical complexity of the MLC and the physical dimensions of the parts in the MLC limit the minimum leaf size possible (Biggs, Capalucci et al. 1991; Vlamynck, Palmans et al. 1999).

On the other hand, although both IMRT and stereotactic irradiation can use small fields to treat lesions in proximity to vital radiosensitive structures, there is no theoretical limitation in their use to other sites and regions of the body. In fact

developments have been made for their use in the treatment of larger tumours (Heydarian, Hoban et al. 1996). Currently, IMRT can treat all clinical sites with the application of MLC segments often within the planning target volume (PTV) itself (Laub and Wong 2003).

Potential clinical benefits from IMRT involve the minimisation of complications due to better target to normal tissue ratios with IMRT compared to 3DCRT. The use of computer optimisation of treatment plans with the use of MLCs with computer automation to deliver complex fluence distributions (Carlson 2001) is superior to manual plans with 3DCRT because 3DCRT is limited by the number of segments (complexity) and also by the experience and skill of the planning personnel (technique).

The potential for dosimetric error of IMRT includes the use of a larger amount of radiation which involves more leakage dose to the patient. With respect to the leakage dose, it was found that IMRT itself did not contribute to greater skin doses (Dogan and Glasgow 2003). The precision in MLC mechanical movement would depend more on the leaf sequencing technique, which involves either the step-and shoot system, the sliding window technique, or the use of multiple dynamic arc (Saw, Siochi et al. 2001; Arnfield, Otto et al. 2005). However, the error between measured and modelled data among five European radiotherapy departments in a study of IMRT quality assurance was attributed primarily to the volume effects in the commissioning data (Arnfield, Otto et al. 2005).

The benefits, which may lead to improved patient treatment and an increase in patient referrals, also involve a more complex measurement and model of small fields (discussed above), and may increase operational costs (Bruch and Zhen 2000). This is due to the more stringent requirements in accuracy and performance of the linear accelerator hardware: IMRT involves acceptance testing and commissioning, routine IMRT QA, and patient specific QA (LoSasso, Chui et al. 2001) because IMRT is more sensitive to MLC characteristics such as the tongue-and-groove design, leaf end curvature, and leaf transmission (Arnfield, Otto et al. 2005).

2.1.3 Lateral electron range and equilibrium

An inherent quantity important in the definition of the small field is also a core issue in the discussion of small field dosimetry. It is the lateral electron range, and not the forward range, that is the critical parameter in the determination of the penumbra (Das, Ding et al. 2007). In the case of charged particle equilibrium (Fidanzio, Azario et al.), dose in the medium equals the kinetic energy released; outscatter electrons (energy from

original interaction site) are replaced with the same amount of energy as in scatter electrons (energy from nearby interaction sites); electron equilibrium fails if the interaction site is in proximity to or in a field edge (in large field sizes) or when the lateral spread of secondary electrons is large compared to the field size (Lee, Pankuch et al. 2002).

The range of secondary particles, relating to the consideration of electron equilibrium, is dependent on beam energy, composition of the medium, and density of the medium (Das, Ding et al. 2007). The maximum lateral range of the primary electrons is approximately equal to the depth of maximum dose, and therefore lateral electron equilibrium is achieved when the radiation diameter is twice the maximum lateral range of primary electrons (Heydarian, Hoban et al. 1996).

In the case of 6 MV photons, which have a nominal d_{\max} (the depth at which the dose is maximum) of 1.5 cm, the estimated maximum diameter at which there is lateral electron equilibrium is 3.0 cm in a water phantom. This is consistent with estimations from other researchers, who have estimated values of 3.0 cm (Crop, Reynaert et al. 2007) and 2-2.6 cm (Björngard, Tsai et al. 1990).

Monte Carlo simulations (Li, Soubra et al. 1995) have also evaluated a relationship between the minimum beam radius required for lateral electron equilibrium (LEE) and the function of beam quality relating to $TPR_{20,10}$ (defined as the TPR at depth 20 cm divided by the TPR at depth 10 cm). The relationship was found to be:

$$r_{LEE} [g / cm^2] = 5.973(TPR_{10}^{20}) - 2.688 \quad (2.1)$$

Relationship between the radius associated with lateral electron equilibrium (LEE) and the beam quality factor $TPR(20,10)$ adapted from (Li, Soubra et al. 1995)

Simulations with this relationship (Equation 2.1) have illustrated the dependence of the beam energy with the minimum radius corresponding to LEE (and therefore, also in essence defining the *small field* criteria).

Table 2.1: Data illustrating the minimum beam diameter corresponding to lateral electron equilibrium (LEE) for different linac beam energies, adapted from (Li, Soubra et al. 1995)

Please see print copy for image

In the region of lateral electron equilibrium, electron energies from zero to maximum photon energies are present but in regions of lateral electron disequilibrium, there is a lack of low energy electrons that would have contributed dose to the central axis at distances near the maximum electron range (Wu 2007). The penumbra region, which is defined by the lateral electron disequilibrium, is therefore also dependent on beam quality (Das, Ding et al. 2007).

Furthermore, the introduction of a detector in field causes increase in lateral electron disequilibrium (Heydarian, Hoban et al. 1996) and this perturbation will be discussed in the chapters to follow.

2.1.4 Relevance of this study to small field research

The study related to this thesis aims to investigate the effect of detector volume on a variety of field sizes that includes both small fields and fields with lateral electron equilibrium. The significance of the detector volume effect can be quantified as dependent on field size.

2.2 PHYSICS IN THE PENUMBRAL REGION

2.2.1 Discussion of the characteristics of the penumbra

The penumbra, normally defined as distance between the normalised dose value of 80% and 20%, characterises the edges of the beam profiles for large field sizes. For small field sizes, however, the penumbra characterises the entire profile due to the lack of lateral electronic equilibrium.

2.2.2 Penumbra change as a function of field size

The jaw motions are designed to be focused on the radiation and therefore the penumbra is expected to show a low dependence on the field size. It was experimentally observed that for divergent blocks, the penumbra was constant in the linear region of the penumbra (80%-50%) with field size. However, the penumbra width increased with the 90%-50% and the 95%-50% definition of the penumbra (Biggs, Capalucci et al. 1991)

The contribution to the penumbra includes the beam spot size, phantom scatter, and the alignment of the collimator edge to the source (Biggs, Capalucci et al. 1991).

2.2.3 What penumbra broadening involves

Penumbra broadening refers to a broadening of the penumbra in the *measured profile* from the *true profile*. The measurement of the profile with the detector introduces this phenomena due to the detector effect (Pappas, Maris et al. 2006). The two aspects of penumbra broadening due to the detector effect are the *volume averaging component* and the *electron transport alteration component*. (Pappas, Maris et al. 2006).

Discussion of these two effects should be explicit to avoid confusion. It has been suggested (Pappas, Maris et al. 2006) that the term *size effect* or *volume effect* to be only be used with respect to volume averaging (unless with an explicit statement indicating the inclusion of the electron transport alteration component), and that the *detector response function* (in relation to the convolution method) be inclusive of all sources of penumbra perturbation.

Another aspect of penumbra broadening is that this error is a systematic error that contributes to the total error (Garcia-Vicente, Bejar et al. 2004), since systematic errors do not average out like random errors. The implication of this is that the penumbra broadening effect is important, and because it is readily measurable, techniques with zero detector size calculations or the use of superior detectors to minimise this effect are readily justified.

2.2.4 Geometric, radiological, and measured penumbra

The penumbra width is contributed to two component effects. Firstly, the *geometric penumbra* refers to the penumbra due to the radiation source spatial distribution (Sharpe, Jaffray et al. 1995). In theory, the geometric penumbra created will have a slanted but straight edge that takes into account attenuation but not scatter (AAPM 2008).

Please see print copy for image

Figure 2.1: Schematic diagram of the collimator geometry illustrating the variables for the calculation of geometric penumbra, from (AAPM 2008). Note that the SCD for Varian machines is 38.0 cm for the X Jaw and 48.3 cm for the Y Jaw.

The concept of similar triangles can be used to calculate the geometric penumbra (Mould 1981; AAPM 2008), with the following relation.

$$\frac{P_d}{AB} = \frac{CE}{AC} = \frac{CD}{BC} = \frac{FH}{OF} \quad (2.2)$$

Rearranging the equation gives

$$P_d = AB \times \frac{FH}{OF} = d_s \times \frac{(SSD + d - SCD)}{SCD}. \quad (2.3)$$

The spatial resolution of the x-ray radiation source consists of an intense and localised focal region and a broadly distributed low intensity extrafocal region (Jaffray, Battista et al. 1993). Partial eclipsing of the penumbra due to the extrafocal region can lead to a degradation of penumbra (Jaffray, Battista et al. 1993) that leads to overestimation of the field size with measurement (Das, Ding et al. 2007). Therefore, there may be a degree of uncertainty in the specification of the diameter of the source size, which is based on the FWHM of a Gaussian function for some RTPS.

Secondly, the *radiological penumbra* refers to scattered photons within the absorbing medium (Sharpe, Jaffray et al. 1995; AAPM 2008). This refers to the lateral scatter of secondary electrons when considering the measurement of radiation profiles. The lateral scatter is dependent on photon energy.

Since the primary energy fluence due to extrafocal radiation decreases with field size, with 12% of the total primary energy fluence due to extrafocal radiation at 40 x 40 cm² field, dropping to 7.2% for a 10x10 cm² field for Clinac 1800 at 15 MV (Sharpe, Jaffray et al. 1995), the effect of the geometric penumbra at small field sizes is not the predominant factor. Comparison of measurements of the penumbra in air and water found that the penumbra change in water was not predominantly due to the effect of altered geometric penumbra. The predominant factor in penumbra with measurement in water is due mainly to phantom scatter by secondary particles (Westermarck, Arndt et al. 2000). Monte Carlo calculations confirmed that the penumbral spread was not due to the geometric penumbra involved with the spread in the source size distribution but due to the radiological penumbra due to lateral electrons (Metcalf, Kron et al. 1993).

Therefore, it is the radiological penumbra that contributes to normal tissue irradiation due to the broadening of the penumbra. It has been postulated that a reduction of the radiological penumbra, and therefore normal tissue dose, could be achieved with lower energies. Simulations indicate that better sparing could be achieved with a 800 kV beam compared to a 6 MV beam in the lateral direction (O'Malley, Pignol et al. 2006).

It is also worth noting that the true penumbra due to the physics of secondary electron scatter is further broadened by the volume effect of the detector, which would add another factor in the broadening of the penumbra (discussed in later chapters).

The measured penumbra, defined as the penumbra that is measured using a physical detector, involves an additional deviation of the dosimetric penumbra with the detector volume and electron transport perturbation.

2.2.5 The issue of penumbra broadening in small fields

The implication of penumbra broadening has been considered to be low in 3DCRT due to the limited region of normal tissue that surrounds the planning target volume (PTV). Field edges in treatment must have a margin to the PTV of at least one penumbra width and therefore the penumbra broadening effect on dose was considered to be minimal under such circumstances but considered important in IMRT (Laub and Wong 2003). However, other studies have noticed that penumbra broadening may cause larger margins in treatments and also introduce errors in the calculation of the penumbra in 3DCRT (Garcia-Vicente, Bejar et al. 2004).

There are also instances where the penumbra effect can be more significant, even in 3DCRT. If the organ at risk (OAR) has a sharp dose-volume effect, or if the

OAR is adjacent to the treatment volume, the increase of margins employed will increase OAR dose volumes, which were clinically observable with increased rectal complication rates with prostate radiotherapy (Garcia-Vicente, Bejar et al. 2004). In other words, penumbra broadening involves unnecessary irradiation of sensitive structures close to the PTV. For IMRT the clinical effects of penumbra broadening are amplified because IMRT involves small field sizes in the PTV as well as field edges from larger segments also within the PTV (Laub and Wong 2003).

2.2.6 The issue of overestimation of FWHM in small fields

Field size determination, which is based on the normalised dose value of 50%, also breaks down and results in overestimated field sizes (Das, Ding et al. 2007). This is because of the overlap of penumbra dose profiles associated with charged particle equilibrium (Fidanzio, Azario et al. 2000), which pushes the FWHM to levels higher than the actual field size setting defined by CPE (see Figure 2.1).

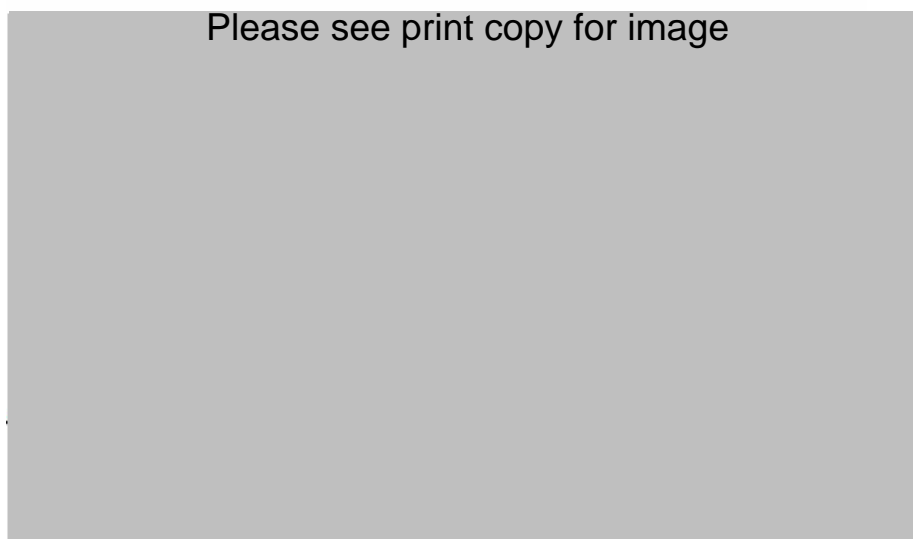


Figure 2.2: For (a), the field size corresponds to charged particle equilibrium and FWHM corresponds to 50% dose level of CPE. For (b), the field size is of the same order as CPE and the penumbra from the opposing field overlaps to cause a small error. For (c), FWHM is overestimated with respect to 50% dose levels of CPE since the resulting curve has a lower maximum value. Adapted from (Das, Ding et al. 2007)

2.2.7 Relevance of this study to literature on physics in the penumbral region

The geometric penumbra increases with depth and a simple mathematical model is used to analyse this in Chapter 9. The radiological penumbra is a function of the geometric penumbra with the inclusion of scatter and is more complicated. An approximation of the radiological penumbra is modelled in the radiotherapy treatment planning system (Pinnacle v. 8.0). Lastly, in this study, a variety of detectors measured the radiological penumbra with the detector volume effect (which was later corrected for) that involved a combination of volume averaging and electron transport averaging. The effect of broadened penumbra was also related to clinical effect with source size variations in Chapter 9 and later in variations in dose distributions in chapter 10.

2.3 REVIEW OF DETECTORS

2.3.1 Detector classification based on dose detectors and photon detectors*

Dose detectors (also known as *electron detectors*) are detectors associated with the measurement of secondary electrons outside of the detector. The instrument is based on the Bragg-Gray cavity theory, which involves a small cavity surrounded by a given medium, usually water in radiotherapy. The conditions for the Bragg-Gray cavity theory are minimal photon interactions inside the cavity itself (air-based cavities satisfy this criteria as the density of air is ~1000 times less than most solids) and secondary electrons that cross the cavity originate from primary interactions within the surrounding medium and are not altered greatly by the cavity (Dawson, Harper et al. 1984). The size of the cavity should be smaller than the range of secondary electrons from the medium to be non-perturbing (Das, Ding et al. 2007). The lateral electron equilibrium has also been found to increase for air-cavity detectors (Heydarian, Hoban et al. 1996).

Photon detectors are detectors associated with measurement of the photon-fluence distribution and have the condition of having the sensitive diameter and the lateral spread of the secondary electrons approaching zero in the detector, this is closely represented by detectors with high density medium such as solid state detectors. In all cases, for equivalent detector sizes the penumbra associated with the photon fluence from a photon detector is equal to or sharper than the measured dose distribution from a dose detector (Dawson, Harper et al. 1984).

The distinction between the fluence-distribution, measured with photon detectors, and the dose-distribution, measured with dose detectors, is associated with the lateral spread of the secondary electrons (Dawson, Harper et al. 1984). With different detectors, the differences in density and geometric configuration alter the range and location of the origin of secondary electrons responsible for the detector response (Dawson, Harper et al. 1984).

The lateral secondary electrons spread more significantly with larger energies (Dawson, Harper et al. 1984; Li, Soubra et al. 1995), which can contribute to a significant amount of broadening of the penumbra for photon energies larger than 6 MeV. Caution must be maintained with such energies with the measurement with dose detectors and not photon detectors due to this significant lateral electron spreading (Dawson, Harper et al. 1984).

2.3.2 Finite size of detector and perturbation

The two effects of detector volume and perturbation can introduce confusion. It has been proposed that the term *size effect* or *volume effect* be restricted to discussions involving volume averaging and that the *detector response function* to be inclusive of all sources of penumbra perturbation (Pappas, Maris et al. 2006). Therefore, penumbra broadening refers to the change the *measured profile* undergoes due to all sources of penumbra perturbation of the *true profile* (Pappas, Maris et al. 2006), which includes volume averaging and electron transport alteration (Lee, Pankuch et al. 2002; Laub and Wong 2003; Pappas, Maris et al. 2006; Das, Ding et al. 2007).

The finite size of the detector has a main contribution of characterising a rounder profile than compared to a point detector. The impact of this is where the second differential to the dose profile is non-zero (Metcalf, Kron et al. 2007), in other words, when the gradient of the profile is not changing the impact of the finite size of the detector is minimal. With small fields, the entire profile exhibits a changing gradient, except for the inflection points and the central axis point.

If a finite sized detector is compared to a point size detector, the upper part of the inside field exhibits an underestimation while outside the field the detector exhibits an overestimation (Metcalf, Kron et al. 1993; Arnfield, Otto et al. 2005). Another line of analysis observes that the measured penumbra width decreases and the distance to the point of inflection also decreases due to decreasing detector size (Laub and Wong 2003). It is also important to note that the penumbra is dependent on the chamber size with a relationship that is dependent on depth, but independent of machine type and energy

(Dawson, Schroeder et al. 1985), and therefore a full characterisation of the effect of chamber size and penumbra may require a characterisation of this relationship across energy and depth.

The effect of the detector on the measurement of profiles is a systematic error, which contributes to the total error in the radiotherapy process for each patient (Garcia-Vicente, Bejar et al. 2004), and can be minimised by making measurements with a small detector size or from the deconvolution of measured profiles.

2.3.3 Detector classification with respect to detector size

An alternate scheme of detector classification is with detector size (Das, Ding et al. 2007), which involves:

- i. Standard detectors referring to volume of a detector of $\sim 10^{-1} \text{ cm}^3$
- ii. Mini detectors referring to volume of a detector of $\sim 10^{-2} \text{ cm}^3$
- iii. Micro detectors referring to volume of a detector of $\sim 10^{-3} \text{ cm}^3$

2.3.4 Detector size with minimal detector volume effect

Estimation of detector sizes that would minimise the volume effect resulted in the conclusion that detectors less than 0.5 mm in diameter would be suitable for small beam dosimetry. (Pappas, Maris et al. 2006).

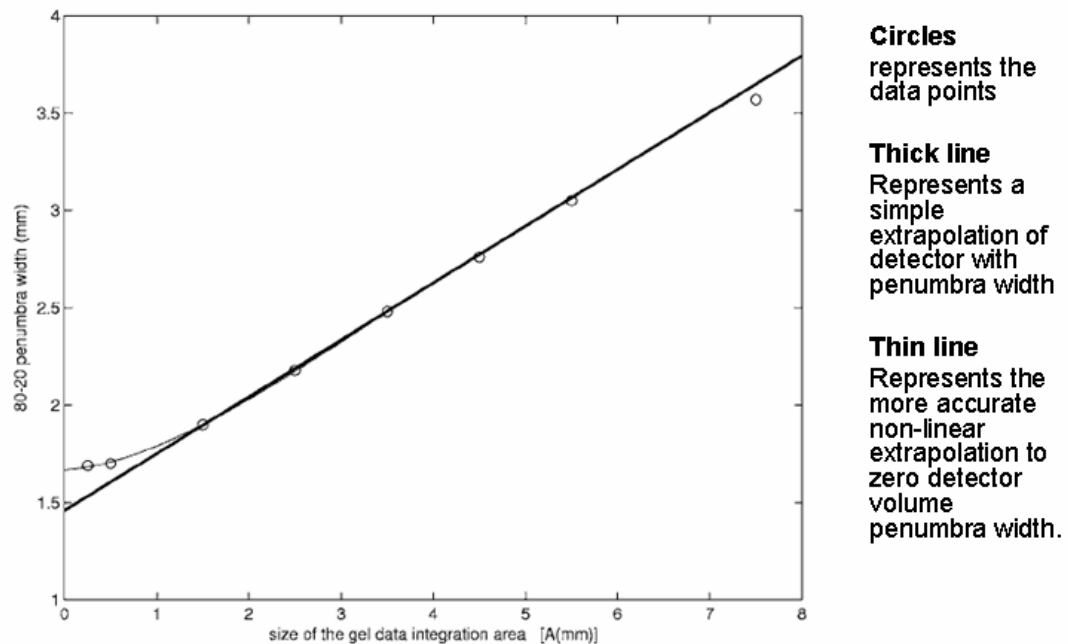


Figure 2.3: The 80-20% penumbra plotted against the detector size A for a 6 MV beam. It was found (Pappas, Maris et al. 2006) that the use of a detector less than 0.5 mm would minimise the volume effect from a detector.

2.3.4 Effective diameter

One method used to resolve the difference between the penumbra of photon-fluence and primary-dose distributions is the concept of effective diameter. The effective diameter of an ionisation chamber is defined as the outside diameter of the annulus which is calculated to match the penumbral dose distribution measured by that chamber.

Effective diameter increases with increasing radiation quality due to the increased lateral spread of secondary electrons. Quantitatively, an ionisation chamber with a diameter of 0.35 cm was calculated (Dawson, Harper et al. 1984) to have an effective diameter of 0.55 cm (Co-60), 0.75 cm (6 MV), and 1.25 cm (31 MV). For ionisation chambers, the effective diameter is larger than the physical diameter and this effective diameter increases with energy.

2.3.5 Overview and comparison of commercial detectors for small fields

In theory, a radiation detector should measure the absorbed dose in terms of energy absorbed per unit mass. However, practical detectors measure radiation indirectly by phenomena such as ionisation and chemical changes (Metcalf, Kron et al. 2007). The direct measurement of radiation is possible with calorimetry, however practical issues such as the need for thermal conductivity in the wall limit its use.

An ideal detector has characteristics (Metcalf, Kron et al. 2007), which although not realisable in practical detectors, can be accounted for a sufficient compromise.

- i. Accuracy: the ideal detector measures the correct dose without a systematic error.
- ii. Precision: the ideal detector measures the data with good reproducibility.
- iii. Detection limit: the ideal detector can detect the lowest readings required by the user.
- iv. Measurement range: the ideal detector should have the ability to measure the lowest readings and also the highest readings required by the user. In the high region, the detector should not undergo saturation.
- v. Dose response: the reading of the detector should have a linear relationship with the dose.
- vi. Dose rate dependence: the reading of an ideal detector should be independent of the dose rate.

- vii. Variation of response with radiation quality: energy independence with respect to water is desired for an ideal detector. However, real detectors may exhibit energy dependence due to the material used in its construction.
- viii. Spatial resolution: Ideally, the dosimeter should measure a point dose. Since this is not achievable, a minimal measurement volume is desired to reduce the volume averaging effect of the detector –which is the theme of this project.

In addition to these criteria, an ideal detector should also show the same reading when radiation is incident on the detector from different angles. If the detector has directional dependence, skewness can appear in profiles (Heydarian, Hoban et al. 1996).

The commercial detectors were the PTW 0.125 cc ionisation chamber, the PTW pinpoint chamber, and the PTW diamond detector (see Tables 3.1, 3.2, 3.3 respectively). The detectors used satisfied the conditions of detection limit, measurement range, and dose response. The precision of the data was improved with a reference detector (0.125 cc ionisation chamber) placed in the corner of the field to minimise the noise associated with the variance of dose rate with time.

Diode, films, and TLD are energy and dose rate dependent (Heydarian, Hoban et al. 1996; Burch, Kearfott et al. 1997), and film and TLD displaying non-reproducibility. Radiographic film is also energy dependent due to an over-response of silver halide at low energies and is usable at 6 MV for a square field sizes of $5 \times 5 \text{ cm}^2$ to $30 \times 30 \text{ cm}^2$ (Butson, Yu et al. 2003). Similarly, the pinpoint chamber over-responds to low energy photons (Laub 2002). The diamond detector is tissue equivalent and is therefore energy independent but requires a correction factor for dose rate dependence (Heydarian, Hoban et al. 1996).

In terms of spatial resolution, there are challenges due to the lack of availability to small detectors with sizes comparable to field dimensions (Das, Ding et al. 2007) – and in addition, photon detectors exhibit increased effective diameters with increasing photon energy due to increased lateral spread of electrons (Dawson, Harper et al. 1984). Detectors can change the local level of the CPE adding more perturbation (Das, Ding et al. 2007). This effect is more pronounced at regions of large dose gradients, where the finite detector volume increases the penumbra (Arnfield, Otto et al. 2005).

Ionisation chambers are close to the ideal detector in terms of independence with energy, dose, dose rate, as well as being reproducible, inexpensive, and being available in various geometrical shapes (van't Veld, Lujik et al. 2001; Metcalfe, Kron et al. 2007). However, profiles by diamond and diode detectors indicate an overestimation of

penumbra measurements by ionisation chambers (Bucciolini, Buonamici et al. 2003) due to the large detector volume. Ionisation chambers of approximately 5 mm diameter typically shows a broadening of 2-3 mm (van't.Veld, Lujik et al. 2001).

A brief overview of selected detectors is shown in Table 2.2. The pinpoint is an ionisation chamber with a smaller detector volume than standard ionisation chambers but suffers from the over response with low energy photons due to the steel central electrode (Laub 2002). Film was also a possible alternative but involved a similar over-response to low energy photons (Martens, Wagter et al. 2000). The diamond detector was chosen for its energy independence, however it has a dose rate dependence (Westermarck, Arndt et al. 1999).

Table 2.2: A comparison of selected features of a sample of detectors

Detector	Features	Reference
PPMC	<ul style="list-style-type: none"> Small volume 	(Lee, Pankuch et al. 2002)
Parallel plate microchamber	<ul style="list-style-type: none"> Tissue equivalency Limited to fields larger than 2.5 cm in diameter without correction factors 	
Standard ionisation chambers 0.1-0.2 cm ³	<ul style="list-style-type: none"> Finite detector size, increases penumbra by 2 mm depending on measurement conditions 	(Arnfield, Otto et al. 2005)
Standard ionisation chambers 0.25 cm ³	<ul style="list-style-type: none"> Increase of true penumbra by 0.25 cm 	(Garcia-Vicente, Delgado et al. 1997)
Film dosimetry	<ul style="list-style-type: none"> Increase of true penumbra by 0.02 cm 	(Garcia-Vicente, Delgado et al. 1997)
Silicon dosimeter	<ul style="list-style-type: none"> Increase of true penumbra by 0.08 cm 	(Garcia-Vicente, Delgado et al. 1997)
Diamond	<ul style="list-style-type: none"> The diamond detector should be placed with its main axis parallel to the scan direction for highest spatial resolution with profiles. 	(Laub 2002)
Diamond	<ul style="list-style-type: none"> Suitable for high-energy photon and electron beams 	(Angelis, Onori et al. 2002)
Diamond	<ul style="list-style-type: none"> Dosimetric properties should be experimentally determined. 	(Angelis, Onori et al. 2002)
Diamond	<ul style="list-style-type: none"> Poor sample reproducibility 	(Bucciolini, Borchì et al. 2005)
Diamond and IC	<ul style="list-style-type: none"> Agreement in PDD up down to 5x5 cm² 	(Bucciolini, Buonamici et al. 2003)
Pinpoint	<ul style="list-style-type: none"> Overestimate of 0.72 mm over true penumbra width for a beam diameter of 5 mm 	(Pappas, Maris et al. 2006)
Ionisation chambers	<ul style="list-style-type: none"> Importance of volume effect small compared to underestimation of correct output factor due to lack of CPE 	(Laub and Wong 2003)
Ionisation chambers	<ul style="list-style-type: none"> Average penumbra increase was 0.27 cm for field size 3-40 cm compared with film 	(Arnfield, Otto et al. 2005)
Gafchromic EBT film	<ul style="list-style-type: none"> Accurately measures penumbra of 5 cm (2.8 mm), 10 cm (3.0 mm), 20 cm (3.2 mm) and 40 cm (3.4 mm) square field sizes Tissue equivalence Energy independence 	(Cheung, Butson et al. 2006) (Hoban, Heydarian et al. 1994; Angelis, Onori et al. 2002; Bucciolini, Buonamici et al. 2003; Bucciolini, Borchì et al. 2005)
Ionisation chambers	<ul style="list-style-type: none"> Not the best detector choice for small field dose measurements 	(Westermarck, Arndt et al. 1999)
Diamond, Diode, Plastic Scintillator	<ul style="list-style-type: none"> Small field sizes >4 mm, agreed in PDD for 6MV and 18 MV 	(Westermarck, Arndt et al. 1999)
X-ray film	<ul style="list-style-type: none"> Over-response to low energy Use of filters can improve dosimetry results in IMRT QA 	(Ju, Ahn et al. 2002)
Parallel plate microchamber PPMC	<ul style="list-style-type: none"> designed for small beam dosimetry. small volume tissue equivalency limited to fields larger than 2.5 cm in diameter or else correction factors are necessary 	(Lee, Pankuch et al. 2002)

2.3.6 Output factor accuracy: Not considered

The output factor measurement correlates the output due to a change in collimator and phantoms scatter and is measured with varying field size, and is used for the dose to monitor unit calculation both manually and with radiotherapy treatment planning systems. For accuracy in dose delivery, both the output factor and the profile of the radiation beam need to be known for all treatment conditions (Sharpe, Jaffray et al. 1995).

Measurements of output factors in large fields are more straightforward than small fields, where inaccuracies due to small field size due to modelling of the transmission and scatter through the jaw and MLC can cause from 5-10% errors in the calculated monitor units (Azcona, Siochi et al. 2002). This is due to the lack of lateral electron equilibrium, which is further worsened when a detector enters a field because the lateral electron disequilibrium increases. There is a lower dose in the air cavity than in tissue (Heydarian, Hoban et al. 1996).

The detector plays a large part in the measurement of the output factor. Ideally, the detector should be at least smaller than the beam radius when electron equilibrium is not established (Cheng, Cho et al. 2007). The diamond detector is ideal as it has a small volume and measures output factors close to ionisation chambers (<1% difference) for field sizes between $3 \times 3 \text{ cm}^2$ and $15 \times 15 \text{ cm}^2$, but overestimates the output factors for larger field sizes and underestimates the output factors for smaller field sizes (Westermarck, Arndt et al. 1999). Ionisation chambers such as the pinpoint detectors, however, produce lower values with small values due to the volume effect as the penumbra is integrated into the effective measurement volume of the chamber (Crop, Reynaert et al. 2007).

There is currently significant work required to calculate factors to correct for field size, beam energy, and detector geometry. In addition there is the issue of the variation of electron spectrum and the change in stopping power ratios for small field in air which may introduce errors –with charged particle equilibrium they are ignored but in small fields the ratio may be significant (Das, Ding et al. 2007). The caveat of this study is that the issue of output factor is isolated and not given attention as the attention is focused on the detector volume effect in the penumbral region.

The divergence of the photon field, which diverges more with increasing field size, exposes an increasing length of the cable with increasing depth in the phantom.

The cable current due to current irradiation depends both on the field size and depth (Lee, Pankuch et al. 2002). This effect is also not considered significant for this study.

2.3.7 Relevance of this study to the literature on detectors

A selection of a *standard* detector of 0.125 cc (the 0.125 cc ionisation chamber), a *mini* detector (the 0.015 cc pinpoint ionisation chamber), and a *micro* detector (the 0.001 cc diamond detector) was used in this study (see Chapter 3 for specifications) to model the significance of detector perturbation at each detector classification based on size.

Ionisation chamber based detectors were favoured due to their reliability but the limitations of these were the significant detector volumes. The diamond detector had an ideal detector volume but involved complex properties (discussed in section 2.4). Lastly, the comparison of the three detectors involves a comparison between two photon detectors (the 0.125 cc ionisation chamber and the pinpoint ionisation detector) and one dose detector (the diamond detector). The distinction of dose detectors and photon detectors is a limitation in this study. The dose-rate dependence of the diamond detector was characterised in this study (see Fig 3.3), however the difference between dose detectors and photon detectors introduces complexities in the comparison of the diamond detector and the ionisation and pinpoint chambers.

2.4 REVIEW OF THE DIAMOND DETECTOR

Diamond detectors are solid-state detectors with large signal to noise ratio and small sensitive volumes. They are ideal for small field measurement and beam profile measurements. (Das, Ding et al. 2007). However, diamond detectors show great individuality of response characteristics depending on size, shape, purity of the crystal. This requires correction factors for dose rate needs to be determined, but once applied agreement with other detectors is good (Westermarck, Arndt et al. 1999).

In the study reported in this thesis, the diamond detector was the smallest detector used. The detector was a research detector with limited clinical use. In other studies, the diamond detector has been established for use with reference dosimetry for small field sizes and steep dose gradients (Fidanzio, Azario et al. 2000). In addition, agreement has been established between Monte Carlo and the diamond detector (Hugtenburg, Johnston et al. 2001). In addition, for intra-operative electron beam radiotherapy (Bucciolini, Buonamici et al. 2003) and external electron beam dosimetry, the diamond detector has also been validated by dose distribution, percentage depth doses, directional dependence, and dose rate dependence (Bjork, Knoos et al. 2000).

2.4.1 Diamond detector mechanism

Diamond detectors are classified as solid state ionisation detectors (PTW-Freiburg 2008), with radiation providing energy to transfer electrons from the valence band to higher energy levels. These high energy level electrons fill electron traps caused by impurities in the crystals and move into the conduction band. In other words, absorption of ionising radiation causes the production of electrons and positive holes that have sufficient energy to move freely through the crystal, which changes the electrical conductivity of the diamond temporarily (Laub, Kaulich et al. 1997).

2.4.2 Diamond asymmetry

Normally, it is assumed that the centre of the sensitive volume with coincident with the geometric centre of the outer casing (Westermarck, Arndt et al. 1999; McKerracher and Thwaites 2006). More accurate studies have investigated the x-ray image of the diamond detector and the angular dependence of the detector was found to be due to a difference in electrode thickness, with the diamond detector having a larger electrode on the back side. An increased amount of back-scatter would be incident on the diamond head on (Westermarck, Arndt et al. 1999). For more accurate measurements in small fields, each solid state detector should be imaged with an x-ray device at various rotational positions to identify the symmetry of the device as well as assess any potential problems (McKerracher and Thwaites 2006).

The angular dependence of the diamond detector has been studied and the maximum deviation measured over all angles less than 2° (Angelis, Onori et al. 2002), which agreed with the PTW specification of 2% over 170° (PTW-Freiburg 2008). In our study, centring of the detector was performed initially with the light field and later a second procedure was followed which centred the detector according to the radiation field. This, in addition to the restriction of the gantry angle to 0 degrees in this study, minimised the effect of the angular dependence of the diamond detector.

2.4.3 Diamond pre-irradiation dose and stability

The required pre-irradiation dose has been experimentally studied and was found to depend on impurity concentration, and the pre-irradiation dose serves to excite electrons from the valence to the conduction band, where the electrons in the conduction band are captured in active gaps. This produces an electron field opposite to the applied field that approaches stabilisation with increasing dose (Angelis, Onori et al. 2002). It is noted that the requirement of a pre-irradiation dose would increase the amount of exposure of

the detector to radiation. The durability of the diamond detector has been verified with the conclusion being that the strong atomic binding of the diamond making the detector radiation hard (Bucciolini, Borchini et al. 2005).

For an initial use of the diamond detector, the manufacturer recommends a 5 Gy pre-irradiation dose (PTW-Freiburg 2008). With this level of pre-irradiation dose, the diamond detector stability was found to be more stable than ionisation chambers (Laub, Kaulich et al. 1999). There was some variability between diamond detectors with standard deviation of reading varying between 0.4 % and 0.1 % at 5 Gy, but with increasing pre-irradiation dose the stability improved to a standard deviation of 0.1 % for all diamond detectors studied at 15 Gy (Angelis, Onori et al. 2002). Although the larger pre-irradiation dose of 15 Gy was advocated to ensure a more steady current by some (Hoban, Heydarian et al. 1994), the required pre-irradiation dose may depend on the need of the measurement.

The pre-irradiation dose also depends on the use of the diamond detector. Daily or regular use of the diamond detector may involve a change in the required pre-irradiation dose due to the stabilisation of the detector prior to use. The pre-irradiation dose required for a stable reading after one day of prior pre-irradiation was found to be 3 Gy (Hoban, Heydarian et al. 1994), significantly less than the 15 Gy suggested for initial use by the same author. This indicates that stabilisation can be partially maintained as the leakages of the electrons from traps are only partial in a period of a day. The decay of the stability with time was also noted with such a scheme, with a short-term stability of 0.1%, daily stability showing a maximum variation of 1%, and a weekly stability of 1% observed (Angelis, Onori et al. 2002). In addition, an operational tip was to allow about 2 seconds of irradiation prior to data collection to obtain better signal stability (Bucciolini, Buonamici et al. 2003).

It is worthwhile to note that there are conflicting studies with regards to stability of the diamond detectors. Another study found the diamond to be the least stable and disagreed with PTW 0.015 cm³ pinpoint detector, PTW 0.125 cm³ ion chamber, PTW 0.6 cm³ ion chamber, 0.009 Exradin A-14 ion chamber, scanitronix-wellhofer stereotactic diode field detector (SFD) with 0.2 mm active volume by more than 10% for PDD and TMR (Cheng, Cho et al. 2007).

2.4.4 Diamond energy independence

The tissue equivalence of the diamond detector and the energy independence has been a large factor in the interest and the study of diamond detectors (Angelis, Onori et al.

2002; Bucciolini, Buonamici et al. 2003). Diamond detectors are considered to be tissue equivalent (Hoban, Heydarian et al. 1994) because of similar atomic and mass numbers with tissue (Bucciolini, Borchini et al. 2005).

There has been validation of the energy independence of diamond detectors in photon and electron beams. For photons in the 6-25 MV energy range, no energy dependence was found by (Laub, Kaulich et al. 1999) while a 1% dependence was found by (Angelis, Onori et al. 2002). For electrons in the 6-20 MeV range, a maximum of 1% dependence was found by (Laub, Kaulich et al. 1999) and a maximum of 1.5% dependence was found by (Angelis, Onori et al. 2002). It is speculated that while the diamond detector may be nearly tissue equivalent, the contact material could be the cause of energy dependence (Laub, Kaulich et al. 1999).

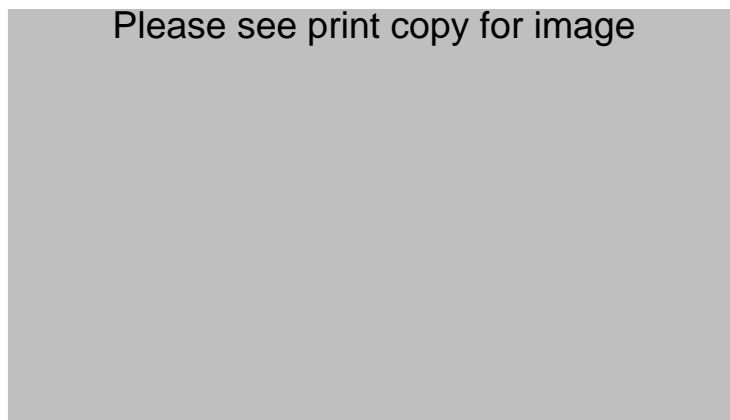


Figure 2.4: Measured response of the diamond detector at photon energies from 4-25 MV with the stopping power ratio of water/carbon and of water/air from (Laub, Kaulich et al. 1997)

Theoretically, the stopping power of water to carbon presents a much more constant response than the stopping power ratio of water to air (see Figure 2.3). The electron transport perturbation of the diamond detector is expected to be smaller than the ionisation chamber, in addition to the volume averaging effect.

2.4.5 Diamond bias voltage

The applied bias voltage affects the relative current measured with the diamond detector, and the manufacturer specifies a bias voltage of +100 V (PTW-Freiburg 2008).

Independent studies of the bias voltage have been made and have found that negative voltages results in non-ohmic behaviour in the diamond detector. The electrical contacts are constructed to be a blocking type for negative voltages, and the non-ohmic behaviour in the negative voltage region is not due to the characteristics of the diamond material itself (Angelis, Onori et al. 2002).

It has been found that the diamond can saturate in terms of all electron-hole pairs being collected between 20-50 V with the specified bias voltage of +100 V ensuring complete charge collection (Angelis, Onori et al. 2002). For complete charge collection, the bias voltage has to be at a level at which the transit time for electrons to pass from one electrode to another to be less than the electron-hole recombination time (Hoban, Heydarian et al. 1994). Investigations into the effects of changing voltage levels found that after a change of voltage level, a 20 second interval was required before the current reached a stable level (Angelis, Onori et al. 2002).

2.4.6 Diamond dose rate dependence

A major aspect of the diamond detector that has received attention from researchers is dependence of the detector to dose rate. The dose rate dependence can be corrected for and the measurement of the correction factor is recommended any use of the diamond detector (Laub, Kaulich et al. 1999; Westermarck, Arndt et al. 1999; Fidanzio, Azario et al. 2000; Hugtenburg, Johnston et al. 2001; Bucciolini, Buonamici et al. 2003). For a given voltage bias, there is no current but with radiation, the current increases approximately proportional to voltage but sub-linearly with dose rate that can be corrected for (Hoban, Heydarian et al. 1994). This implies that the larger the dose rate the more effect the dose rate dependence will be.

Recombination in semiconductors is more significant than in ionisation chambers because the density in semiconductors are higher than in air (Hoban, Heydarian et al. 1994). The physics of recombination in a diamond detector involves the impurities in the crystals. With impurities, metastable states that are introduced trap electrons which would have otherwise recombined with holes. Consider the equilibrium density of free electrons as m and the equilibrium density of electrons in traps as n . The number of holes is equal to $m + n$ and increases as dose rate increases. Now the recombination time, proportional to conductivity, has an inverse relationship to the number of holes. Therefore, with increasing dose rate there will be a sub-linear increase in conductivity (see Figure 2.4) (Fowler 1966).

$m = \text{Equilibrium density of free electrons}$

$n = \text{Equilibrium electrons in traps}$

$\text{Number of holes} = m + n$

$\text{Conductivity} \propto \text{Recombination time}$

$\text{Recombination time} \propto (\text{Number of holes})^{-1}$

$\text{Conductivity} \propto (m + n)^{-1}$

$(\uparrow \text{Dose rate}) \rightarrow (\uparrow m + n)$

$(\uparrow \text{Dose rate}) \rightarrow (\downarrow \text{Conductivity})$

Figure 2.5: Logic diagram highlighting the relationship of recombination time, conductivity, dose rate, and the number of holes in the diamond detector

There is a variation in methodology of measurement of Δ . An accepted method of calculation involves the determination of Δ as the slope of the line in a log-plot of normalised diamond response versus dose rate (Hoban, Heydarian et al. 1994; Westermarck, Arndt et al. 1999). Note that there is a link between the trap concentration, recombination, and pre-irradiation dose. A higher concentration of traps will give more independence with dose rate but will require higher pre-irradiation doses and is also linked to a lower detector sensitivity (Angelis, Onori et al. 2002). Theoretically, for a pure semiconductor without any traps Δ is expected to be a value of 0.5 while a semiconductor with a uniform trap distribution will have a Δ of 1 (Bucciolini, Borchini et al. 2005).

The current of the diamond detector is related to the dose rate by

$$I_{norm} = (D_{norm})^{\Delta} \quad (2.4)$$

Relationship of the dose dependence due to $I \propto D^{\Delta}$ (Hoban, Heydarian et al. 1994)

Once Δ is determined, the percentage depth dose can be corrected for with,

$$PDD(d) = [M(d) / M(d_{max})]^{1/\Delta} \times 100. \quad (2.5)$$

Correction for the percentage depth dose of diamond measurements (Fidanzio, Azario et al. 2000)

Alternatively, readings measured from a diamond detector for both profiles and depth doses can be corrected with the following equation

$$D_{\text{rel}}(d) \rightarrow D_{\text{rel}}(d)^{1/\Delta} \quad (2.6)$$

Correction for profile dose measurements for diamond measurements (Laub, Kaulich et al. 1997; Bjork, Knoos et al. 2000)

In equation 2.1, I_{dark} refers to the dark current, R is a fitting parameter, and the dose-rate correction factor relates to the term Δ . The dose-rate correction factor corrects for measurements in the PDD with equation 2.2 and relative measurements in the profile are corrected for with equation 2.3. Without correction, percentage depth doses (PDD) measured with the diamond detector will involve a small over-response by the diamond detector with respect to ionisation chambers (Laub, Kaulich et al. 1999). However, with correction, it has been confirmed that PDDs measured with diamond detectors confirm with ionisation chamber measurements (Laub, Kaulich et al. 1999; Angelis, Onori et al. 2002)

The measured dependence of Δ with dose rate was found to exist with a second-order polynomial fit (Hoban, Heydarian et al. 1994), however the variance in Δ with dose rate was considered to be negligible (Laub, Kaulich et al. 1997), and the dependence of Δ with energy type was also found to be negligible (Fidanzio, Azario et al. 2000). Measurements of Δ vary within a limited range, with values of 0.95-1.0 (Bucciolini, Buonamici et al. 2003; Bucciolini, Borchini et al. 2005), 0.963 (Laub, Kaulich et al. 1999), 0.96 (Westermarck, Arndt et al. 1999), and 0.993 (Fidanzio, Azario et al. 2000). The variation of Δ between 0.95-1.0 suggests that the PTW 60003 diamond detector has a trap distribution close to uniform trap distribution. If the measurement of Δ is close enough to 1.0 (e.g. 0.995), use of the readings without correction is possible without a significant compromise in accuracy.

2.4.7 Diamond and leakage current

The diamond detector specified leakage current was less than 5 pA (PTW-Freiburg 2008). This is due to the high energy band gap ensures a low dark current (Bucciolini, Borchini et al. 2005), which is confirmed with the observation of small leakage currents (Hoban, Heydarian et al. 1994).

2.4.8 Other aspects of the Diamond Detector

The linearity of the diamond detector was measured and confirmed to be less than 0.2% deviation from linearity of dose from 0.25-15 Gy range (Angelis, Onori et al. 2002).

The diamond detector has a large useful sensitivity range of dose rates from 0.05 to 30 Gy/min (PTW-Freiburg 2008) due to its high sensitivity. (Hoban, Heydarian et al. 1994). The sensitivity of the diamond detector was measured to be $4.1 \times 10^{-7} \text{ C/Gy}$ (Laub, Kaulich et al. 1997).

2.4.9 Relevance of this study to the literature on diamond detectors

The diamond detector was selected as an example of a *micro* detector but exhibited many characteristics that were different to the commonly used ionisation chamber. The literature has showed the diamond to be an excellent detector in terms of stability, energy independence, leakage, linearity, and sensitivity. (In fact, another limitation of this study is the energy dependence of the pinpoint detector which was not modelled.) However, it was noted that the diamond detector does have additional operational requirements with the need for pre-irradiation dose, sufficient bias voltage, and dose-rate dependence. Lastly, the asymmetry of the diamond detector was noted as another caveat that could be minimised with a suitable setting of the gantry or collimator setting of the linear accelerator. The beam aligns perpendicular to the diamond detector face for optimal detector geometry.

2.5 REVIEW OF THE MULTILEAF COLLIMATOR (MLC)

As most measurements for this report involved a multi-leaf collimator (MLC), some characteristics are discussed here. A variety of parameters, including the minimum gap between opposing leaves, maximum leaf velocity and leaf length influence the accuracy of the dose calculation (Arnfield, Wu et al. 2001). Improvements can be made in terms of agreement between measured and modelled dose distributions by measurement and adjustment of values such as MLC leaf transmission and dosimetric leaf gap (Arnfield, Otto et al. 2005).

Detailed modelling of the MLC is important to fully account for the contribution of leaf leakage, scatter and tongue and groove effects to patient dose distribution. For IMRT, the sum of these contributions for multiple subfields is significant compared to dose received by sensitive structures blocked by MLC fields. (Heath and Seuntjens 2003)

2.5.1 Overview of basic MLC parameters

Multi-leaf collimators, also known as MLCs, function to collimate the field to a user-defined shape. The shape is collimated with multiple leaves, which allows an arbitrary shape with a resolution defined by the number of leaves in the MLC. The design of the MLC varies between manufacturers and products as well (Arnfield, Wu et al. 2001), with features such as:

- i. Number of leaves;
- ii. Width of leaves;
- iii. Average leakage (usually defined with a 10×10 field);
- iv. Double or single focus leaves;
- v. Rounded or straight leaf end design;
- vi. Whether the MLC(s) replaces or is in addition to one or both of the jaws

2.5.2 The Varian 120 leaf Millennium MLC

The Varian 120 leaf *millennium* MLC design is a single-focused configuration with rounded leaf end, and with a tongue and groove pattern in the leaf side that links adjacent leaves together. In comparison with most Siemens MLC designs which are double-focused with a straight leaf end design, the Varian system has the movement of its leaves in a simpler in-field movement (in the beam plane) whereas the previous Siemens system has the movement of its leaves in a curved movement focused on the radiation focal spot. In terms of calibration, reliability, and the reproducibility and precision of position, the Varian system is easier to maintain but the Siemens system has potential advantages in terms of smaller penumbra and less leaf end scatter. As the Varian 120 millennium is used in this study it will be the focus of this discussion.

2.5.3 Leaf end and leaf side



Figure 2.6: Illustration of a general leaf from a MLC with a curved end, adapted from (AAPM_TG_50 2001)

The nomenclature with MLC involves the distinction between the leaf end and the leaf side (see Figure 2.6), with the leaf end being at the end of the leaf in the direction of the leaf motion and the leaf side being the side perpendicular to the leaf motion. In addition, others have named the leaf end direction the *parallel* direction and the leaf side direction the *perpendicular* direction. There are significant differences with the two sides from a radiological perspective: for a 5 mm MLC for a 6 MV beam, the leaf edge (perpendicular) penumbra measured was 2.5 mm and the leaf tip (parallel) penumbra was measured to be 3.2 mm for a 3 cm diameter field (Clark, Teke et al. 2006).

In general, leaf ends have penumbral values of 1-2 mm larger than the penumbra of upper jaws while leaf sides have penumbras similar to upper jaws (Boyer, Ochran et al. 1992; Butson, Yu et al. 2003). The penumbra of the MLC also varies with the tip curvature of the rounded leaf end, with increasing penumbra with increasing tip curvature (Carlson 2001; Pawlicki and Ma 2001).

The AAPM TG 50 Report (AAPM-TG50 2001) is the generally accepted naming convention for leaf width, length, height, end, and side. Another distinction is that since the leaf end direction exhibits movement, there is a variable gap between the leaf ends. In Pinnacle, the penumbra width of the leaf side direction is modelled well but in the leaf end direction, if the leaf gap is less than 1 cm, the dose in the penumbra

region decreases by 6% for a 1 cm gap and 20% for a 0.5 cm gap with respect to the model (Chow, Wettlaufer et al. 2006).

2.5.4 MLC tongue and groove effect

Another distinction between the two sides is that in the perpendicular direction, there is a tongue-and-groove design which can be seen in the previous figure. The tongue and groove design aims to reduce the leakage between MLC leaves in the leaf side direction due to the mechanical difficulty in the manufacture of two leaves with no gap in between.

The magnitude of a measured dose profile parallel to the direction of leaf motion (X) may differ significantly from another x profile displaced only several millimetres in the Y direction (perpendicular to leaf motion) even when there is no variation in the Y direction in the optimised fluence. This is due to the MLC tongue and groove effect (Arnfield, Otto et al. 2005)

2.5.5 MLC and resolution

MLC leaves have a fixed value and with commercial MLCs, the large projected leaf-width of 1 cm or 0.5 cm at the isocentre is an inherent limitation in attaining conformality with small field radiotherapy (Vlamynck, Palmans et al. 1999). This is related to the resolution of the MLC, and is comparable to the pixel size in image analysis. Some have termed this effect *stepping*. Various methods have been suggested to reduce this effect.

One option is to rotate the MLC with respect to tumour contour such that the contour edge is at right angles (or close to right angles) to the direction of leaf movement. Other options include the reduction of the leaf width (by purchasing a MLC system that has a smaller leaf width), or shifting each segment by a fraction of the leaf width at isocentre (Bortfield, Oelfke et al. 2000; Xue, Zhang et al. 2002). The effective resolution can also be improved by the use of collimator rotation (Bortfield, Oelfke et al. 2000). Another option is to reduce width (e.g. Varian 2.5 mm). This requires more leaves and motors and due to beam divergence the manufacture of very thin MLCs at the leaf location.

2.5.6 MLC leaf width

In clinical practice, MLCs with smaller leaf widths generally yield superior PTV coverage and conformity. With an improved approximation of the desired PTV shape, more normal tissue can be shielded thus increasing a better coverage of the PTV. On the

other hand, the number of MLC segments can potentially increase with smaller leaf widths due to the larger amount of possibilities in dose optimisation in inverse planing possible (Nill, Tucking et al. 2005).

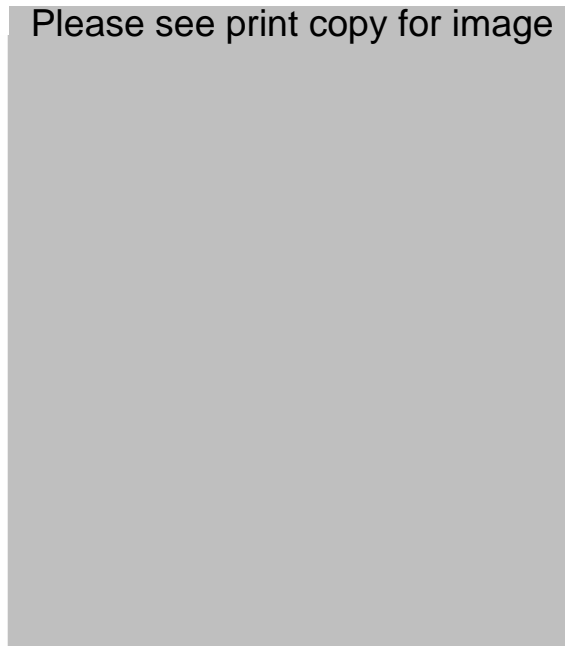


Figure 2.7: Cross-sectional views of the Varian 120-leaf MLC with the (a) end view and the (b) side view (Kim, Siebers et al. 2001)

In one study, the MLC-80 (leaf width 1.0 cm) and the MLC-120 (leaf width 0.5 cm) were compared (see Figure 2.6). In the head and neck region, average NTCP for 10 mm 13.72%, for 5 mm 8.24%. (Fiveash, Murshed et al. 2002), with dosimetric advantages of 5 mm over 10 mm leaf widths confirmed by other researchers (Crop, Reynaert et al. 2007). Differences expected to be more pronounced for stereotactic radiosurgery or when tolerance of the sensitive organ is less than or close to the target volume prescription. (Fiveash, Murshed et al. 2002). However, further reduction of leaf width may even lead to worse results with more leakage radiation because the ratio between the minimum leaf separation (to account for mechanical tolerances) and the leaf width will increase (Bortfield, Oelfke et al. 2000).

Sampling theory and theory of linear systems used to identify MLC leaf width such that no further improvement in physical dose distribution could be obtained. Width calculated to be 80%-20% penumbra divided by 1.7. Without couch or collimator rotation, degradation of the physical dose distribution is expected if the leaf width exceeds 1.5-1.8 mm for a 6 MV beam. (Bortfield, Oelfke et al. 2000). Current MLC designs have not exceeded such a leaf width, with micro MLC with leaf widths between

1.6 mm and 4.5 mm constructed (Bortfield, Oelfke et al. 2000) and the Varian commercial MLC system going down to 5 mm leaf width and more recently to 2.5 mm.

2.5.7 MLC leakage

The leakage from most MLCs is larger than jaw leakage because of a lower thickness of attenuating material in the MLC and also because of the junction effects between different leaves which is absent from the solid material in a jaw system. In terms of the relationship between the MLC leakage and the MLC design, the MLC transmission ratio is strongly dependent on both leaf density and the interleaf air gap (Jang, Vassiliev et al. 2006).

Measurement of MLC leakage involves the separation of MLC leakage into two components of leaf transmission and leaf scatter. For a 10×10 cm² field, the total MLC leakage was 1.68%, with 1.48% transmission and 0.20% due to leaf scatter (Arnfield, Siebers et al. 2000). The MLC transmission is the predominant factor outside the field and does not contribute to dose inside the field but the scatter from leaves contributes dose even within the field (Arnfield, Siebers et al. 2000).

End-leaf transmission of energy fluence was greater than inter-leaf transmission by a factor of 15. However because of the lateral transport of radiation the measured dose of the MLC varied by only up to a factor of 1.5 (Arnfield, Siebers et al. 2000).

Treatment planning systems may not model the intraleaf and the interleaf leakage properly. The Pinnacle planning system underestimates the end leaf leakage by 20-40%. Significant extra dose can be introduced due to end leaf leakage, with maximum leakage 0.39 cGy/MU for 0 mm gap and 0.51 cGy/MU for 6 mm gap (Hardcastle, Metcalfe et al. 2007). In Eclipse as in most planning systems, no distinction is made between dose in regions under the full thickness of a MLC (midleaf) versus dose points that are underneath the projection of the junction region between leaves (interleaf) (Arnfield, Otto et al. 2005).

2.5.8 MLC focusing of light and radiation



Figure 2.8: For rounded leaf end MLCs, the actual field size calibration differs for light (X_{light}) and radiation field (X_{rad}) edges, and depends in a complex way on the motion of the leaves (X_{mlc}) (Graves, Thompson et al. 2001)

The positioning of the MLC requires consideration into the light and radiation positioning methods for a rounded leaf-end MLC system. As shown in figure 2.8, the light field is completely blocked at the edge of the leaf-end but the radiation field is attenuated to varying degrees (in other words being defined as *outside* in the leaf-shape intersection in the figure below), with the radiation field edge being drawn at some point within the leaf end curvature –with the radiation edge being defined at 50% dose (in other words being defined as *middle* in the leaf-shape intersection in the figure below). Non-focused MLCs, such as the curved leaf end of Varian MLC, permit variable amounts of radiation through different thicknesses of the leaves and therefore the radiation field is not congruent with the light field (Carlson 2001; Das, Ding et al. 2007), and requires an MLC offset to correct for this. This positional variance further complicates small field sizes.

Measurements do not find a large difference in 50% between single focused and double focused MLCs but larger differences are observed in 20-80% and 20-90% penumbras. (Killoran, Giraud et al. 2002) Single focus MLC have larger oscillations at the 50% isodose line for a prescribed field edge of a circular field, compared to double focus MLC, due to the rounded leaf ends. However, some single focus MLC designs

may have a sharper penumbra, due to its position from the source being further. (Killoran, Giraud et al. 2002).

2.5.9 MLC calibration and accuracy

There are two sources of systematic MLC gap errors: centreline mechanical offset (CMO) and radiation field offset (Burch, Kearfott et al.) for rounded leaf end MLC systems. CMO is used to prevent leaf-to-leaf collisions at zero gap opening. RFO is used in planning computers to compensate for the penetration of radiation into rounded leaf ends (Zygmanski and Kung 2001). The accuracy of the leaf position itself is a source of random error, while the radiation field offset calibration, is a systematic error that either causes leaf to leaf gaps to be too large or too small (Zygmanski and Kung 2001; Parent, Seco et al. 2005).

Measurement reported have found that the MLC leaf positioning accuracy is 0.08 mm with corresponding dose uncertainties due to leaf positioning accuracy to be 1.7% (Low, Sohn et al. 2001) for the Varian 5 mm MLC. Another study using an EPID found that the reproducibility of the MLC was within 0.4 mm and was not affected by gravity (Parent, Seco et al. 2005).

Studies into the radiation field offset calibration involved the absolute location of reference jaw. This involved measuring the position of the jaw at both ends of a 180 degree collimator rotation and taking half the distance between the two edges (Graves, Thompson et al. 2001). Comparison of the default correction table for radiation field offset from Varian and from the study was done, which found that the default Varian settings involved an order of 1 mm error along all MLC position readouts compared to an order of 0.3 mm with the investigators (Graves, Thompson et al. 2001).



Figure 2.9: Radiation field measurements of original and corrected averages (right) between measured and readout (Graves, Thompson et al. 2001)

2.5.9 Relevance of this study to the review of MLCs

An understanding of the intricacies of the MLC design was required in the consideration of the measurement conditions in this study. The intraleaf leakage in the leaf side (perpendicular to the leaf direction) was studied in this project (see Appendix A) in order to ensure small field measurements did not involve contributions of scatter from unwanted contributions in the MLC with the use of end-leaf offsets (see section 3.2.3). The accuracy of the MLC in terms of leaf position and calibration with relation to the curved leaf end and the leaf side was noted as a limitation in treatment but was not a function of the error involved with the detector volume effect in the measurement of profiles. In other words, MLC measurements in this study involved limitations due to MLC but these were not modelled or corrected for as these effects were not dependent on the detector volume effect.

Chapter 3: Experimental Method

3.1 EQUIPMENT USED FOR DATA COLLECTION

3.1.1 Linear accelerator model

All data was collected at St. George Hospital with a linear accelerator made by the manufacturer Varian. The linear accelerator model used was a Clinac 600. The software interface *service mode* was used, which allowed manual adjustment of linear accelerator parameters which included beam on times, dose rate, and field size. A collimator and gantry angle of 0 degrees was used in all beams, with an energy of 6 MV and a dose rate of 250 MU/min.

3.1.2 Multi-leaf collimator model

The MLC studied in this thesis is a Varian 120 leaf *millennium* MLC, with a single focus, rounded leaf end design, and with the MLC as an addition to two perpendicular jaws (X1/X2 and Y1/Y2 jaws). There are 60 leaf pairs, with leaf 10B to 50B being in the centre of the field with 5 mm width each to cover 20 cm and with leaf 1B to 9B and leaf 51B to 60B with 10 mm width each to cover an extra 10 cm either side of the central leaves.

3.1.3 MLC control software used

The MLC Shaper software was used to create MLC shapes which were then loaded on to the treatment console computer connected to the linear accelerator. The software used was sourced from Varian Medical Systems Inc. (Version 6.3). The file revision used was “Rev H –MLC Ver. 4.10”, the display scale used was “Varian IEC”, the MLC model used was Millennium 120”, and the treatment type selected was static. In addition to the settings outlined above, there are variations to settings in the leaf positions where the leaf-shape intersection and the closed leaf contact are selectable. With these settings, the leaf-shape intersection was chosen to be the middle. The closed leaf contact was chosen to be the centre (see Figure 3.1).

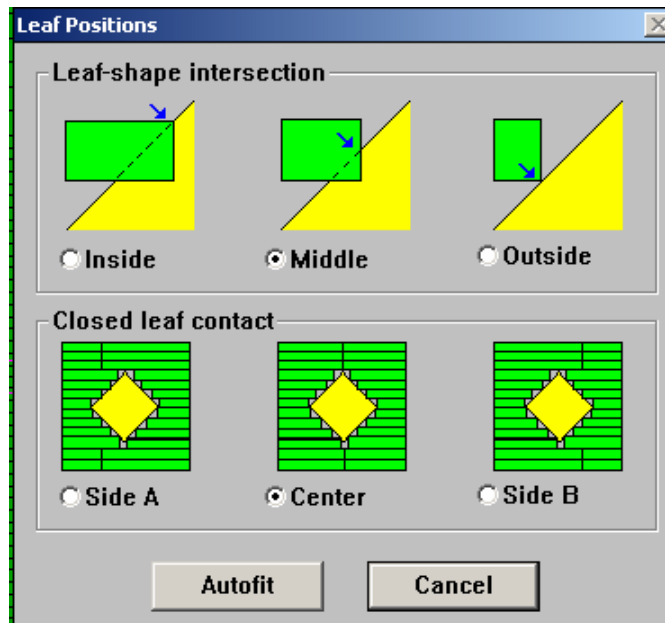


Figure 3.1: MLC SHAPER Options

Individual leaves or groups of leaves were manually selected to move into the desired positions. The jaw position set in *MLC SHAPER* was not necessarily adhered to as the field size defined by the jaw could be adjusted independently in *service mode*. The collimator was kept at collimator 0^0 at all times.

3.1.4 Automatic MP3-M water phantom

The MP3M water tank (A), the MP3 TANDEM Dual Electrometer (B), and the MP3 Control Unit (C) are connected to a dedicated computer and also to the *field* and *reference* chambers. The MP3M Water Tank is responsible for providing the necessary water phantom for measurements as well as housing and powering the stepping motors for the measurement of profiles with detectors. The MP3M Water Tank is also capable of fine adjustment, and of a vertical drive on the tank that allows the desired source to surface distance (SSD) to be adjusted.

(A) The MP3M Water Tank (see Figure 3.2) has the following features

- i. Large open measurement area
- ii. 500 x 500 x 407.5 mm detector movement in three dimensions
- iii. 600 x 600 x 600 mm water medium
- iv. Tank walls and bottom are 2 cm thick to eliminate *bulging* during prolonged use
- v. High-speed stepping motors are mounted above the water surface and to the side of the tank away from the beam. Hence they do not interfere with data collection
- vi. Levelling pedestal for precise in-out, right-left, and rotational positioning.

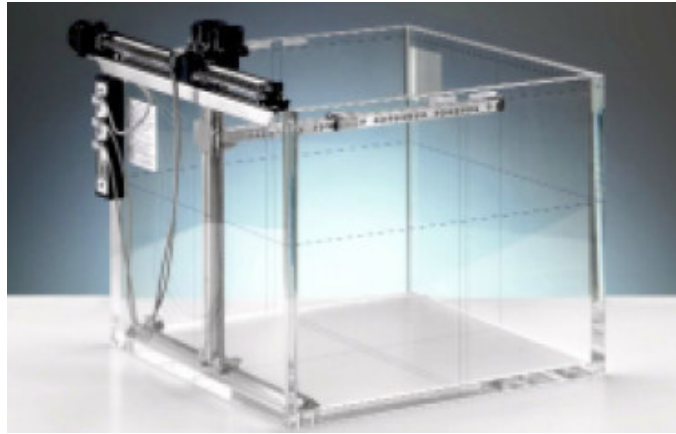


Figure 3.2: PTW water tank

(B) The MP3 TANDEM Dual Electrometer (see Figure 3.3) had the following features

- i. Standalone ADCL calibration grade electrometer
- ii. 50 msec integration time
- iii. 0 to ± 400 V in 50 V steps

(C) The MP3 Control Unit (see Figure 3.3) had a high precision 3D drive mechanism which positioned the detectors within 0.1 mm of the specified location.



Figure 3.3: MP3 Electrometer (above) and MP3 Control Unit (below)

3.1.5 IC: 0.125 cm³ thimble-type ionisation chamber

The 0.125 cc ionisation chamber (see Table 3.1) is based on a design known as the *thimble ionisation chamber*. This is a cylindrical shaped air cavity with a central electrode in the middle and a spherical end mounted to the cylindrical chamber wall. A high voltage bias was maintained at a value of 300 V, and as the gas volume is irradiated ionisation pairs are formed. These ionisation pairs are attracted by the voltage bias and create currents that correspond to dose (PTW-Freiburg 2008). This ion chamber was used as the reference chamber in all cases and was used as the field chamber for one set of measurements.

Table 3.1: Specifications for the 0.125 cc ionisation chamber used in this study (PTW-Freiburg 2008)

0.125 cm³ Semiflex chamber	
Detector	
Type	31010
Certificate number	975921
Specification	
Type of product	vented cylindrical ionisation chamber
Application	absolute dosimetry in radiotherapy beams
Measuring quantity	absorbed dose to water, air kerma, exposure
Reference radiation quality	Co 60
Nominal sensitive volume	0.125 cm ³
Design	waterproof, vented, fully guarded
Reference point	on chamber axis, 4.5 mm from chamber tip
Direction of incidence	Radial
Nominal response	3.3 nC/Gy
Long-term stability	Less than 1% per year
Detector bias voltage	400 V nominal, +- 500 V maximal
Polarity effect	Less than 1 %
Photon energy response	Less than 2% (140 kV...280 kV), less than 4% (140 kV...60Co)
Directional response	Less than 0.5% for rotation around chamber axis and for tilting of the axis up to 10 degrees
Leakage current	Less than 4 fA
Cable leakage	Less than 1 pC/Gy.cm
Materials and measures	
Wall of sensitive volume	0.55 mm PMMA, 1.19 g/cm ³ , 0.15 mm graphite, 0.82 g/cm ³
Total wall area density	78 mg/cm ³
Dimensions of sensitive volume	radius 2.75 mm, length 6.5 mm
Central electrode	Al 99.98, diameter 1.1 mm
Build-up cap	PMMA, thickness 3 mm
Ion collection efficiency at nominal voltage	
Ion collection time	100 microsec
Max dose rate for:	
>99.5 % saturation	6 Gy/s
>99.0% saturation	12 Gy/s
Max dose per pulse for	
>99.5 % saturation	0.5 mGy
>99.0% saturation	1.0 mGy
Useful ranges	
Chamber voltage	plus minus (100...400) V
Radiation quality	66 keV...50 MV photons, 10...45 MeV electrons, 50...270 MeV protons
Field size	(2x2) cm ² ... (40x40) cm ²
Temperature	(10...40) degrees Celsius
Humidity	(10...80) %,
Air pressure	(700...1060) hPa

3.1.6 PP: Pinpoint ionisation chamber*

The pinpoint ionisation chamber (see Table 3.2) is in principle the same as the IC except that it has a smaller effective volume. A bias voltage of 300 V was used.

Table 3.2: Specifications for the Pinpoint Chamber used in this study (PTW-Freiburg 2008)

Detector	Pinpoint detector
Type	31015
Certificate number	505079
Specification	
Type of product	vented cylindrical ionisation chamber
Application	dosimetry in high-energy photon beams with high spatial resolution
Measuring quantity	absorbed dose to water, air kerma, exposure
Reference radiation quality	Co 60
Nominal sensitive volume	0.015 cm ³ , 0.03 cm ³
Design	waterproof, vented, fully guarded
Reference point	on chamber axis, 3.4 mm from chamber tip
Direction of incidence	radial, axial (31014)
Pre-Irradiation dose	2 Gy
Nominal response	400 pC/Gy, 800 pC/Gy
Energy response	n/a
Long-term stability	Less than 1% per year
Detector bias voltage	400 V nominal, +- 500 V maximal
Polarity effect	Less than 1 %
Directional response	<0.5% for rotation around chamber axis, <1% for tilting of the axis up to 20° radial incidence and 15° axial incidence
Leakage current	Less than 4 fA
Cable leakage	Less than 1 pC/Gy.cm
Materials and measures	
Wall of sensitive volume	0.57 mm PMMA, 1.19 g/cm ³ , 0.09 mm graphite, 1.85 g/cm ³
Total wall area density	85 mg/cm ²
Dimensions of sensitive volume	radius 1 mm, 1.45 mm length 5 mm
Central electrode	Al 99.98, diameter 0.3 mm
Build-up cap	PMMA, thickness 3 mm
Ion collection efficiency at nominal voltage	
Ion collection time	20 microsec, 50 microsec
Max dose rate for:	
>99.5 % saturation	265 Gy/s, 29Gy/s
>99.0% saturation	580 Gy/s, 55Gy/s
Max dose per pulse for	
>99.5 % saturation	3.5 mGy, 1.2 mGy
>99.0% saturation	7 mGy, 2.3 mGy
Useful ranges	
Chamber voltage	plus minus (100...400) V
Radiation quality	60Co...50MeV photons
Field size	(2x2) cm ² ... (30x30) cm ²
Temperature	(10...40) degrees Celsius
Humidity	(10...80) %,
Air pressure	(700...1060) hPa

3.1.7 DD: Diamond detector

The diamond detector (see Table 3.3) is physically based on a diamond disk with contact wires to the measuring instrument, and embedded in a water-protective material. Irradiation pushes electrons from the valence band to higher energy levels to which initially fills the electrons caused by impurities and then electrons to the conductivity band. Pre-irradiation is used to ensure a stable current with dose (PTW-Freiburg 2008). A bias voltage of 100 V was used.

Table 3.3: Specifications for the Diamond Detector used in this study (PTW-Freiburg 2008)

Detector	Diamond Detector
Type	60003
Certificate number	930645
Specification	
Type of product	diamond detector
Application	Dosimetry in radiotherapy beams
Measuring quantity	Absorbed dose in water
Reference radiation quality	Co 60
Nominal sensitive volume	(1...6) mm ³
Design	waterproof, disk-shaped sensitive volume perpendicular to detector axis
Reference point	on detector axis, 1 mm from detector tip
Direction of incidence	Radial
Pre-Irradiation dose	(5...15) Gy
Nominal response	(50...500) nC/Gy
Energy response	at higher depths than d _{max} , the percentage depth dose curves match curves measured with ionisation chambers to within 0.5 %
Detector bias voltage	positive 100 V, tolerance 1%
Directional response	< +2% for tilting less than 170 degrees
Leakage current	Less than 5 pA
Cable leakage	Less than 1 pC/Gy.cm
Charge collection time	Less than 10 nS
Measures	
Sensitive area	(3...15) mm ²
Thickness of sensitive area	(0.1...0.4) mm
Water-equivalent window thickness	1.15 mm
Outer dimensions	diameter 7.3 mm
Useful ranges	
Dose rate	(0.05...30) Gy/min
Radiation quality	80 keV ... 20 MV photons, (4...20) MeV electrons
Temperature	(10...40) degrees Celsius
Humidity	(10...80) %,
Air pressure	(700...1060) hPa

3.1.8 Measurement of the diamond detector dose rate dependence

Characterisation of the diamond detector was performed, as recommended in the literature. The diamond detector PDD was compared to the PDD of the 0.125 cc ionisation chamber (see Figure 3.4). The PDD values after d_{\max} were used, which corresponded to electron equilibrium with depth.

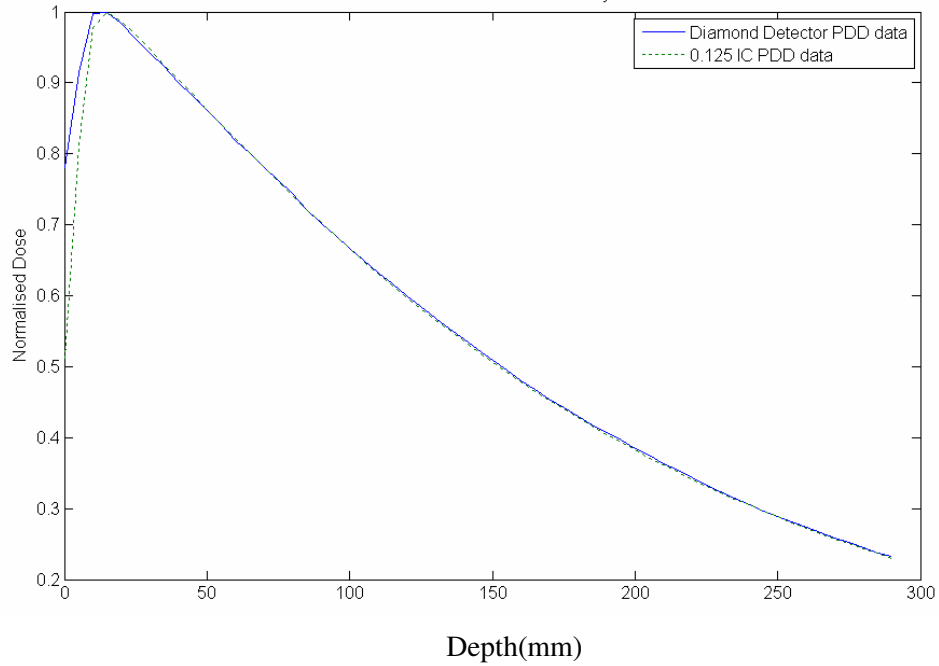


Figure 3.4: Comparison between PDD data for diamond detector and 0.125 cc ionisation chamber for jaw defined 10×10 cm² field

Both sets of data at d_{\max} was normalised to a dose rate of 250 MU/min, or 2.5 Gy/min. The log of both sets of normalised data was plotted against each other. The relationship between the plots was correlated with a linear fit (see Figure 3.5).

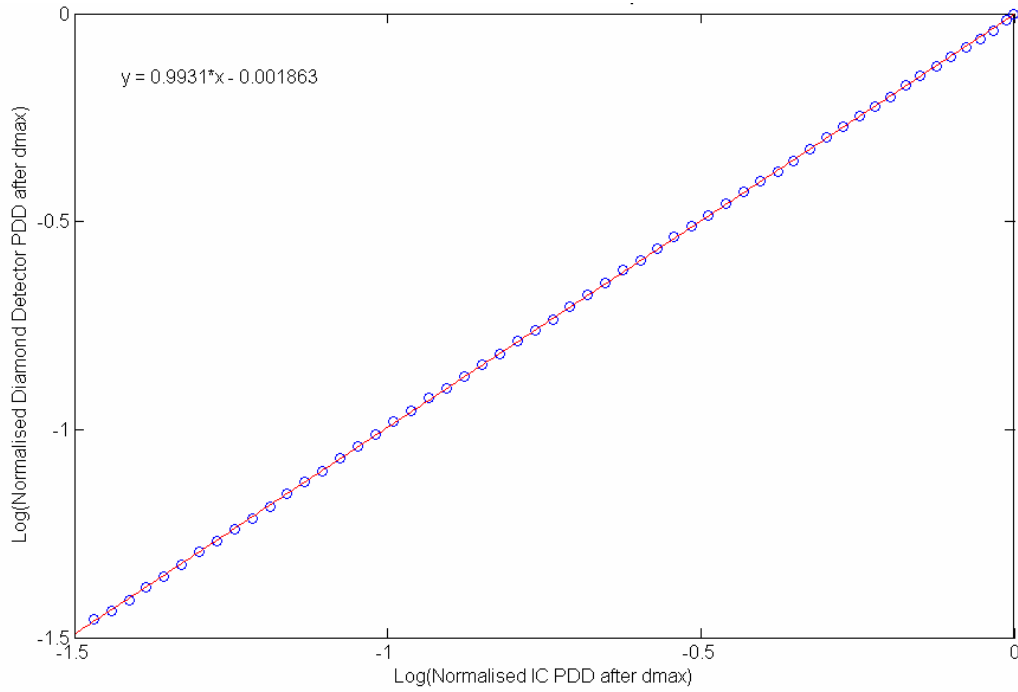


Figure 3.5: Derivation of diamond detector dose rate dependence with log of diamond PDD and log of IC PDD

The original relationship between the measured data and the dose rate was multiplied on both sides with the log function. The dose rate correction factor Δ was determined by evaluating the slope of the log of the measured data and the log of the dose rate, shown graphically in Figure 3.5 and shown mathematically with Equation 3.1 and 3.2

$$I_{norm} = (D_{norm})^{\Delta} \quad (3.1)$$

$$\log(D_{norm}) = \Delta^{-1} \log(I_{norm}) \quad (3.2)$$

, relating the slope of the log graphs with the diamond dose rate dependence factor.

Therefore, the dose rate correction factor Δ was calculated to be the inverse of 0.9931, which is 1.009. The dependence factor is close to unity. To correct for dose rate dependence of the diamond detector, relative readings need to have the following correction applied

$$\begin{aligned} D_{rel}(d) &\rightarrow D_{rel}^{1/\Delta} \\ D_{rel}(d) &\rightarrow D_{rel}^{0.993} \end{aligned} \quad (3.3)$$

.which shows the correction required for diamond dose rate dependence (equation 3.3).

The effect of this correction on profile data was evaluated using dose differences (which is defined as the closest dose point to an original point that has the same spatial value) as well as dose to agreement (which is defined as the closest spatial point to an original point that has the same dose value). Variation of the maximum dose difference

over field sizes from $1 \times 1 \text{ cm}^2$ to $20 \times 20 \text{ cm}^2$ (at d_{max}) showed a maximum dose difference of 0.03% and a maximum DTA of 0.08 mm. Variation of maximum dose difference over depths from 15 mm to 200 mm (at $1 \times 1 \text{ cm}^2$ field size) showed the same maximum dose difference and DTA.

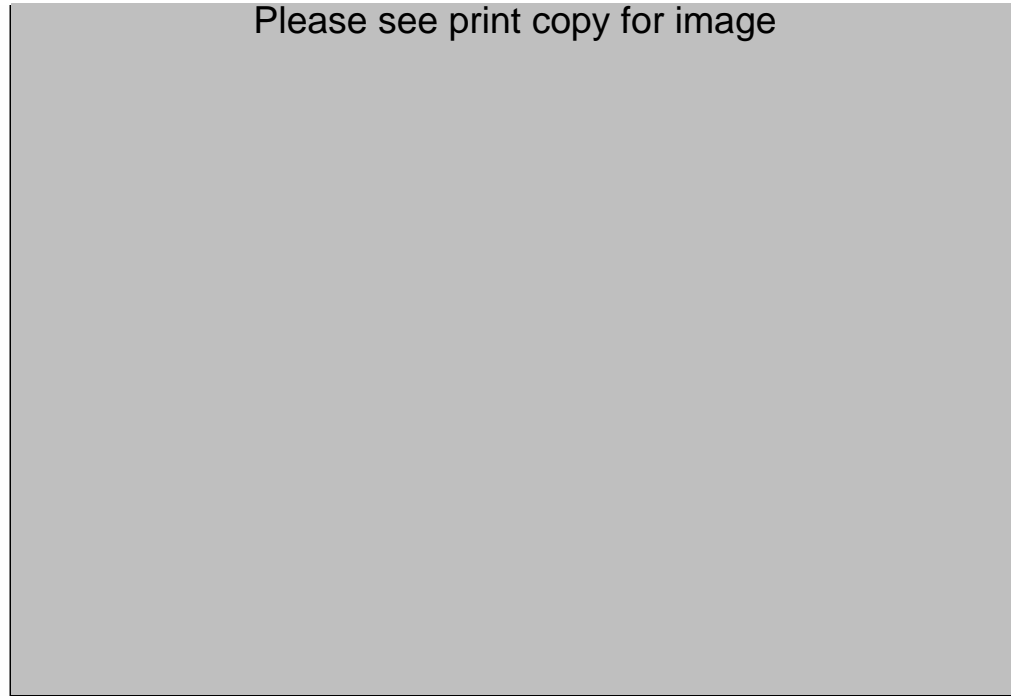


Figure 3.6: Profile showing the raw diamond detector profile and the profile with dose-rate correction applied (Topolnjak, Heide et al.) with the dose difference (bottom)

Graphically, a plot of the profiles shows the effects of the dose rate correction (see Figure 3.6). The correction is nearly indistinguishable visually and, as described above, of the order of 0.3% which peaks in the penumbral region, where there is the largest dose difference. For profiles, since the diamond detector dose rate dependence was found to be negligible, it was not applied. For PDDs however, the dose rate dependence was applied for all diamond detector data used.

3.1.9 Data Collection Software: MEPHYSTO MC²

The MEPHYSTO mc² (Version MEPHYSTO mcc 1.3, © 2008 PTW FREIBURG) software package was used to control the automatic water tank MP3-M motor positions as well as receive the measurement data from the chambers during data acquisition.

3.2 METHOD OF DATA COLLECTION

3.2.1 Note on the orientation of Linac and MLCs

Table 3.4: Orientation of linear accelerator to illustrate the different in naming conventions as well as commonly used terms.

Local Institution (St. George Hospital)	Gun	Target	East	West
Phillips Pinnacle Manual	Bottom	Top	Left	Right
Mephysto Software	Inplane	Inplane	Crossplane	Crossplane
Multileaf Collimator	Perpendicular		parallel	
Jaw Orientation	Y2	Y1	X2	X1
Water Tank Motor Movement	C (C+ towards gun)		A (A+ towards East)	

Table 3.4 illustrates the dimensions for a collimator angle and gantry angle of 0. Unless otherwise noted, the inplane direction is used for the majority of profile analysis. Note that these orientations are valid for the setup conditions in this study only.

For further clarification, the orientation of the leaf with the Jaws can be further discussed. As shown in table 3.4, the MLC moves in the parallel direction to the Y Jaws. In other words, the leafs move in the direction of the X Jaws and therefore the rounded leaf ends are usually associated with crossplane profiles unless the collimator is rotated 90^0 . Similarly, the perpendicular movement of the MLCs are associated with the Y Jaws. The MLC leaf bank A is towards the X2 Jaw while leaf bank B is towards X1 Jaw, while leaf number 1 starts at the open Y1 Jaw and leaf number 60 ends at the open Y2 Jaw.

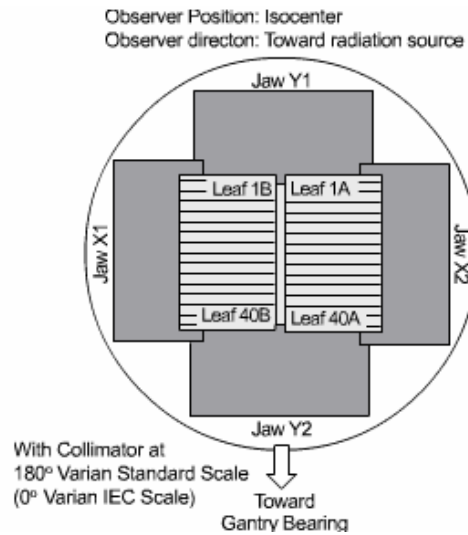


Figure 3.7: Diagram showing the direction of the position of the MLC leaf motion with respect to the Jaw positions. Note that this diagram is not the Varian 120 leaf MLC system used in the study.

3.2.2 Setup of water tank

The setup of the water tank is crucial to ensure the accurate measurement of profiles in the direction and at positions required –or, in other words, to ensure that the measurement of the profiles are not skewed and that the incident beam angle is orthogonal to the surface of the water.

Procedure used:

- i. Water tank is roughly parallel laterally to crosshair in both planes
 - a. Adjustments to water tank position to correct for this.
- ii. Movement of detector limits set
- iii. Movement of detector laterally is parallel to crosshair in both planes
 - a. Adjustments to collimator angle to correct for this.
- iv. Movement of detector laterally is parallel to water level in both planes
 - a. Adjustment to water tank tilts to correct for this.
- v. Movement of detector downwards is parallel to beam axis
 - a. Adjustment of gantry angle to correct for this.
- vi. Lateral component of zero point of detector in the middle of the beam axis
 - a. Initial adjustment with light field.
 - b. Second adjustment with radiation field.
- vii. Depth component of zero point of detector set to middle of detector
 - a. Visually set with the reflection of the detector on the water.
- viii. Field and reference chambers connected.
- ix. Reference chamber placed in the corner of the field.
- x. SSD set to 100 cm with the water tank motor.

3.2.3 Definition of chamber and leaf-end offset

For the measurement of profiles and PDD with MLC fields, the end-leaf junction dose becomes an issue and is dealt with in various ways (see Appendix A). Briefly, the end-leaf junction refers to the junction between the two rounded leaf ends in the direction parallel to the leaf motion. The figure below illustrates the position of the end-leaf junction.

The two methods of dealing with this issue are the use of detector offsets, or the use of leaf-end junction offsets. The use of detector offset involves measuring the perpendicular profile away from the central axis to evade the dose contribution from the end-leaf junction (see Figure 3.7). The leaf-end junction offset involves moving the end-

junction offset away from the central axis (see Figure 3.8), for which the MLC leaf positions were programmed using *MLC Shaper*. The issues with leaf-end junctions and the dosimetric effects of leaf-end junction offsets are discussed further in Chapter 4.

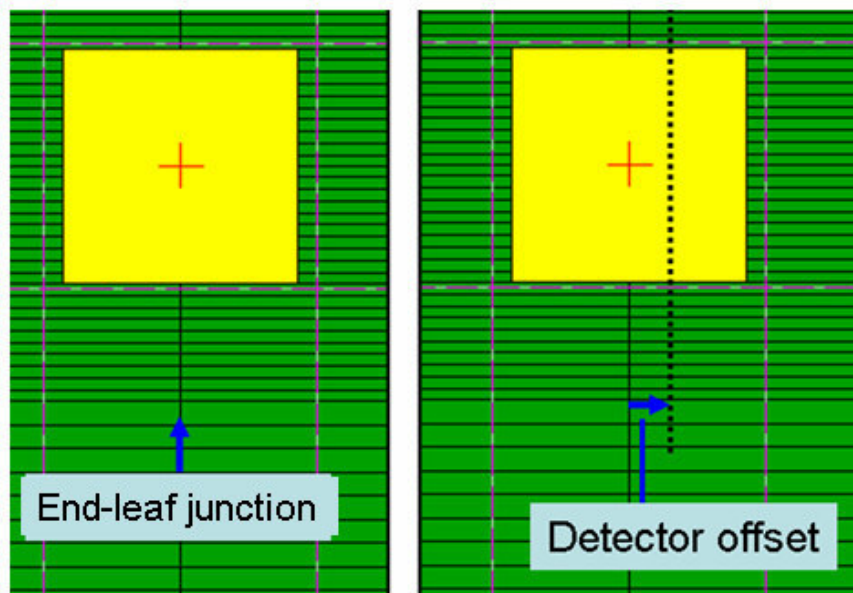


Figure 3.8: The end-leaf offset contributes significant dose in the perpendicular profile (left) if measured without any offset. The detector can be offset so that it measures the perpendicular profile away from the central axis, so that the out-of-field perpendicular profile does not measure the end-leaf junction dose.

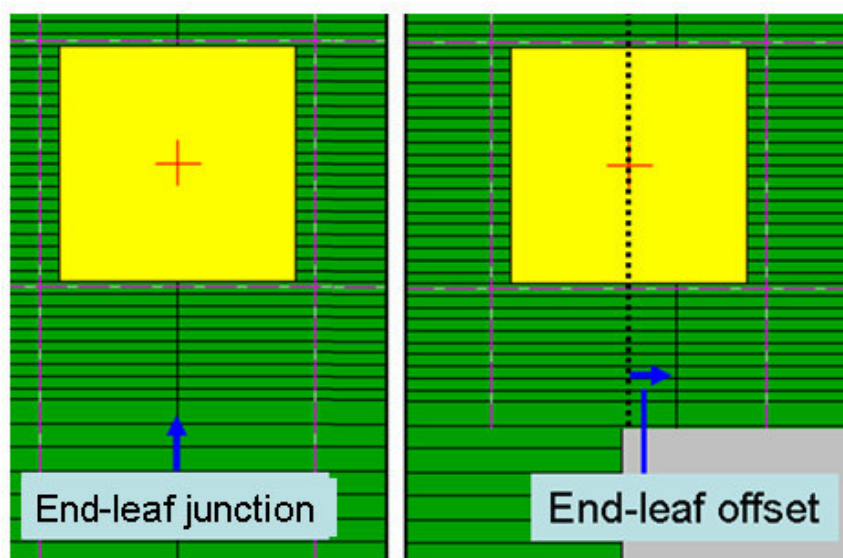


Figure 3.9: The end-leaf offset contributes significant dose in the perpendicular profile (left) if measured without any offset. The end-leaf junction can be offset (right) so that the out-of-field perpendicular profile does not measure the end-leaf junction dose.

3.2.4 Parameters set for measurement of Jaw Data

For each set of measurements, each chamber (IC, PP, DD) was used with the 0.125 cm³ ionisation chamber used as the reference chamber.

For square field sizes 1×1 cm², measurement was done without a reference measurement due to difficulty in placement of the reference detector in the field without perturbation of the primary detector. To compensate for an increase in signal variation, longer measurement times were used.

Table 3.5: Settings used for Jaw data acquisition.

Constant parameters		Variable parameters	
Collimator (degrees)	0	Jaw Square Field size (cm ²)	1, 2, 5, 10, 20
Gantry (degrees)	0	Depths (cm)	1.5, 5, 10
SSD (cm)	100		
Energy	6 MV		
Dose Rate	250 MU/min		
MLC settings	Retracted		
Measurement resolution	0.5 mm (min) in penumbra and 1.0 mm (max) elsewhere		

3.2.5 Parameters set for measurement of MLC Data

For each set of measurements, each chamber (IC, PP, DD) was used with the 0.125 cm³ ionisation chamber used as the reference chamber. For square field sizes 1×1 cm², measurement was done without a reference measurement. To compensate for an increase in signal variation, longer measurement times were used.

Table 3.6: Settings used for MLC data acquisition

Constant parameters		Variable parameters	
Collimator (degrees)	0	MLC Square Field size (cm ²)	1, 2, 5, 10, 20
Gantry (degrees)	0	MLC Rectangular Field sizes (cm ²)	20x10, 10x20
SSD (cm)	100	Depths (cm)	1.5, 5, 10
Energy	6 MV	MLC end-leaf offset	0.5 cm (see Chapter 3 for more information)*
Dose Rate	250 MU/min	<i>*Note: Compare with manual setting</i>	
Jaw Square Field size (cm ²)	30	<i>Detector offset</i>	<i>0.5 cm (not used)</i>
Measurement resolution	0.1 cm (min) and 0.25 cm (max) (ADAC 2000b)		

3.2.6 CentreCheck: Centering the chamber with the radiation field*

Initially, the *CentreCheck* software, which is part of the MEPHYSTO mc² software package, is used to measure and set the centre of the radiation beam. Initially, the chamber is zeroed to minimise leakage currents. Then, for both all data collection procedures, a field size of 10×10 cm² was set with depths of 1.5 cm and 10 cm. The *CentreCheck* software calculates the necessary shift in the zero position of the chamber in the MP3-M water tank geometry to be centred with the irradiated radiation field (see Figure 3.9).

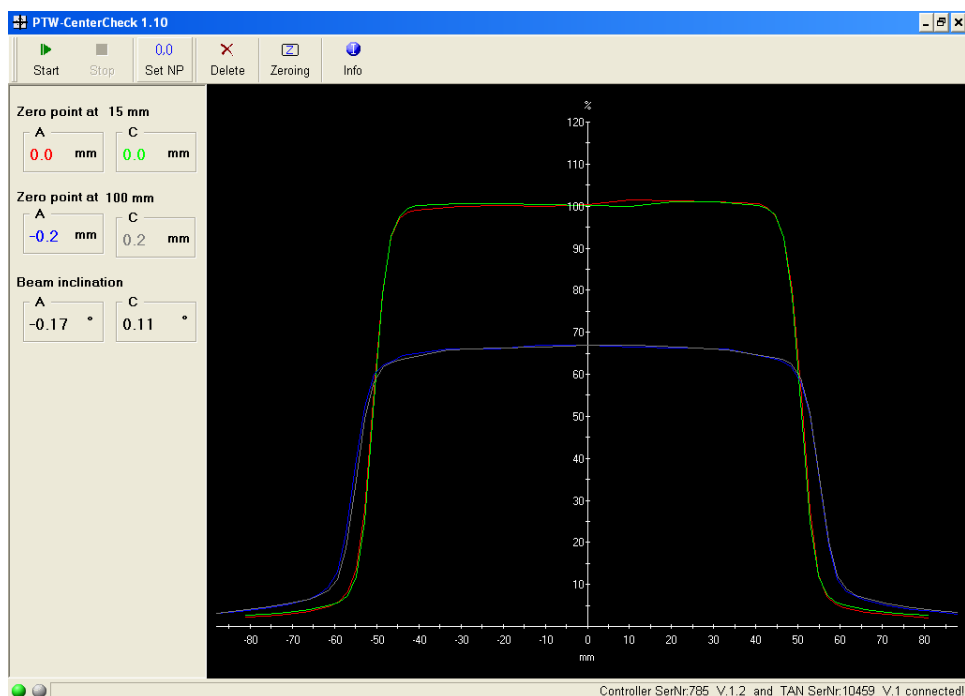


Figure 3.10: *CentreCheck* software indicating that the chamber position requires no shift to be in the centre with the radiation field.

3.2.7 TBAScan: PDD and profile measurements

After *CentreCheck* is complete, *TBAScan* is used to control the chamber for PDD and profile measurements. Initially, the chamber is again zeroed in order to minimise leakage currents. Then, the linac, modality, energy, wedge, block, field size, SSD, gantry angle, and collimator are set.

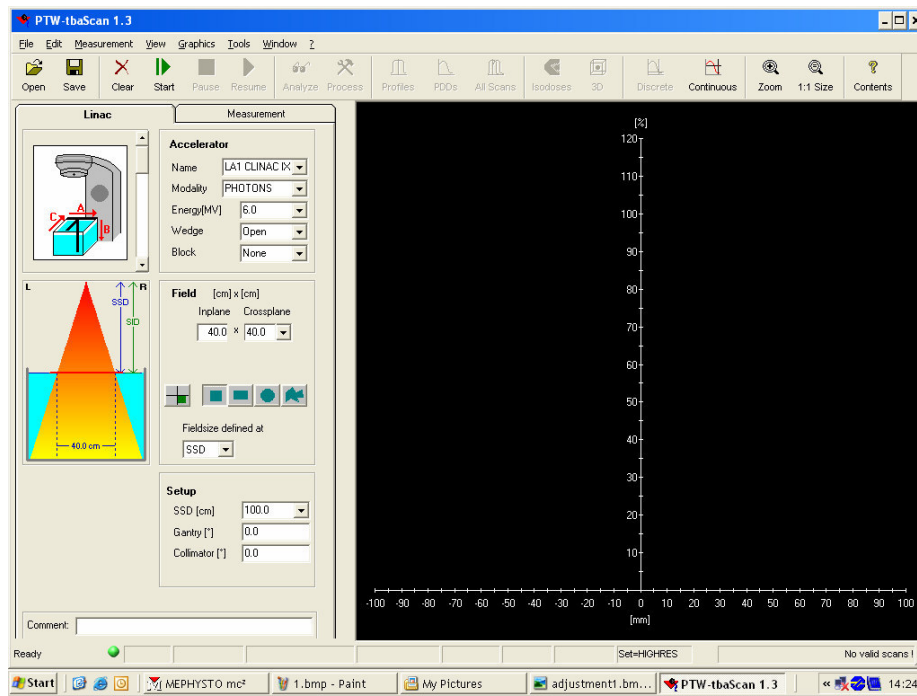


Figure 3.11: First group of settings required in TBAScan

After the initial group of settings are entered in TBAScan (see Figure 3.10), the second group of settings required involves selection of the field chamber, entering of measurement time per point, checking whether the reference chamber is to be used or not, selection of whether the PDD is to be measured or not, specifying the angle of profile measurement desired, specifying whether Inplane and/or crossplane profiles are to be measured, and specifying what depths are to be used (see Figure 3.11).

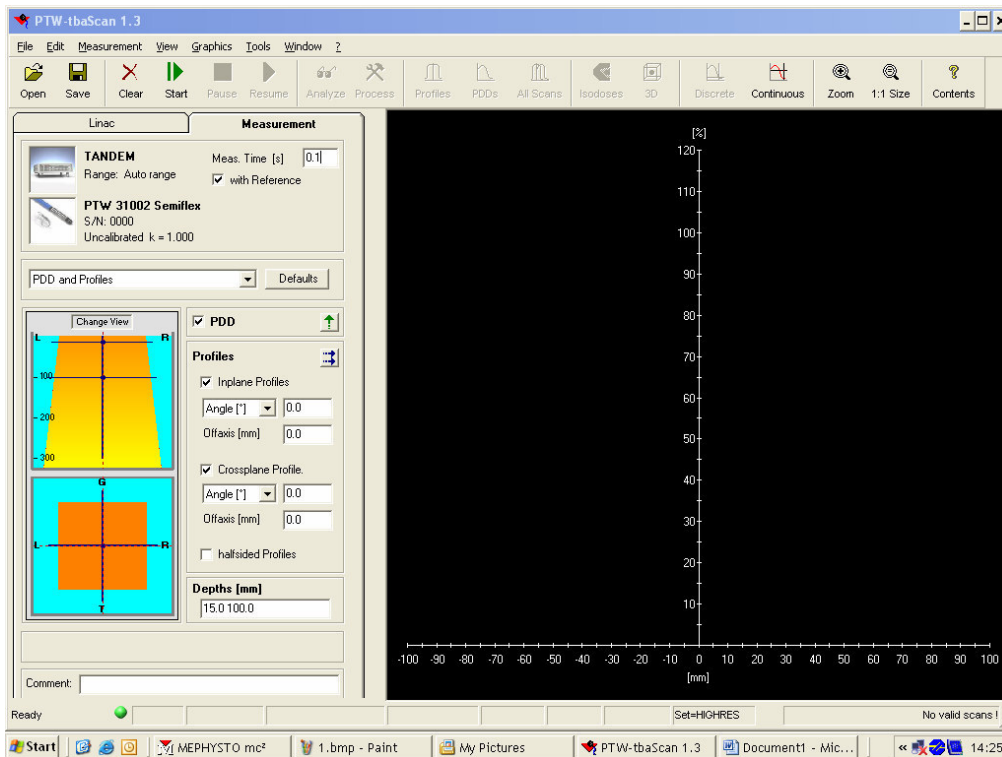


Figure 3.12: Second group of settings in TBAScan

Lastly, the number of points to be measured is set. This is related to the spacing of measurements, or in other words, the resolution required. The step sizes that can be set can be varied with different ranges. This is setup so that with higher dose gradients, lower steps can be set to acquire with higher precision.

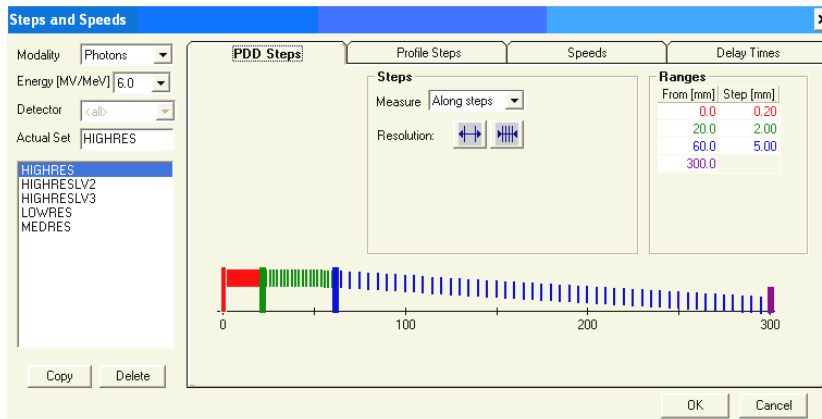


Figure 3.13: Step settings for PDD



Figure 3.14: Step settings for profiles

In addition to step settings for both PDD (see Figure 3.12) and profiles (see Figure 3.13), the speed of the chamber movement can be set to increase accuracy and decrease the effect of water movement (see Figure 3.14).

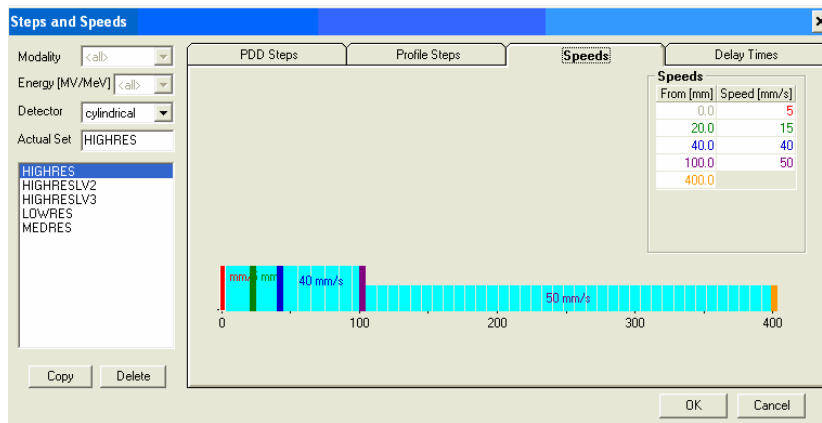


Figure 3.15: Speed settings for chamber movement

Lastly, delay times (see Figure 3.15) can be set to allow for water stabilisation. Realising the need for practical settings due to the time consuming nature of measurement, a setting of zero was used. As far as the author is aware, there is no literature detailing the quantitative effects of water rippling in dosimetry.

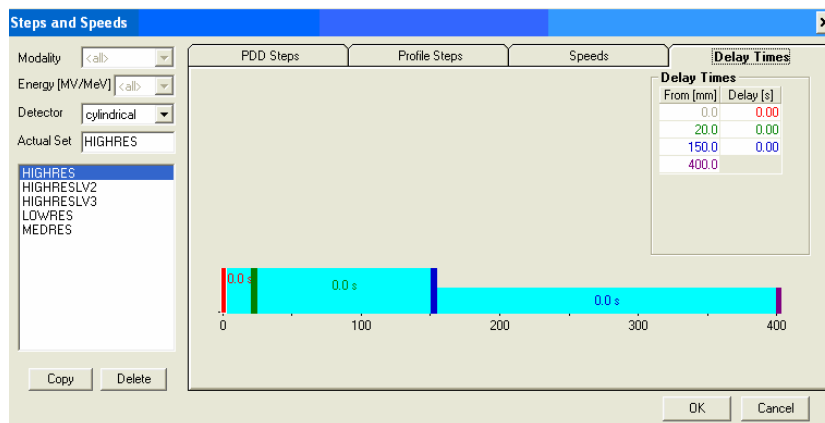


Figure 3.16: Delay times for chamber positions (zero was set for all positions)

3.3 DATA ANALYSIS AND PROCESSING

3.3.1 DataAnalyse: Centering and smoothing of data*

Data obtained from *TBAScan* was opened with *DataAnalyse* to centre and smooth the data. All PDDs were smoothed with the smooth function. The symmetrise and the smooth function was applied to all profiles (see Figure 3.16).

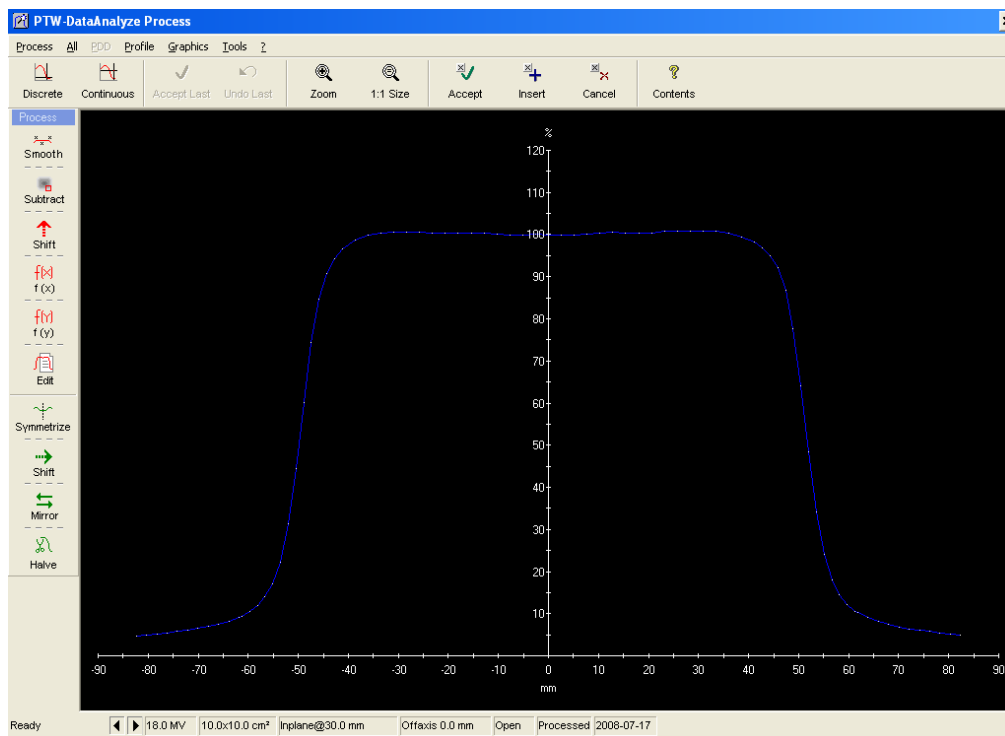


Figure 3.17: Processing functions, showing the symmetrise and smooth function on the left hand side of the screen

3.3.2 Custom EXCEL script: Conversion of mcc files into txt files

The MEPHYSTO mc² software package uses a proprietary file format which ends with mcc. This file format is detailed in the table below. An excel script was written to run an algorithm that sorted each set of data with the field size, depth, and the detector used. The script was also able to detect the direction of the profile measured. The output of the script was in the excel worksheet format, which was then saved as a txt file. Each column in the txt file could be referred to the field size, depth, detector used, and profile direction in the excel file (see Appendix Table 9.1).

3.3.3 MATLAB data analysis and data processing

The MATLAB software package (Version R2007a, The MathWorks, Inc.) was used to analyse and process files. A variety of functions, which include interpolation, curve fitting, search functions, were used to perform analysis of parameters such as the detector volume effect.

MATLAB was also used for data processing, for use in exporting files into the format required by the radiotherapy treatment planning system (RTP) Pinnacle³. The required format of profiles in Pinnacle³ is described in Table 3.7.

Table 3.7: Illustration of the data format required by Pinnacle³

512		Integer specifying the number of rows in the data
-75	0.02953	First column specifying the position with the second
-74.707	0.02953	column specifying the measured data. The two
-74.4141	0.02953	values are separated with a "space".
-74.1211	0.02953	
-73.8281	0.02953	
-73.5352	0.02953	
-73.2422	0.02953	
-72.9492	0.02953	
-72.6563	0.02953	
-72.3633	0.02953	
-72.0703	0.02953	
...	...	

3.4 RADIOTHERAPY TREATMENT PLANNING SYSTEM

MODELLING

Note that three sets of data was measured with both jaw and MLC profiles and PDDs measured with the IC, PP, and DD. A single model was modelled with the IC, and later the source size parameter was modified in order to model the penumbral effects observed with different detectors.

3.4.1 The Pinnacle³ Convolution Superposition Dose model

The Pinnacle³ treatment planning system's dose calculation is based on a model based system working on first principles and not a correction-based system (McNutt and Gehring 1997; ADAC 2000b). The Convolution Superposition dose model employed is based on three main components (McNutt and Gehring 1997):

1. Modelling of incident energy fluence as a two dimensional array which is perturbed by the flattening filter, the blocks or MLC, the off scatter from the treatment head, wedges, and finally the geometric penumbra is convolved with a focal spot blurring function.
2. The energy fluence is used to compute the TERMA through a CT patient/phantom representation and attenuated using mass attenuation coefficients. Beam hardening through the patient, off-axis softening of energy spectrum, and patient heterogeneity is taken into account.
3. The TERMA volume is superpositioned with the energy deposition kernel, which is calculated dependent on the energy of the voxels where the TERMA transverses. The kernel represents the spread of energy from the primary photon interaction site which is computed towards the dose deposition site at a radiological distance (the radiological distance allows the kernel to be scaled to account for heterogeneities).

3.4.2 Depth dose region: Effect of energy Spectra

The original beam spectra from a pre-loaded machine as used as the starting point for modelling of the energy spectra in order to fit the measured data. Changes in the beam hardness was adjusted to fit the latter part of the curve (ADAC 2000b) with the shape of the modelled depth dose curve most dependent on the relative number of mid to high energy photons (see Figure 3.17).

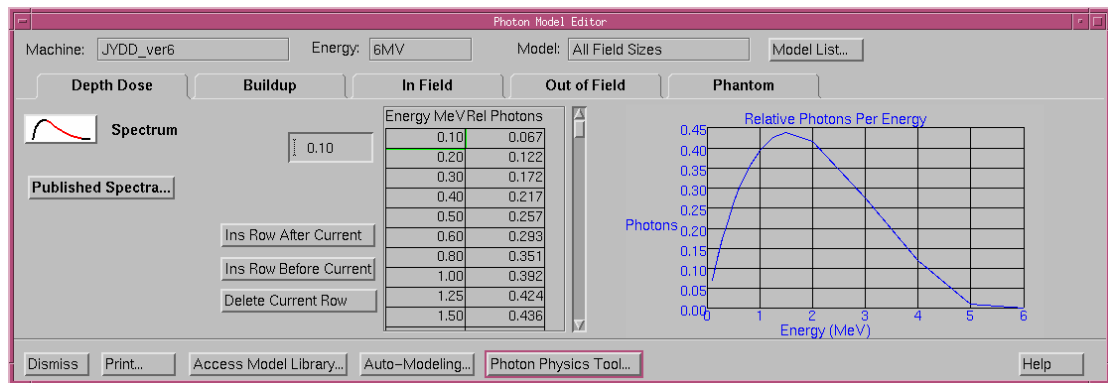


Figure 3.18: The depth dose tab for beam modelling in Pinnacle³

The figure below shows the comparison in agreement between the computed and measured PDD. The nature of optimisation was performed iteratively: each change in energy spectra was followed by a comparison of measured and modelled PDDs until a close agreement was achieved.

The initial part of the PDD was not optimised fully until the next section (build-up tab) was performed, as the initial part of the PDD corresponds to depths above d_{\max} , where the electron contamination dose is significant with respect to the dose contributed by the main fluence from the beam.

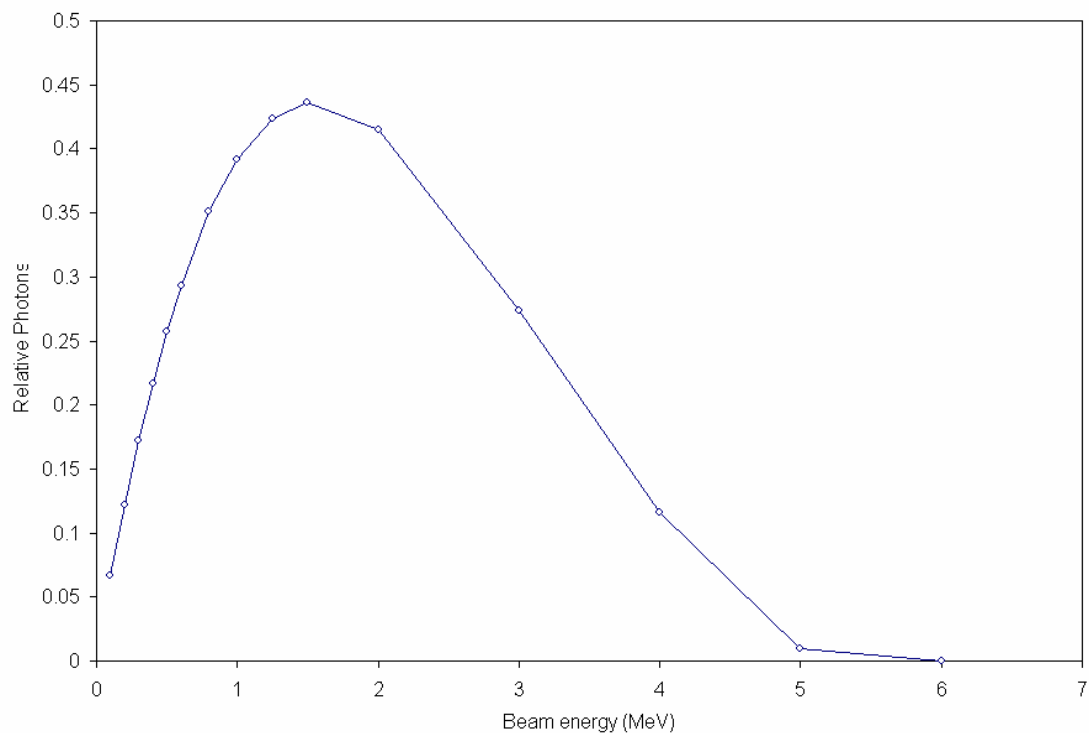


Figure 3.19: Actual energy spectra used in the study

The actual energy spectra that corresponded to a good fit between model and measured data is presented in the Figure 3.18 and showed a maximum amount of photons (relative) at an energy slightly less than 1/3 of the maximum energy (2 MeV), as expected. The virtual spectrum generated by Pinnacle to match the beam properties. Part of the data used was used to produce TERMA and dose spread arrays (Mohan, Chui et al. 1985).

3.4.3 Comparison between measurement and model in the PDD

As discussed in the previous sections, the tail region of the PDD is affected predominantly by the energy spectra whereas the shallow region of the PDD is affected predominantly by the electron contamination. Optimisation concentrated on the PDD (see Figure 3.19) relating to field sizes of 1×1 cm², 5×5 cm², and 10×10 cm².

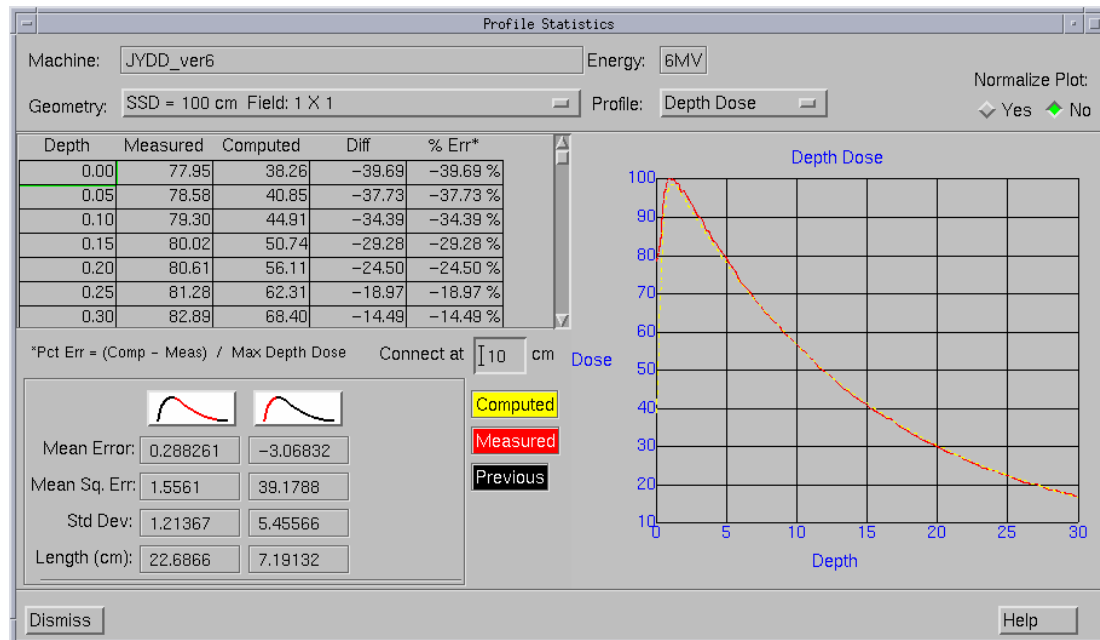


Figure 3.20: Comparison between computed and measured PDD in Pinnacle³

3.4.4 Build-up region: Effect of electron contamination*

The electron contamination is modelled here (see Figure 3.20) to improve the agreement between the computed and measured PDD in the shallow region of the curve. Pinnacle³ models electron contamination by modelling an added electron dose to the photon dose (ADAC 2000b), as a modified exponential curve. Again, an iterative approach was taken to optimise the agreement between measured and model PDD, especially at a

depth of 0.25 cm. The electron contamination parameters used in this study are listed in Table 3.8.

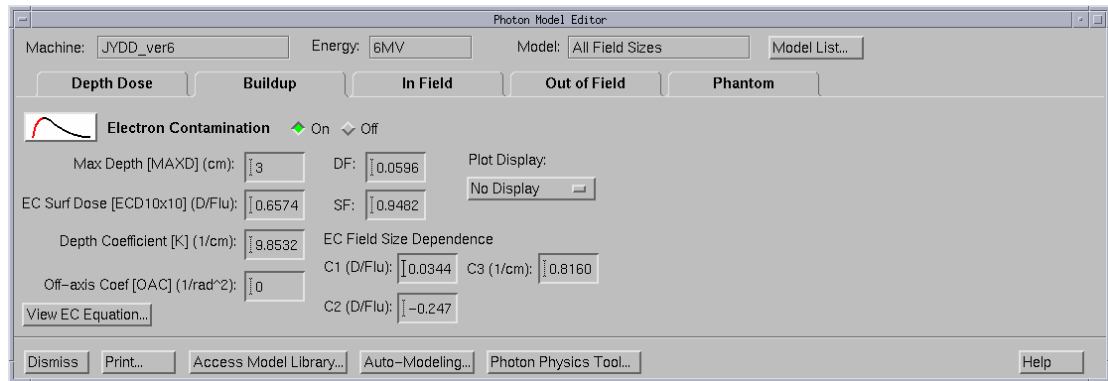


Figure 3.21: The build-up tab in the beam modelling section in Pinnacle³

Table 3.8: Infield tab parameters used

Electron Contamination	ON
Max Depth MAXD (cm)	3
EC Surf Dose (D/flu)	0.6574
Depth Coefficient (1/cm)	9.8532
Off-axis Coefficient (1/rad ²)	0
DF	0.0596
SF	0.9482
EC Field Size Dependence:	
C1 (D/flu)	0.0344
C2 (D/flu)	-0.247
C3 (1/cm)	0.816

3.4.5 Infield region: Effect of flattening filter*

The infield region models the effect of the flattening filter. The flattening filter changes the fluence of the beam as a function of off-axis distance and also changes the beam energy as a function of off axis distance (ADAC 2000b). The off-axis softening factor (see Figure 3.21) was modified so that similar errors were observed at depths of 5, 10, and 20 cm at a profile of 10×10 cm².

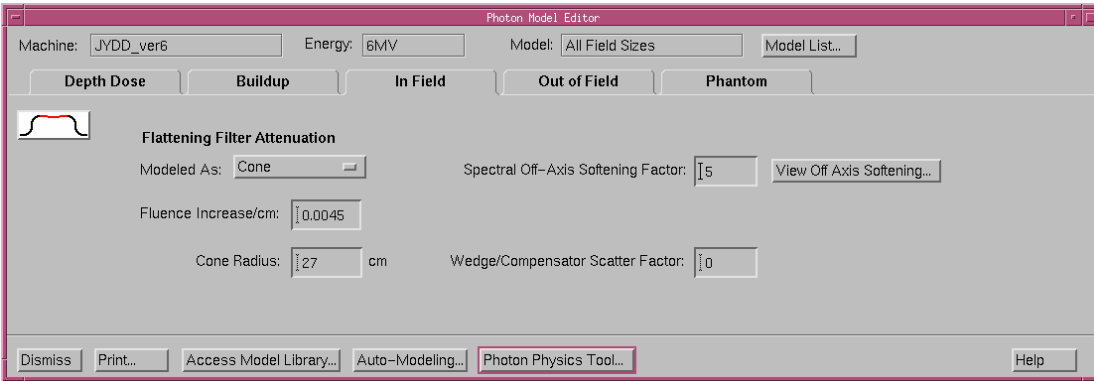


Figure 3.22: The infield tab in beam modelling in Pinnacle³

3.4.6 Out of field region: Effect of source size, scatter source, and transmission

The parameters in the out of field region affect the penumbra and tails in the profiles (see Figure 3.22). The effective source size acts as a blurring kernel that blurs the incident fluence model (ADAC 2000b). A larger effective source size effectively increases the penumbra of a profile and makes it rounder –similar to the effect of the detector size effect.

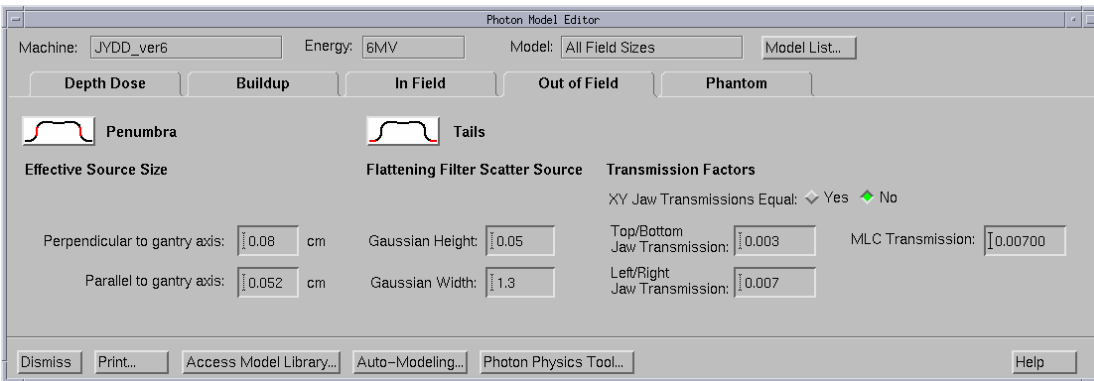


Figure 3.23: The out-of-field tab in the beam modelling section in Pinnacle³

The tail of the profile is modelled by the parameter relating to the flattening filter scatter source parameter. The flattening filter is modelled as a source of secondary scatter radiation that contributes dose across the whole profile but most noticeably in the tail region (ADAC 2000b). The jaw and MLC transmission model the transmission of radiation through the jaws and MLCs. The parameters used are presented in Table 3.9.

Table 3.9: Out-of-field parameters used

Penumbra		
Effective Source Size		
Perpendicular to gantry axis	0.0452	Note that these two parameters were modified with each chamber model
Parallel to gantry axis	0.0271	
Tails		
Flattening Filter Scatter Source		
Gaussian Height	0.08127	Note that the X jaw affects the LEFT/RIGHT direction and the Y jaw affects the TOP/BOTTOM direction
Gaussian Width	4.76333	
Transmission factors		
XY Jaw transmission equal	YES	
Jaw Transmission	0.0074537	
MLC Transmission	0.03	

3.4.7 Comparison between measurement and model in profiles

The profile consists of three main regions, as shown Figure 3.23: The in-field region, the out-of-field region, and the tail region. The effect of the flattening filter was predominant in the in-field region and had to be modelled as a function of depth as well as off-axis distance due to a change in beam fluence and energy with off-axis distance.

The out-of-field region, which describes the penumbra, was predominantly modelled with the effective source size which blurred the initial fluence distribution and the tail region was a function of transmission through the MLC and jaws as well as the model of the flattening filter as a scatter source.

Optimisation concentrated on the profiles relating to field sizes of $1 \times 1 \text{ cm}^2$, $5 \times 5 \text{ cm}^2$, and $10 \times 10 \text{ cm}^2$ at 10 cm depth; and for the optimisation of the off-axis softening factor, depths of 5 cm and 20 cm were also considered.

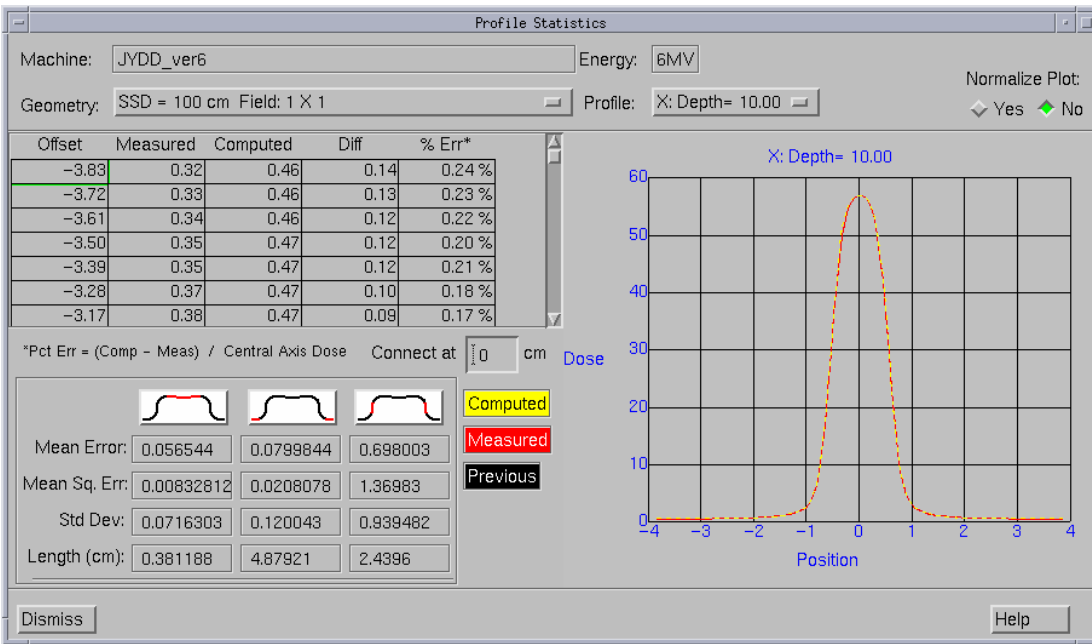


Figure 3.24: Comparison of measured and computed profiles in Pinnacle³

3.4.8 Phantom tab: Effect of grid resolution and phantom size

The effect of fluence grid resolution was significant, especially for small field sizes such as 1x1 cm² fields (see Figure 3.24). For the initial set of iterations, a fluence grid resolution of 0.4 cm was used. At the later stages 0.2 cm was used. Technical limitations such as the lack of memory (RAM) prevented the use of smaller grid sizes such as 0.1 cm. The default phantom size, 50 x 50 cm², was sufficient to provide the necessary scatter to any dose calculation point within our maximum field size of 20x20 cm².

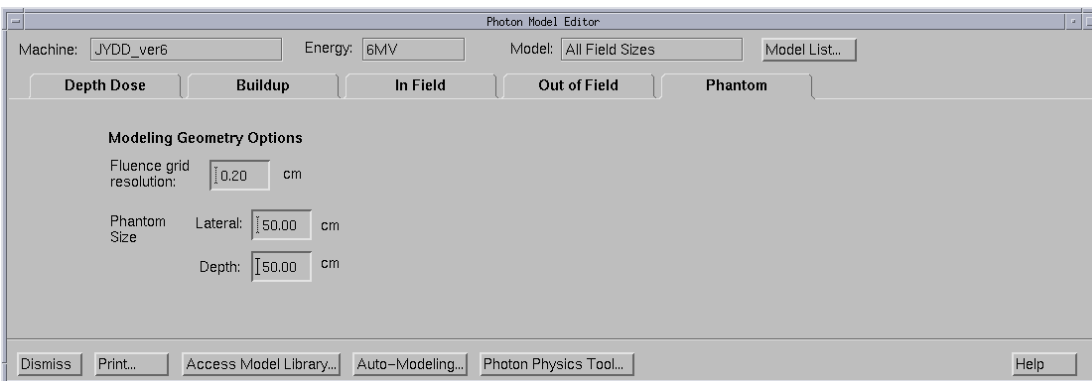


Figure 3.25: The phantom tab in the beam modelling section in Pinnacle³

3.4.9 Note on the limitation of the modelling used in this study

Note that it is possible to generate multiple models for various field sizes. If multiple models are created, intermediate field sizes are interpolated between the two models corresponding to the larger and the smaller field size.

The recommendation (ADAC 2000b) was that multiple models should be used only if unacceptable matches between measured and computed dose profiles were the case. It was also noted that IAEA TRS. 430 specify tolerances for dose deviation and distance deviation as 2 % and 2 mm for penumbra for square fields, which involve simple geometry. Tolerances differ for MLC-defined fields, inhomogeneous phantoms, and with complex geometry (e.g. wedges). In this study, only a single model was used with the caveat that the study is focused on small field sizes and that larger field sizes and wedges were not fully accounted for.

3.5 RADIOTHERAPY TREATMENT PLANNING SYSTEM PLANNING

3.5.1 RTPS plans

Beam simulations were performed in the *Planning* section of the Pinnacle RTPS. An selection of plans were formulated to test the effect of the variance in the RTPS model due to detector diameter (i.e. changes in the source size) on small fields, large fields, junctioned fields, and a simple 5-field prostate 3DCRT plan (see Chapter 10).

3.5.2 Creation of planar dose maps

MATLAB was used to write a script in order to produce the planar dose files that were required in order to export dose distributions for data analysis. A programming language is required to produce such files (see Appendix I for the code) as the dose points need to be specified –the dose points are specified in a text file (see Table 3.10 for the dose map format). Control of the specification of the dose points allows the user to select the coronal, sagittal, or axial planes as well as the position of the slice required. In addition, arbitrary geometrical dose maps can be programmed, such as spiral dose maps or cylindrical dose maps.

Table 3.10: The Pinnacle³ dose map format required. The file ends with “pts”.

250	250	0.4	The integers in the first two columns specify how many points are in the X and Y direction of the image.
-50	0	-50	
-50	0	-49.6	
-50	0	-49.2	
-50	0	-48.8	
-50	0	-48.4	The integers in the third column specifies the resolution of the dose map.
-50	0	-48	
-50	0	-47.6	
-50	0	-47.2	
-50	0	-46.8	
-50	0	-46.4	Each row specifies a dose point. Each dose point has to be specified; in this case this would involve $250^2=62500$ dose points.
-50	0	-46	
-50	0	-45.6	
-50	0	-45.2	
-50	0	-44.8	
...	

3.5.3 Evaluation of isodose distributions

After the dose map is selected and loaded into Pinnacle³, the dose model calculates the planar dose distribution in the plane due to a single beam. After the calculation, the planar dose distribution can be exported into a file with an ASCII format, as shown in table 3.11..

Table 3.11: The file format of the exported Pinnacle³ planar dose distribution

Version:	8.0d				
Patient:	Prostate	John			
MR Number:					
Plan Name:	AAM_IGRT				
Plan revision:	R03.P03.D03				
Date:	7/5/2008 2:23:45 PM				
Trial:	6				
Beam:	1				
Machine:	JYIC_comm_may08				
SPD:	110				
	-8.9	-8.7	-8.5	...	
-8.9	0	0	0	...	
-8.7	0	0	0	...	
-8.5	0	0	0	...	
-8.3	0	0	0	...	
-8.1	0	0	0	...	
-7.9	0	0	0	...	
-7.7	0	0	0	...	
...

MATLAB was used to import the file which contains a two dimensional array of dose values, with positional values, as well as a 11 line header (one line is a spacer). The two dimensional array is easily handled as an array variable in MATLAB and was processed with contour plots and addition/subtraction/normalisation algorithms.

3.5.4 Plan evaluation in the treatment planning system

Once the planning has been completed, Pinnacle³ is able to calculate the dose to specified volumes in the patient plan. The cumulative dose volume histogram (DVH) is a commonly used plan evaluation tool (see Figure 3.26). Voxels within a dose distribution are classified into frequency groups based on dose levels, and a histogram is plotted in terms of cumulative dose to produce a cumulative dose volume histogram

(DVH) (Metcalf, Kron et al. 2007). The cumulative DVH shown in figure 3.26 has volume normalised to 1 in the y axis and total dose in the x axis.

The mean dose of the target and of the organs at risk was of the main interest in our study. Under further investigation, it is expected that the volumes that have margins in close proximity to penumbras will have a larger change in dose depending on penumbra width. This in turn will influence the DVH.

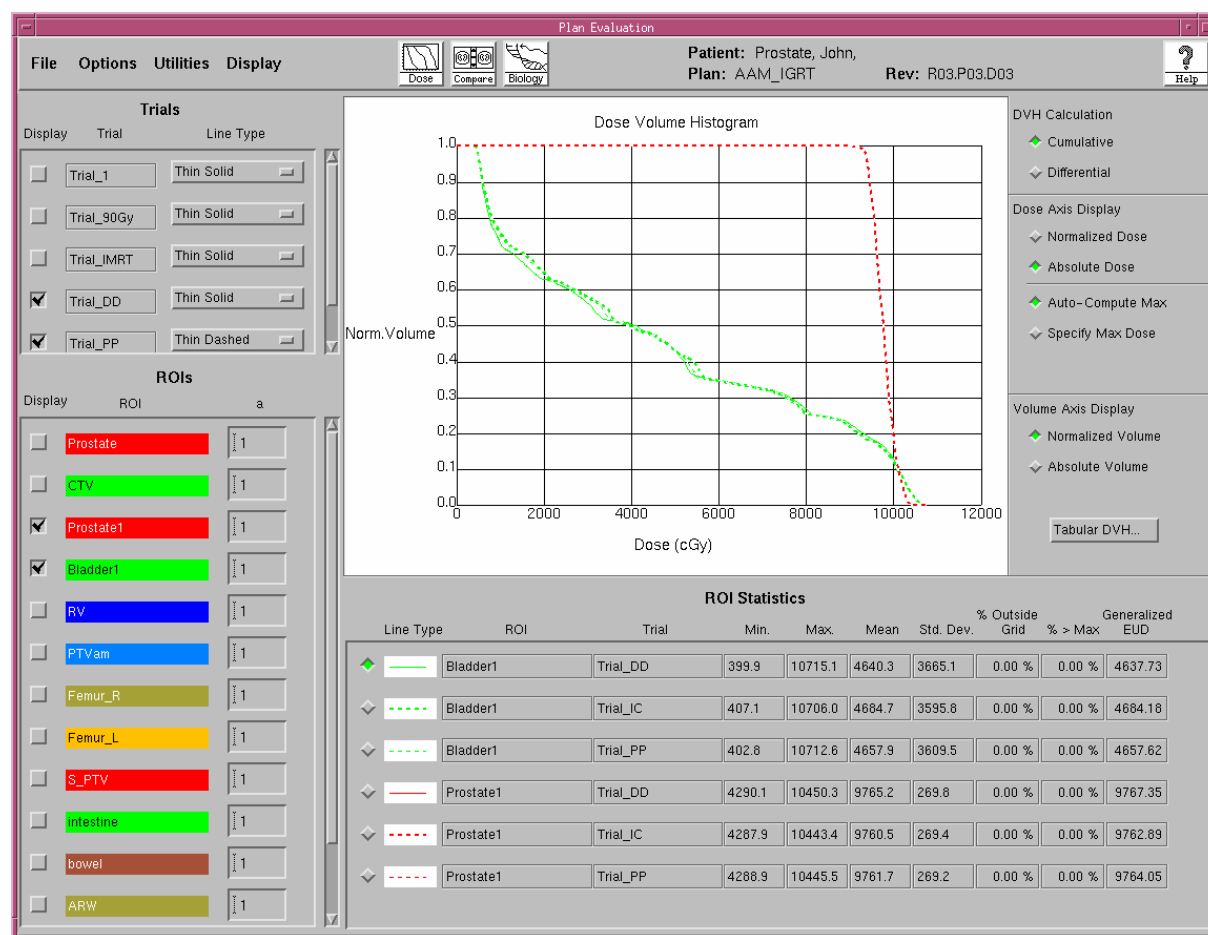


Figure 3.26: The DVH in the Plan Evaluation menu in Pinnacle³

3.6 DISCUSSION OF BEAM PARAMETERS USED

3.6.1 Penumbra width

The generally accepted definition of penumbra (see Figure 3.27) accepted is the spatial distance subtended by the normalised dose value of 20% and 80% in a profile (PTW 2006), and is usually measured 10 cm deep (IAEA 2005).

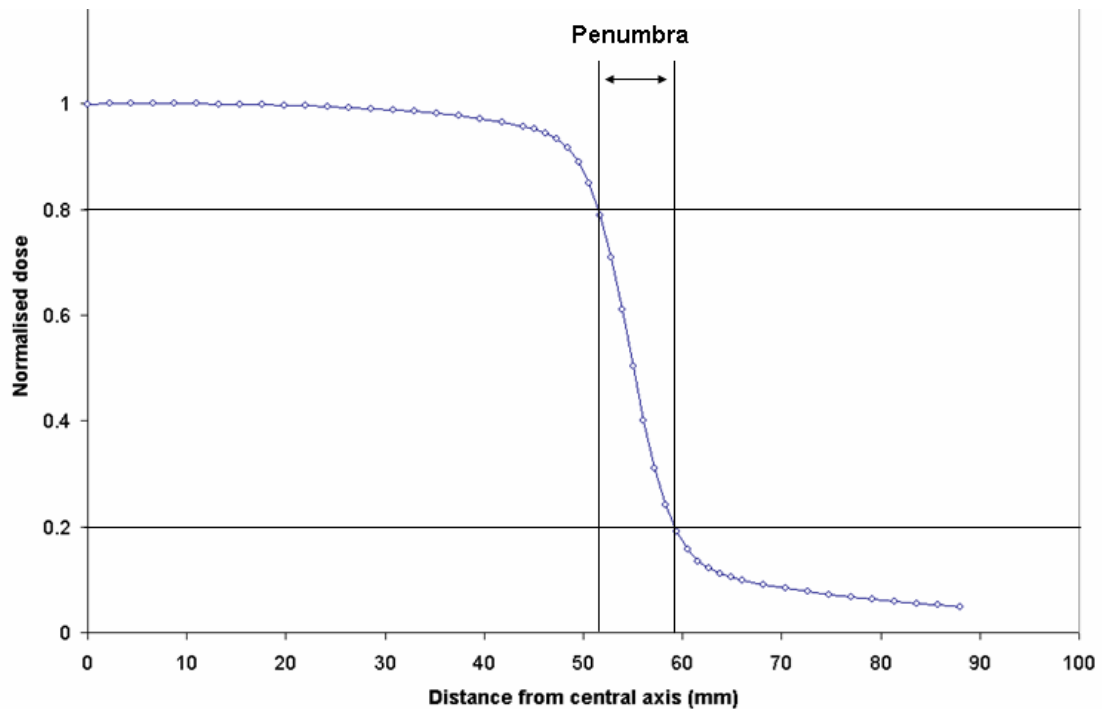


Figure 3.27: Illustration of the penumbra width, which is the distance subtended from normalised dose values of 20% and 80%

3.6.2 Percentage depth dose (PDD)

The percentage depth dose (PDD), as shown in Figure 3.26, was measured in a water tank at a SSD of 100 cm.

Please see print copy for image

Figure 3.28: An illustration of the percentage depth dose, with the surface dose D_s being the surface dose, d_{\max} being the dose corresponding to maximum dose, and D_{ex} being the exit dose. The region before d_{\max} is referred to as the build-up region. Figure adapted from (IAEA 2005)

3.6.3 Tissue Phantom Ratio (TPR)

The beam quality called the tissue-phantom ratio (TPR) is the absorbed dose at any point divided by the absorbed dose at the same point but with a different depth of phantom that attenuates the beam (Metcalf, Kron et al. 2007). The use of TPR is discussed more in Appendix H.

3.6.4 Calculation of TPR from PDD

In the case of the field size defined at a distance $f+d_m$ at the source, the calculation of TPR from PDD and PSF can be calculated by :

$$TPR[d, S] = \frac{PDD[d, f, S(f + d_m)/(f + d)]}{PDD[d_r, f, S(f + d_m)/(f + d_r)]} \frac{PSF[S(f + d_m)/(f + d)]}{PSF[S(f + d_m)/(f + d_r)]} \left(\frac{f + d}{f + d_r} \right)^2$$

(3.4)

Equation 3.4 was used St. George Hospital because most protocols involve SAD setups. An example of this calculation is demonstrated with the sample parameters outlines in table 3.12. The steps used to calculate the TPR value is performed in equation 3.4. The programming algorithm used is outlined in figure 3.29 and was used to produce the results in Appendix H.

Table 3.12 Tabulated data of parameters used in example calculation of TPR from PDD and PSF

<i>Variable</i>	<i>Parameter</i>	<i>Value</i>
D	Depth	4cm
S	Square Field Size	10cm
d _m	Depth at Dose Max.	1.5cm (6MV)
F	SSD	100cm
d _r	Reference depth	10cm

$$\begin{aligned}
 TPR[d, S] &= \frac{PDD[d, f, S(f + d_m)/(f + d)]}{PDD[d_r, f, S(f + d_m)/(f + d_r)]} \frac{PSF[S(f + d_m)/(f + d)]}{PSF[S(f + d_m)/(f + d_r)]} \left(\frac{f + d}{f + d_r} \right)^2 \\
 TPR[4, 10] &= \frac{PDD[4, 100, 10(100 + 1.5)/(100 + 4)]}{PDD[4, 100, 10(100 + 1.5)/(100 + 10)]} \frac{PSF[10(100 + 1.5)/(100 + 4)]}{PSF[10(100 + 1.5)/(100 + 10)]} \left(\frac{100 + 4}{100 + 10} \right)^2 \\
 TPR[4, 10] &= \frac{PDD[4, 100, 9.78]}{PDD[4, 100, 9.23]} \frac{PSF[9.78]}{PSF[9.23]} (0.89)
 \end{aligned}
 \tag{3.5}$$

1. Input depth
2. Input field size
3. Input SSD
4. Calculate $(f + d_m)/(f + d)$
5. Interpolate PDD (1)
6. Interpolate PSF (1)
7. Get PSF data point (1)
8. Calculation of single point TMR
 - a. Increment depth
 - i. Repeat 1-8
 - ii. Put data in a single column
 - iii. Increment Row with each value
 - iv. Finish TMR for all depth
 - b. Increment field size
 - i. Repeat 1-8
 - ii. Increment column once
 - iii. Increment Row with each value
 - iv. Finish TMR for all field size

Figure 3.29: Illustration of the program structure used to calculate TMR

Chapter 4: Analysis of the curve properties of the dose profiles measured with different detectors

4.1 OVERVIEW

In the literature, to the authors knowledge there is no discussion of the intersection or inflection points of measured profiles. These properties effect the dose distribution of the profile with respect to the measurement with a specific detector. A simple form of analysis of the detector effect in measured profiles can be made in terms of analysing the intersection point. The intersection point represents the point where the dose is the same for all measured profiles with different detectors. It delineates the regions of over-response and under-response due to the detector effect. The deviation of the intersection point from the expected 50% dose (albeit a slight deviation) also implies that the detector effect influences the measured radiation field size (discussed in the Chapter 7).

The inflection point refers to the point where the change in the first derivative is constant, and is determined by finding the zero point in the second derivative of the profile. The inflection point for each detector is not at 50% and is not the same as the intersection point of the detectors. While the clinical relevance of the inflection point is not clear, being unaware of the detailed study of its features in the literature thus far seemed sufficient reason to report its features.

The two main methods of accounting for the effect of the detector volume are deconvolution (discussed in Chapter 6) and extrapolation (discussed in Chapter 5). Both methods rely heavily on the detector parameters supplied by the manufacturers and each method is involved has some limitations.

The calculation of the virtual zero detector data allows the quantification of the deviation from true profiles associated with the use of measured data with finite detector volumes (discussed in Chapter 7). The methods of obtaining virtual zero detector data is also verified where possible with variations in depth and field size. Correlation of penumbra and linear coefficients were performed in order quantify the effects of field size, and depth with other parameters in an equation capable of correcting for the effects of detector volume (discussed in Chapter 8).

A discussion of the effects of the variation of data due to the detector effect in the model of the radiation treatment planning system (RTPS) is quantified (discussed in Chapter 9) and the dose distribution due to variation in the models due to variations in the detector effect are compared (discussed in Chapter 10).

4.2 SENSITIVE DETECTOR DIAMETER DATA

The physical dimensions that were used are derived from the data from the manufacturer (PTW-Freiburg 2008). It is to be noted that for ionization chambers, there is an outer diameter that includes the wall and also an inner diameter that excludes the wall to exclusively define the air cavity of the chamber (See Figs 4.1, 4.2, 4.3).

The diamond detector has a small dimension of 0.1-0.4 mm thickness (Angelis, Onori et al. 2002) quoted which is smaller than the thickness in the PTW diagrams (0.5 mm). A value of 0.3 mm for the diamond detector was chosen (Buccioli, Buonomici et al. 2003), although there was some variation with 0.33 mm (Hoban, Heydarian et al. 1994) and 0.32 (Laub 2002).

In addition, the sensitive thickness of a detector and the FWHM of the kernel was significantly different as pointed out by some authors (Garcia-Vicente, Delgado et al. 1997; Bednarz, Huq et al. 2002). In addition to the values of sensitive thickness and the FWHM of deconvolution kernels, there is also the term “effective diameter” (Dawson, Harper et al. 1984) which described the detector diameter as a function of energy.

The lack of complete data with regards to kernel FWHM and effective diameters for all detectors used was a limitation to the accuracy of the detector diameters used. For consistency and reproducibility, the sensitive thickness values were used from PTW and these are displayed in Table 4.1.

Table 4.1: Tabulated volume, active size, and physical size for detectors used (PTW-Freiburg 2008)

Manufacturer	Detector Type	Volume (cm ³)	Active size (mm)	Physical size (mm)
PTW	Ion Chamber	0.125	D=5.5 L=6.5	6.5+0.75w
PTW	Pinpoint Chamber	0.015	D=2.0 L=5.0	5.0+0.70w
PTW	Diamond detector	0.001	D=0.3 L=3.3*	D=1.0 L=N/A

**Physical size measured from the diagram of the diamond detector (may not be the sensitive diameter)*

Please see print copy for image

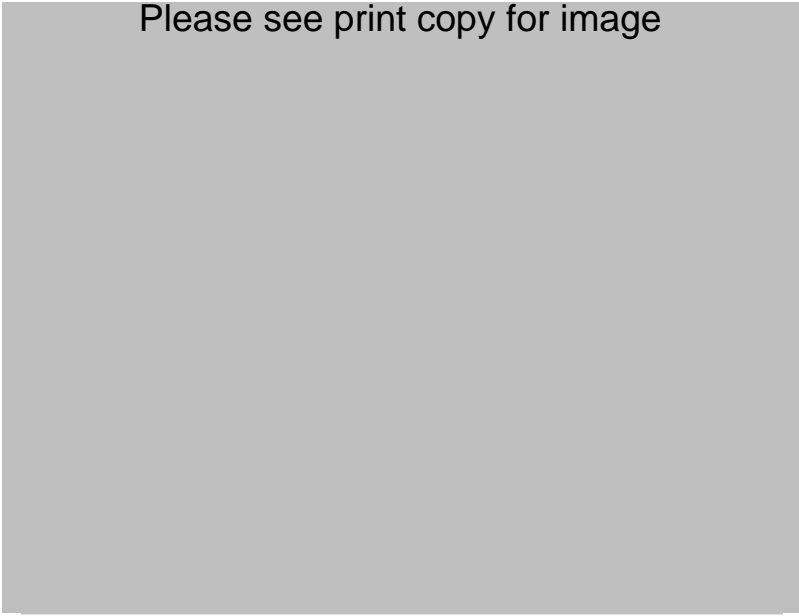


Figure 4.1: Diagram illustrating the dimensions of the 0.125 cc Ionisation Chamber from the manufacturer (PTW-Freiburg 2008)

Please see print copy for image



Figure 4.2: Diagram illustrating the dimensions of the Pinpoint Detector from the manufacturer (PTW-Freiburg 2008)

Please see print copy for image

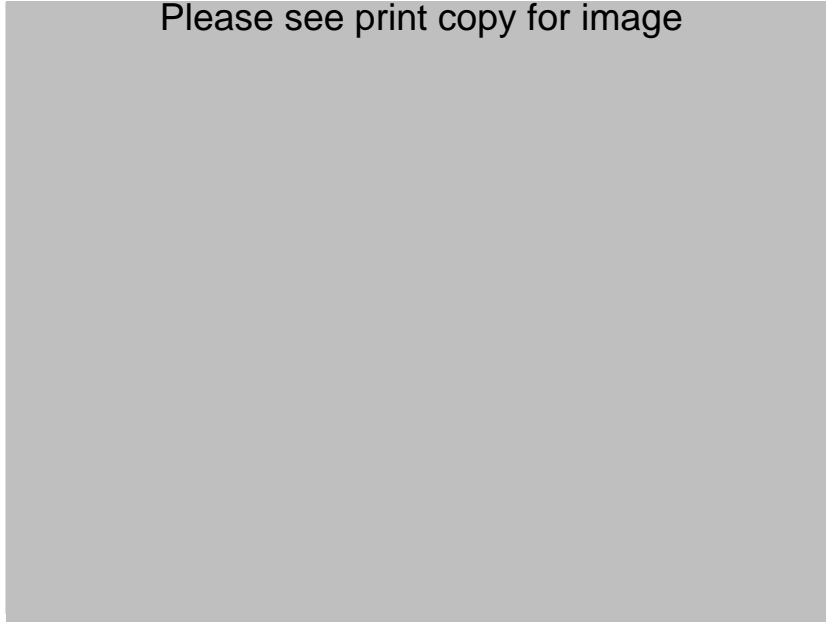


Figure 4.3: Diagram illustrating the dimensions of the Diamond Detector from the manufacturer (PTW-Freiburg 2008).

The black section, the sensitive volume, was used to estimate the sensitive diameter perpendicular to the long-axis of the detector (i.e. 3.3 mm).

4.3 INFLECTION POINT OF PROFILES

The inflection point of the penumbra dose profile can also be calculated analytically for a theoretical Gaussian curve. The inflection point can be solved by differentiating twice and finding the conditions for a value of zero at the second differential (i.e. the position where the change in the gradient is zero). Substitution into the Gaussian profile gives the expected answer, which is in contrast with the depth dependent inflection point that was measured.

$$\begin{aligned} y &= e^{-x^2} \\ y' &= -2xe^{-x^2} \\ y'' &= -2e^{-x^2} + 4x^2e^{-x^2} \end{aligned} \tag{4.1}$$

When $y''=0$

$$\begin{aligned} 4x^2e^{-x^2} &= 2e^{-x^2} \\ 4x^2 &= 2 \\ x &= \sqrt{1/2} \\ y &= e^{-1/2} = 0.60653 \end{aligned} \tag{4.2}$$

The first derivative of the dose component was calculated not analytically as were equations 4.1 and 4.2 but empirically using

$$dy = y_1 - y_2, \quad (4.3)$$

Due to the significant step size involved, the spatial position related to the first derivative was

$$x_{dy} = \frac{1}{2}(x_1 + x_2) \quad (4.4)$$

At a depth of 10 cm, a plot of the profile and the first derivatives of the IC, PP, and DD data is shown in figures 4.4 (1×1 cm² field) and G.2 (10×10 cm² field). Note that figure 4.5 is scaled to highlight the penumbral region (the x axis spans from 40 mm to 70 mm).

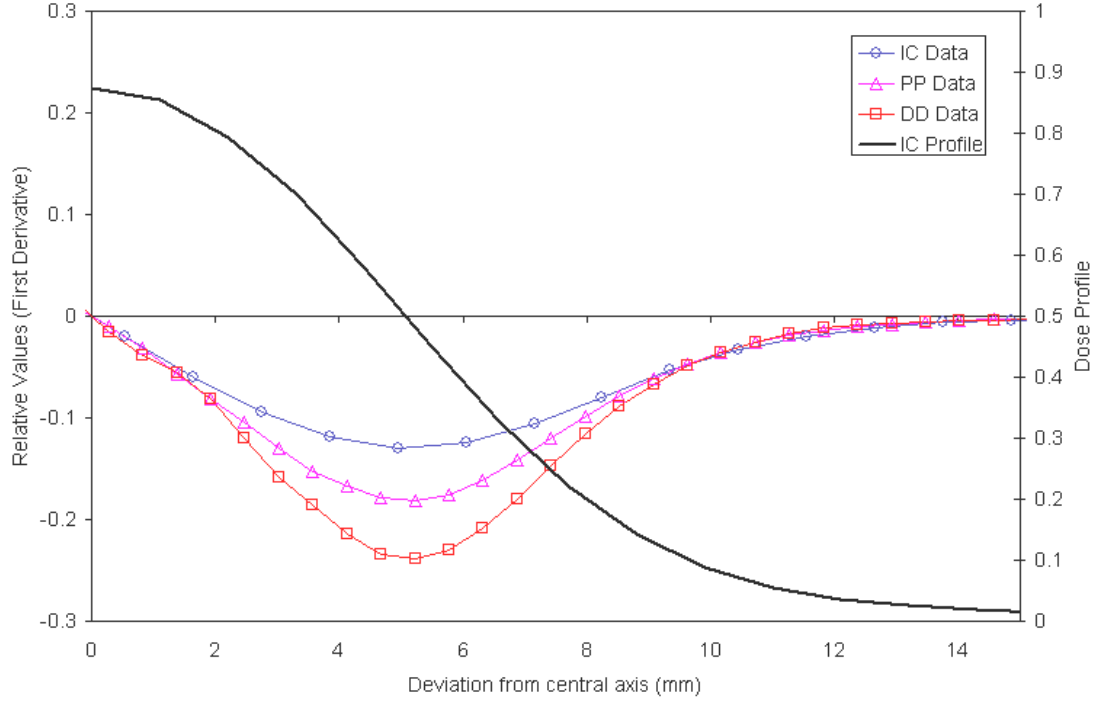


Figure 4.4: Figure showing the first derivative of a 1×1 cm² field at 10 cm depth

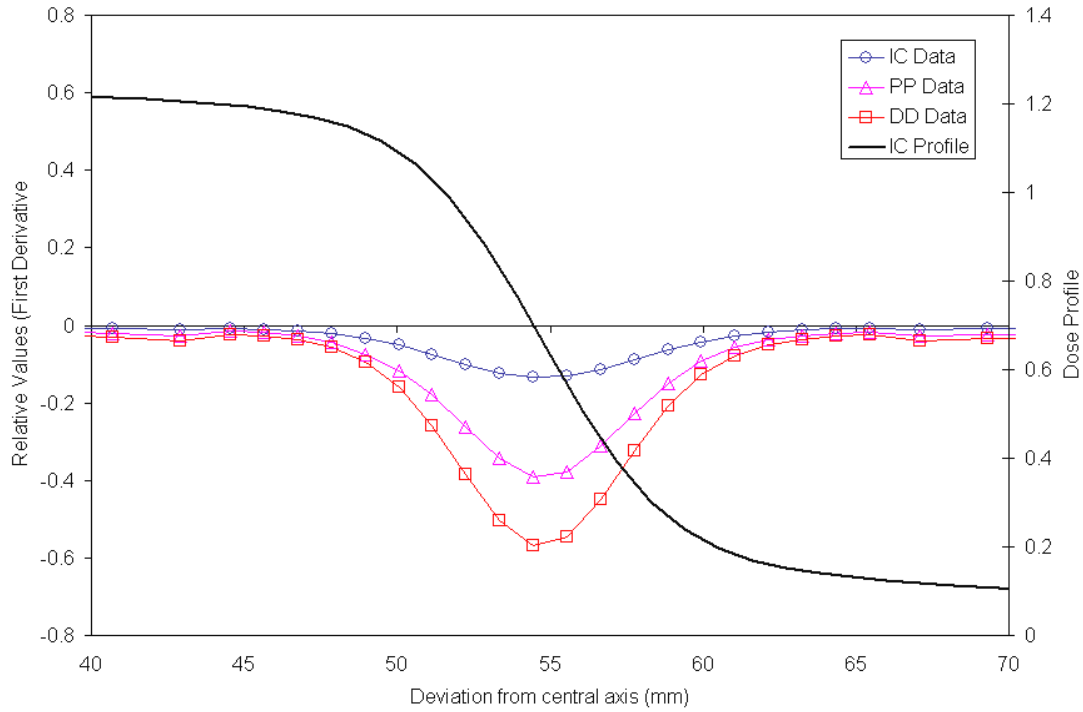


Figure 4.5: Figure showing the first derivative of a 10×10 cm² field at 10 cm depth

Similarly, the second derivative of the dose component was calculated empirically with the terms from the first derivative in equation 4.2

$$d^2 y = dy_1 - dy_2, \quad (4.5)$$

The spatial position related to the second derivative was

$$x_{d^2 y} = \frac{1}{2} (x_{dy,1} + x_{dy,2}) \quad (4.7)$$

At a depth of 10 cm, a plot of the profile and the second derivatives of the IC, PP, and DD data is shown in figures 4.6 (1×1 cm² field) and 4.7 (10×10 cm² field). Note that figure 4.5 is scaled to highlight the penumbral region (the x axis spans from 40 mm to 70 mm).

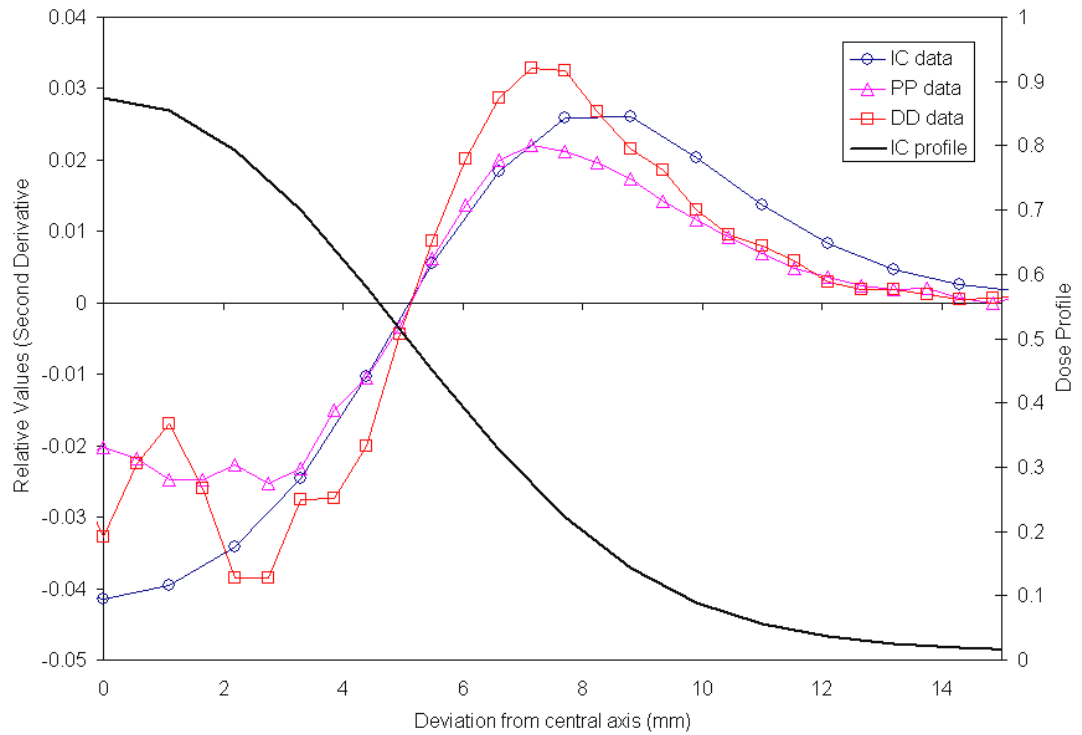


Figure 4.6: Figure showing the second derivative of a $1 \times 1 \text{ cm}^2$ field at 10 cm depth

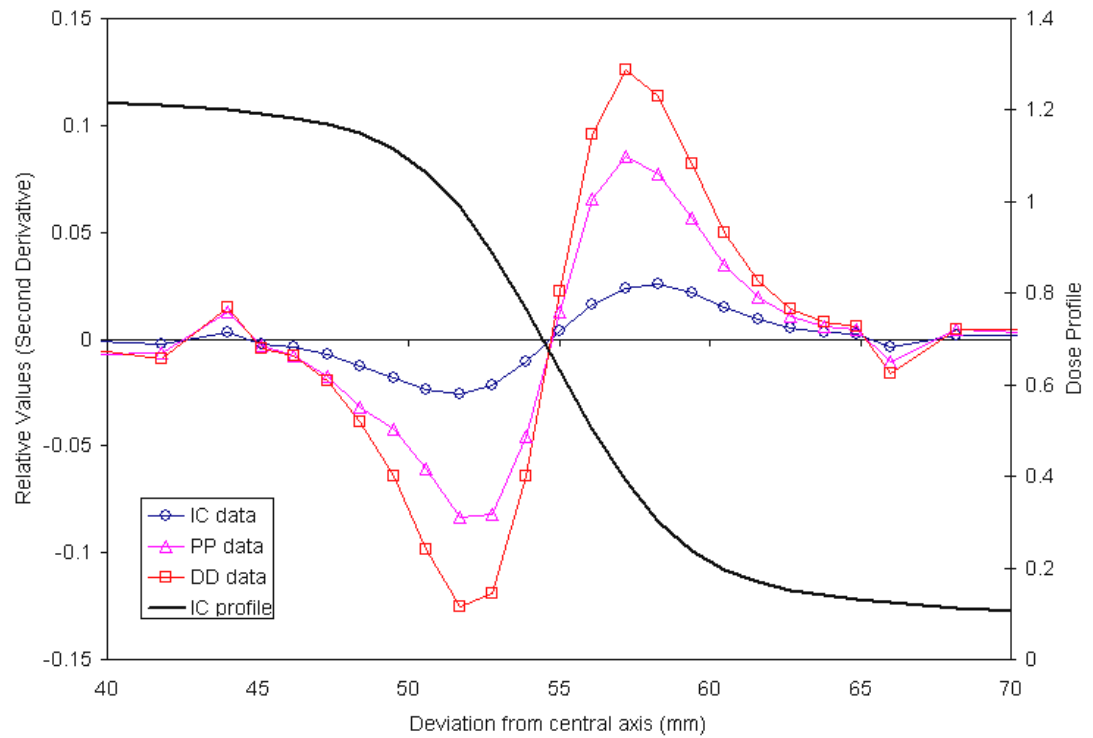


Figure 4.7: Figure showing the second derivative of a $10 \times 10 \text{ cm}^2$ field at 10 cm depth

An analysis of the second derivatives was made by determining the position at which the second derivative crossed zero in the penumbral region. The results indicated that all sources of data corresponded to the same spatial position in terms of inflection point (within 0.1 mm). In addition, these values did not correspond with the position of the field edge. The expected position of the field edge was calculated by

$$\text{Field Edge} = \frac{1}{2} (\text{Square Field Size}) \times \frac{\text{SSD} + \text{Depth}}{100 \text{ cm}} \quad (4.7)$$

Equation 4.7 was used to calculate the third column in table 4.2. The fourth column in table 4.2 was calculated by dividing the spatial position of the inflection point by the spatial position of the field edge at 10 cm depth and SSD 100 cm.

Table 4.2: Tabulated data showing the spatial position of the inflection point, the field edge, and the ratio of the two values

<i>Square Field Size (cm²)</i>	<i>Spatial position of inflection point (mm)</i>	<i>Spatial position of light field edge at 10 cm depth and SSD 100 cm (mm)</i>	<i>Spatial position of inflection point divided by field edge</i>
1	5.1	5.5	0.927
2	10.5	11	0.955
5	27	27.5	0.982
10	54.7	55	0.995

A plot of the spatial position of inflection point divided by the field edge was made in figure 4.8. Graphically, it can be seen that as the square field size increases, the ratio approaches a value of 1.0. In other words, the spatial position of the inflection point approaches the geometric field edge with increasing field size with the caveat that the data collected and analysed involved a maximum field size of 10×10 cm².

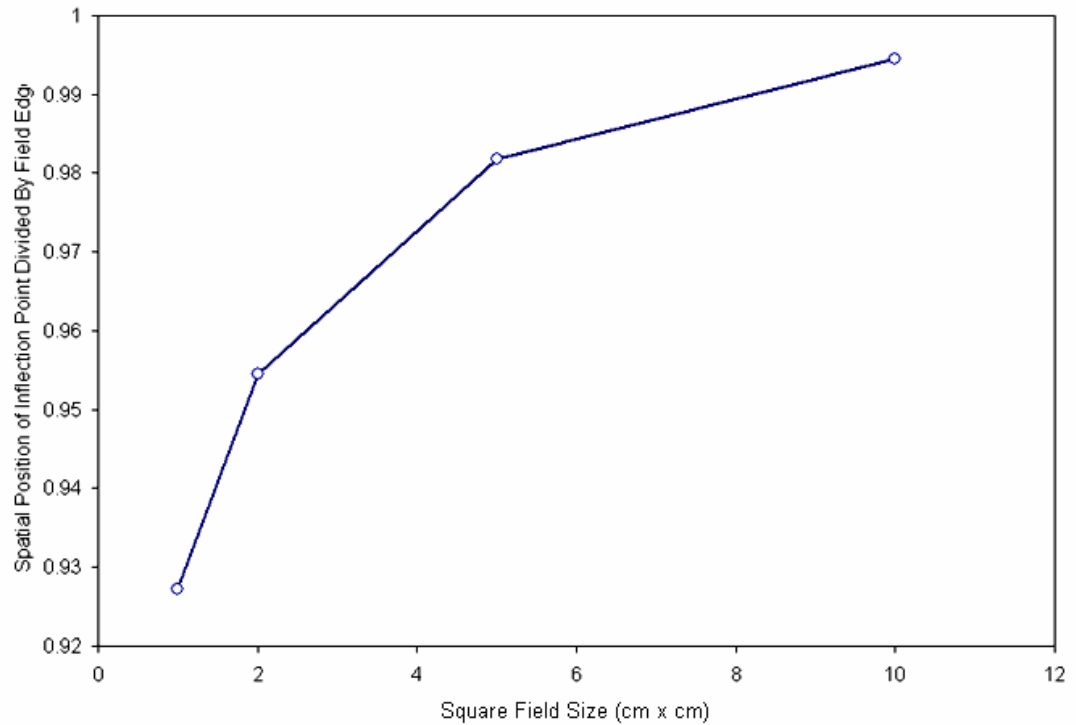


Figure 4.8: Plot of the ratio of the spatial position of inflection point over field edge with square field size at 10 cm depth

In addition to the spatial component, the dose component was also investigated. The spatial position of the inflection point was correlated to the dose component of each set of data (IC, PP, and DD) with interpolation because of finite data resolution. Figure 4.9 shows the normalised dose at the inflection point for each set of data. Even though the spatial position at the inflection point is the same in all sets of data, because of the detector effect the normalised dose values were significantly different.

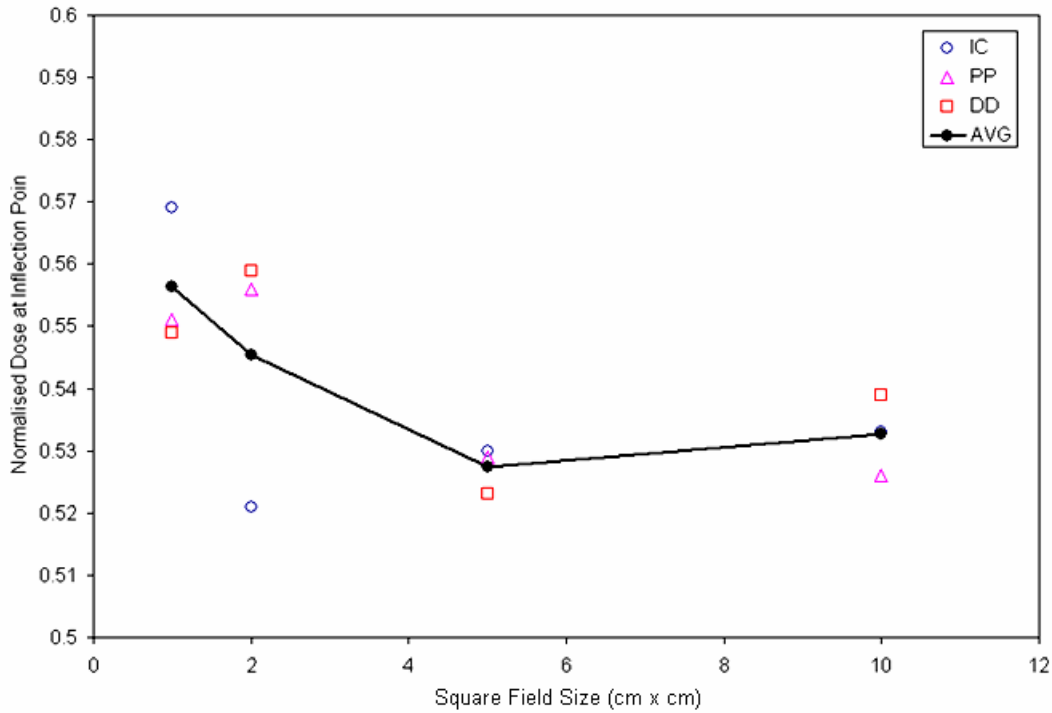


Figure 4.9: Plot of the normalised dose at inflection point for each set of data with square field size at 10 cm depth

Figure 4.9 indicates that there is a significant deviation in normalised dose at the inflection point from a value of 0.50 for all field sizes. For a $1 \times 1 \text{ cm}^2$ field size, the average deviation was 0.06 higher (i.e. 6% of dose from 50% dose) while for field sizes of $5 \times 5 \text{ cm}^2$ or larger, the dose at the inflection point was $53 \pm 1\%$ (0.53 in figure 4.9). The dose at the inflection point agreed between all data sets except for the IC, which had a value of 0.52 at a field size of $2 \times 2 \text{ cm}^2$ whereas the PP and the DD had values of approx. 0.56. This could indicate a deviation in response for the dose at the inflection point in the region of field sizes corresponding to the junction between *small* field sizes and field sizes with lateral electron equilibria where the actual peak value at the top of the profile is reduced due to lateral electron equilibria and the inflection point is higher when the profiles are renormalised to one at the profile peak.

4.4 INTERSECTION POINT OF DETECTORS

An analysis of the intersection points of the measured profiles is significant because the intersection point of the measured profiles indicates the point where the detector dose averaging coincides. The simplification of these three detectors to a function of chamber volume includes caveats such as the function of individual energy responses for each chamber and thus it may be an oversimplification to assume a constant intersection point of 50% over all conditions of field size and depth.

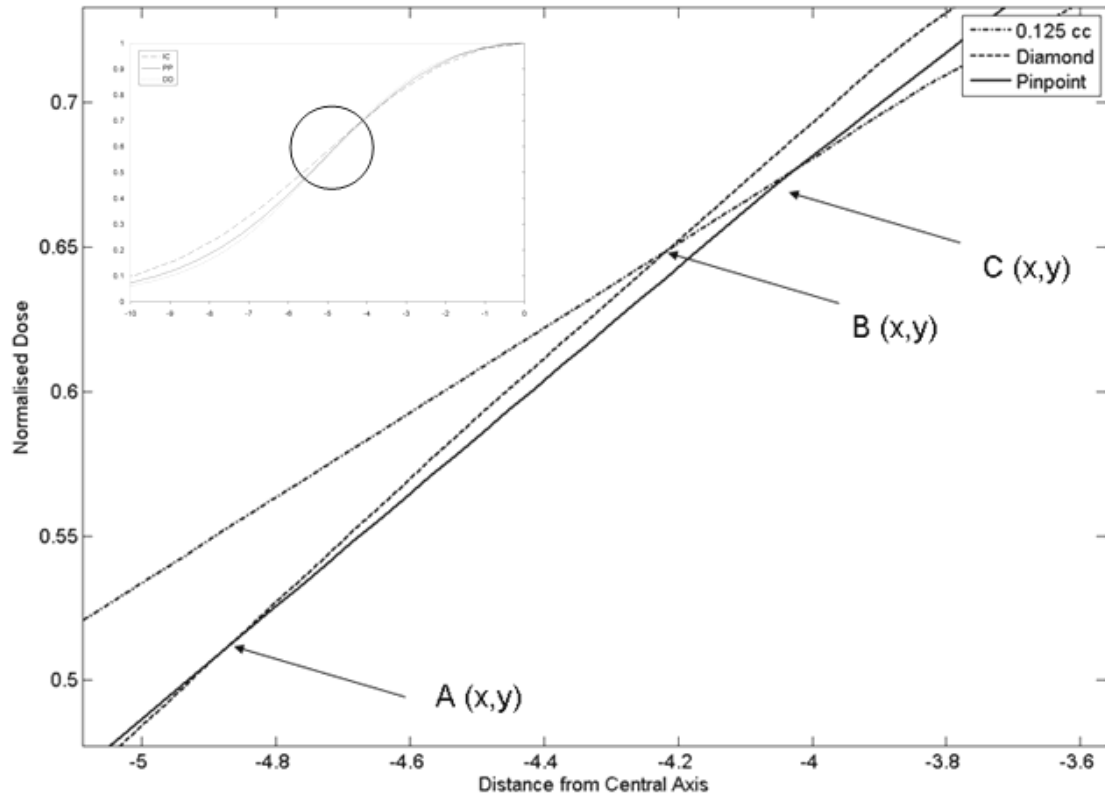


Figure 4.10: Enlarged region showing the intersection of the profiles relating to the IC, PP, and DD profiles

A zoomed plot of the measured profiles (see inset of fig. 4.10) can be used to illustrate the conditions of the intersection points of the measured profiles. It can be observed that there is, in fact, no single intersection point where the three curves intersect.

It can be seen that Point A is the intersection of the diamond and the pinpoint detector, point B is the intersection of the 0.125 cc and the diamond detector, and point C is the intersection of the pinpoint and the 0.125 cc detector.

MATLAB was used to plot the profiles together in one curve, with the zoom function used to enlarge the intersection point until the scale approached a constant

value to a resolution of 0.01. The dose at point A, B, and C were recorded and the average dose was plotted in figure 4.5.

Analysis of the intersection point at a field size of $1 \times 1 \text{ cm}^2$ for depths from 1.5 cm to 20 cm showed a negligible deviation of intersection point with depth (within 0.01 normalized dose).

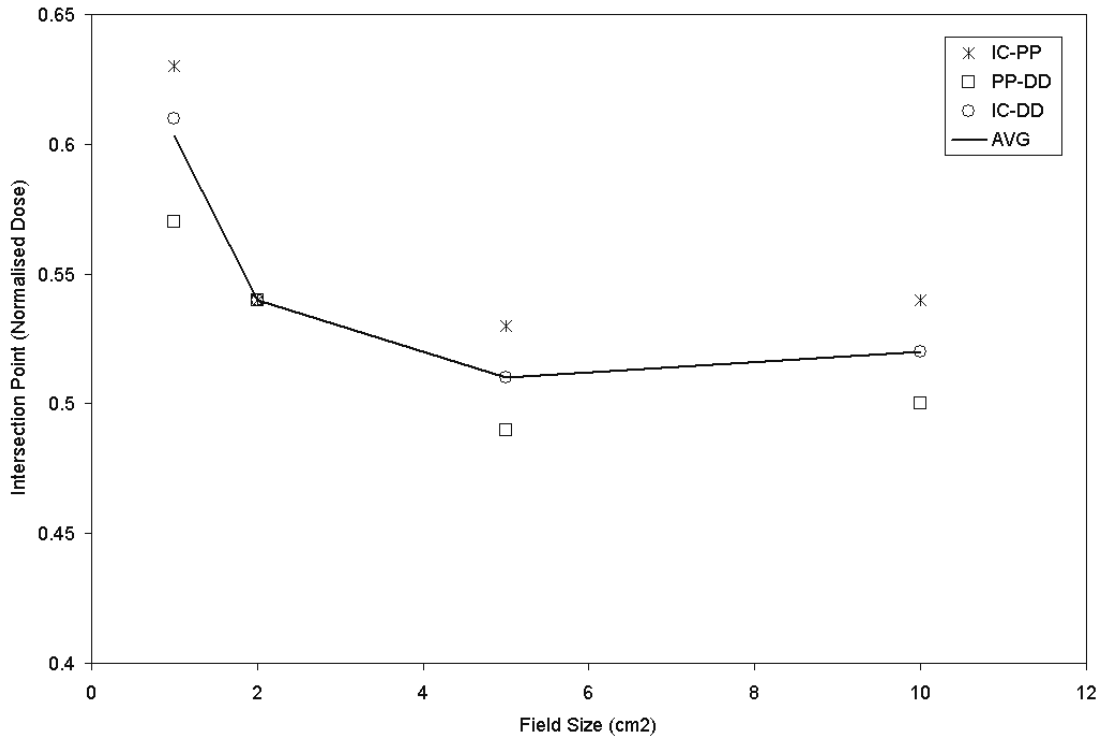


Figure 4.11: Figure showing the dependence of intersection point on field size

The data is derived from a depth of 10 cm at various field sizes.

It is interesting to note that the average dose at inflection point (see Table 4.2) deviates from the expected inflection point for 50% predominantly at field sizes relating to *small fields*, where there is a lack of lateral electron equilibria. An important implication of this refers to the measured field size. If the inflection point is at 50%, which it is for large field sizes (to within 0.02), the effect of measured field size is small. However, for a significant variation from 0.05 (e.g. +0.10 for $1 \times 1 \text{ cm}^2$), there can be considerable effects in the spatial position of dose points (such as the 50% dose point) or dose differences which are discussed further in Chapter 7.

Table 4.3: Tabulated data showing the average dose at the intersection point and the deviation from expected inflection point

The data is derived from a depth of 10 cm at various field sizes.

Data	Average dose at the intersection point	Deviation from expected intersection point of 0.50
Field size: 1×1 cm ²	0.60	+0.10
Field size: 2×2 cm ²	0.54	+0.04
Field size: 5×5 cm ² to 10×10 cm ²	0.52	+0.02r

In terms of the effect on dosimetry, the intersection point indicates which regions of the profiles undergo overestimation and underestimation. For clarity, intersection point(x) will denote the position at which the intersection point (dose) is achieved. In terms of the analysis of the intersection and inflection points, it was noted that neither the intersection and inflection points were at the 50% dose points. It was also quite likely that the overestimated and underestimated dose were not equal. In other words, if the overestimated and underestimated doses are not equal, then the detector effect will influence the integral dose as well.

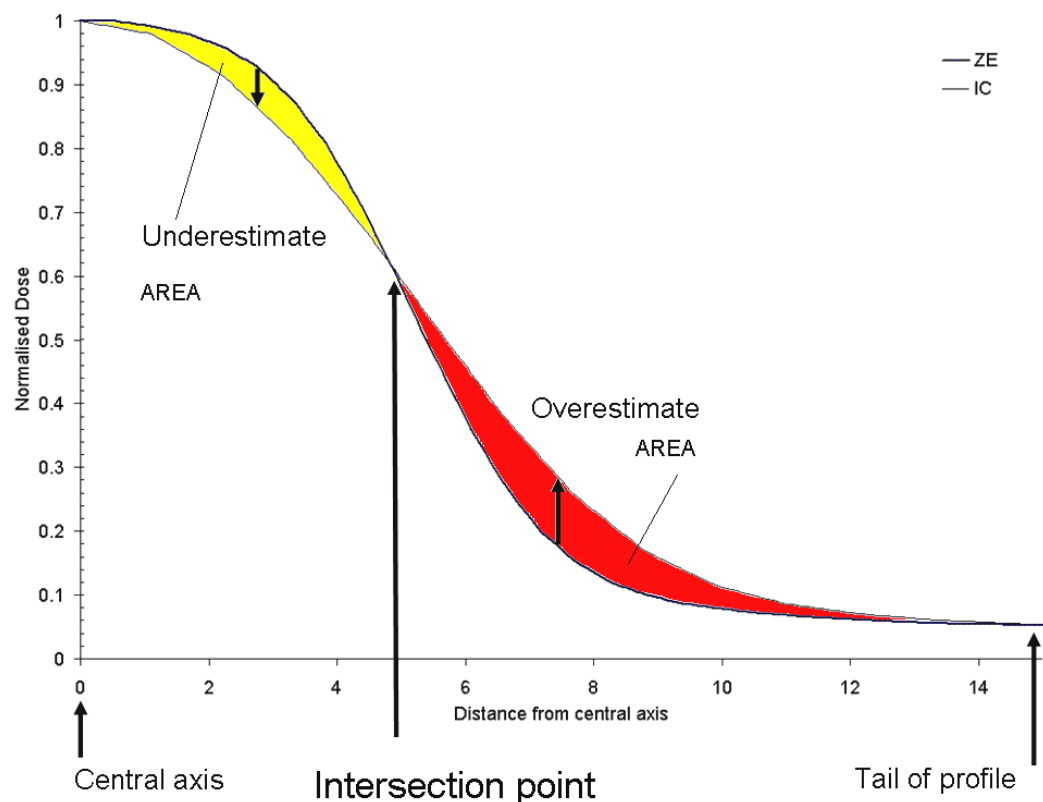


Figure 4.12: Plot highlighting the underestimate area and the overestimate area in a profile with relation to the intersection point.

Figure 4.12 indicates that the importance in the intersection point. The intersection point delineates the regions of underestimate and overestimate. Figure 4.6 illustrates this with the profiles from the IC and the ZE. A similar pattern is followed out for detectors of smaller detector diameters (e.g. the PP) but with smaller levels of overestimate and underestimate.

Table 4.4: Tabulated data showing the effect of detector volume on dose with respect to the regions in the profile.

Region	Effect of detector volume on dose
Central Axis(x) (or inter-umbra for large fields)	Negligible change in dose
Central Axis(x) to +Inflection Point(x) Or -Inflection Point(x) to Central Axis(x)	Underestimates dose
+Inflection Point(x) Or -Inflection Point(x)	Negligible change in dose
+Inflection Point(x) to +Tail(x) Or -Tail(x) to -Inflection Point(x)	Overestimates dose
+Tail(x) Or -Tail(x)	Negligible change in dose

Table 4.4 indicates that the underestimation occurs in the central area whereas the overestimation occurs in the peripheral areas of the beam. If the beam model is calculated using a large detector diameter the data indicates that the clinical dose to the PTV will have an underdose in the central region where the dose is 100% to ~60%, with a slight overdose at ~60% to 50%. Outside the PTV there would be a small overestimation of dose calculated.

4.4 DISCUSSION OF INTERSECTION AND INFLECTION POINTS

The investigations into the inflection position of measured profiles yielded interesting properties with respect to field size, namely that:

- i. The spatial position of the inflection point was found to be within 0.1 mm for all data sets over field sizes ranging from $1 \times 1 \text{ cm}^2$ to $10 \times 10 \text{ cm}^2$. This suggests that the spatial position of the inflection point is independent of detectors.
- ii. The spatial position of the inflection point was 7% less than the geometric field size at a field size of $1 \times 1 \text{ cm}^2$.
- iii. The spatial position of the inflection point approached the geometric field size with increasing field sizes, with the spatial position of the inflection point within 1% of the geometric field size with a field size of $10 \times 10 \text{ cm}^2$.
- iv. The dose at the inflection point for all data sets was 6% higher (with a variance of 1% between data sets) than the 50% dose point at a field size of $1 \times 1 \text{ cm}^2$.
- v. The dose at the inflection point (at a field size of $10 \times 10 \text{ cm}^2$) approached 53% (with a variance of 1% between data sets) with increasing field sizes.
- vi. The dose at the inflection point for all data sets agreed to within 1% except at the junction between small field sizes and field sizes with lateral electron equilibria ($2 \times 2 \text{ cm}^2$), where the IC measured 52% while the PP and the DD measured 56%. This could be an outlier or another phenomena.

In terms of the intersection point analysis, the following was observed:

- i. The average dose at the intersection point was found to be 10% higher than the 50% dose point at a field size of $1 \times 1 \text{ cm}^2$.
- ii. The average dose at the intersection point (at a field size of $10 \times 10 \text{ cm}^2$) approached 52% with increasing field sizes.
- iii. The larger the penumbra measured, the larger the region of overestimation and underestimation by a real detector on a measured profile. This is because the entire region of the penumbra contains, apart from the inflection points, regions of overestimation and underestimation.
- iv. The smaller the penumbra measured, the more will be the maximum dose difference (due to higher dose gradients) and conversely the larger the penumbra, the smaller the maximum dose difference between profiles measured with different detector volumes.

- v. If the intersection point and the inflection point were situated at half the maximum dose, the integral of the overestimated dose and the integral of the underestimated dose would be expected to be the same. Neither the intersection point nor the inflection point were at 50% dose for any field size studied and thus the integral dose was confirmed to be affected by the detector used in profile measurements (further verified in Chapter 7).

4.5 CONCLUSIONS OF INTERSECTION AND INFLECTION POINTS

In taking account of both the intersection and inflection analysis:

- i. With large field sizes ($\sim 10 \times 10 \text{ cm}^2$), both the intersection and the inflection analysis lead to a normalised dose value of 52%. At large field sizes, the intersection and inflection are relatively points coincide with the light field and coincide with each other.
- ii. Figure 4.8 shows that the inflection point always being below the geometric field size. This means that the inflection point will always have a normalised dose value above 50%. It can further be induced that since the intersection point is also always above 50%, that the intersection point is also located below the geometric field 50% dose point as well.
- iii. At small field sizes (1×1 to $2 \times 2 \text{ cm}^2$), the deviation of the spatial position from the geometric field size (see figure 4.8) and the deviation of the dose at the inflection and the intersection point is largest (60% dose at intersection point and 56% dose at inflection point for a $1 \times 1 \text{ cm}^2$ field). This indicates that the effect of intersection point and inflection point deviation is more significant at *small* field sizes.
- iv. The dependence of the inflection and intersection point, in both spatial positions and dose components, on the square field size suggest that the inflection point and the intersection point is related to lateral electron scattering.
- v. The independence of the spatial point of the inflection point amongst detectors was unexpected and the consequences or implications of this are not modelled at this stage. However, due to the detector volume effect, the dose values at the inflection points are different but are still within 1% for most cases (see figure 4.9). The weakness of the inflection point is that although the inflection points may be the same spatially, the amount of inflection (specified in the first

derivative) may not be the same and will cause differences in dose values. This is discussed more in Chapter 7.

Further investigations could include the following:

- i. Modelling of profiles using analytic solutions such as the double exponential forming function, the cosine forming function, and the square root forming function could be checked for inflection points. In addition, the superposition/convolution model (or other models) used in RTPS produces profiles that can also be checked for its inflection point.
- ii. The inflection and intersection analysis could be done for different photon energies.
- iii. The inflection and intersection analysis could be done over a larger range of field sizes of up to $40 \times 40 \text{ cm}^2$.
- iv. A more in depth model to explain the correlation of inflection point with physical phenomena.

The primary aim of this thesis was to explore detector volume correction methods. Further study into the cause of the shift in position of the inflection and intersection positions is recommended as a separate project for another investigator.

Chapter 5: Deriving virtual zero detector volume profiles based on extrapolation of data from multiple detector diameters

5.1 THEORY

The extrapolation to a zero profile measures the true width of the penumbra that is associated with the combined effects of primary photon-fluence distribution and the lateral spread of the secondary electrons (Dawson, Harper et al. 1984). This is due to the use of data which exhibits the volume effect and the perturbation of electron transport (discussed in Chapter 2).

The method of extrapolation is not linear over all types of detectors. Experimentally, extrapolation of penumbra with detector size was found to have an invalid linearity (see figure 5.15) in the region of low detector size region (Pappas, Maris et al. 2006), which agreed with results from computer simulations (Chang, Yin et al. 1996).

A linear relationship is observed for detector diameter values between 1.5 mm and 5.5 mm. The sublinearity of the diamond detector that is introduced as it is smaller than 1.5 mm is another caveat, which other authors also identified (Laub 2002).

The method of extrapolation to zero detector size involves the determination of the slope of penumbra to detector size to be independent of machine type and energy (Dawson, Harper et al. 1984).

Linear extrapolation is not limited to penumbra, but is performed discrete points (Laub and Wong 2003) from 10% to 90% in 10% increments between points. In this work, every data point measured was (typically every 1.0 mm or 0.5 mm in penumbral regions) involved a correction based on the extrapolation method.

5.2 METHOD

Each set of dose profile data from each detector was stored in arrays, with each dose value forced to the same spatial position using interpolation. This was done to standardise all sets of data because not all data sets involved the same resolution across the profile. Each spatial position involved three dose values corresponding to each detector and this was treated as an individual extrapolation procedure.

For each extrapolation procedure, the Y values, corresponding to dose, were correlated to the x values, corresponding to the detector diameter in mm. The detector volumes are known values, where the 0.125 cc ionization chamber had a value of 5.5 mm, the pinpoint detector having a value of 2.0 mm, and the diamond detector having a value of 0.3 mm (see table 4.1).

Linear extrapolation resulted in a curve with the form $y = mx + b$, where Y corresponds to the value of dose and x corresponds to the value of the detector volume. m is the coefficient of dose change with detector volume, and b is the dose when the detector volume is zero. When x, the detector volume, is zero, then Y is equal to b. Extrapolation is the method that solves for b, which becomes the dose value of the extrapolated data set. This method of extrapolation of detector diameters to a ZE (Zero extrapolation) diameter follows that described in (Laub and Wong 2003).

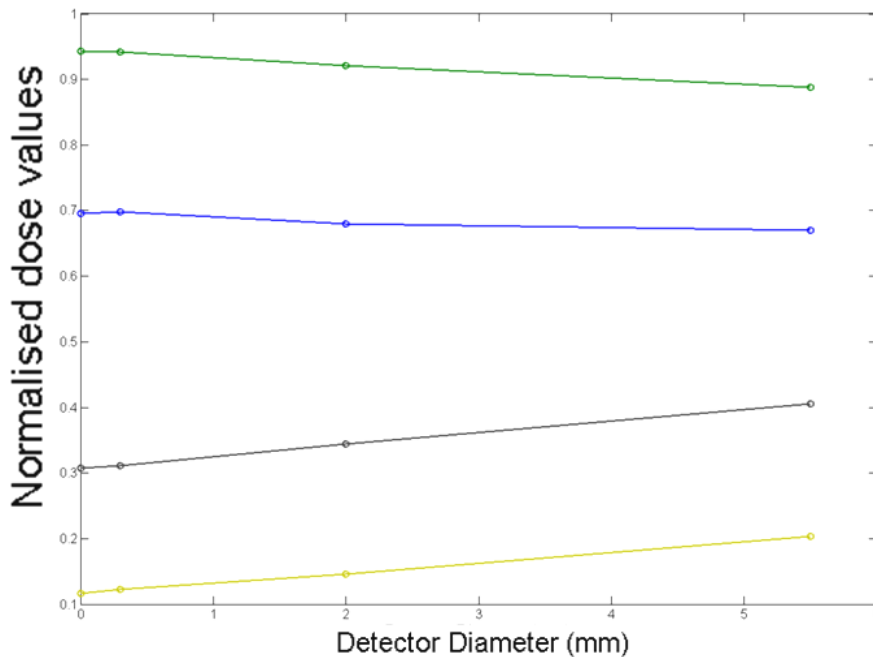


Figure 5.1: Illustrating the extrapolation procedure for MLC Crossplane 1×1 cm² square field at 10 cm depth.

Figure 5.1 illustrates the linear extrapolation performed. On the x-axis is the detector volume; while on the y-axis is the dose values for one point in the profile measured. Each line represents a single linear extrapolation of a single point (see Fig 5.1). The b value is extracted as the new point for the zero extrapolation (ZE) profile. This linear extrapolation is performed for all points in every profile over different field sizes, depths, collimator types (Jaws and MLCs), and measurement directions (Crossplane and Inplane).

In addition, there was a fitting coefficient R^2 which correlates the fit of the curve to the data. For good fits, where the data measured lies close to the extrapolated curve, R^2 approaches unity. This value was saved for each extrapolation procedure (with every point and with every profile).

5.3 RESULTS

Figure 5.2 shows a typical example that can be used to illustrate the difference between the ionization chamber (IC), pinpoint (PP), diamond (DD), and the zero extrapolated (ZE) profile. The IC is always the broadest profile, followed by the PP, the DD, and then the ZE. This order is usually maintained, with the exception being the DD and the ZE. As the detector diameter of DD is so small, there are cases where the ZE exhibits a broader profile than the DD. However, the differences between the broadness of the ZE and the DD profiles are miniscule –visually the ZE and the DD are difficult to distinguish on a graph.

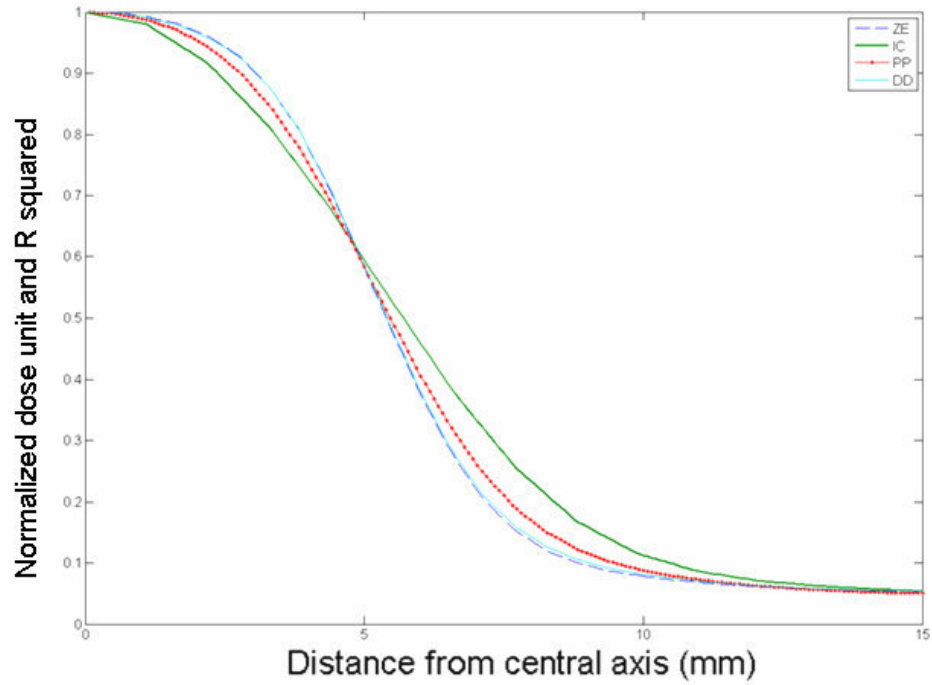


Figure 5.2: Plot of the results of the extrapolation profile MLC Crossplane 1×1 cm² square field at 10 cm depth.

A selection of ZE profiles (figures 5.3-5.6) with various field sizes are presented to illustrate the difference with the ionization chamber (IC) profile, which is typically used in dosimeter measurements. The PP and the DD profiles fit in between the IC and the ZE profiles. In addition, the R^2 value is also plotted to indicate the goodness of the linear fit.

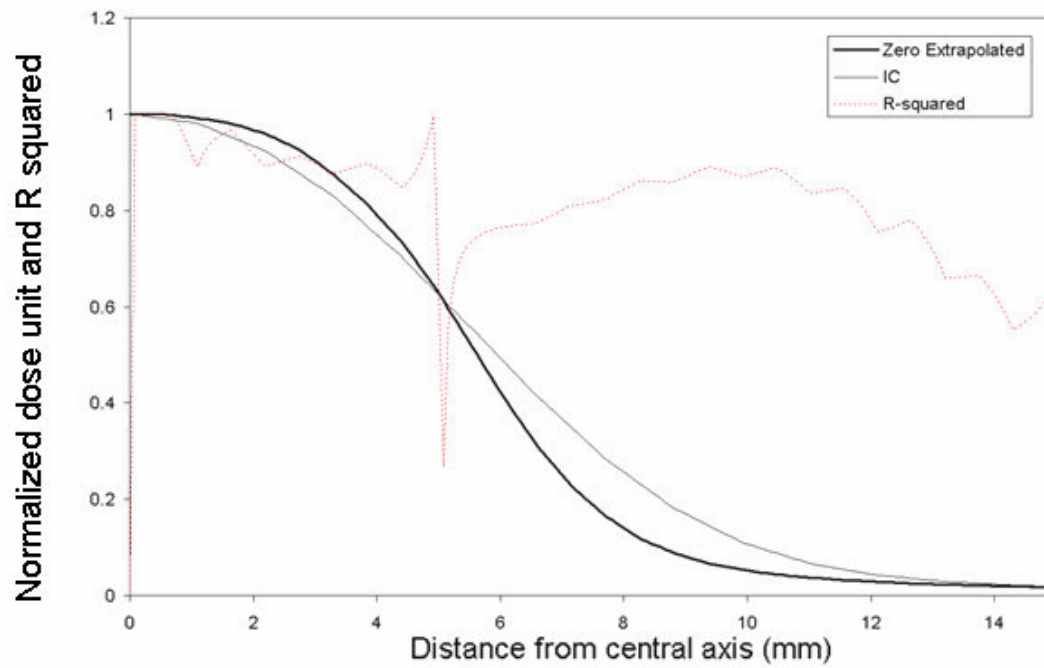


Figure 5.3: Extrapolation Profile with R^2 (dotted), compared with data from profiles at a depth of 10 cm and field size $1 \times 1 \text{ cm}^2$ (Jaw Crossplane data).

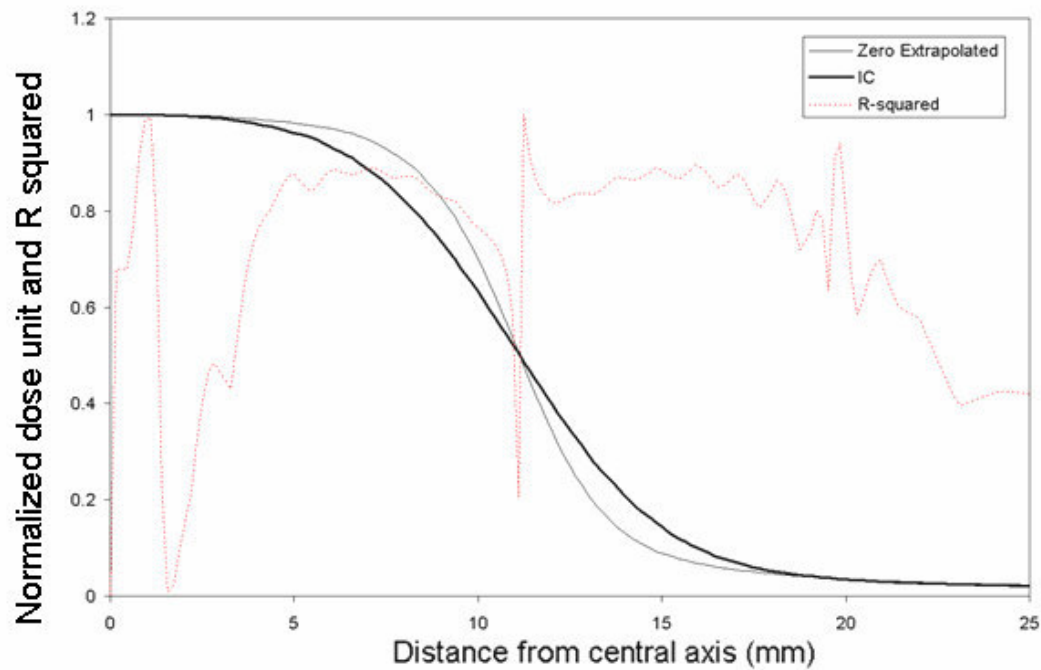


Figure 5.4: Extrapolation Profile with R^2 (dotted), compared with data from profiles at a depth of 10 cm and field size $2 \times 2 \text{ cm}^2$ (Jaw Crossplane data).

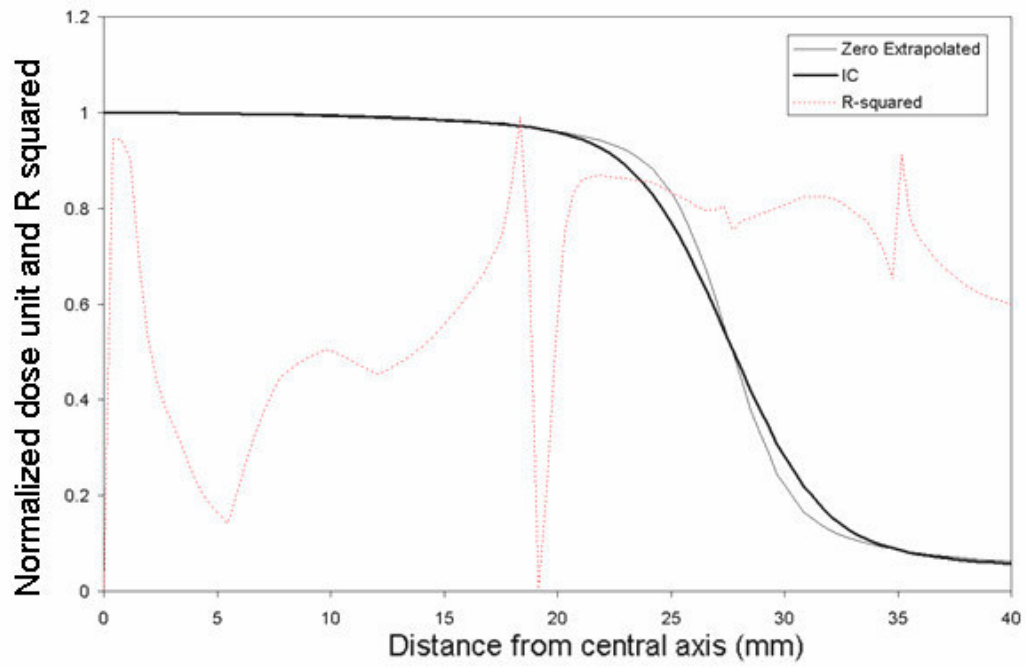


Figure 5.5: Extrapolation Profile with R^2 (dotted), compared with data from profiles at a depth of 10 cm and field size $5 \times 5 \text{ cm}^2$ (Jaw Crossplane data).

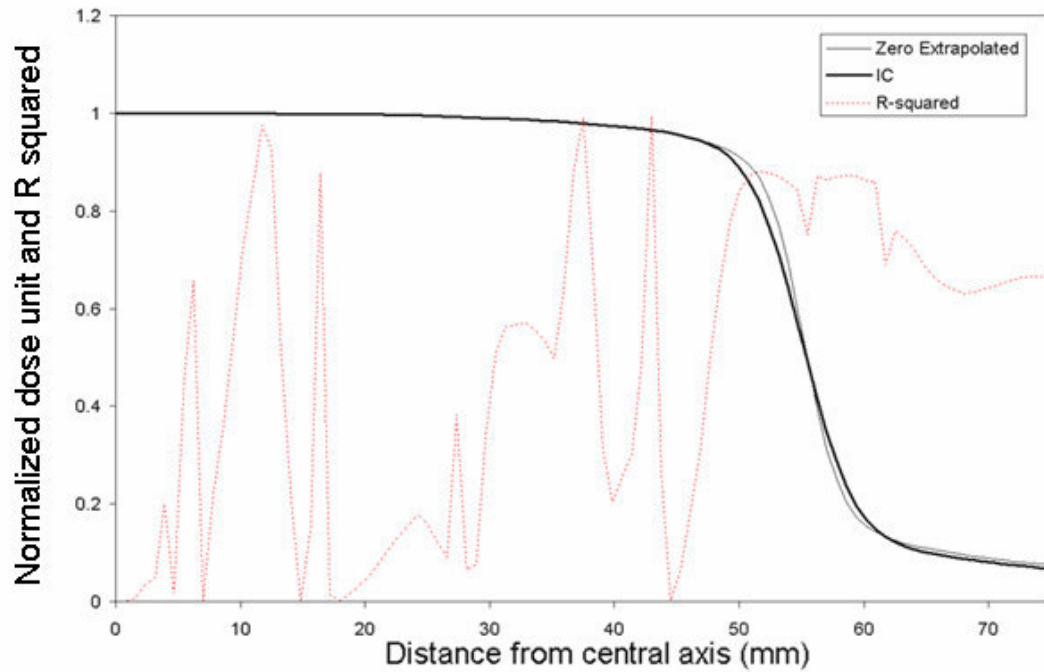


Figure 5.6: Extrapolation Profile with R^2 (dotted), compared with data from profiles at a depth of 10 cm and field size $10 \times 10 \text{ cm}^2$ (Jaw Crossplane data).

5.4 VALIDATION OF METHOD

The plot of the R^2 value showed an erratic variation of values across the profiles (see fig. 5.3-5.6). The plot of R^2 values, however, can be compared with the variation in dose difference between the IC and the ZE profiles (see fig. 5.7).

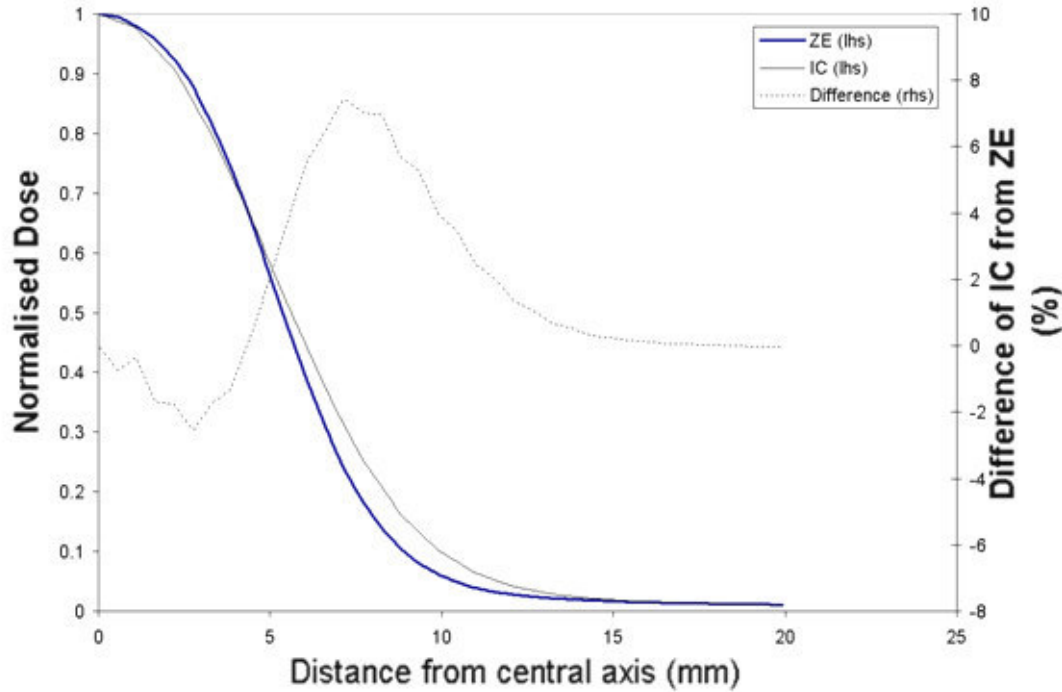


Figure 5.7: Dose difference of Extrapolation Profile with IC (dotted), compared with data at a depth of 10 cm and field size $1 \times 1 \text{ cm}^2$ (Jaw Crossplane data).

The analysis resulted in the following conclusions:

- When the dose difference is 0, the R^2 doesn't matter as the dose value of the ZE will not differ from the dose value of the measured data.
- When the dose difference is higher, then the R^2 becomes more significant.

A valid extrapolation procedure is characterized by having most high dose difference points corresponding to high R^2 values with inconsequential dose difference points corresponding to any R^2 points.

The R^2 values have been plotted as the x-axis versus the dose difference from the ZE as the Y axis for each detector in individual graphs. Good fits involve a correlation of high dose difference with high values of R^2 . Examples of good fits are the Crossplane Jaw and MLC profiles (figs. 5.8 and 5.10 respectively). Bad fits involve inaccurate extrapolation exhibited with low values of R^2 at high levels of dose differences.

Examples of bad fits are the Inplane Jaw and MLC profiles (figs. 5.9 and 5.11 respectively), where high levels of dose differences involve R^2 values typically lower than 0.9.

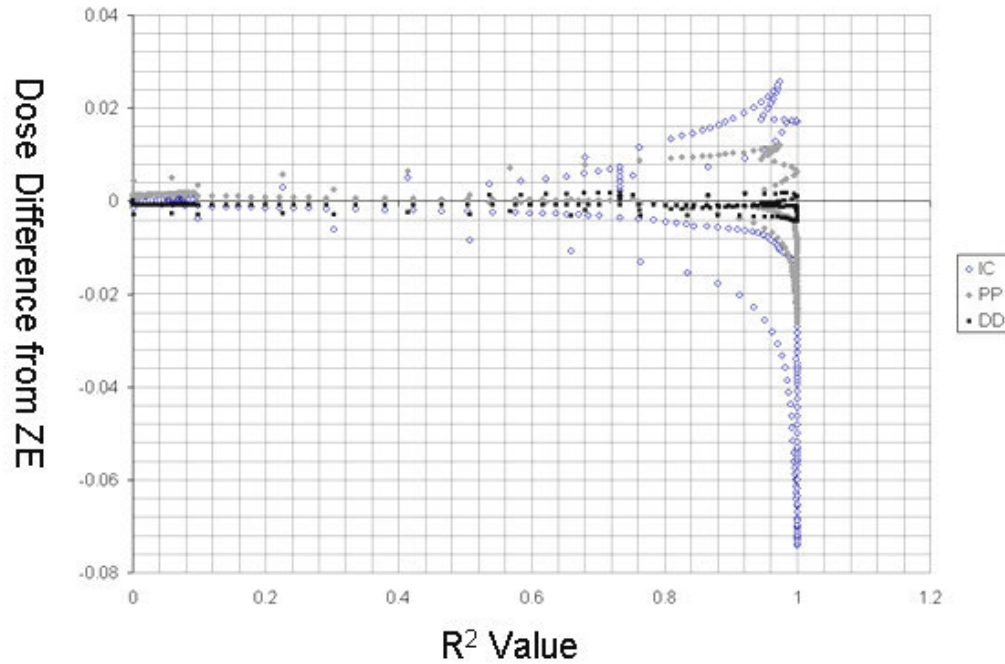


Figure 5.8: Plot of R^2 versus dose difference for Crossplane Jaws, $1 \times 1 \text{ cm}^2$ at 10 cm depth.

It is also noteworthy that larger dose differences are associated with the detector with the larger detector diameter. In figures 5.8-5.11, the IC (large open circle) shows the largest range of dose differences, followed by the PP (grey open circles), and then the DD (dark closed circles).

It can also be observed that in figures 5.8 and figures 5.10 (which correlate with valid extrapolation procedures), the maximum underestimate is higher than the maximum overestimate. This dosimetric effect is dependent on field size and with the spatial position of the dose point and is further discussed in Chapter 7.

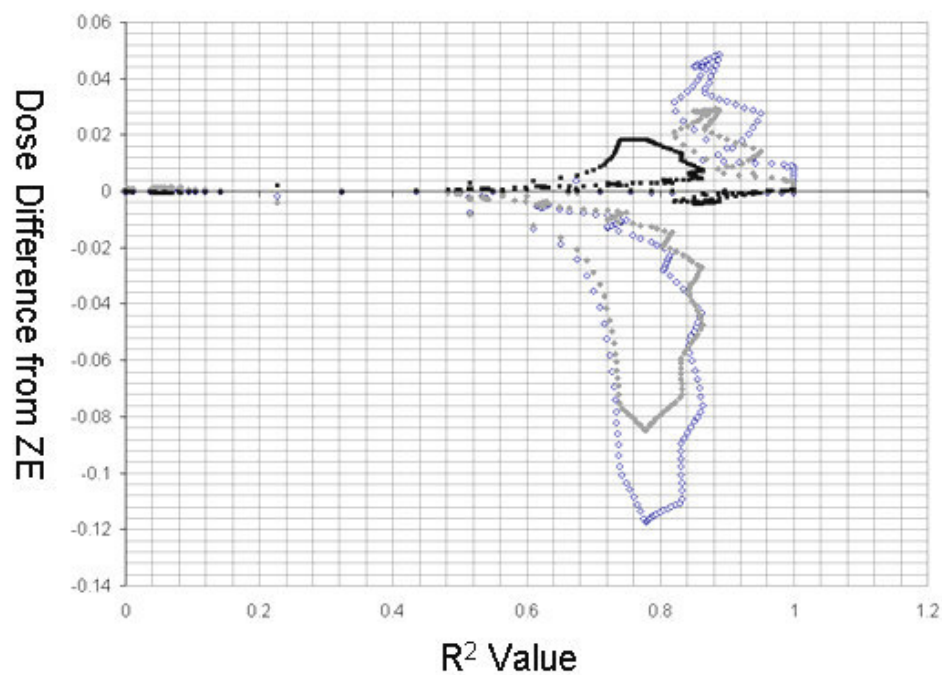


Figure 5.9: Plot of R^2 versus dose difference for Inplane Jaws, $1 \times 1 \text{ cm}^2$ at 10 cm depth.

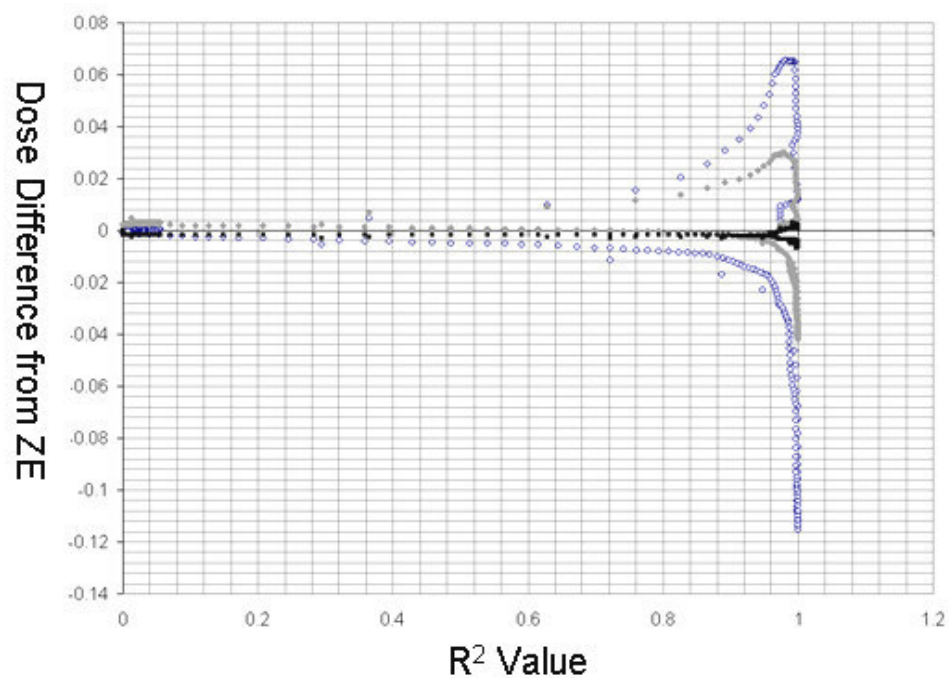


Figure 5.10: Plot of R^2 versus dose difference for Crossplane MLC, $1 \times 1 \text{ cm}^2$ at 10 cm depth.

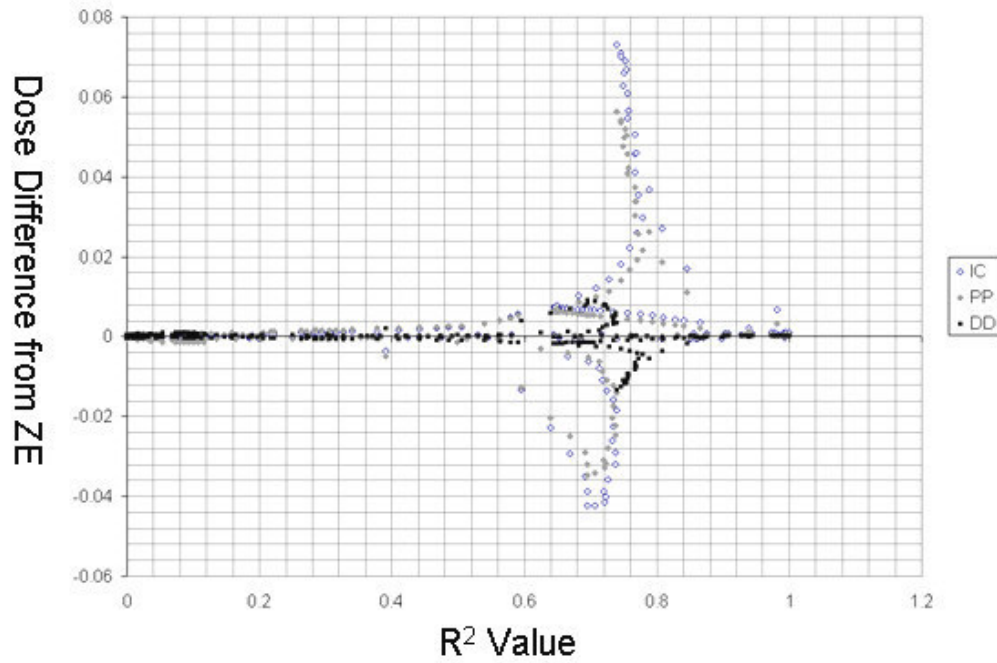


Figure 5.11: Plot of R^2 versus dose difference for Inplane MLC, $1 \times 1 \text{ cm}^2$ at 10 cm depth.

The reason the Inplane Jaw and MLC profiles were associated with high dose differences at low R^2 values is that the use of the same sensitive detector diameters cannot be used for both planes because the detectors used did not have the same sensitive detector diameter in both the transverse and the longitudinal direction.

The analysis of data is restricted to the Crossplane data in this study due to the invalidity of Inplane ZE profiles with the diameters of IC 5.5 mm, PP 2.0 mm, and DD 0.3 mm used in the Crossplane direction.

A cost function can be formulated to combine the dose difference and the R^2 value, such that a high cost function represents the error in the linear extrapolation algorithm:

- i. When R^2 is high, this should correspond to a lower cost function. Conversely, when R^2 is low, this should correspond to a higher cost function. A function of the form $(1-R^2)$ satisfies this requirement.
- ii. When the error is high, this corresponds to a higher cost function. Conversely, when the error is low this should correspond to a lower cost function.

A cost function satisfying the criteria proposed is:

$$\text{Cost Function} = \text{Error} \times (1 - R^2) \quad (5.1)$$

The cost function across the profile reveals a varying magnitude of good and low cost function regions in the profile (see fig. 5.12). The region in the profile corresponding to 50% dose, which defines the field size, exhibits approximately 50% of the cost function. The region in the profile corresponding to 80% dose has a minimal dose function while the region in the profile corresponding to 20% dose is associated with maximal cost function.

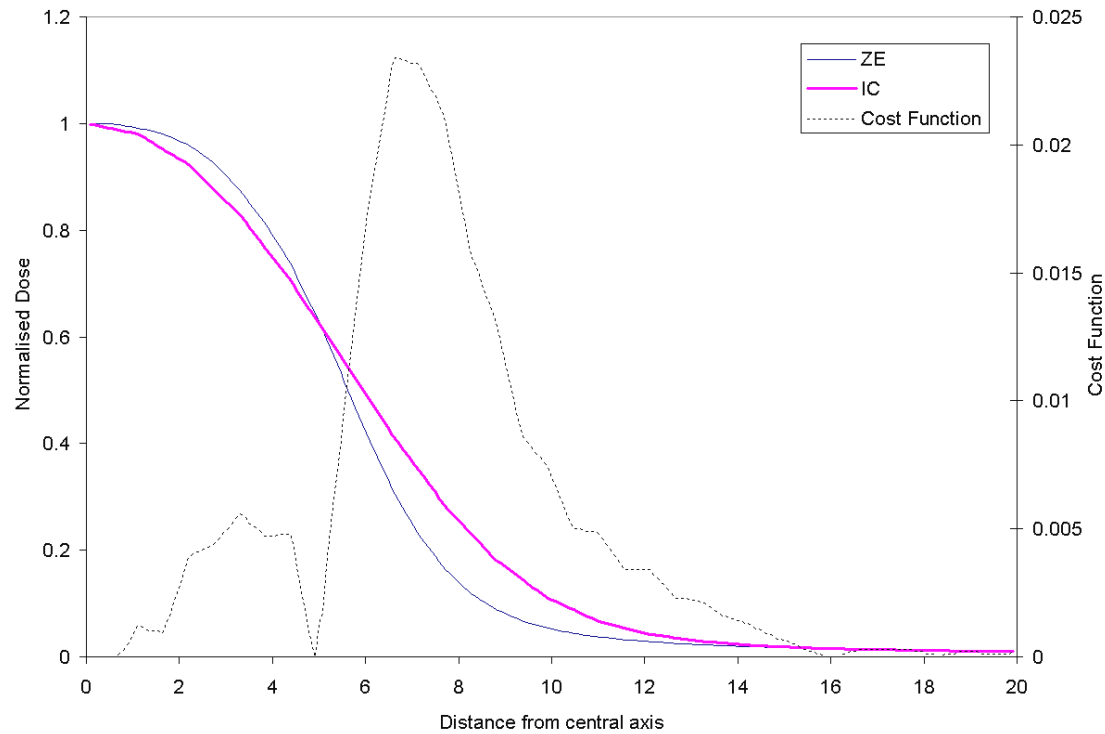


Figure 5.12: Showing the plot of the cost functions (rhs) with the ZE and IC profiles (lhs) for 1×1 cm² field defined by jaw at a depth of 10 cm. The cost function is calculated with EQ. 5.1.

Analysis of the ZE profile with various field sizes suggests that the cost function is most significant in the penumbra region, with a minimal cost function in the inter-umbra region (see fig. 5.12). In regions of low dose gradients, the effect of detector on measured values is minimal and leads to minimal differences in dose. Hence, the linear extrapolation to correct for detector effects in the inter-umbra region is valid, but at the same time, unnecessary as the dose values for measured values from different detectors are nearly identical.

The cost functions for the PP and the DD were also calculated and the regions of highs and lows matched with the cost function for the IC but the absolute values were lower due to lower differences between the PP and the DD and the ZE profile.

The cost function produces relative values for analysis. The analysis of the cost function profile reveals areas where the extrapolation is weakest. Figure 5.12 shows that the region around the 20% region shows the maximal cost function with significant values of cost function around the field edge and the profile tail as well.

In addition, if it can be assumed that there is a linear relationship between R^2 and the dose difference (such that when $R^2=1$ the error is minimum and when $R^2=0$ the error is maximum), then the following analysis can be applied: Figure 5.12 indicates absolute values of cost function a maximum of 0.023. The max cost function 0.023 would then correspond with a difference of 2.3% for a R^2 value of 0.0. The good continuity and lack of aberrations of the ZE profile between regions of low cost function suggest that extrapolation procedure exhibits good consistency.

A more comprehensive analysis was performed that was able to analyse the validity of the extrapolation method over profiles of different depths or square fields (see fig. 5.13). All cost function points corresponding to points where the dose was more than 10% were averaged for each profile. The analysis of points more than 10% was done to avoid analysis of the penumbral tails which were not of primary concern in this study. The averaged cost function would be a function of the validity of the extrapolation technique.

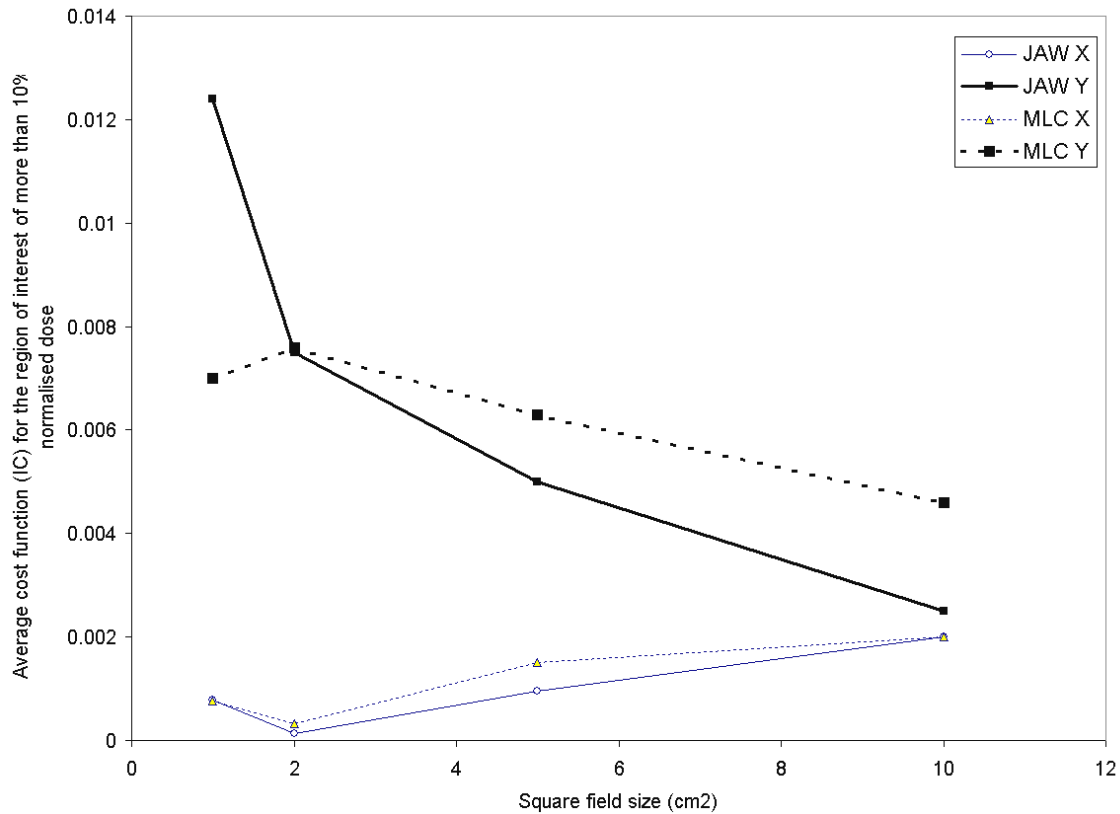


Figure 5.13: Averaged cost function for the IC for dose points more than 10% at a depth of 10 cm.

The difference between the Inplane (Y) and the Crossplane (X) profiles is again illustrated clearly. Furthermore, the trend of increasing average cost function with square field size suggests that the detector diameter and dose relationship is more linear for small field sizes than for larger field sizes.

The data shows the sensitive diameters used for the extrapolation of the Inplane profiles as invalid. The sensitive diameter across the length of the detectors, and not the diameter, is the value that correlates with the Inplane profiles. However, the sensitive length of the diamond detector was not available in the literature and so an estimate of this value was made with the physical length using the schematic diagram supplied by the manufacturer (see Fig. 1.2).

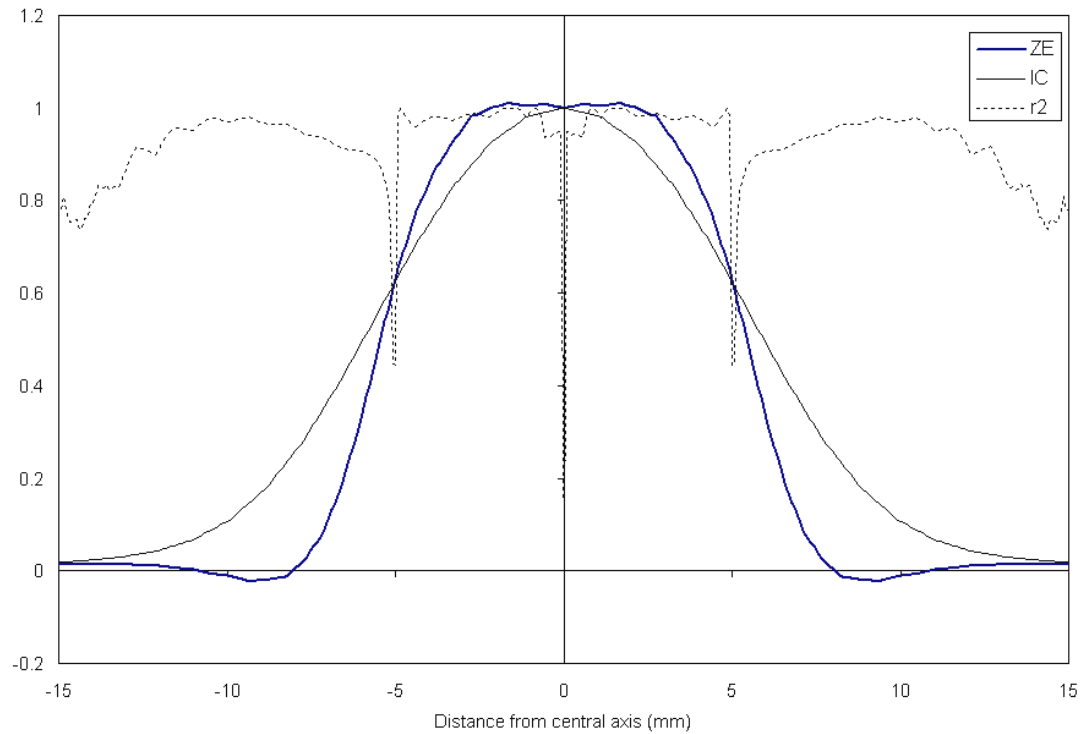


Figure 5.14: ZE profile in the Inplane direction for a 1×1 cm² field at a depth of 10 cm

The result of the extrapolation technique using the IC length of 6.5 mm, PP length of 5.0 mm, and DD length of 3.3 mm is shown in Fig. 5.14. Parts of the zero extrapolated profile resulted in negative dose values, which is not the case in reality. The data indicates that the physical length estimated from the DD is not valid as the sensitive length required by the extrapolation technique.

5.5 DISCUSSION

To the authors knowledge, no previous literature has investigated the validity of the extrapolation technique quantitatively with the analysis of R^2 , dose differences, cost function, with field size, and with the value used for detector diameter. The results from investigations into verification of the validity of the extrapolation technique involved:

- i. The analysis of R^2 with dose difference to verify the extrapolation technique: The R squared value used in extrapolation was analysed throughout the profile. For extrapolated profiles, each point involved an extrapolation. The analysis of R^2 found the importance of R^2 to be dependent on the dose difference between the measured and the extrapolated dose point. With a valid extrapolation technique with negligible dose differences, the R^2 values decreased –however in such circumstances the extrapolation procedure does not introduce errors since the measurement of dose at such a point involves negligible dose difference among detectors of different measurement volumes.
- ii. A plot of R^2 and the dose difference was used as a technique to verify the extrapolation method: for a valid extrapolation technique, large dose differences corresponded to large R squared values (approx. 1.0). Invalid extrapolation techniques, such as using the parallel detector diameter for the perpendicular detector diameter, resulted in large dose differences corresponding to R squared values that were significantly deviating from 1.0 (0.8 in the Crossplane in this study).
- iii. The use of R^2 and dose difference to create the cost function: The cost function was formulated to account for this. The dose difference is multiplied by one minus the R squared value (see equation 5.1). The cost function is low when the dose differences are negligible and when the R squared values approaches 1.0 (which corresponds to a perfect extrapolation). The cost function was found to be maximum around the region of 20% dose, indicating that the 80-20 penumbra may have a significant amount of uncertainty. The cost function was also analysed in terms of field size and was found to increase with increasing field size (for a valid extrapolation technique).
- iv. The analysis of the cost function across the profile and with field size: The cost function provided a qualitative analysis as to the validity of the extrapolation technique over the various regions of the dose profile. Over a limited sample of data ($1 \times 1 \text{ cm}^2$ fields), it was found that the extrapolation technique was weakest in the region of 20% dose, with other regions of significant cost function being in the region of 50% dose (field edge) and in the dose tail. The cost function was minimal in the

central axis and the 80% dose regions.

It should be noted that large values of cost function is both a function of dose difference and R^2 . Therefore, areas of large cost function may not be because of errors in the extrapolation technique in the region. The reason for the large size of the cost function could be due to large dose differences.

The cost function showed a dependence with field size in figure 5.13. The average cost function increased with field size for the valid extrapolation technique (crossplane). This suggests that the extrapolation technique is better suited to small areas but is nevertheless useable with larger field sizes. For invalid extrapolation techniques (in the Inplane where incorrect detector diameter values were used), larger field sizes reduced the cost function suggesting that the importance of the detector diameter used decreases with increasing field size.

It was also observed in figure 5.13 that the cost function is significantly higher in the 20% dose region than in the 10% dose region. The P10-90 penumbra is therefore more independent of the detector effect than the P20-P80 penumbra and could be a more reliable benchmark of the lateral scatter. In the literature, it was found that the P10-90 penumbra was independent of machine type and energy while the P20-80 penumbra was also found to be similar independent but with a slight dependence between Co-60 and 6 MV beams (Dawson, Harper et al. 1984).

- v. Verification of the extrapolation technique by examining polarity and inflection: The curve type after extrapolation can be checked visually for abnormal aberrations. Two physically unfeasible features that were noted in an invalid extrapolation technique (see figure 5.14) when the physical diameter (and not the sensitive diameter, because the sensitive diameter was not available in the datasheet) was used in the extrapolation technique as a trial involved negative dose values and values of dose below the dose tail.

The accuracy of the extrapolation technique is dependent on the variation of properties of each detector used.

- i. Measurement with photon detectors and dose detectors: The sensitive diameter used in the extrapolation is a major factor in the extrapolation technique. The detectors used in this study were a combination of photon detectors (DD) and dose detectors (PP and IC). The difference between photon detectors which measure photon-fluence and dose detectors (also *electron detectors*) which measure dose-distributions are related to the

beam energy and lateral electron spread of secondary electrons (Dawson, Harper et al. 1984).

- ii. The value of the detector diameter used in the extrapolation technique: Due to dose detectors having an increased range because of the secondary electrons, dose detectors have a larger effective diameter. The term *effective diameter* is dependent on energy and increases with increasing beam energy. For the 0.125 cc IC, the effective diameter calculated (Dawson, Harper et al. 1984) was 5.5 mm for Co-60, 7.5 mm for 6 MV x rays, and 12.5 mm for 31 MV x rays. The importance of electron fluence is increased for higher photon energies.

For consistency, the PTW supplied values of sensitive diameter were used. There is an absence of effective diameter modelling for the pinpoint detector. At the time of writing, the method the manufacturer used to determine sensitive diameter is unknown. In addition, the dependence of the sensitive diameter on energy is also not specified and may require more detailed study.

Lastly, the sensitive diameter of the diamond detector perpendicular to detector was not specified. Measurement of the diamond detector perpendicular to the detector would worsen the effect of detector volume due to a larger effective detector diameter. The use of strongly asymmetric detectors such as diamond detectors may involve rotation of collimator or water tank in order to maintain the same measurement direction. Weakly asymmetric detectors such as the IC may have more practical benefits in this regard. The clarification of the effective diameter of the diamond detector perpendicular to the detector will allow a valid extrapolation routine in the future.

- iii. The sublinearity of the extrapolation technique: The extrapolation technique itself involves a dependence on the linearity of the detector diameter to the dose at each point in the profile. The sublinearity has been studied experimentally with gel integration data (Pappas, Maris et al. 2006) and theoretically with computer simulations (Chang, Yin et al. 1996). The conclusion made by researchers is that detector sizes of approximately 0.5 mm were found to be adequate for high dose regions. This was consistent with the results in this study as the ZE profile and the DD profile typically were in agreement to within 0.2 mm for the 80-20 penumbra (see the next section).

The use of detector data outside the recommended linearity range of 1.5 mm to 5.5 mm by including the diamond detector data introduced a limit in the accuracy in the extrapolation method. However, this is, and will be, a significant limitation of the

extrapolation technique itself due to the constraints of the available detectors of the researcher at his/her department.

The possible errors due to sublinearity are small, compared to the known errors due to using large detectors without a volume correction. According to fig. 5.15, the deviation between the extrapolated 80-20 penumbra (which is not fully accurate due to the sub-linearity of the extrapolation technique) and the measurement of the true 80-20 penumbra with detector volumes approximating zero volume detectors is 0.2 mm. In other words, extrapolation of detectors within the linearity range of 1.5 mm to 5.5 mm underestimates the true penumbra by 0.2 mm. However, the measurement of 80-20 penumbra by a typical ionisation chamber (0.125 cc IC with 5.5 mm effective diameter) overestimates the true penumbra by an order of 1 mm to 2 mm.

Please see print copy for image

Figure 5.15: Profile illustrating the effect of extrapolating penumbra with detector diameter with the inclusion of a dose point measured with a detector diameter less than 1.5 mm (the dotted line was added to highlight the effect of the inclusion) adapted from (Pappas, Maris et al. 2006)

In addition, the use of data from detectors smaller than 1.5 mm in the extrapolation technique effectively averages the penumbra between the true penumbra (see fig. 4.20) and the extrapolated penumbra that has error due to sub-linearity. In other words, inclusion of detectors smaller than 1.5 mm reduces the (small) error in extrapolation due to the sub-linearity of the extrapolation method.

- iv. The dependence of the extrapolation technique on measurement direction: Future work may involve a repeat of Inplane scans with either a rotation of the water tank assembly or a rotation of the collimator such that the profile is scanned parallel to the detector motion. In other words, the scan would employ the detector using the diameter and not the long axis of the detectors.

Alternatively, further modelling can be done to effectively calculate the sensitive diameter of each detectors in question. One possible method of achieving this is to measure profiles with two detectors parallel to the detector motion and then the last detector perpendicular to the detector motion. If the extrapolation technique is valid, the sensitive detector diameter can be calculated from the measured penumbra of that detector. On the other hand, the availability of data involving the sensitive length of detectors by manufacturers would allow the extrapolation technique of the Inplane profiles without the need for detector or collimator rotation.

Lastly, the verification of the extrapolation technique has also confirmed that the sensitive detector diameters used in this study (PTW-Freiburg 2008) were valid in the axis of detector motion corresponding to both ion chamber detectors. The validity of the extrapolation technique allows the use of ZE profiles and ZE parameters as a reference value in other analysis.

- v. Note on the workload involved with the extrapolation technique: The major disadvantage of the extrapolation technique is the increased workload involved. Compared to the work required to measure profiles with one detector, each extrapolated detector volume added, adds to the workload required by a multiple of the original workload.

The minimum amount of data for work involving a verified extrapolation technique involves triple the amount of measurement time. The time required for the water tank setup is the same, however, there will be added time involved with centering of the chamber with radiation and light as well as zeroing the point relating to the water surface.

The next step involves transferring the measured profile data from the manufacturer's data format into the in-house data package (e.g. excel or MATLAB) for analysis. There needs to be a clear method by the user in terms of classifying each profile into measurement plane, field size, depth, and detector. Lastly, there needs to be a software package developed in-house that is capable of an algorithm that can perform extrapolation using a scripted algorithm as the amount of linear fits is too large for manual calculation (one linear fit is required for each point in each profile).

5.6 CONCLUSIONS

The extrapolation technique can be verified with an analysis of R^2 , dose difference, and cost function. An invalid sensitive detector diameter can be detected with these analysis techniques, in addition to a visual analysis of the profile for any abnormalities such as extra inflection points or negative dose values.

The sub-linearity of the extrapolation technique (Chang, Yin et al. 1996; Pappas, Maris et al. 2006) reduces the accuracy of the extrapolated penumbra by approx. 0.2 mm. This is in agreement with estimations of the error due to extrapolation of 0.3 mm difference in the literature based on deconvolution with an Elliptic and Gaussian kernel (van't.Veld, Lujik et al. 2001).

Use of the extrapolation technique with data less than 1.5 mm improves the accuracy of the extrapolated penumbra to between 0 and 0.2 mm (in this case approx. 0.1 mm). The acquisition of data depends on the equipment available to the user and this may be a limitation of extrapolation studies.

The sensitive diameter used in this study was the values supplied by the manufacturer of the detectors. The sensitive diameter for the diamond detector in the direction perpendicular to the detector was not available and this prevented the extrapolation technique from being used in a valid way. The effective diameter accounts for the lateral electron spread due to secondary electrons for dose detectors and is dependent on energy.

However, the lack of sufficient effective diameter data for all detectors used limited the effectiveness of the concept to practice. Future work involving the extrapolation technique would be aided by the availability of information regarding the sensitive diameter of photon detectors in both directions perpendicular and parallel to detector as well as the energy dependence of the effective diameter change with beam energy would also be helpful. One limitation of the extrapolation method is that multiple data sets need to be collected for each detector. For three detector data sets, the amount of work required is tripled.

Chapter 6: Deriving virtual zero detector volume profiles by deconvolution based on detector data

6.1 THEORY

Different detectors have varying degrees of effective detector volume, which in effect means an individual dose averaging component with measurement of the penumbra.

The effect of the finite size of any detector in the dose profile can be described with

$$D_m(x) = \int_{-\infty}^{+\infty} D(u) \cdot K(u-x) \cdot du, \quad (6.1)$$

Where $D_m(x)$ is the measured profile, $D(u)$ is the real profile, and $K(x)$ is the convolution kernel that is representative of the measuring system. The measured profile, the real profile, and the convolution profile can be illustrated graphically (see fig. 6.1).

Please see print copy for image

Figure 6.1 A diagram illustrating the concepts of the detector response function, the true profile, and the measured profile (Chang, Yin et al. 1996)

Long dashed line is a step function signal, small dashed line is a plot of the response function of the circular detector, the solid line is the measured penumbras of the step function signal when scanned with a circular detector of radius R . The solid circle is the circular detector of radius R .

The kernel models the detector response and is important because the accuracy of the kernel determination determines the error involved with deconvolution (Bednarz, Huq et al. 2002). If the calculation of the kernel is based on extrapolation of Monte Carlo data, then the accuracy is dependent on the transport parameters used (Wieslander and Knoos 2007).

Table 6.1: A selection of models of kernels used for deconvolution.

Geometric kernel approximation (Ju, Ahn et al. 2002)	$K(x) = 2h\sqrt{r^2 + x^2} + \frac{\pi(r^2 - x^2)}{2}, \text{ for } x < r$ $K(x) = 0, \text{ for } x > r$
	(6.2)
Parabolic function (Higgins, Sibata et al. 1995)	$S(x) = \frac{2}{\pi R^2} (R^2 - x^2)^{1/2}$
	(6.3)
Line spread function (LSF) (Charland, El-khatib et al. 1998)	$LSF = \frac{2}{\pi R^2} (R^2 - x^2)^{1/2} \text{ if } \ x\ < R$ $LSF = 0 \text{ otherwise}$
	(6.4)
Gaussian fit (Garcia-Vicente, Delgado et al. 1997)	$K(x) = \frac{1}{\sqrt{2\pi}\sigma} \exp\left(-0.5 * \frac{x^2}{\sigma^2}\right)$ $= \frac{1}{2.51\sigma} \exp\left(-0.5 * \frac{x^2}{\sigma^2}\right)$
	(6.5)
Combination of elliptic and Gaussian terms (van't.Veld, Lujik et al. 2001)	$S_{fit}^{IC}(x) = A_1 \sqrt{R_{eff}^2 - x^2} + A_2 \left(\sqrt{R_{out}^2 - x^2} - \sqrt{R_m^2 - x^2} \right)$ $+ A_3 \sqrt{R_{ced}^2 - x^2} + A_4 e^{-x^2/2\sigma^2}$
	(6.6)

Note that x refers to the distance away from the centre of the detector while R refers to the detector radius. Other parameters defined for each equation (6.2-6.6) are outlined in the original references.

There are a variety of models of the detector kernels (see table 6.1). One study found little differences between the step function, parabolic function, and the Gaussian function in terms of detector response (Higgins, Sibata et al. 1995), while the Gaussian fit was found to be the best fit for ion chambers and diodes based on a study by (Garcia-Vicente, Delgado et al. 1997).

In this study, the Gaussian kernel was used, where the width of the Gaussian, given by 2σ , is approximately equal to the width of the detector, and can be estimated

in that way. Based on the Gaussian approximation of the kernel model, the calculated 2σ for the diamond detector was found to be 2.1 mm (Garcia-Vicente, Delgado et al. 1997; Bednarz, Huq et al. 2002). In terms of physical representation, the inverse parabolic function conforms to the idea of a finite detector volume whereas the Gaussian function has a kernel that tails off outside the boundaries of the spatial detector volume.

In contrast to direct deconvolution, an iterative approach to kernel determination with the minimisation of variance given by

$$Variance = \sum_i^m \frac{(dose_m - dose_c)^2}{m} \quad (6.7)$$

This requires a known true profile, where variations of the variables in the kernel function are applied until the variance is minimised (Renner, Norton et al. 2005). The iterative approach was not taken in this study due to the limitations of the Gaussian fit with measured profiles (discussed in a later section).

6.2 METHOD

The deconvolution technique used in this study involved multiple steps:

- 1) Prepare Gaussian fit of measured profile
- 2) Spacing around data for deconvolution algorithm
- 3) Calculate required kernel
- 4) Apply deconvolution
- 5) Find centre of new deconvolved profile
- 6) Centre and cut-off data used as for spacing

The measured data involved problems when deconvolved in its raw form. Due to the limited sampling of the profile, the analysis of the profiles with techniques such as differentiation and deconvolution can become limited. The use of Gaussian profiles with convolution and deconvolution techniques is practical as the Fourier transform of a Gaussian is also a Gaussian.

Using the MATLAB package, a curve fit of the Gaussian with the profiles was attempted with *CFTOOL*. The use of the curve fit tool involves the Gaussian as an analytic functions, which was optimized with empirical fit parameters. These

parameters can be altered to find a compromise for a good agreement between model and data (Sharpe, Jaffray et al. 1995).

It was found that application of the deconvolution technique amplified the noise in the measured data. Results indicate that application of deconvolution of the data involved a visible “stair case” effect in the deconvolved profiles (see fig. 6.2) due to the effects of noise and limited amount of data points due to a finite distance between measured points (typically, ~1 mm). Comparison was made with the deconvolution performed after a Gaussian fit of the measured data, which gave good results.

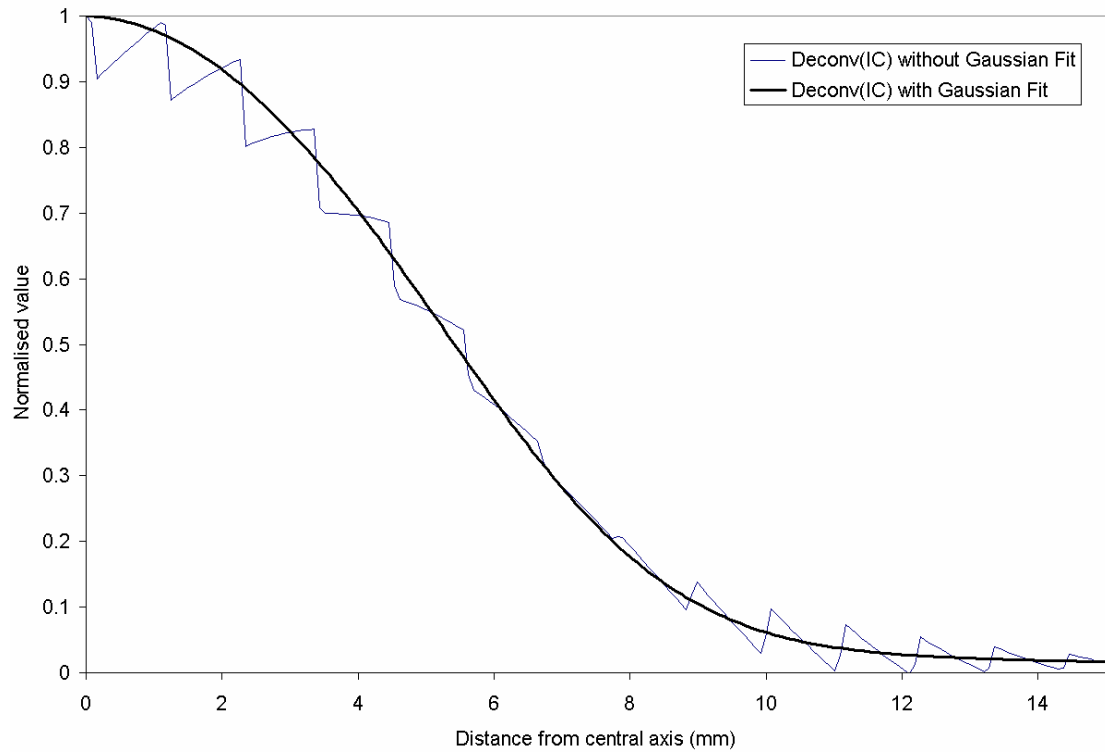


Figure 6.2: Figure showing the deconvolution of raw IC data and the deconvolution of a Gaussian fit of IC data.

The Gaussian fit algorithm used was Levenburg-Marquardt, and initially different orders of the Gaussian function was tested. The test with a $1 \times 1 \text{ cm}^2$ field showed that an increase in the order improved the fit between model and data. The worst fit was associated with a first order Gaussian fit, which resulted in an error of up to 0.3% between the model and the data (see table 6.2). It was found to be always preferable to use an order above the third order polynomial to minimize errors, with fits larger than the third order resulting in less than 0.3% error. The selection of the order of the polynomial involved manual verification but generally the third order polynomial was optimal.

Table 6.2: Equations relating to the different orders of Gaussian function, and maximum differences from measured data.

	Gaussian function parameter	Maximum difference
$a1 \cdot \exp(-((x-b1)/c1)^2)$	1 st order	2.40%
$a1 \cdot \exp(-((x-b1)/c1)^2) + a2 \cdot \exp(-((x-b2)/c2)^2)$	2 nd order	2.20%
$a1 \cdot \exp(-((x-b1)/c1)^2) + \dots + a3 \cdot \exp(-((x-b3)/c3)^2)$	3 rd order	0.29%
$a1 \cdot \exp(-((x-b1)/c1)^2) + \dots + a4 \cdot \exp(-((x-b4)/c4)^2)$	4 th order	0.14%
$a1 \cdot \exp(-((x-b1)/c1)^2) + \dots + a5 \cdot \exp(-((x-b5)/c5)^2)$	5 th order	0.16%
$a1 \cdot \exp(-((x-b1)/c1)^2) + \dots + a6 \cdot \exp(-((x-b6)/c6)^2)$	6 th order	0.11%
$a1 \cdot \exp(-((x-b1)/c1)^2) + \dots + a7 \cdot \exp(-((x-b7)/c7)^2)$	7 th order	0.09%
$a1 \cdot \exp(-((x-b1)/c1)^2) + \dots + a8 \cdot \exp(-((x-b8)/c8)^2)$		

For a 1C 1x1 profile at a depth of 10 cm. The variables a1, a2, ..., b1, b2, ..., and c1, c2, ... are coefficients of the Gaussian function that is determined from the data.

For a 1x1 cm² field (see fig. 6.3), the Gaussian fit of the profiles was successful to within 1% within the region of interest (dose more than 20%). For a 2x2 cm² field (see fig. 6.4), the Gaussian fit of the profiles was successful to within 2% within the region of interest. However for a 5x5 cm² field (see fig. 6.5), the Gaussian fit of the profiles involved errors of up to 5% in the region of interest and approached 10% for the DD fit. Additionally, the Gaussian fit did not model the inter-umbra region well, which was confirmed for larger field sizes.

The use of the Gaussian kernel is therefore best limited to a field size of less than 5x5 cm² due to a poor fit between the model and the data for larger fields. This was observed by the rippling effect of the Gaussian curve fit on the measured data in the inter-umbra region due to the difficulty in modelling flat regions by the Gaussian function (see the inter-umbra region in fig. 6.5). Since the Gaussian curve seems to work well for regions of profiles without a central flat region, it is ideal for the modelling of small fields.

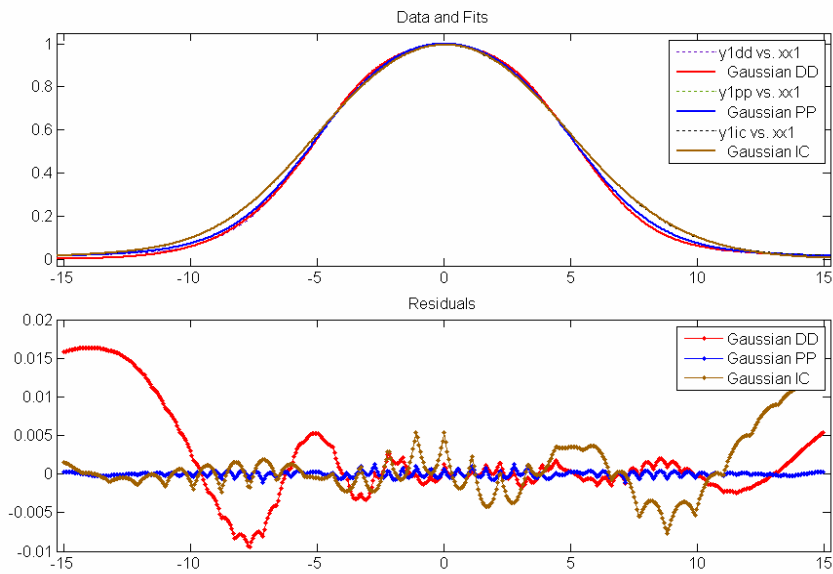


Figure 6.3: Gaussian curve fit for $1 \times 1 \text{ cm}^2$ at 10 cm depth

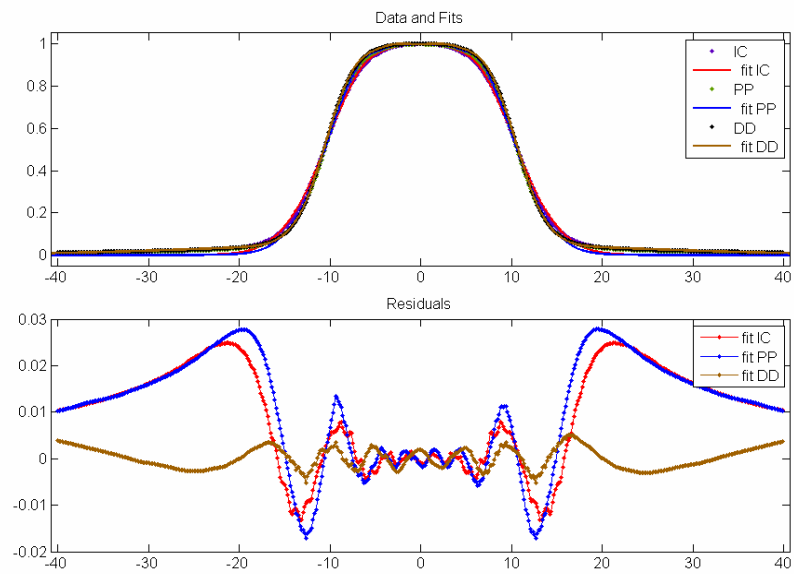


Figure 6.4: Gaussian curve fit for $2 \times 2 \text{ cm}^2$ curve at 10 cm depth

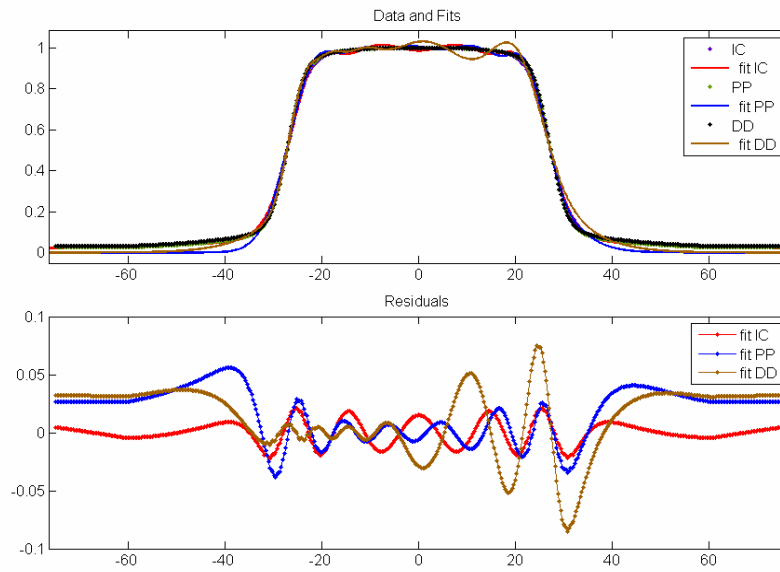


Figure 6.5: Gaussian curve fit for 5x5 cm² curve at 10 cm depth

The sensitive detector diameter values that were used in the extrapolation procedure were used to fit the kernel equation

$$K(x) = \frac{1}{\sqrt{2\pi}\sigma} \exp\left(-0.5 * \frac{x^2}{\sigma^2}\right) = \frac{1}{2.51\sigma} \exp\left(-0.5 * \frac{x^2}{\sigma^2}\right) \quad (6.8)$$

The resultant kernel functions (see fig. 6.6) were used in the deconvolution algorithm. The deconvolution algorithm was based on the *deconv* method in MATLAB. Sufficient spacing was introduced around the profile by reproducing the out-of-dose readings further out of the field –this involves packing the kernel with dose in the out-of-field region with the dose points in the ends of the penumbral tail.

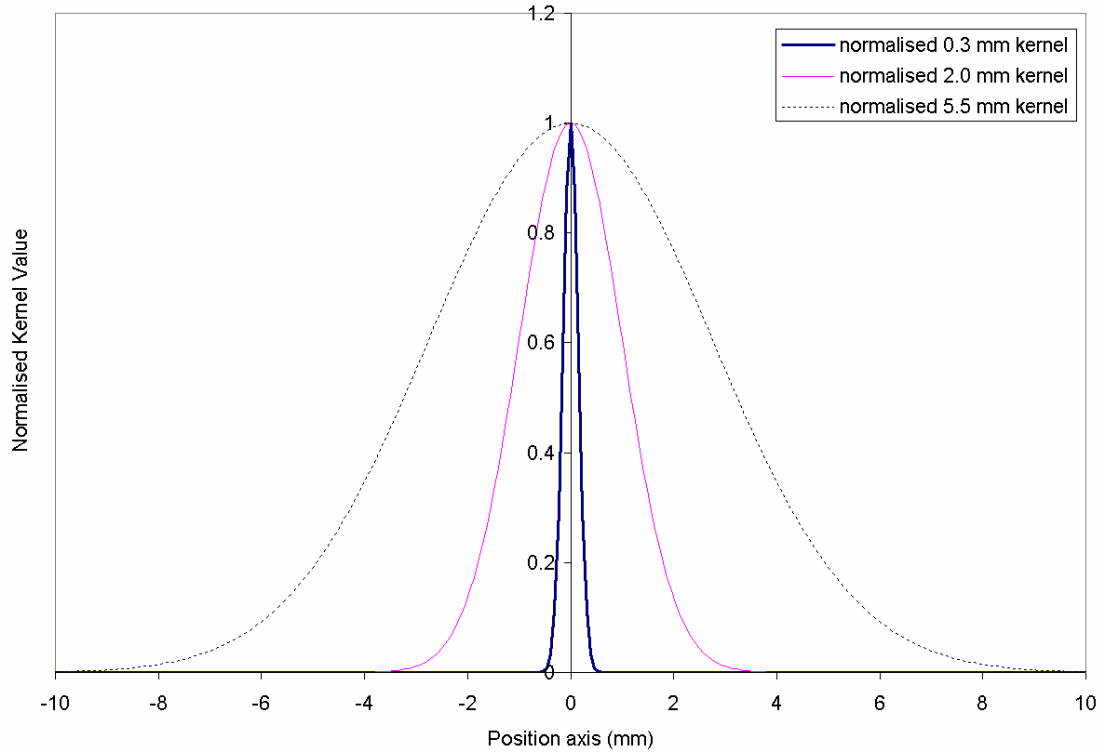


Figure 6.6: Figure showing the plot of the kernel functions

The deconvolved profile involved spacing data as well and was centred and re-sampled. This technique was based on finding the maximum value and centering the data points on the maximum point. The deconvolved profile was also normalized.

6.3 RESULTS

With the deconvolution of the IC, it was observed that the deconvolved profile shape differed significantly with the ZE profile. Most importantly, the intersection point between detectors also differed significantly for each deconvolved IC profile with different kernels.

The intersection and inflection point (discussed in chapter 4), while previously measured to be close to the 50% dose point, for convolved profiles the point differed significantly in the deconvolved profiles (see fig. 6.7). This could indicate that higher order fits of the Gaussian function involve a function that increasingly deviates from the single order Gaussian function. Alternatively, it could be an error in the deconvolution code or technique, or an error associated with the deconvolution of broad penumbras.

To visualise the effect of deconvolution on the profiles, a sample of kernel radii close to the final kernel radius was used to deconvolve the measured profiles. The notation used in figures 6.7, 6.8, and 6.9 are as follows:

Table 6.3: Notation used in figures 6.7, 6.8, 6.9.

ZE	Virtual zero volume data from extrapolation
IC	IC data
d(IC) 1 mm	Deconvolved IC data with 1 mm radius kernel
d(IC) 2 mm	Deconvolved IC data with 2 mm radius kernel
d(IC) 3 mm	Deconvolved IC data with 3 mm radius kernel
PP	PP data
d(PP) 0.5 mm	Deconvolved PP data with 0.5 mm radius kernel
d(IC) 1.0 mm	Deconvolved PP data with 1.0 mm radius kernel
d(IC) 1.5 mm	Deconvolved PP data with 1.5 mm radius kernel
DD	DD data
d(DD) 0.1 mm	Deconvolved DD data with 0.1 mm radius kernel
d(DD) 0.2 mm	Deconvolved DD data with 0.2 mm radius kernel
d(DD) 0.3 mm	Deconvolved DD data with 0.3 mm radius kernel

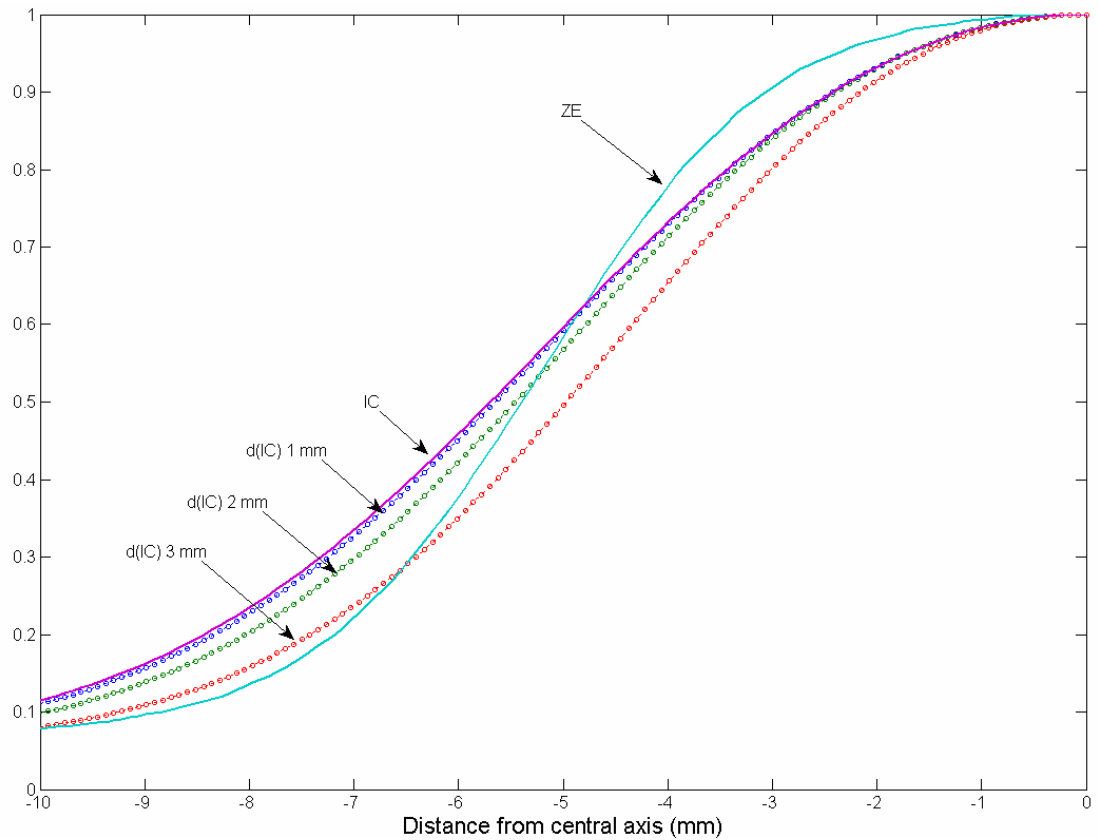


Figure 6.7: Deconvolution of IC with various kernels compared with ZE for a $1 \times 1 \text{ cm}^2$ field at 10 cm depth (Jaw Crossplane)

Figure 6.7 shows the effect of deconvolution of the largest ion chamber dose profile data (i.e. IC profile) with kernels of various kernel radii (ranging from 1 to 3 mm).

Figure 6.8 shows the effect of deconvolution of the PP profile with kernels of various kernel radii (ranging from 0.5 to 1.5 mm) while figure 6.9 shows the deconvolution of the DD profile (with kernel radii ranging from 0.1 to 0.3 mm). In agreement with theory, the results indicate that the smaller the kernel, the less significant the impact of deconvolution correction because of the smaller detector volume. It is also noted that for large kernels (such as in fig 6.7), errors in the specification of the kernel diameter results in large errors as seen by the large differences between the deconvolution of profiles with 1 mm, 2 mm, and 3 mm.

The deconvolution of the IC, which involved large kernel radii, produced profiles which were significantly different from the original uncorrected data. The difference in the deconvolved profiles with different kernel radii involved different 50% dose points which do not coincide with the likely physical 50% position (see fig. 6.7), while the sharper penumbra associated with larger kernel radii is expected. This abnormality in deconvolved data could be the result of the error involved in fitting the

Gaussian curve to the measured data because the assumption that the measured data is a Gaussian may be unjustified. Alternatively, the deconvolution technique used in this study may have had a significant error in terms of the algorithm or in the use of the sensitive diameter as the kernel diameter.

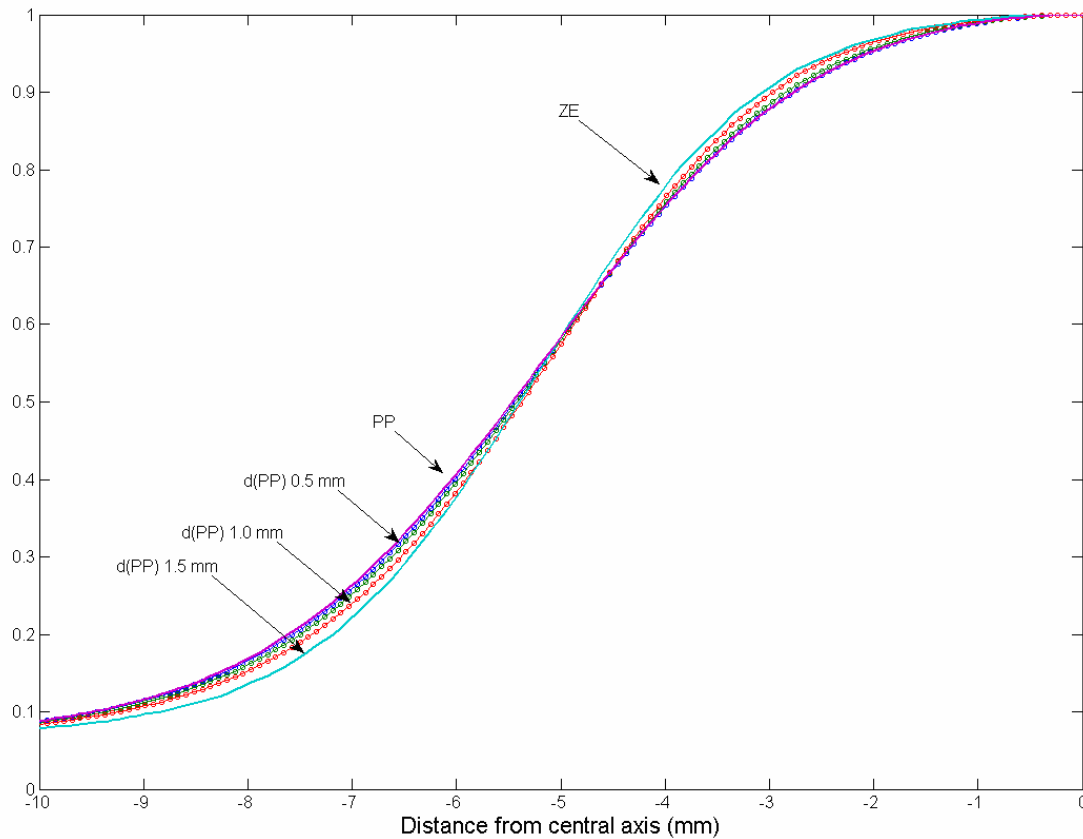


Figure 6.8: Deconvolution of PP with various kernels compared with ZE for a 1×1 cm² field at 10 cm depth (Jaw Crossplane)

The deconvolution of the PP yielded results conforming to expectations with the deconvolved data intersecting with the original data at the 50% dose region and being associated with sharper penumbras (see fig 6.8). The deconvolution of the DD produces profiles which are nearly identical to the original DD profile (fig 6.9).

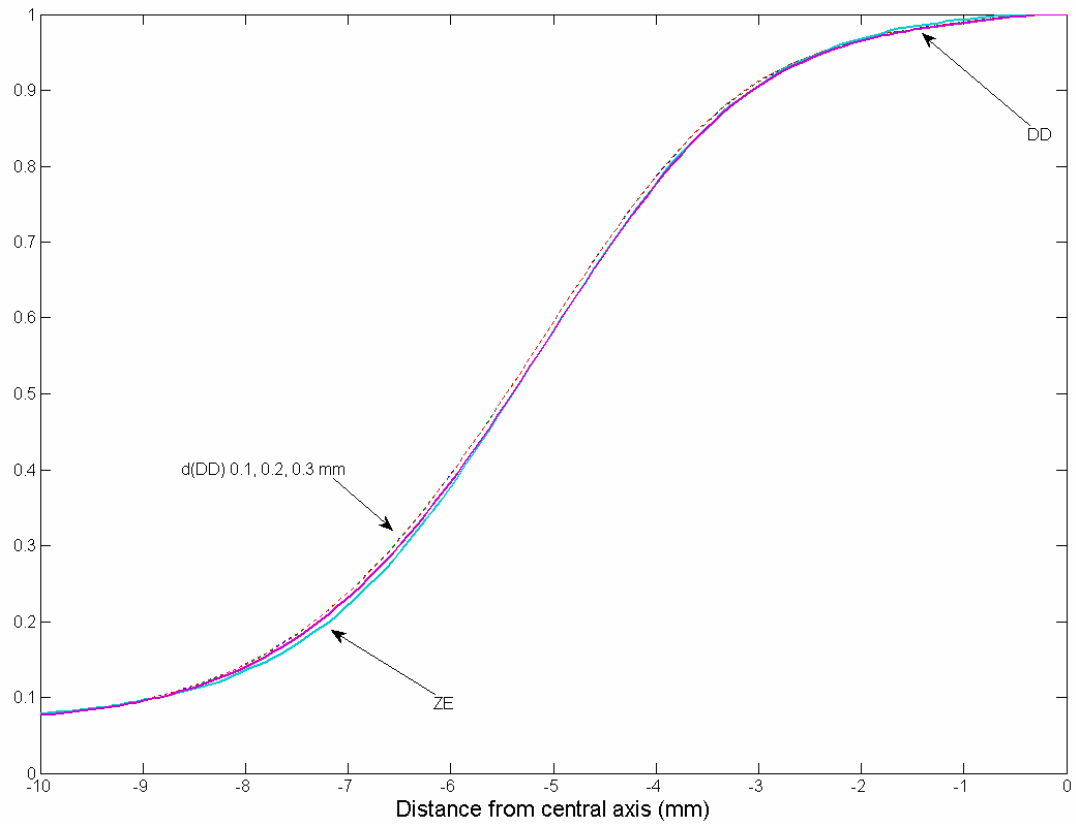


Figure 6.9: Deconvolution of DD with various kernels compared with ZE for a $1 \times 1 \text{ cm}^2$ field at 10 cm depth (Jaw Crossplane)

In contrast, the deconvolution with the PP yielded results conforming closer to expectations. The larger the kernel, the sharper the profile became. For the deconvolution of the DD, the deconvolved profiles were nearly visually indistinguishable to the original profile due to the small kernel.

6.4 DISCUSSION

The deconvolution technique involved pre-processing of the input data before the algorithm can be initiated. The following points were noted:

- i. The deconvolution is noise sensitive (Charland, El-khatib et al. 1998) and therefore a fit of the measured data to a model may be a requirement for the deconvolution technique. This was confirmed with the observation of the stair-case effect (see fig 6.2) which was observed with the deconvolution of raw data. It was found that it was necessary to use a fitting function to the measured data in order to reduce the effect of noise.
- ii. In the literature, it was found that the Gaussian kernel was more consistent than an alternative, the parabolic kernel (Garcia-Vicente, Delgado et al. 1997). In addition, the modelling of the measured data with a Gaussian fit was necessary in order to satisfy an optimised deconvolution technique of deconvolving a Gaussian with a Gaussian. Therefore in this study, both the kernel and the measured data were modelled with a Gaussian model. There are possible flaws with this due to inaccurate representation of the inflection point of the measured profile with the Gaussian fit (discussed in chapter 4). In other words, the data was forced to have an inflection point of 50% (a property of a Gaussian) which is not indicative of measurements. In addition, studies that have noted the Gaussian model of the kernel for the ionisation chamber serves as only an approximation of the true kernel (van't.Veld, Lujik et al. 2001)
- iii. Due to the deviation from the measured profiles from the expected, the deconvolution technique used in this study limited the study to profiles with field sizes of $2 \times 2 \text{ cm}^2$ or smaller. The inter-umbra region was not modelled well with Gaussian functions. In addition, the first order Gaussian function did not fit the measured functions well. The penumbra was modelled well with the first order Gaussian function but the central axis dose involved significant variations. Higher order Gaussian functions were used for closer fits. The higher order Gaussian fits involved the superposition of a number of Gaussian fits with the CFTOOL algorithm in MATLAB until the fit was optimised, similar to other researchers (Pappas, Maris et al. 2006).
- iv. The use of the Gaussian fit limited the deconvolution technique to small field sizes which approximated the Gaussian function. Larger field sizes such as $10 \times 10 \text{ cm}^2$ have a flat inter-umbra region due to lateral electron equilibrium extending across most of the inter-umbra profile. Such a profile could not be fitted without significant errors

with a Gaussian function as tested with the method described in this chapter. From the data used in this study, it was observed that field sizes of up to $2 \times 2 \text{ cm}^2$ could be fit with the Gaussian fit. Other profiles without lateral electronic equilibrium would also be likely candidates for a Gaussian fit and, therefore, also be eligible for the deconvolution technique.

The selection of the parameters for the fitting of the kernels was a crucial part of the deconvolution process and the following were noted:

- i. Techniques, such as using a slit image or otherwise, to form a step functions in order to determine the FWHM of deconvolution kernels (Charland, El-khatib et al. 1998) have found that the FWHM of the kernels measured has a dependence on field size (Pappas, Petrokokkinos et al. 2005). The variation of the deconvolution kernel with field size was not modelled in this study.
- ii. The lack of comprehensive literature on the FWHM of the kernels for the detectors used in this study was a major limiting factor on the potential accuracy of the study. The deviation between the detector diameter and the FWHM was a maximum of 1.8 mm and not all detectors corresponded to a well established relationship. The ionisation chamber is known to have a larger effective radius than the dimension of its sensitive volume alone (van't.Veld, Lujik et al. 2001) but the degree of increase is not described by a simple mathematical model.

Additionally the FWHM of the kernels relating to the detector does not correlate with the effective size of the detector for various types of detectors –for example, the film/densitometer has an effective size of 0.8 mm but a FWHM of 1.08 mm, the diode has an effective size of 2.5 mm but a FWHM of 2.24 mm, and the RK chamber has a effective size of 4.0 mm but a FWHM of 5.42 mm (Garcia-Vicente, Delgado et al. 1997). The determined FWHM of the diamond detector was 2.1 mm in the literature (Bednarz, Huq et al. 2002) while the sensitive diameter was 0.3 mm (PTW-Frieburg 2008). The IC15 with a detector length of 5.8 mm (similar to the 0.125 cc ionisation chamber detector length of 5.5 mm) involved a measured FWHM of 6.9 mm at 6 MV while the NAC detector with a 3.0 mm detector length (same as the PP detector length and similar to the PP detector) involved a measured FWHM of 2.6 mm (van't.Veld, Lujik et al. 2001). The deviation between the effective size of a detector and the FWHM is also a potential source of error. This is an unavoidable issue because the kernel of a detector is only a model of the detector response. In contrast, the effective size of a detector may be less accurate than the kernel of a detector because use of the

effective size of a detector implies a step function, which is considerably different to the case of a Gaussian (or other kernel function).

For consistency, the values for sensitive diameter for the detectors were used as the FWHM for the kernels because only the sensitive diameter information was available in this study. This limits the accuracy of the deconvolution technique. It was noted that sensitive diameters were used in this study and the literature indicates that the sensitive diameter is an underestimate of the FWHM.

- iii. The use of the sensitive diameter underestimated the kernel FWHM and this would be a contributing factor in the decreased accuracy of the deconvolved datasets. The deconvolved datasets in this study would involve under-correction with respect to the detector effect. Therefore, where there is penumbral overestimation in the original data, the penumbral overestimation would be reduced with the deconvolution in this study but not eliminated –this is discussed further in the analysis of profile parameters in chapter 7.
- iv. Furthermore, it was noted that the kernel of an IC was dependent on detector size, electron fluence variance caused by the replacement of water by air, and the generation of electrons in the detector wall and the central electrode (van't.Veld, Lujik et al. 2001). The kernels of diamond detectors are considered small but as the diamond detector shows a direct photon response the dose contributions from photons is heightened and the detector no longer acts as a Bragg-Gray cavity but instead as an intermediate-sized cavity (Mobit and Sandison 1999).
- v. The values for the FWHM of deconvolution kernels have been measured in the literature for the diamond detector but neither for the pinpoint nor the 0.125 cc ionisation chamber. Data with verification of the FWHM of deconvolution kernels for the detectors used in the study would improve the deconvolution technique.

Measurement of the FWHM of the kernel directly is possible with established techniques but this increased the complexity of the study considerably. The determination of kernels experimentally is time consuming and is restricted to detector types and beam spectrum (Mobit and Sandison 1999). Additional equipment and setup procedures would need to have been introduced to derive experimental kernels for this project.

The deconvolution comes with several caveats that were not investigated fully in this study. Some properties were observed during coding for the algorithm in this study and some were discussed in the literature:

- i. Before deconvolution, the profile may require transformation in such a way as to have a beam profile that is symmetric around the inflection point (Charland, El-khatib et al. 1998). This was not done in this study because this would involve an artificial alteration of measured data without a correction based on a physical model.
- ii. The deconvolution technique also has an inherent assumption in that the two-dimensional deconvolution kernel is equivalent to two one-dimensional deconvolution kernels (Chui and Mohan 1987). Such may not be the case due to the strong asymmetry of the diamond detector and the weaker asymmetry of the pinpoint and the 0.125 cc ionization chamber (see table 4.1). The reason for this is because while the IC and the PP are designed as cylindrical chambers (weak asymmetry) with air cavities, the DD is designed as a solid state detector with a geometry consisting of a thin chip that is much thinner in the direction of the detector axis than perpendicular to the direction of the detector axis.
- iii. The coding of the algorithm for deconvolution is considerable. Manual care needs to be taken in the curve-fit of the data as lower-order Gaussian fits do not fit well with the measured data but higher-order Gaussian fits may introduce artefacts such as extra inflection as compared to the measured profile. The curve fit procedure was visually analysed each time to ensure a reasonable fit. Coding algorithms to do this step could be done by analysing the dose differences in the future to verify the curve fit.
- iv. There was also code required relating to the padding of data by the measured profile to deconvolve the data points at the edge of the profile. After deconvolution, the central axis points were retrieved by locating the maximum and the data padding was undone to return the deconvolved profile to the original spatial spacing.

6.5 CONCLUSIONS

The deconvolution technique has potential for correction of the detector volume effect in measured profiles. However, the deconvolution technique involves intricacies such as:

- i. sensitivity to noise in the data,
- ii. a requirement to fit the data with a Gaussian curve,
- iii. restrictions of the technique to small fields (less than $2 \times 2 \text{ cm}^2$),
- iv. a requirement to perform additional experiments to confirm the FWHM of the detector kernels or to use approximations of the FWHM based on effective diameters,

- v. an implicit assumption of symmetry of the detector kernels in the direction parallel and perpendicular to the detector.

The potential benefits of the deconvolution technique involve a general, theoretically sound, model that is able to transform an arbitrary (small field) profile into a profile that corresponds with a zero detector profile by inputting the FWHM of the kernel. The absence of modelling of the field size dependence of kernels is a smaller caveat.

Another significant weakness of the deconvolution method is the weakness in the application of the model to field edges with low out-of-field tails (van't.Veld, Lujik et al. 2001). This indicates that the deconvolution technique is best used at depths of dose maximum and worse at deeper depths as the value of the out-of-field tail increased in terms of normalised dose.

Chapter 7: Analysis of the effect of detector volume on smearing of dose profiles

The results from the calculation of the virtual zero volume detector profile from extrapolation (see Chapter 5), the deconvolved detector data (Chapter 6), and the measured data are analysed and compared with in this chapter. The virtual zero volume detector profile data from extrapolation was used as the reference.

7.1 PENUMBRA ANALYSIS

The penumbra is characterised by the edge of the beam profile, where there is lateral electron disequilibrium and which involves significant dose gradients. The penumbra is dependent on depth, where there is a variation in exposure to the extrafocal component of the source, scattering in the collimator, and scattering in the phantom. The penumbra also broadens with field size due to the divergence of the beam and the contribution of scatter from the planes above the plane of measurement. Thus, the effect of detector size on the penumbra was verified over various field sizes (1×1 to 10×10 cm²) and depths (1.5 to 20 cm). Note that the 80% and 20% dose values were interpolated from the measured data.

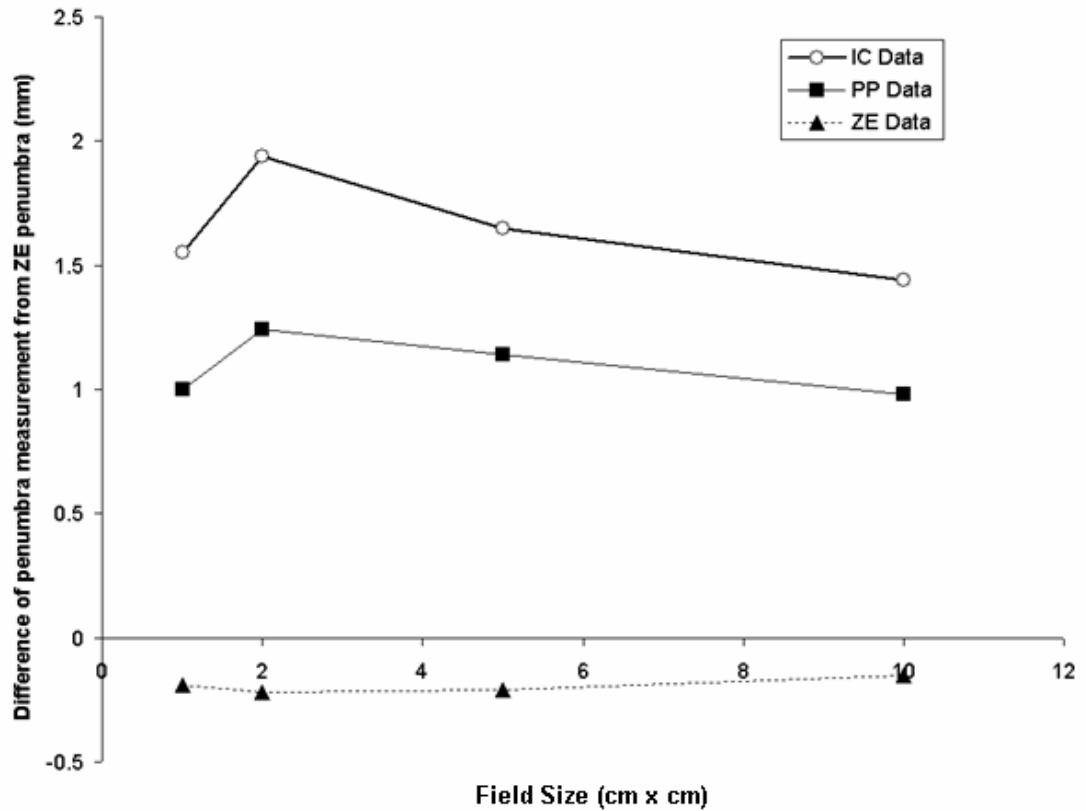


Figure 7.1: Plot of Penumbral variation over field sizes (10 cm depth)

Plot showing the dependence of the difference in penumbra measurement from the ZE penumbra with field size.

The variation of overestimation of the penumbra (fig. 7.1) with respect to the virtual zero volume data from extrapolation (ZE) was within 0.2 mm over set radiation field sizes of between 1×1 and 10×10 cm² (table 7.1) for both the PP and the DD. For the IC, the variation was more significant with 0.4 mm over the same range of field sizes, which suggests that large volume detectors not only have a larger overestimate of penumbra but that the variation of the penumbra over field sizes is also larger.

Y axis is calculated with: measured penumbra (mm) – ZE penumbra (mm)

Table 7.1: Overestimate of the penumbra from ZE penumbra in mm with variation with field size

Data	Measured IC	Measured PP	Measured DD
Field size:			
1×1 cm² to 10×10 cm²	+1.6 mm to +2.0 mm	+1.0 mm to +1.2 mm	-0.2 mm to -0.1 mm
Variance in range	0.4 mm	0.2 mm	0.1 mm

The variation of penumbra overestimation over depths (see fig. 7.3) from 1.5 cm to 20 cm was within 0.2 mm (see table 7.3) for all data sets (both original and deconvolved). In terms of penumbra, the deconvolution technique reduced the penumbra overestimation by 0.5 mm for the IC data and by 0.6 mm for the PP data.

It was observed that the deconvolution technique, using the sensitive diameter as the kernel diameter, was not able to minimise the penumbra completely. The deconvolved data involved significant penumbra overestimation at 1.0 mm for the deconvolved IC data and 0.5 mm for the deconvolved PP data. Note that both the original DD data and the deconvolved DD data involved minimal penumbra overestimation.

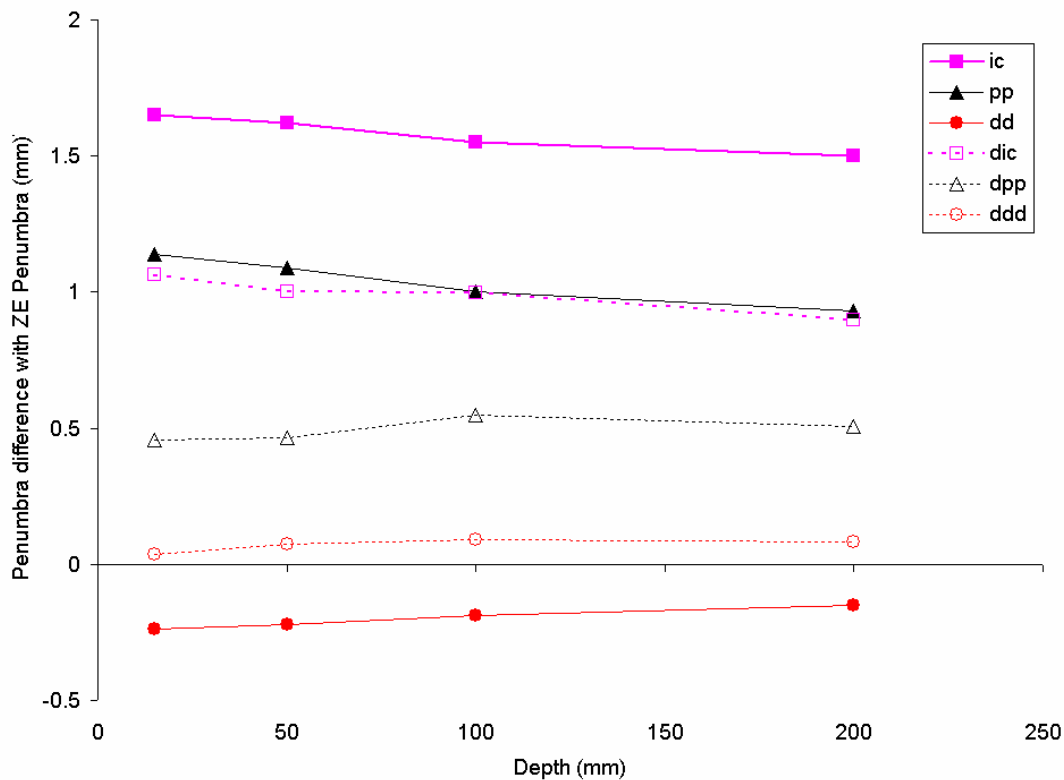


Table 7.2: Penumbral Variation over depths (1×1 cm² field size); Plot showing the dependence of the difference in penumbra measurement from ZE penumbra with depth.

Y axis is calculated with: measured penumbra (mm) – ZE penumbra (mm)

Figure 7.2 shows that the variation of measured field size with depths between 1.5 cm and 20 cm was within 0.2 mm (see table 7.5) for all the data (except the deconvolved PP data which varied by 0.3 mm). The results show that only the original IC data involved a significant measured field size overestimation of 0.5 mm.

Table 7.3: Overestimate of the penumbra from ZE penumbra in mm with variation with depth.

Data	Measured IC	Deconv IC	Measured PP	Deconv PP	Measured DD	Deconv DD
Depths	+1.5 mm	+0.9mm	+1.0 mm	+0.4 mm	-0.2 mm	+0.0 mm
1.5 to 20 cm	to +1.6 mm	to +1.1 mm	to +1.2 mm	to +0.5 mm	to -0.1 mm	to +0.1 mm
Variance in range	0.1 mm	0.2 mm	0.2 mm	0.1 mm	0.1 mm	0.1 mm

7.2 FIELD SIZE ANALYSIS

To the author's knowledge, no literature has discussed the detector effect on the measured field size. The measured field size is defined as the full width half maximum of the profile. The measured field size should be equal for all profiles if the intersection points cross at 50% dose.

However, a detailed analysis of the intersection points in Chapter 3 revealed that the intersection point for measured profiles with different detectors does not in fact cross at 50%. In addition, the work done involving the verification of the cost function (see Fig. 5.12) shows a significant cost function in the extrapolation algorithm in the 50% dose region. Therefore, the position at which the dose measured is 50% is proposed to be different for each set of data (both measured and processed).

The y-axis of the curves in this section involved the following relation:

$$DEV(ZE) = FS(data) - FS(ZE) \quad (7.1)$$

The x-axis of the curves in this section used the calculated ZE penumbra values.

Notes regarding the plots:

- i. The y-axis of the curves in this section was calculated using equation 6.9.
- ii. The x-axis of the curves in this section used the calculated ZE field size.
- iii. Note that the 50% dose values were interpolated from the measured data.

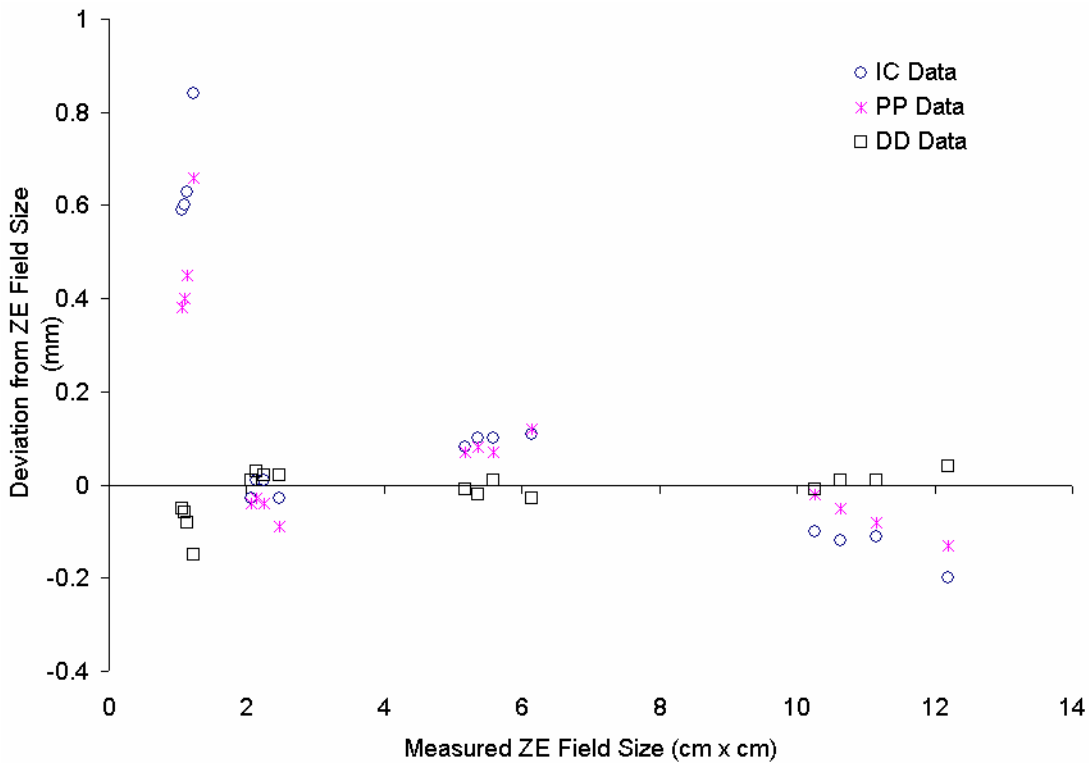


Figure 7.2: Measured Field Size variation over set field size (over depths 1.5 to 20 cm and set field size 1×1 to 10×10 cm²)

Plot showing the overestimation or underestimation of field size compared with the ZE measured field size with field size. The Y-axis was calculated with equation 7.1.

Figure 7.2 contains data from a variation in jaw field sizes and measured depths, both of which influence the measured ZE field size. In figure 7.2, it is observed that for measured ZE field sizes more than ~2 cm, all the data points are within 0.2 mm. This indicates that for field sizes greater than 2x2 cm², the detector diameter has negligible effect on measured radiation field size (see table 7.4). For a field size of 1×1 cm², the IC data overestimates the field size by up to 0.9 mm (column 2 of table 7.4) while the PP data overestimates the field size by up to 0.7 mm (column 3 of table 7.4), and the DD is within 0.2 mm of the ZE field size (column 4 of table 7.4).

Table 7.4: Overestimate of the field size from ZE field size in mm with field size (see fig. 7.2)

Data	Measured IC	Measured PP	Measured DD
Field size:	+0.6 mm to	+0.4 mm to	0.0 mm to
1×1 cm²	+0.9 mm	+0.7 mm	-0.2 mm
Field size:			
2x2 cm² to 10×10 cm²	±0.1 mm	±0.2 mm	±0.2 mm

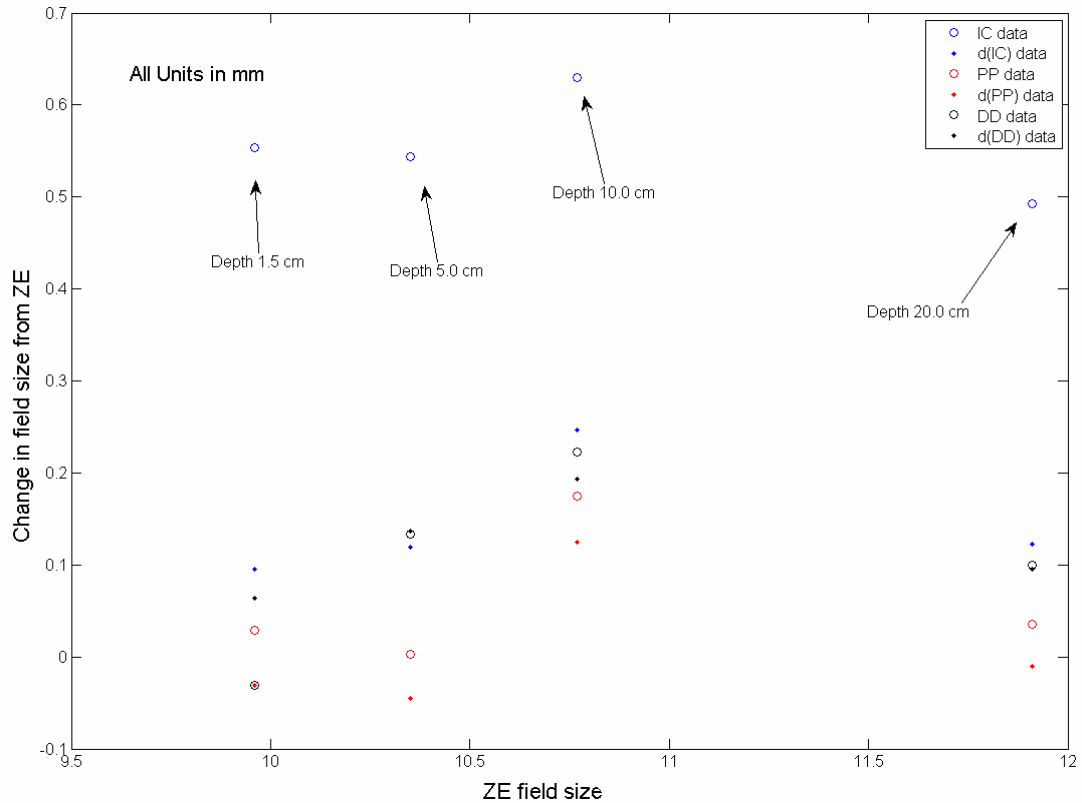


Figure 7.3: Measured Field Size variation over depth (1×1 cm² field size)

Plot showing the overestimation or underestimation of field size compared with the ZE measured field size with depth. The Y-axis was calculated with equation 7.1.

Figure 7.3 illustrates the dependence of the change in field size as compared to the virtual zero volume data with depth. In table 7.5, it was observed that for both the original and the deconvolved PP and DD data, that the measured field size was within 0.2 mm of the virtual zero volume field size. For the measured IC data, the overestimate of the field size (average 0.6 mm overestimate) was consistent with depth (within a

range of 0.2 mm). It was also noted that the deconvolved IC data reduced the overestimation by 0.4 mm to an overestimation of 0.2 mm (average).

Table 7.5: Overestimate of the field size from ZE field size in mm with depth (see fig. 7.3)

Data	Measured IC	Deconv IC	Measured PP	Deconv PP	Measured DD	Deconv DD
Depths	+0.5 mm	+0.1mm	+0.0 mm	+0.2 mm	+0.0 mm	+0.1 mm
1.5 to 20 cm	to	to	to	to	to	to
	+0.7 mm	+0.3 mm	+0.2 mm	-0.1 mm	+0.2 mm	-0.1 mm
Variance in range	0.2 mm	0.2 mm	0.2 mm	0.3 mm	0.2 mm	0.2 mm

7.3 DOSE ANALYSIS

The significance of the field size and penumbra variation studied in the earlier sections influence the dose delivered to the phantom/patient. Furthermore, in clinical cases, the factor that is important for the clinician and the patient is the summation dose to the tumour and normal cells. In this study, the whole dataset is considered which would correlate loosely to the summed dose in a real clinical treatment.

The link is not complete because in this section a 1D dose profile is considered whereas in a real clinical case there is a 3D dose distribution. The effect of the detector volume in the measurement of data would change the summed dose. If the region of interest is confined to a smaller area that corresponds to the treatment volume, then the effect of the detector volume on the measurement data could be studied to quantify the detector effect on the mean dose. A 1D analysis is performed in this section using measured and processed profiles while in Chapter 10, a 2D analysis is performed using RTPS dose distributions.

In terms of dosimetric modelling in this study, the difference in the profiles based on different detector volumes are of interest. This section aims to quantify the effect of detector volume on the dose differences measured. In other words, while penumbra and field size analysis involved the distance across the central axis as the variable, a dose difference analysis uses the measured dose as the variable.

The maximum dose difference was calculated with

$$MAX \text{ Dose Difference (\%)} = 100 \times MAX \left(|Dose(measured)_i - Dose(ZE)_i| \right) \text{ \{for all points\}} \quad (2.7)$$

Notes regarding the dose difference plots (see figure 7.4):

- i. The y-axis of the curves in this section involved equations 7.1.
- ii. The x-axis of the curves in this section used the calculated Linac field size and phantom depth.
- iii. Note that the maximum dose difference was converted from normalized dose (max 1.0) to percentage difference (max 100).

In Figure 4.3, the underestimate area and overestimate area can be observed. If the underestimate area is larger than the overestimate area, the summed dose of the measured curve will be lower than the true summed dose. In the example illustrated by figure 4.3, the overestimate area is larger than the underestimate area which indicates that the measured IC profile overestimates the total 1D dose. The total 1D dose refers to the total area under the profile. The total 1D dose is calculated by the summation of all dose points over the 1D curve times the step size:

$$\text{Total1D Dose} = \sum_i D_i(\text{data}) \times \text{StepSize}_i(\text{data}) \quad \{\text{Over all } i \text{ points}\}$$

(7.2)

The total 1D overestimate is calculated by the summation of all positive dose difference points over the 1D curve times the step size;

$$\text{Total1D Overestimate} = \sum_i (D_i(\text{data}) - D_i(\text{ZE})) \times \text{StepSize}_i(\text{data})$$

{for all points where $D_i(\text{data}) > D_i(\text{ZE})$ }

(7.3)

while the total 1D underestimate was calculated by the summation of all negative dose difference points over the 1D curve times the step size

$$\text{Total1D Underestimate} = \sum_i (D_i(\text{data}) - D_i(\text{ZE})) \times \text{StepSize}_i(\text{data})$$

{for all points where $D_i(\text{data}) < D_i(\text{ZE})$ }

(7.4)

The step size used refers to the distance between measurement points. This setting was set in the MEPHYSTO dosimetry software and was used in the calculations (see equations 7.2-7.4) because the step size is lower for the penumbral regions and higher for the tails and the inter-umbral regions.

Lastly, the total 1D overestimate as a percentage of total 1D dose (used in figures 7.6, 7.7) was calculated by

$$\text{Total 1D Overestimate as \% of total 1D Dose} = 100 \times \frac{\text{Total 1D Overestimate}}{\text{Total 1D Dose}}$$

(7.5)

While the total 1D underestimate as a percentage of total 1D dose (used in figures 7.6, 7.7) was calculated by.

$$\text{Total 1D Underestimate as \% of total 1D Dose} = 100 \times \frac{\text{Total 1D Underestimate}}{\text{Total 1D Dose}}$$

(7.6)

The overall change in dose due to the detector diameter on measured profiles (used in figures 7.6, 7.7) was calculated by

$$\text{Overall Change (\%)} = \text{Total 1D Overestimate (\%)} - \text{Total 1D Underestimate (\%)}$$

(2.8)

The properties of the areas of overestimate and underestimate was discussed previously in chapter 4 (see figure 4.12) with respect to the intersection point and inflection point. Table 4.4 outlined the areas with respect to intersection point. This section, however, quantifies the amount of overestimate and underestimate by the analysis of the summed doses of the overestimate (equation 7.5) and underestimate (equation 7.6) in terms of the total dose (equation 7.2).

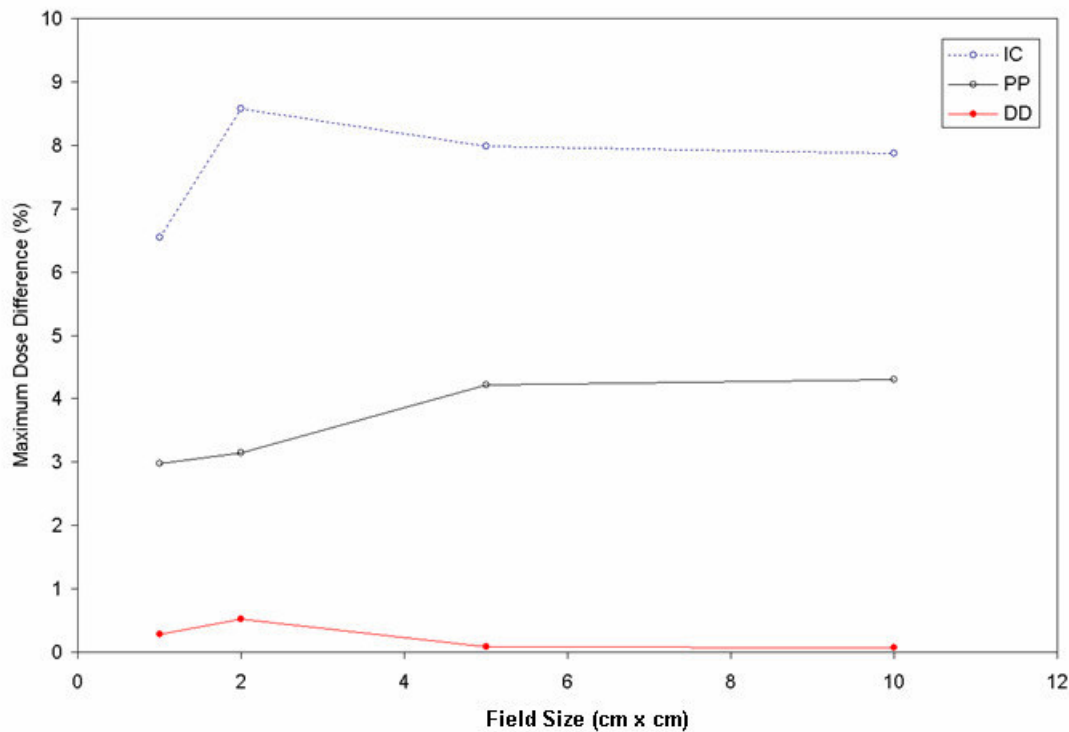


Figure 7.4: Dose difference variation over field size (10 cm depth); Plot of the maximum dose difference as a percentage over field sizes. The y-axis is calculated using equation 7.1.

The maximum dose difference (see equation 7.1) between the measured profile and the virtual zero volume detector profile was calculated for each measured profile at a depth of 10 cm for field sizes between 1×1 cm² and 10×10 cm². Results indicated that the larger the detector volume, the larger the maximum dose difference (see fig. 7.4). Table 7.6 shows a summary of the results and indicates that a large detector volume involved both a larger maximum dose difference but also a larger variance in maximum dose difference with field size. The maximum dose difference for the IC was ~7.5% with ~2% variance, with the PP with ~3.5% with ~1% variance, and the DD with ~0.2% with 0.2% variance.

Table 7.6: Maximum dose difference along the profile over field size (see fig. 7.4)

Data	Measured IC	Measured PP	Measured DD
Field Sizes: 1×1 to 10×10 cm ²	+6.5 % to +8.5 %	+3.0 % to +4.2 %	+0.1 % to +0.3 %
Variance in range	2%	1.2%	0.2%

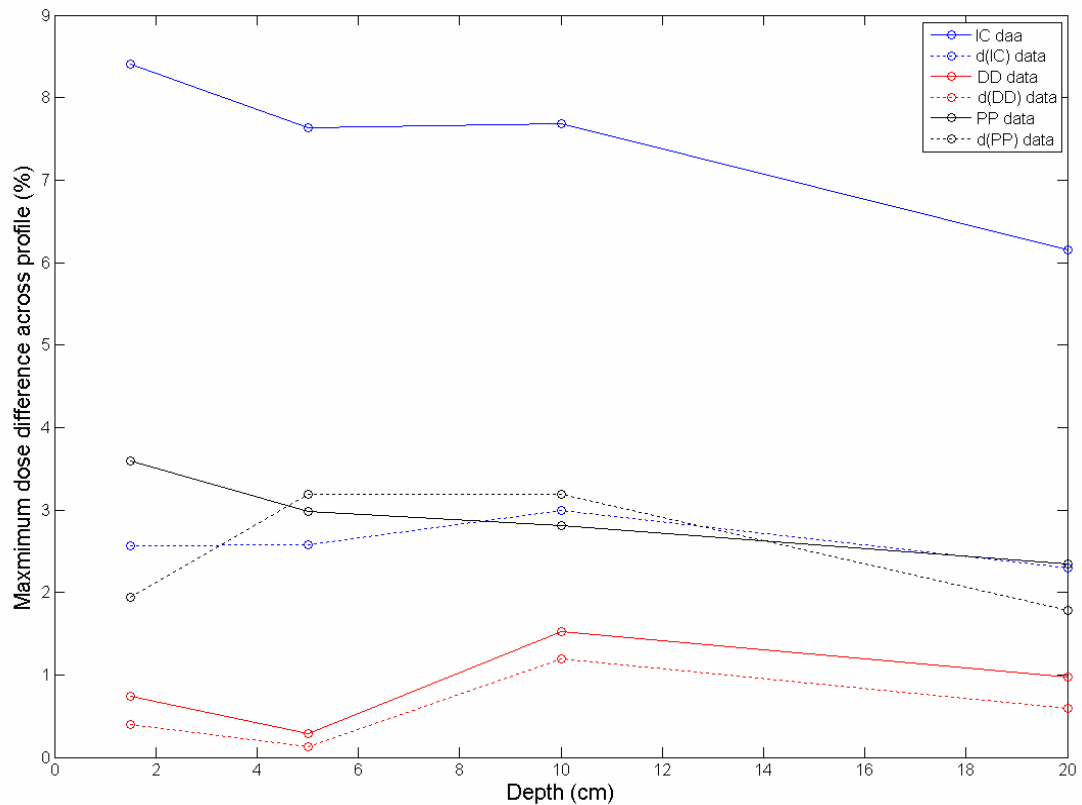


Figure 7.5: Dose difference variation over depth (1×1 cm² field size); Plot of the maximum dose difference as a percentage over depth.

In addition, the maximum dose difference was analysed with variation with depth at a field size of $1 \times 1 \text{ cm}^2$. Figure 7.5 illustrates these results with both the original measured data and the deconvolution of the measured data. Table 7.7 indicates that for measured data, the variation in maximum dose difference with depth is similar to the variation with field size (see table 7.6). The deconvolved data shows a significant decrease in the maximum dose difference from the virtual zero volume data. The deconvolved IC data involved a maximum dose difference of $\sim 2.5\%$ which was $\sim 5\%$ lower than the measured, the deconvolved PP was $\sim 2.5\%$ which was $\sim 0.5\%$ lower, but the deconvolved DD was $\sim 0.5\%$ and was similar to the measured DD data.

Table 7.7: Maximum dose difference across the profile with depth (see fig. 7.5)

Data	Measured IC	Deconv IC	Measured PP	Deconv PP	Measured DD	Deconv DD
Depths						
1.5 to 20	+6.2 % to +8.5 %	+2.5 % to +3.0 %	+2.3 % to +3.6 %	+1.9% to +3.2 %	+0.1 % to +1.4 %	+0.1 % to +1.2 %
cm						
Variation	2.3%	0.5%	1.3%	1.3%	1.3%	1.1%

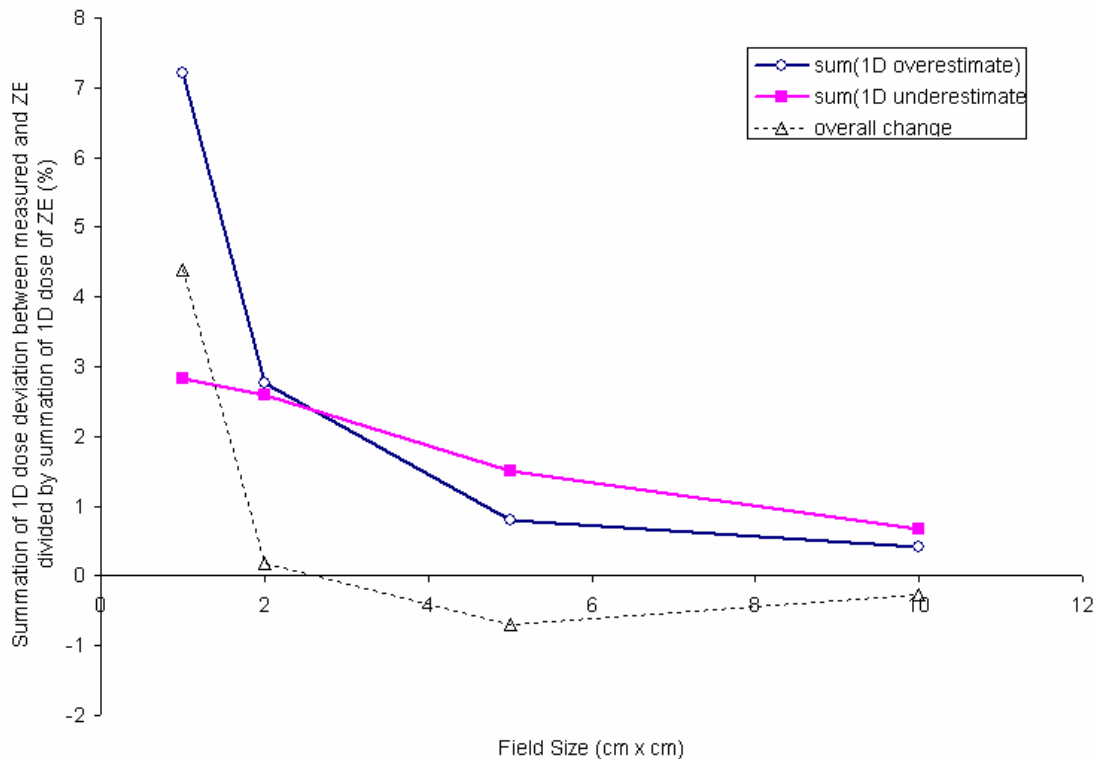


Figure 7.6: Plot of the summed of the overestimate and underestimate as a percentage of the total summed dose in the profile with field size. The summed(overestimate) is calculated using EQ. 7.5, summed(underestimate) uses EQ. 7.6, and overall change uses EQ. 7.7.

The summation of 1D overestimate, underestimate, and overall change (see equations 7.5, 7.6, 7.7 respectively) in dose was calculated and plotted in figure 7.6 for the case of the IC. The variation of these values with field size is significant, with a variation of ~7% for 1D overestimate, ~2% for 1D underestimate, and ~4.5% for overall change (see table 7.8). The summed 1D overestimate and underestimate are maximal at low field sizes and approach zero with increasing field size.

The summed 1D overestimate involves a higher value of 7.2% at a field size of $1 \times 1 \text{ cm}^2$ (see table 7.9) while the summed 1D underestimate involved an underestimate of 2.8% and decreases at a slower rate with increasing field size than the summed 1D overestimate. The overall change in dose, which is calculated by the difference of the summed 1D overestimate and 1D underestimate, illustrates the interplay of the summed 1D overestimate and 1D underestimate in fig. 7.6 The overall change in dose was +4.4% at a field size of $2 \times 2 \text{ cm}^2$, crosses the x-axis (no overall change) at a field size of $2.3 \times 2.3 \text{ cm}^2$, and is at approximately -0.5% for field sizes larger than $2.3 \times 2.3 \text{ cm}^2$ (see table 7.8)

Table 7.8: Tabulated data of overestimates and underestimates of profile with field size (see fig. 7.6)

Data	Summed of overestimate	Summed of underestimate	Overall change in summed dose
Field Sizes: 1×1	7.2%	2.8%	+4.4%
Field Sizes: 2x2	2.8%	2.6%	+0.2%
Field Sizes: 5x5	0.8%	1.5%	-0.7%
Field Sizes: 10×10	0.4%	0.7%	-0.3%

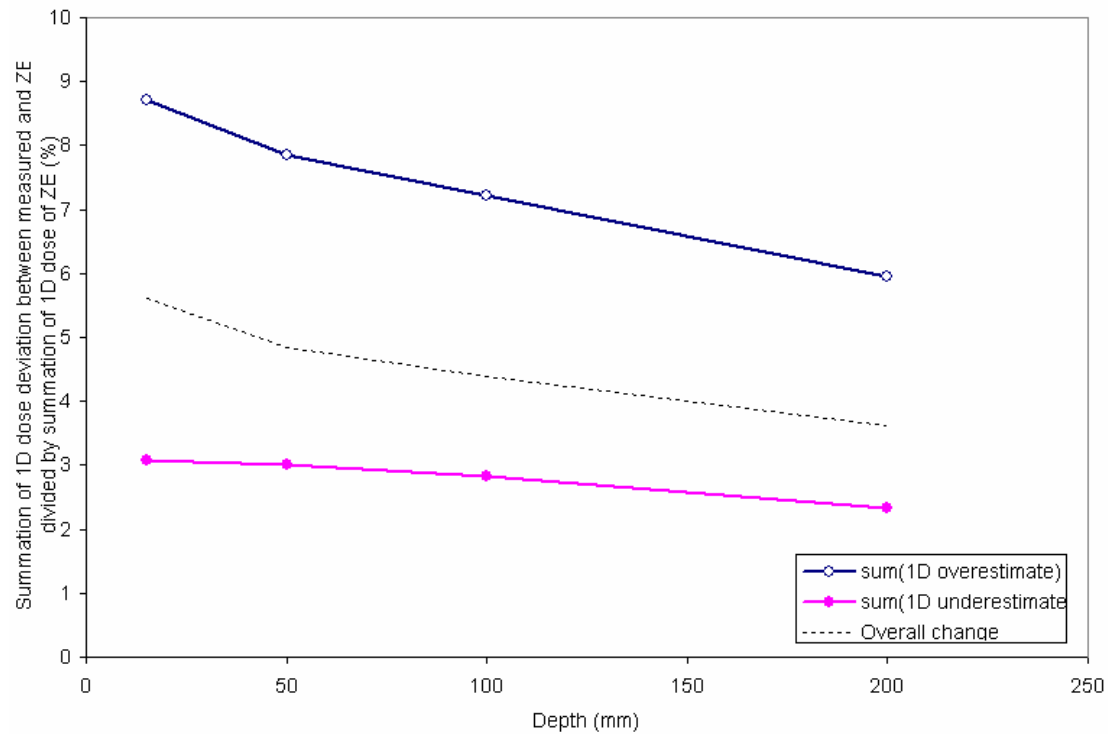


Figure 7.7: Plot of the summed of the overestimate and underestimate as a percentage of the total summed dose in the profile with depth. The summed(overestimate) is calculated using EQ. 7.5, summed(underestimate) uses EQ. 7.6, and overall change uses EQ. 7.7.

The variation of the summed 1D doses with depth is a slower function. The summed 1D overestimate and 1D underestimate decrease with increasing depth (see figure 7.7).

Over depths of 1.5 cm to 20 cm the 1D overestimate decreases from 9% to 6%, the 1D underestimate decreases from -2% to -3%, and the change in overall dose decreases from 6% to 3% (see table 7.19)

Table 7.9: Tabulated data of overestimates and underestimates of profile with depth (see fig. 7.7)

Data	Summed of overestimate	Summed of underestimate	Overall change in summed dose
Change in summed from depth 1.5 cm to 20 cm	6% to 9%	-2% to -3%	+3% to +6%

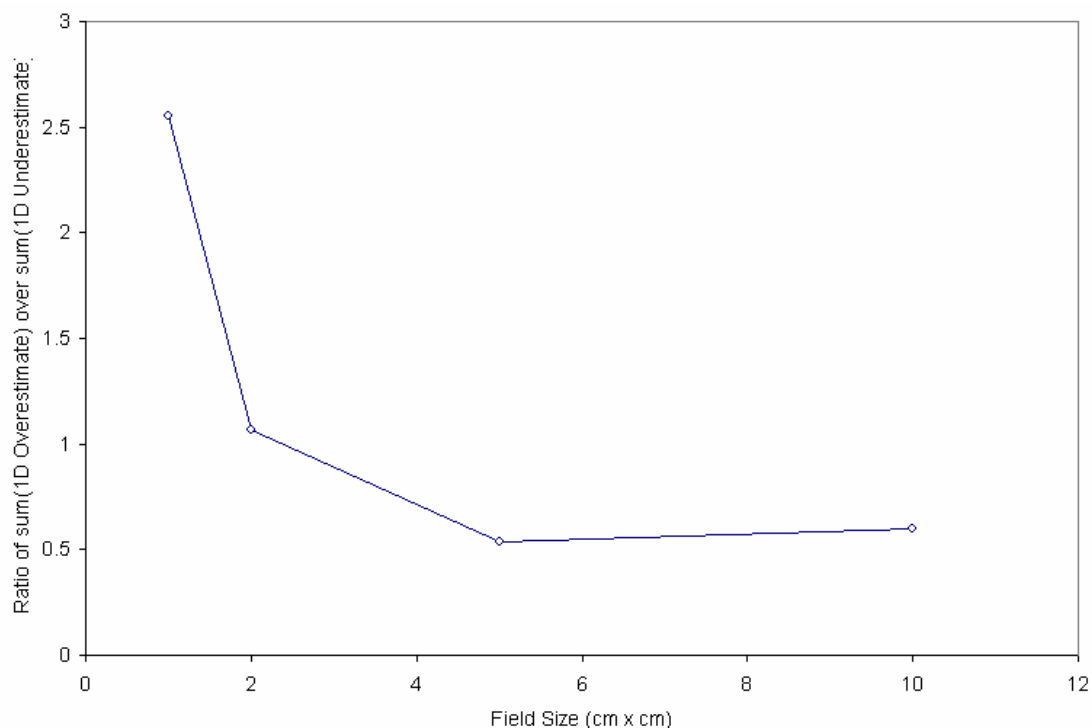


Figure 7.8: Plot of the ratio of the summed overestimate and underestimate in the profile with field size.

Figure 7.8 shows the ratio of 1D overestimate to the 1D underestimate and is based on the data from figure 7.6 and table 7.8. Figure 7.8 illustrates that the ratio is initially at ~2.5 but decreases to 0.5 at a field size of 5x5 cm² or above. The curve crosses at a ratio of 1.0 at a field size of 2.3x2.3 cm² (by interpolation) and this is shown in table 7.10.

This indicates that there are two regions where the effect on overall change is significant. For field sizes smaller than 2.3x2.3 cm², the overall dose is increased (by +4.4% at 1x1 cm²) while for field sizes larger than 2.3x2.3 cm², the overall dose is decreased (by ~0.5%). It should be noted that for smaller detector volumes than the IC, the same region delineation is expected but with smaller changes in overall dose.

Table 7.10: Tabulated data of the ratio of overestimates and underestimates of profile with field size. The field size of 2.3x2.3 cm² was interpolated from the graph in figure 7.8.

Data	Ratio of Summed of overestimate over underestimate
Field Sizes: 1x1 to 2.3x2.3	>1
Field Sizes: 2.3x2.3	=1
Field Sizes: 2.3x2.3 to 10x10	<1

7.4 DISCUSSION OF PROFILE PARAMETERS

Observations from the penumbral analysis include:

- i. Figures 4.31 and 4.32 indicate that large detectors tend to overestimate the penumbral width. The underestimation of the DD corresponds to the sublinearity of the linear extrapolation. The variation in the overestimation and underestimation can be analysed by the range of values in table 4.6. From $1 \times 1 \text{ cm}^2$ to $10 \times 10 \text{ cm}^2$, the penumbra variation from the average is within 0.2 mm. From depths of 1.5 cm to 20 cm, the penumbra variation from the average is within 0.1 mm (see table 4.8).
- ii. The effect of the detector size is to overestimate the true penumbra width. With regards to the 80-20 penumbra width, Over the field sizes ($1 \times 1 \text{ cm}^2$ to $10 \times 10 \text{ cm}^2$) and depths (1.5 cm to 20 cm) analysed, the IC generally overestimates the penumbra by ~2 mm, the PP generally overestimates the penumbra by ~1 mm, and the DD is within 0.2 mm of the ZE penumbra. The overestimation of the IC agrees with the expected 2-3 mm overestimation of penumbra of detectors with 4-6 mm internal diameter (van't.Veld, Lujik et al. 2001).
- iii. The use of the deconvolution technique was analysed in the reduction in penumbra overestimation at a field size of $1 \times 1 \text{ cm}^2$ (see figs 4.27, 4.28, and 4.29). Over the depths of 1.5 cm to 20 cm, the deconvolution of the IC reduced the overestimate of the penumbra from ~1.5 mm to ~1.0 mm while the deconvolution of the PP reduced the overestimate of the penumbra from ~1.0 mm to ~0.5 mm and the DD produced negligible changes in penumbra overestimation (within 0.2 mm).
- iv. The significance of the penumbra shift is larger as a ratio of the measured penumbra for smaller field sizes and shallower depths. Clinically, it may cause the use of fields larger than required due to an overestimation of the penumbra consistently for all patients treated in a clinical radiotherapy centre. In addition, the overestimation in penumbra may influence the major determinant of the penumbra in the treatment planning model software, the source size. The effect of penumbra on source size is discussed in the subsequent chapter.

Observations from the field size analysis include:

- i. It was observed that a small penumbra corresponded with sharp dose gradients. Moreover, for pairs of profiles where the intersection point is not at 50%, the difference in measured field size will be larger. This hypothesis agrees with the measured data in that smaller field sizes had greater deviation of the virtual zero detector volume data (see fig. 7.3).
- ii. The intersection point had a value of ~ 0.60 of normalised dose for a field size of $1 \times 1 \text{ cm}^2$ and a value of 0.55 for a field size of $2 \times 2 \text{ cm}^2$. For field sizes larger than $5 \times 5 \text{ cm}^2$, however, the intersection point approached 0.52 which approximates 0.5 of normalised dose.
- iii. The effect of intersection point on field size was verified by measurements of the measured field size of profiles based on different detector sizes. For a field size of $1 \times 1 \text{ cm}^2$, the IC overestimated the field size by up to 0.9 mm, the PP by 0.7 mm, while the DD was within 0.2 mm of the true field size (see fig. 7.2). The variation in field size overestimation at a field size of $1 \times 1 \text{ cm}^2$ over depths from 1.5 cm to 20 cm was also investigated (see fig. 7.3) and was negligible (within 0.2 mm).
- iv. Since the intersection point was always measured to be more than 0.5 cm in our dataset, the field size will always be overestimated because profiles with finite detector sizes overestimate the dose from the intersection point to the profile tail (see Table 4.4).
- v. The overestimation of field size was negligible (within 0.2 mm) for field sizes other than $1 \times 1 \text{ cm}^2$ for all measured profiles with the IC, PP, and DD. The intersection point approximated 0.50 sufficiently. The measurable variation in intersection point at a field size of $1 \times 1 \text{ cm}^2$ and the subsequent variation in measured field size implies a gradual dominance of detector perturbation over the detector volume effect at field sizes at or smaller than $1 \times 1 \text{ cm}^2$.

Observations from the dose analysis include the following:

- i. The maximum dose difference between the ZE profile and the measured profiles was larger with larger detector diameters. The IC exhibited the largest dose difference of +8%, with the PP at +4% and the DD within 0.2%. The variation of maximum dose difference with depth was within 1% over depths of 1.5 cm to 20 cm.

- ii. The percentage of the over- or underestimate dose over the summed dose was more significant for small field sizes. From a field size to $1 \times 1 \text{ cm}^2$ to a field size of $2.3 \times 2.3 \text{ cm}^2$, the overestimate summed is larger than the underestimate summed. Conversely, from a field size to $2.3 \times 2.3 \text{ cm}^2$ to a field size of $10 \times 10 \text{ cm}^2$, the underestimate summed is larger than the overestimate summed. It is most interesting to note that the ratio of the overestimate to underestimate summed inflects at the field size of $2.3 \times 2.3 \text{ cm}^2$, which is also the field size that delineates the start of lateral electron equilibrium extending to the field centre.
- iii. The data indicates that the percentage over- and underestimation, as a fraction of total summed dose, decreases with field size due to the larger inter-umbra region of dose summed in the total summed dose. For field sizes of $2 \times 2 \text{ cm}^2$ or above, the total change in summed dose due to measurement of a profile with a finite detector diameter is within 1%. For a field size of $1 \times 1 \text{ cm}^2$, the total summed dose is overestimated by 4.4% (for an IC). The overestimation is higher with shallow depths and lower with deeper depths.
- iv. The individual components of overestimation and underestimation are also significant not in terms of summed dose but in terms of the variation in dose distributions they will create due to the detector effect. In other words, in this section the 1D overestimate and underestimates in dose were analysed but the same technique can be applied for a 2D dataset. The 2D dose distribution can be illustrated with isodoses difference maps which will be discussed in chapter 10. A 2D dose analysis will correlate to real clinical situations better, where 3D dose distributions are the important parameter.

It is worth noting that the summed dose is important because an incident beam does not only deposit dose to the tumour but also through normal tissue in planes where the tumour does not lie. There are two effects to consider:

- i. In all dose planes where the tumour does not lie, the effect of the summed dose from the detector effect increases the absorbed dose to normal tissue.
- ii. In dose planes where the tumour does lie, the effect of overestimated dose and underestimated dose on the tumour dose and the normal tissue dose is dependent on the spatial distribution of the dose and the tumour volume. As discussed previously, areas of underestimation involve the region between the central axis and the field edge*, which implies underestimating dose in the region of the tumour volume. The areas of overestimation involve the region between the field

edge* and the profile tail, which implies overestimating the dose in the region of normal tissue volume. Note that this type of analysis is valid only for simple types of 3D conformal beams and not necessarily valid for complex IMRT beamlets.

*The intersection point is approximately equal to the field edge and was not discussed in the above sentence for simplification and clarity. Technically speaking the term field edge in the above paragraph should be substituted for intersection point.

7.5 CONCLUSION

The theme of both extrapolation and deconvolution in the study is that both techniques are able to reduce the errors associated with finite detectors.

The extrapolation technique is superior if there is sufficient manpower, beam on time to collect the extra data needed, and the data processing skills to extrapolate profiles point-by-point. The time required for the technique for a full data set is not always clinically feasible as there is nearly always a tight deadline during beam commissioning volume. This technique may be reserved for a single set of data points relating to the most relevant field size and depth that is dependent on the clinical centre. The extrapolation technique allows verification of the technique internally with various methods relating to the linear fit.

The deconvolution method does not require more beam on time to collect extra profiles as one detector collection is sufficient. The data processing is complex and full automation of scripts was not possible due to possible artefacts in the Gaussian curve fit of the measured profiles. The programming of the semi-automatic deconvolution script also requires the use of FWHM of the detector kernels. The deconvolution halved the error in the penumbral estimation by the IC but did not change the PP and the DD penumbras. The use of the effective diameters as parameters for the FWHM of the detector kernels is a significant caveat in the deconvolution method used in this study.

Errors relating to the techniques are inherent in terms of an insufficient modelling of effective diameter and kernel FWHM over the required range of detectors and also over beam energy and field size. Detailed Monte Carlo simulations may be possible in the future as a means of detailed modelling of the effective diameter and kernel FWHM over a more exhaustive range of conditions. Due to the small detector diameter of the diamond detector parallel to the detector axis, both the extrapolation and the deconvolution techniques yielded corrected profiles with negligible difference to the

original profile. This study confirms the diamond detector as a suitable detector for small field dosimetry, as found by other researchers (Charland, El-khatib et al. 1998).

The diamond detector consistently showed penumbra closest to the ZE estimated penumbra widths.

The commonly used 0.125 cc ionization involves various perturbations in the measured profile from the zero detector size profile that depends on field size. A summary of all findings, with clinical implications, can be summarized in table 7.12. Note that for generalisation purposes, the IC has been selected as a representative of a *standard* detector, the PP as a *mini* detector, and the DD as a *micro* detector (see section 2.3.3 for definitions).

Table 7.11: Summary of the dose analysis with comments on the clinical implications over field sizes.

	Penumbra overestimate*	Clinical implications
Field sizes: 1×1 to 10×10 cm ²	Standard: +1.8 ±0.3 mm Mini: +1.1 ±0.6 mm Micro: -0.1 ±0.6 mm Field size overestimate	Modelling of source size affected
Field sizes: 1×1 cm ²	Standard: +0.75 ±0.15 mm Mini: +0.55 ±0.15 mm Micro: -0.1 ±0.10 mm	Reduced coverage of tumour volume if field size calibrated with radiation profile.
Field sizes: 2x2 to 10×10 cm ²	Standard: within ±0.2 mm Mini: within ±0.2 mm Micro: within ±0.2 mm Max. dose difference (point)	
Field sizes: 1×1 to 10×10 cm ²	Standard: +7.5 ±1.0% Mini: +3.6 ±0.6% Micro: +0.6 ±0.6% Summation of 1D dose	Correlates with intensity of hot spots in regions of profile relating to ~80% of dose.
Field sizes: Less than 2.3x2.3 cm ²	Standard: Max(overest.): +7.5% Max(underest.): -2.8% Max(overall): +4.4% Mini & Micro: not modelled	Max. (overest.) in regions outside of field edge (normal tissue) Max. (underest.) in regions inside of field edge (normal tissue)
Field sizes: More than 2.3x2.3 cm ²	Standard: Max(overest.): +0.8% Max(underest.): -1.5% Max(overall): -0.7% Mini & Micro: not modelled	Max. (overall) involves effect of detector in changing the overall risk of secondary cancer in the patient

There is a possibility to manually subtract the expected overestimation over the measured data to get an approximation of the ZE penumbra. With such a procedure, the

user will have to accept the uncertainties of the penumbra variation over depth and field size (and also jaw and MLC and machine variations). However, a non-linear penumbral correction with detector volume was proposed and is discussed in chapter 8.

The effect of the detector on measurement parameters such as field size and penumbral width are key clinical issues that are related to the under- and over- response of the detectors with relation to each other.

Issues involving the scope of the extrapolation method include:

- i. The measurement of at least three sets of data for each profile
- ii. Linearity of the method for detectors between 1.5 to 5.5 mm diameter
- iii. Code for extrapolation of each point with the dose and the known detector diameter

The extrapolation method was also evaluated with the R^2 fitting parameter, which as far as the author is aware, has not been quantitatively evaluated before. The findings include:

- i. That the R^2 varies from 0 to 1 with small dose differences but is important with this technique.
- ii. That the average R^2 values for significant dose differences (1%) are high (~0.95) for field sizes from 1×1 to 10×10 cm² but less desirable (~0.7) for a field size of 10×10 cm². This suggests that there are limitations to this technique in terms of field size.
- iii. A cost function was developed that combined the dose difference and the curve fitting parameter and was evaluated over the profile.

Recommendations to improve the quality of findings in this thesis could include:

- i. Rotation of the collimator to measure the profile with the diamond's small sensitive volume across the profile
- ii. Further modelling or measurement of the effective diameter of the detectors for more accurate deconvolution
- iii. Deconvolution of Inplane profiles where the longer side of the diamond detector was measured could be possible by using a different integer value of detector lengths in the deconvolution kernel.

The concept of geometric penumbra, dosimetric penumbra, and measured penumbra can be explored further. The geometric penumbra only takes into account attenuation and the effective source size. The dosimetric penumbra takes into account scattering in the collimator and the phantom/patient from the geometric penumbra. The measured penumbra takes into account the detector perturbation and the influence of the detector volume.

- i. If the lateral spread of electrons is known and the source size is accurately known, theoretical calculations of the dosimetric penumbra is also possible
- ii. The approach used here is to take the measured penumbra and then take away the effect of the detector volume. However, the effect of detector perturbation is not taken into account, and the effective diameters and FWHM of kernels are not measured extensively in the literature for all detectors used.
- iii. It is also noted that if the dosimetric profile can be accurately measured for small fields, this data would be ideal for source size modelling in the RTPS because small fields are particularly sensitive to the source size setting because of the lateral electron disequilibrium.

Note on future work on profile parameter investigation should include the following considerations:

- i. In the outer regions, the normalized dose converges to the same points (1.5 cm or more from the central axis, in other words, well away from the irradiated region of interest). From the central region to approximately 5 mm from the centre, larger chamber volume detectors have an under-response compared to smaller chamber volume detectors, while from approximately 5 mm from the centre to the outer region, larger chamber volume detector has a over-response when compared to smaller chamber volume detectors.
- ii. The amount of under-response and over-response of the IC can be analysed with the plot of the difference profiles, which involve the subtraction of small volume detector profiles with the IC profile. The amount of over-response corresponds to the maximum value in the difference profiles and, as discussed previously, is located in the central region of the profile. The amount of under-response corresponds to the minimum value in the difference profiles and is located in the penumbra region.
- iii. Results indicate that the 0.125 cc ionization chamber exhibits over- and under-response issues in the penumbra across all field sizes likely due to volume

averaging, and is not limited to *small field sizes*. This is because the penumbra remains with increasing field size –in fact penumbra increases with increasing field size. The large dose gradient in penumbras contributes to the importance of the detector volume on the profile shape measured. The amount of over- and under- response remains with larger field sizes however the region of these over- and under- responses becomes further and further away from the central axis.

- iv. Further analysis into the dependence of the over-estimation and under-estimation of the IC with field size was investigated at a depth of 10 cm. Compared to the diamond detector, the maximum overestimation by the IC was 5.5% and did not follow a clear trend with field size. The maximum underestimation by the IC was -7.0% at a field size of $1 \times 1 \text{ cm}^2$, which decreased and stabilised to a value of approximately -2% at a field size of 10×10 to $20 \times 20 \text{ cm}^2$.
- v. Compared to the pinpoint detector, the maximum overestimation by the IC was 3.1% at a field size of $2 \times 2 \text{ cm}^2$ with an overestimation of approximately 2% at all other field sizes. The maximum underestimation by the IC was -4.8% at a field size of $1 \times 1 \text{ cm}^2$, which also decreased and stabilised to a value of approximately -2% at a field size of 10×10 to $20 \times 20 \text{ cm}^2$.

Chapter 8: A non-linear extrapolation equation using penumbra data to calculate virtual zero detector volume penumbras

Note: The virtual zero volume detector penumbra data from extrapolation (ZE) was used as the reference.

8.1 THEORY

Since individual dose points can be extrapolated with detector size, then the penumbra (which is an equation linking two dose points) can also be extrapolated with detector size. The linear relationship between penumbra and detector size needs to be quantified with respect to field size and depth. A method of correlating penumbra with respect to field size and depth is to plot the x-axis as penumbra –the measured penumbra consists of both the effects of field size and depth.

There exists a predictable pattern between an increase in penumbra due to detector volume and measured penumbra and this can be verified by plots. Figure 8.1 shows this relationship with an increase in penumbra with increasing field size (same colour) and with increasing depth (same symbol). The analysis in this case is done for both the MLC and Jaws (crossplane).

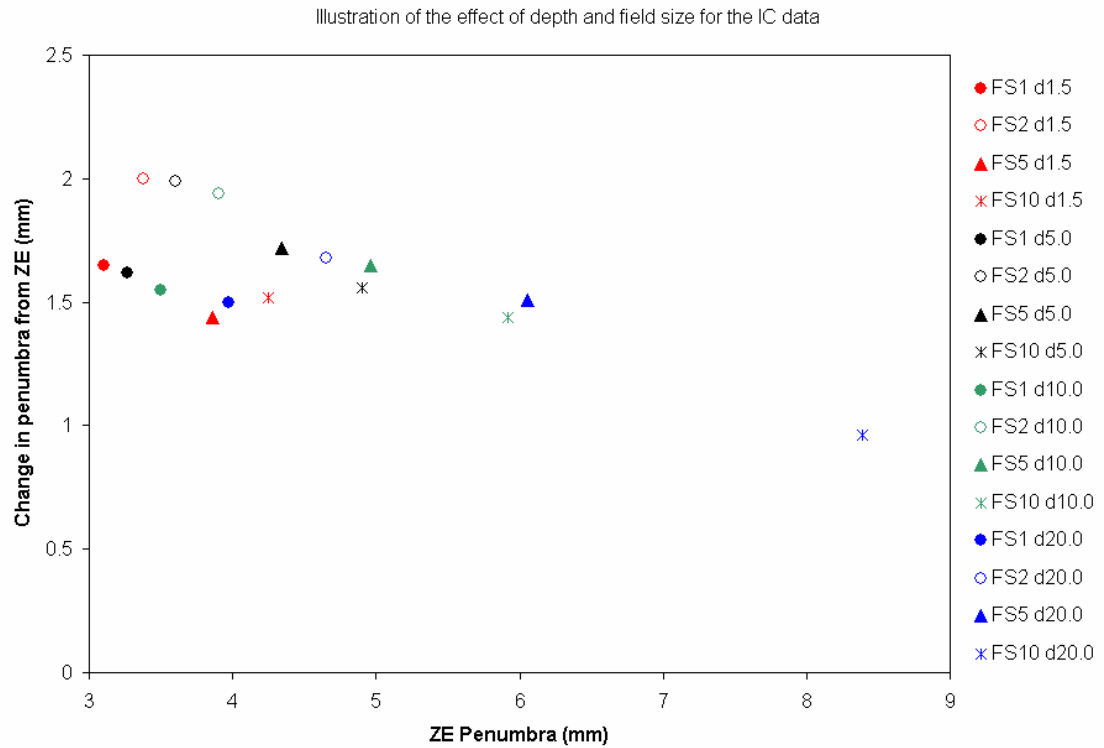


Figure 8.1: Figure illustrating a plot which includes both the effects of penumbral increase due to field size (illustrated with closed circles $1 \times 1 \text{ cm}^2$, open circles $2 \times 2 \text{ cm}^2$, triangles $5 \times 5 \text{ cm}^2$, and stars $10 \times 10 \text{ cm}^2$) and depth (illustrated with red for depth 1.5 cm, black for depth 5.0 cm, green for depth 10.0 cm, and blue for depth 20.0 cm).

In figure 8.1, for every unique combination of field size and depth, the ZE penumbra was used as the x-axis and the penumbral corresponding to the data was subtracted with the ZE penumbra (which is the change in penumbra from ZE) to calculate the y-axis.

The ZE penumbra increases with both field size and depth. In figure 8.2 the Jaw data is plotted while in figure 8.3 the dataset used involved MLCs.

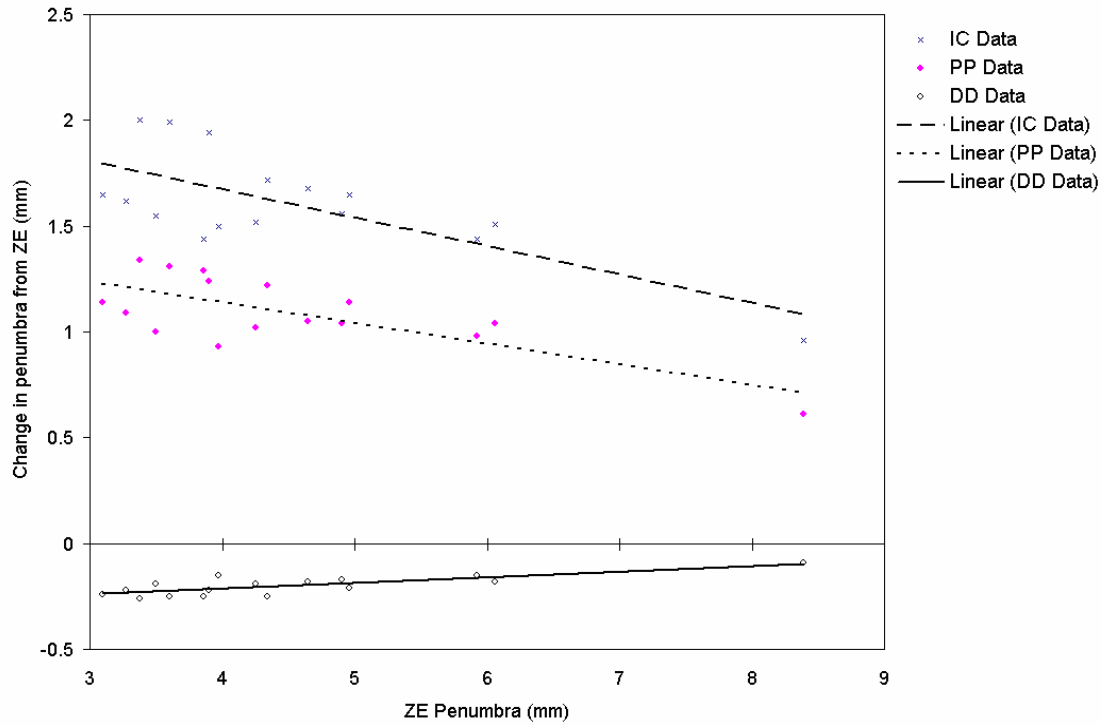


Figure 8.2: Plot showing the relationship between the change in penumbra size due to detector diameter and the measured ZE penumbra for the Jaw crossplane data

The relationship in penumbra between the IC, PP, and DD data sets is not constant with ZE penumbra (see figures 8.2 and 8.3). The gradients of the lines connecting the measured data sets are not parallel to each other implying a change in relationship between penumbra and detector volume with varying measured penumbras. A more complex model than linear relationship between the penumbra and detector volume will therefore be required for increased accuracy.

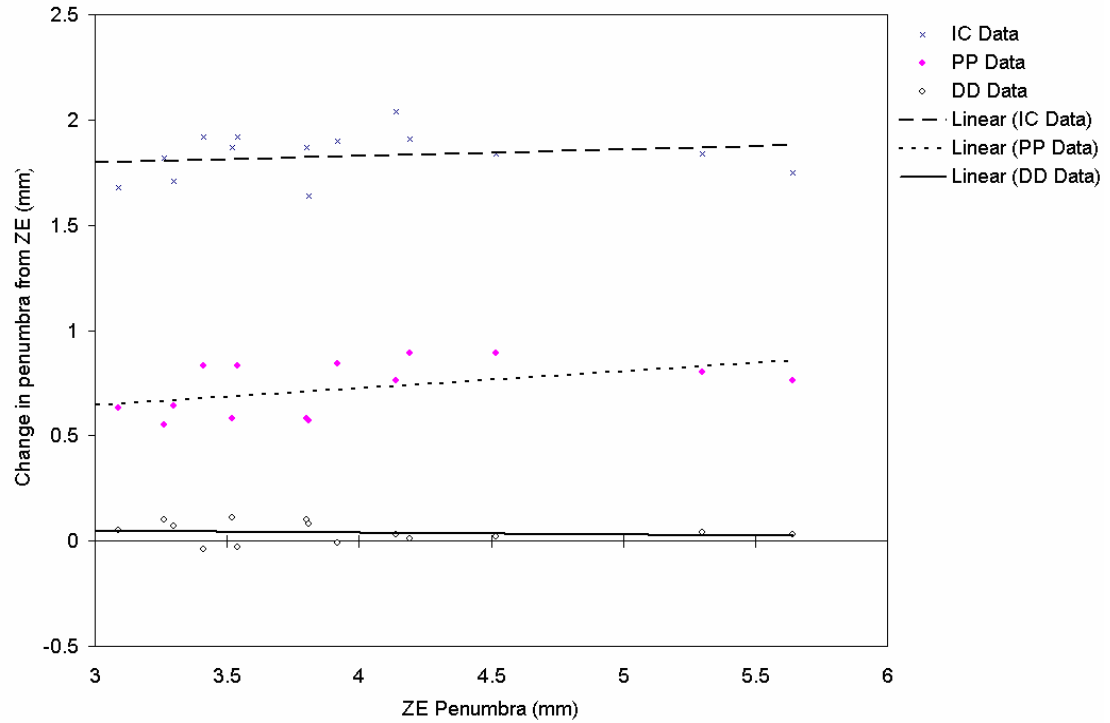


Figure 8.3 Plot showing the relationship between the change in penumbra size due to detector diameter and the measured ZE penumbra for the MLC crossplane

In figure 8.3, it was observed that the linear fit involved insignificant changes in changes in penumbra from ZE (y-axis) with ZE penumbra (x-axis). This correlation was factored into the model formulated (see equation 8.3).

8.2 METHOD

The first step involves the correlation of detector diameter with an increase in penumbra. To quantify this relationship, a linear fit of detector diameter and the increase in penumbra from the ZE penumbra is calculated (see fig. 5.3). The data points involve the ZE calculated penumbra (diameter 0 mm), DD penumbra (diameter 0.3 mm), PP penumbra (diameter, 2.0 mm), and IC penumbra (diameter 5.5 mm). The linear fit is forced to have a zero intercept as, by definition, the ZE penumbra is measured if the detector diameter is zero.

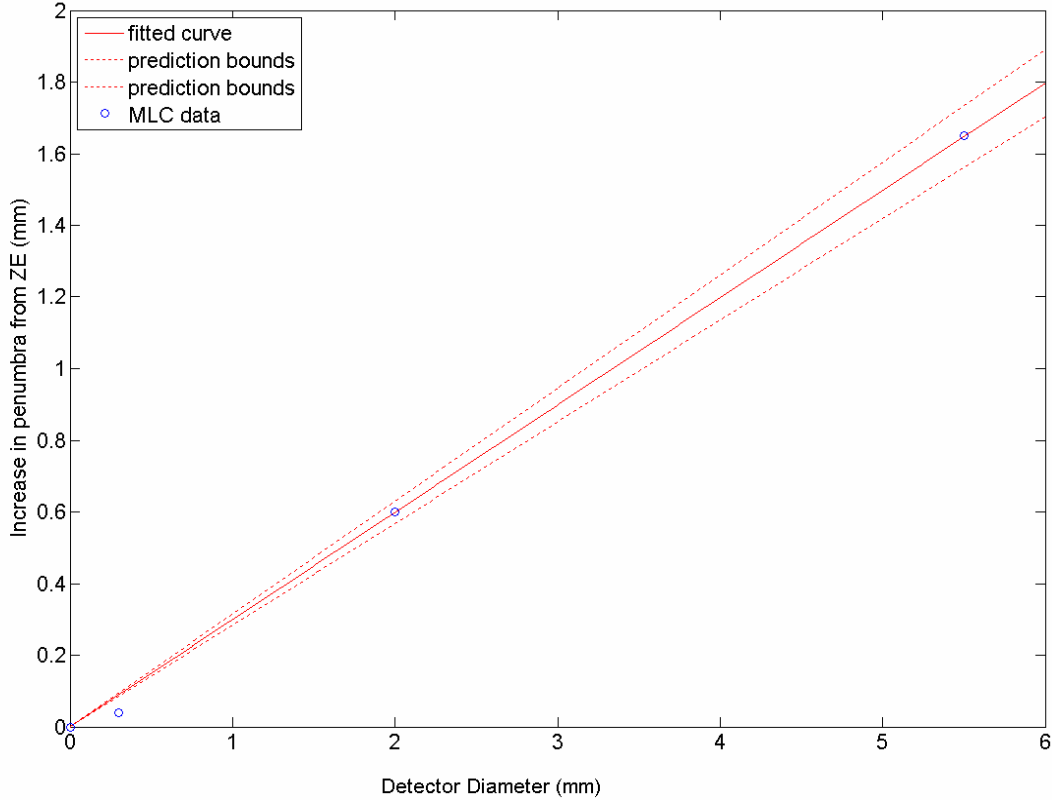


Figure 8.4: Diagram illustrating the correlation between the increase in measured penumbra from ZE penumbra with detector diameter (see equation 8.1)

The relationship can be expressed mathematically as

$$P_0 - P_{ze} = m_1 x_d . \quad (8.1)$$

where

- P_0 is the measured penumbra
- P_{ze} is the zero extrapolated penumbra
- $P_0 - P_{ze}$ is the increase in measured penumbra from ZE penumbra and is the y-axis in fig. 8.4.
- m_1 is the calculated penumbra-increase linear coefficient
- x_d is the detector diameter of the data point.

Each linear fit was performed for a single profile. The penumbra-increase linear coefficient, m_1 , was determined for each profile involving the combination of field sizes and depths available.

Since the dose gradient of a penumbra depends on the size of the penumbra, it can be induced that the penumbra-increase linear coefficient also depends on the size of the penumbra because the detector effect is based on the dose gradient. The penumbra-increase linear coefficient was plotted against the ZE penumbra.

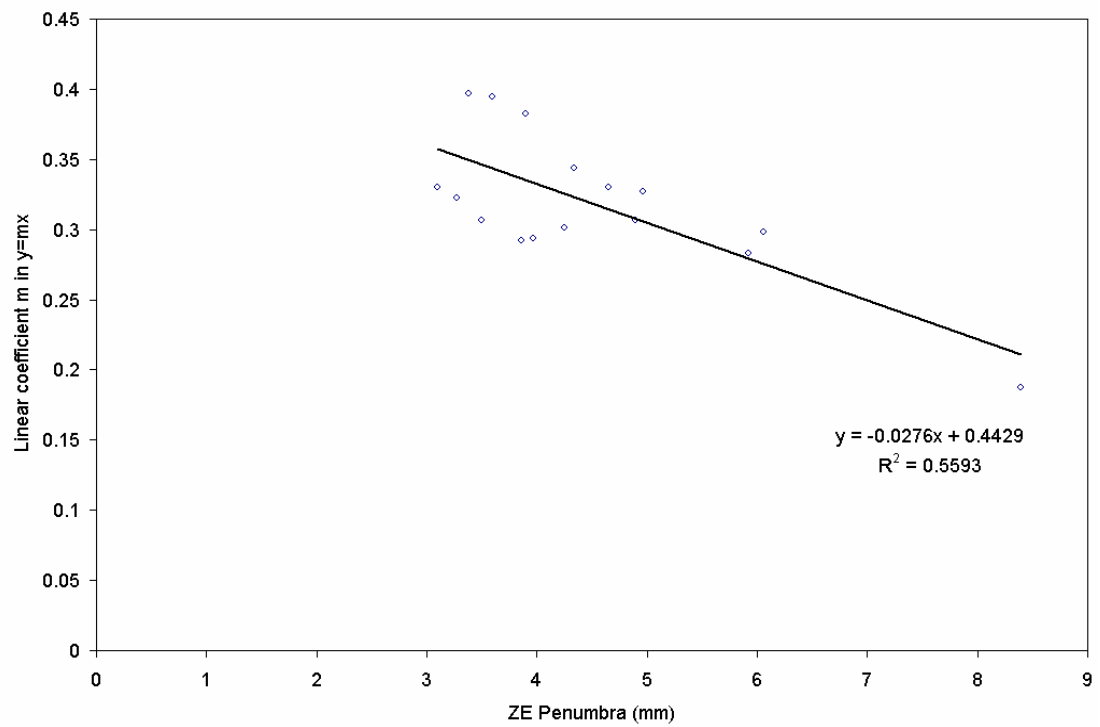


Figure 8.5: Plot of the relationship between the linear coefficient m1 and the ZE penumbra for the Jaw crossplane data

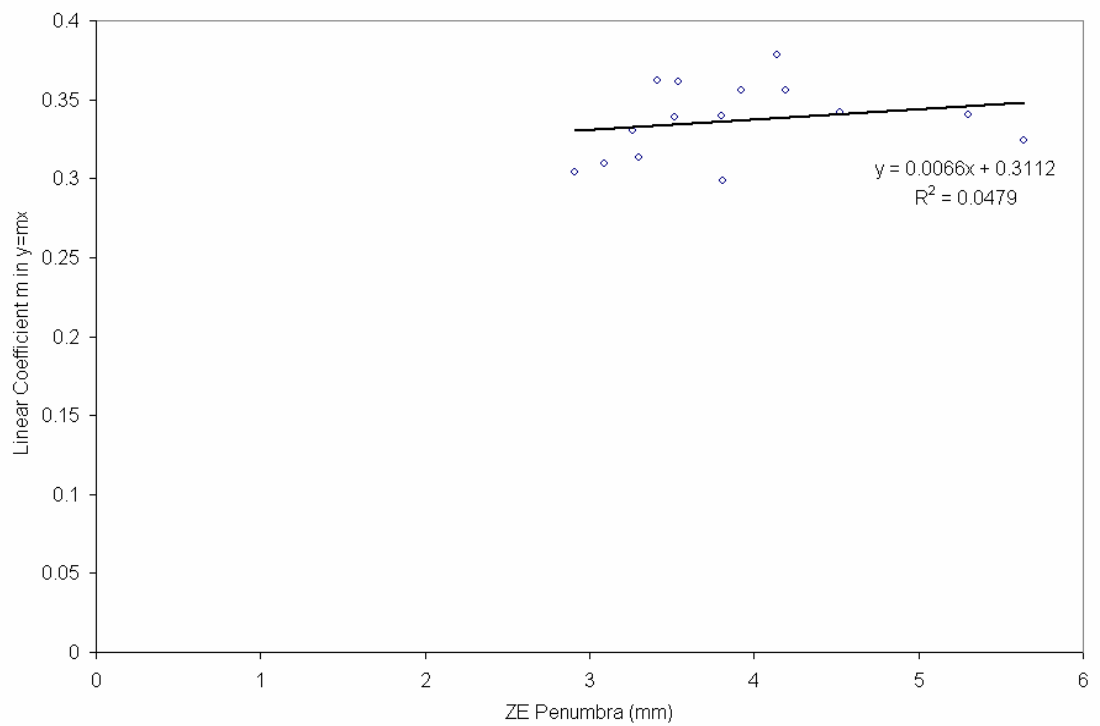


Figure 8.6: Plot of the relationship between the linear coefficient m1 and the ZE penumbra for the MLC crossplane data

A linear relationship was found for the Jaw data which indicated a change in linear coefficient with ZE penumbra (see fig. 8.5). The data suggests that for sharper penumbras, the effect of the detector effect is larger. However, the MLC data suggested a constant linear coefficient with ZE penumbra (see fig. 8.6). The effect of the detector volume is implied to be constant with various lateral scattering conditions for penumbras involved with rounded leaf edges.

A general linear relationship between the linear coefficient and the ZE penumbra is:

$$m_1 = m_2 P_{ze} + c \quad (8.2)$$

where

- m_1 is the calculated penumbra-increase linear coefficient
- m_2 is the calculated coefficient-increase linear coefficient
- c is the calculated coefficient-increase linear constant

Rearranging the equation to solve for the ZE penumbra gives the non-linear ZE equation penumbra:

$$\begin{aligned} P_0 - P_{ze} &= x_d (m_2 P_{ze} + c) \\ P_0 - P_{ze} &= x_d m_2 P_{ze} + x_d c \\ P_0 - x_d c &= P_{ze} (1 + x_d m_2) \cdot \\ P_{ze} &= \frac{P_0 - x_d c}{1 + x_d m_2} \end{aligned} \quad (8.3)$$

Note that the equation satisfies the requirement of.

$$as \ x_d \rightarrow 0, P_{ze} \rightarrow P_0. \quad (8.4)$$

The ZE penumbra is dependent on the measured penumbra and the detector diameter.

The linear coefficients are calculated from existing data (see table 8.1).

Table 8.1: Experimentally determined coefficients for the non-linear ZE penumbra equation

Jaw Data	
Calculated	$m_2 = -0.0276$
Parameters:	$c = 0.4429$
Equation for calculating the ZE penumbra:	$P_{ze} = \frac{P_0 - 0.4429x_d}{1 - 0.0276x_d} \quad (2.9)$
MLC Data	
Calculated	$m_2 = 0.0066$
Parameters:	$c = 0.3112$
Equation for calculating the ZE penumbra:	$P_{ze} = \frac{P_0 + 0.0066x_d}{1 + 0.3112x_d}$

The ZE penumbral equations for the Jaw and MLC data were simulated in excel (see fig. 5.6). Measured penumbra values of 2 mm, 4 mm, 6 mm, and 8 mm were combined with various detector diameters from 0 mm to 5.5 mm to calculate the expected ZE penumbra.

The x-axis of the plot in figure 5.6 is the detector diameter and the y-axis of the plot is the calculated non-linear ZE calculated penumbra. The line pairs represent Jaw data (continuous lines) and the MLC model (dashed lines). The four line pairs represent modelling of measured penumbra values by a detector.

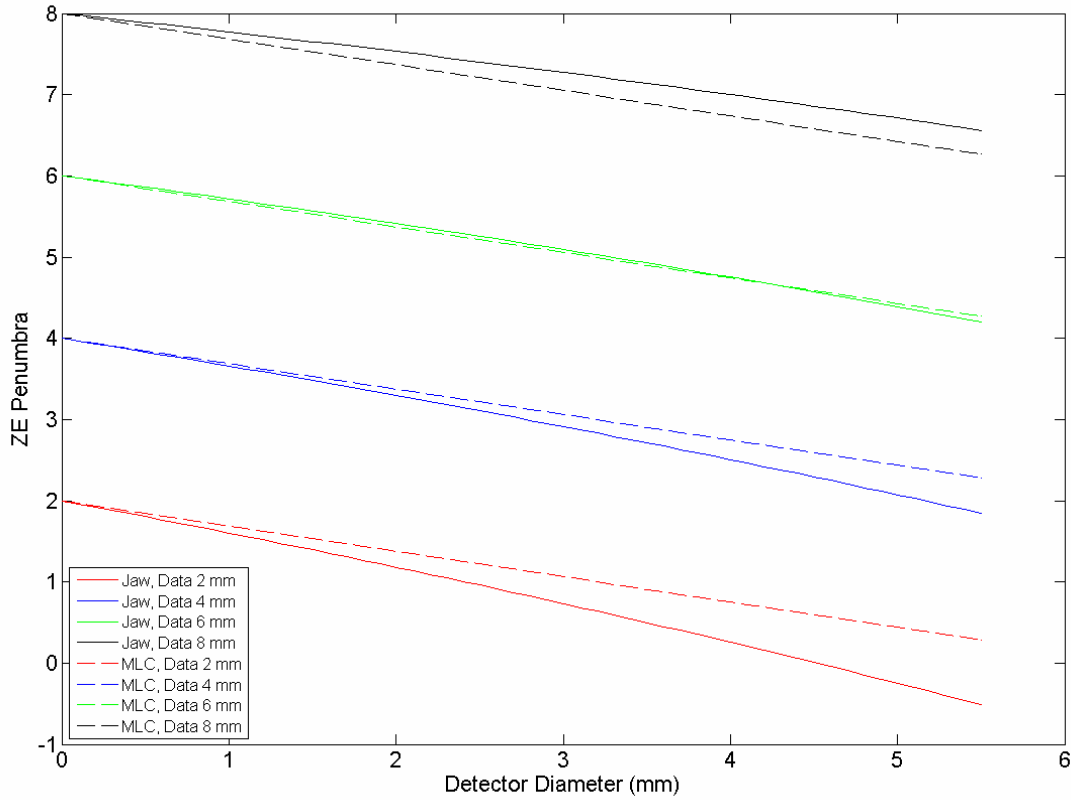


Figure 8.7: Plot of the simulated ZE penumbra calculated by the non-linear ZE penumbra equation for an arbitrary detector diameter

The calculated ZE penumbra is always lower than a measured penumbra with finite detector diameter. The relationship between detector diameter and ZE penumbra is different for Jaws and MLCs. This relationship is approximately linear for most cases except for a combination of larger detector diameters and small measured penumbras (large dose gradients).

8.3 RESULTS

For each measured profile, the detector diameter and the measured penumbra were used in the non-linear ZE penumbra equation to calculate the non-linear ZE calculated penumbra. In the plots, the measured penumbra is denoted IC, PP, and DD while the non-linear ZE (NLZE) calculated penumbra is denoted ICC, PPC, and DDC. A comparison can be made between the NLZE calculated penumbra's and the measured penumbras.

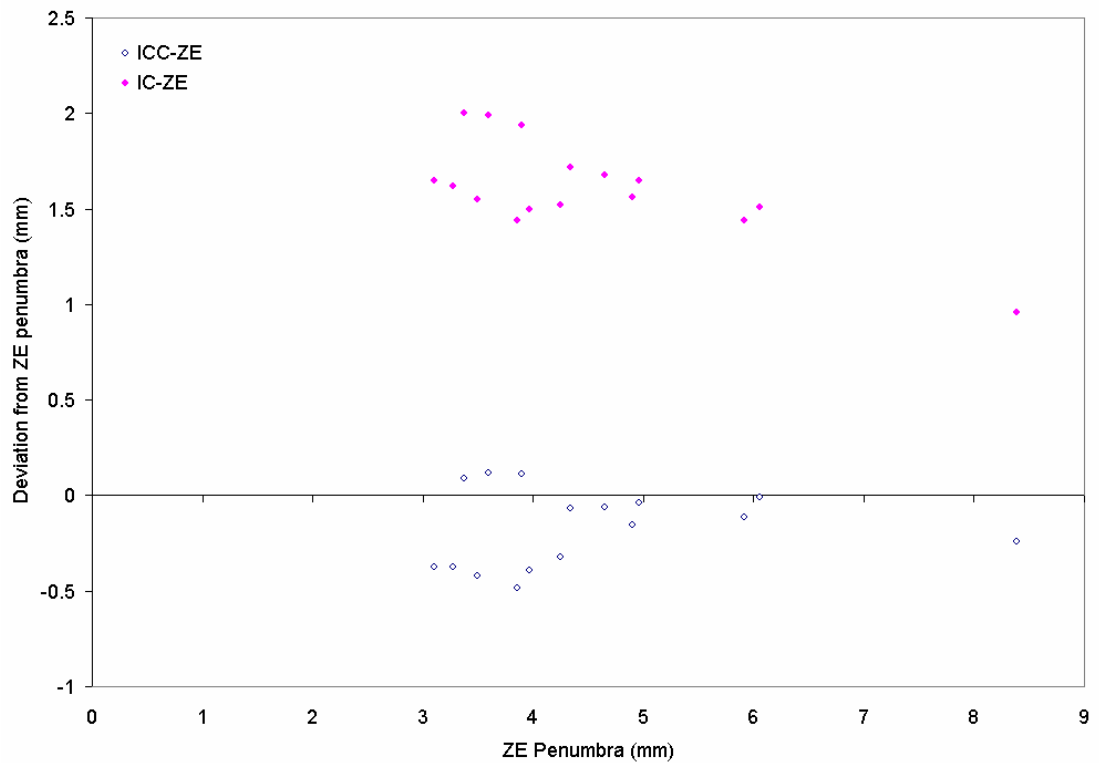


Figure 8.8: Plot showing the deviation from the ZE penumbra with the IC data with and without the correction made with the non-linear penumbra equation with the Jaw Crossplane data

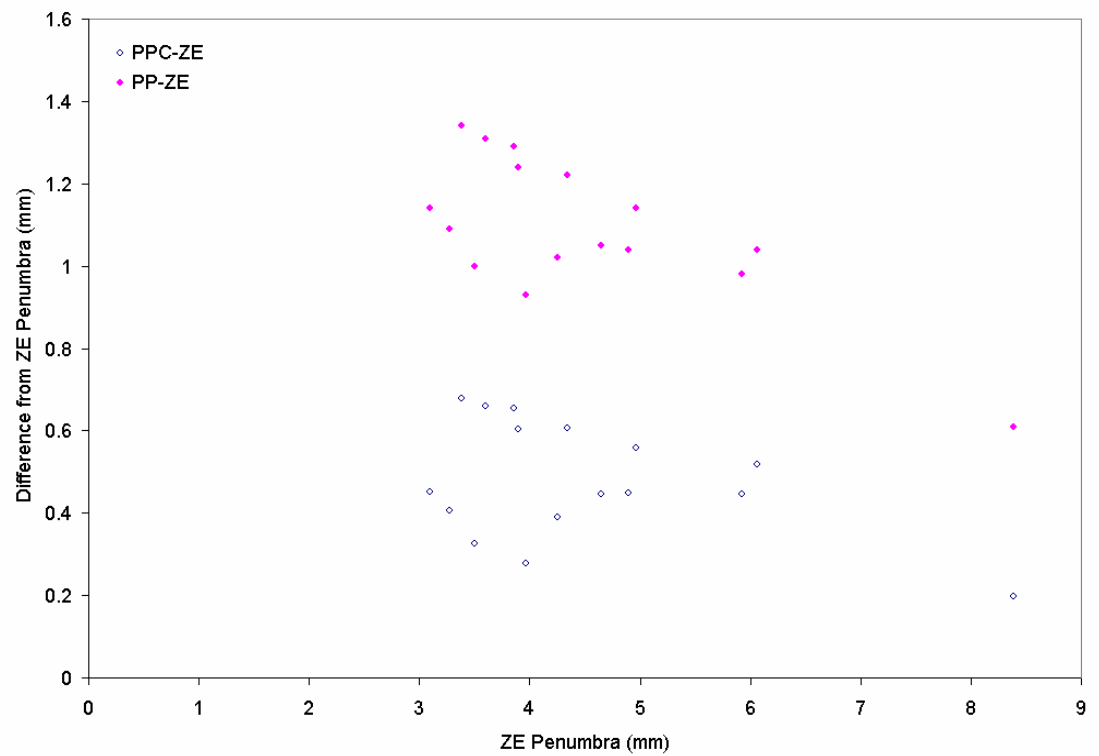


Figure 8.9: Plot showing the deviation from the ZE penumbra with the PP data with and without the correction made with the non-linear penumbra equation with the Jaw Crossplane data

In figures 8.7, 8.8, and 8.9, the Jaw data represented both changes in the penumbra due to field size and depth and were calculated with equation 8.5 (Jaw Crossplane data). In figures 8.7 and 8.8, it can be observed that the points correlating to the measured data corresponds to significant overestimation as well as a significant trend of overestimation with measured ZE penumbra. The application of the non-linear correction extrapolation equation, however, reduced both the overestimation as well as the trend of overestimation with measured ZE penumbra. The variation of values in the dataset, however, was not correctable with the non-linear correction.

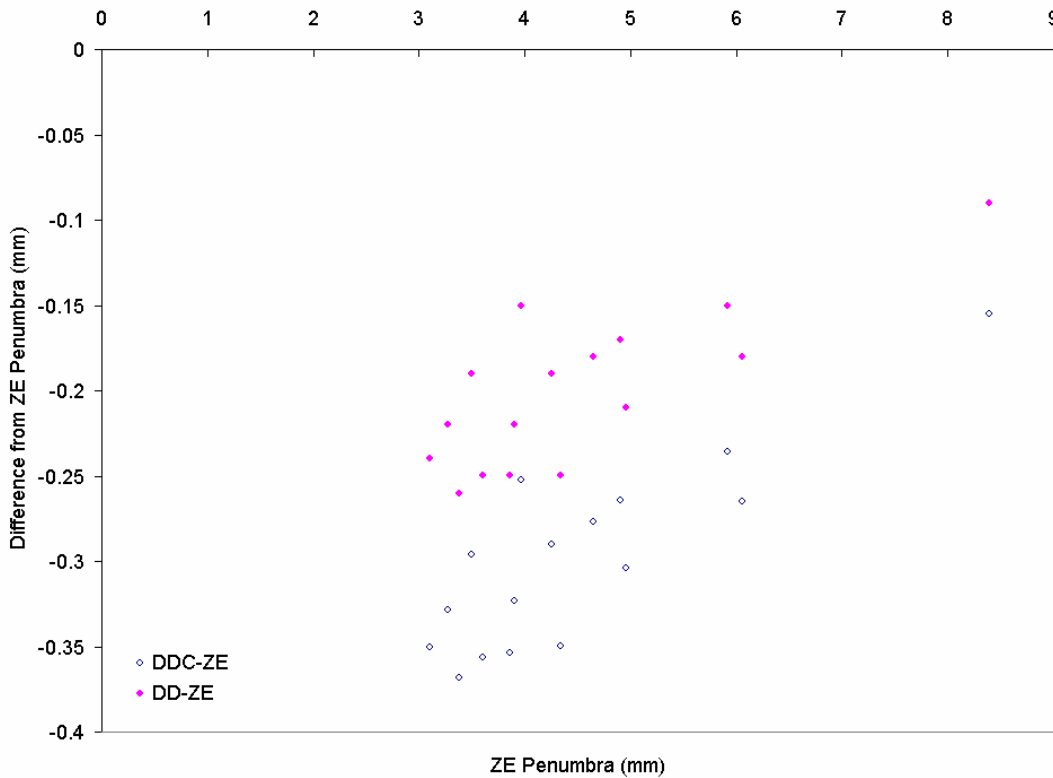


Figure 8.10: Plot showing the deviation from the ZE penumbra with the DD data with and without the correction made with the non-linear penumbra equation with the Jaw Crossplane data

Figure 8.10 shows that the non-linear correction applied to the DD increased the deviation from the ZE dataset, and worsened the dataset by approximately 0.1 mm (see table 8.3). Table 8.3 indicates that the non-linear corrected IC penumbra overestimation involved a -0.3 ± 0.3 mm deviation from the ZE penumbra cf. to the measured IC penumbra overestimation of $+1.5 \pm 0.5$ mm. The decrease in the variation in the data set is also observable in figure 8.8, where the non-linear corrected IC data is close to being parallel with the x-axis. There was a similar effect with the PP data in figure 8.8, where

the non-linear corrected PP penumbra overestimation was $+0.5 \pm 0.3$ mm as compared to the measured PP penumbra overestimation of $+1.0 \pm 0.4$ mm.

Table 8.2: Tabulated data showing a summary of the change in errors in terms of variation of penumbra from the ZE penumbra due to the application of the non-linear penumbra equation for the Jaw Crossplane data

Data	After		After		After	
	Measured	NLZE	Measured	NLZE	Measured	NLZE
	IC	Calc.	PP	Calc.	DD	Calc.
		IC		PP		DD
Field						
sizes: 1×1						
to 10×10	+1.0 mm	-0.5 mm	+0.6 mm	+0.2 mm	-0.1 mm	-0.2 mm
cm²	to	to	to	to	to	to
Depths:	+2.0 mm	+0.1 mm	+1.3 mm	+0.7 mm	-0.3 mm	-0.4 mm
1.5 to 20						
cm						
Average	+1.5 mm	-0.3 mm	+1.0 mm	+0.5 mm	-0.2 mm	-0.3 mm
and error	(± 0.5 mm)	(± 0.3 mm)	(± 0.4 mm)	(± 0.3 mm)	(± 0.1 mm)	(± 0.1 mm)

Similarly, in figures 8.11, 8.12, and 8.13, the MLC data represented both changes in the penumbra due to field size and depth and were calculated with equation 8.5 (Jaw Crossplane data). It was also observed that the points correlating to the measured data corresponded to significant overestimation but the trend of overestimation with measured ZE penumbra was not as clear. The application of the non-linear correction extrapolation equation reduced the overestimation but the trend of overestimation with measured ZE penumbra remained similar to the measured dataset (observed from a visual analysis of figures 8.11, 8.12, and 8.13). The variation of values in the dataset, however, was again not correctable with the non-linear correction.

Figure 8.13 shows that the non-linear correction applied to the DD dataset involved a negligible change from the measured dataset (see table 8.4). Table 8.4 indicates that the non-linear corrected IC penumbra overestimation involved a -0.1 ± 0.2 mm deviation from the ZE penumbra cf. to the measured IC penumbra overestimation of $+1.8 \pm 0.2$ mm. The variation in the data set of the non-linear corrected dataset was similar to the measured dataset which is observable both numerically (see table 8.4) and visually from figure 8.8. There was a similar effect with the PP data in figure 8.9, where

the non-linear corrected PP penumbra overestimation was $+0.2 \pm 0.2$ mm as compared to the measured PP penumbra overestimation of $+0.8 \pm 0.2$ mm.

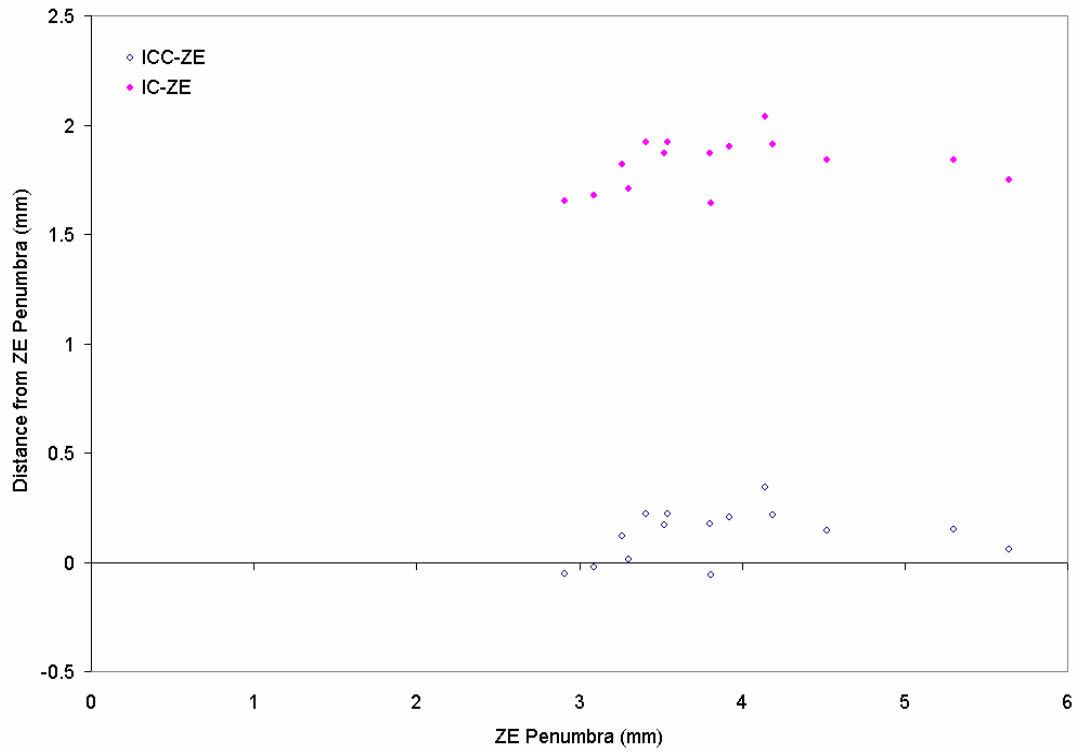


Figure 8.11: Plot showing the deviation from the ZE penumbra with the IC data with and without the correction made with the non-linear penumbra equation with the MLC Crossplane data

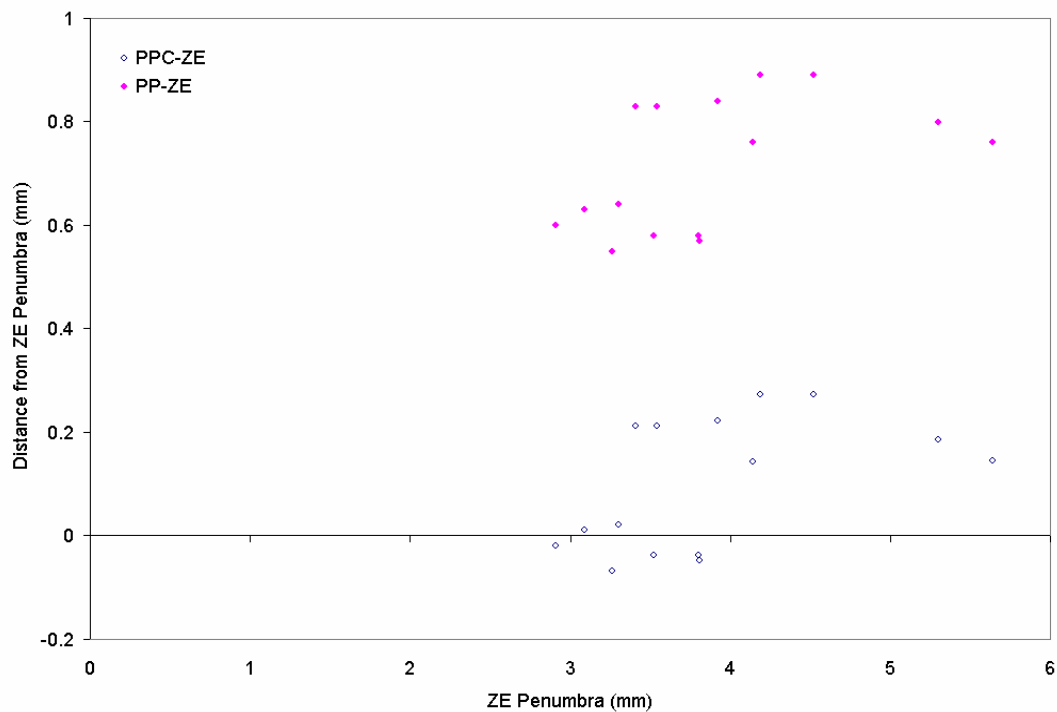


Figure 8.12: Plot showing the deviation from the ZE penumbra with the PP data with and without the correction made with the non-linear penumbra equation with the MLC Crossplane data

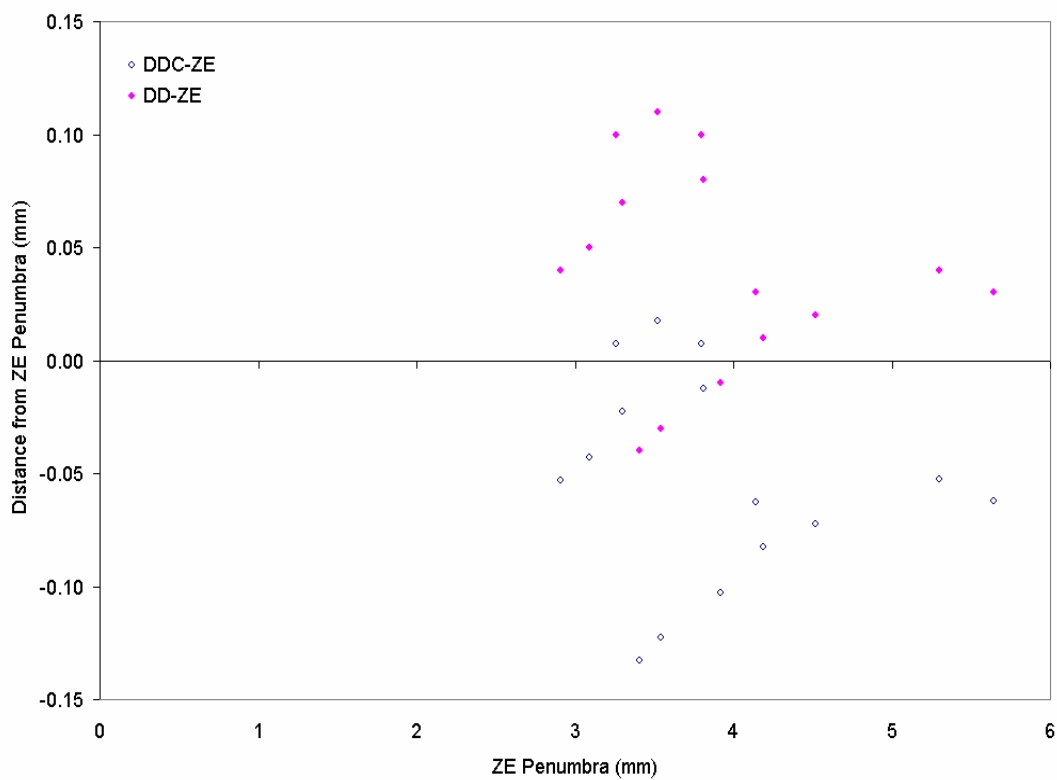


Figure 8.13: Plot showing the deviation from the ZE penumbra with the DD data with and without the correction made with the non-linear penumbra equation with the MLC Crossplane data

Table 8.3: Tabulated data showing a summary of the change in errors in terms of variation of penumbra from the ZE penumbra due to the application of the non-linear penumbra equation for the MLC Crossplane data

Data	After		After		After	
	Measured	NLZE	Measured	NLZE	Measured	NLZE
	IC	Calc. IC	PP	Calc. PP	DD	Calc. DD
Field						
sizes: 1×1						
to 10×10	+1.6 mm	-0.1 mm	+0.6 mm	-0.1 mm	-0.1 mm	-0.1 mm
cm²	to	to	to	to	to	to
Depths:	+2.0 mm	+0.3 mm	+0.9 mm	+0.3 mm	+0.1 mm	+0.1 mm
1.5 to 20						
cm						
Average	+1.8 mm	+0.1 mm	+0.8 mm	+0.2 mm	0.0 mm	0.0 mm
and error	(±0.2 mm)	(±0.2 mm)	(±0.2 mm)	(±0.2 mm)	(±0.1 mm)	(±0.1 mm)

8.4 DISCUSSION

The concept of the theory involves the following points:

- The non-linear penumbra equation is based on the premises of the linear extrapolation technique between the detector diameter and measured penumbral width (Laub and Wong 2003) as illustrated in figure 5.1. The validity of this technique was verified in Chapter 5 and was dependent on the authenticity of the detector diameter value used.
- The linear relationship, quantified with the linear coefficient between the detector diameter and the penumbral width, were observed to vary with field size and depth strongly for the Jaw data (see fig. 8.1) and weakly for the MLC data (see fig. 8.2). The physical reason for this involves the following hypothesis: the effect of the detector volume is dependent on the dose gradient and hence be a function of the true penumbral width (ZE penumbral width).
- The relationship between the coefficient of linear fit between the detector diameter and penumbra was found to vary with the ZE penumbral. The amount of variation of the coefficient of linear fit with ZE penumbra is linked to the coefficient m_2 (see equation 8.3). The value of m_2 for the Jaw was significantly

higher than that of the MLC (-0.0276 vs. 0.0006). A low value of m_2 indicates that the coefficient between detector diameter and the penumbral width is approximately linear (MLC data).

The validity of the theory involves the following points:

- i. The data in this study involved predominantly measured ZE penumbras of 3-6 mm (see fig. 8.1 for Jaws and fig. 8.2 for MLC data). Larger ranges of penumbras were studied (see fig. 5.13) with respect to deviation from the ZE (model) penumbra in the literature (van't.Veld, Lujik et al. 2001). The relationship between the measured penumbra width and the deviation of measured penumbra width from true penumbra width may approximate a linear function over a short range of data but figure 8.13 indicates a non-linearity in this relationship over a much larger range.

It is also noted that the relationship in fig. 8.13 involved measurement of penumbra with slits, which was not done in this study. The deviation in the relationship between the increase in penumbra and model penumbra also differed between the Jaw and the MLC, which indicates that the importance of the structure of the attenuating material in the measurement conditions in the relationship discussed. Therefore, the variables in equation 8.2 is not valid for arbitrary types of attenuating materials (e.g. Jaws and MLC).

Please see print copy for image

Figure 8.14: The effect of various IC15 line spread functions on the broadening of 20%-80% penumbra as modelled by the deconvolution model involving the Elliptic and Gaussian kernel function (van't.Veld, Lujik et al. 2001).

- ii. The confirmation of a set of non-linear penumbra equation coefficients over machine and attenuator type (but not field size and depth as the non-linear penumbra equation includes these two variables) will need to be determined. This will indicate how applicable this equation in a variety of circumstances.
- iii. Nevertheless, the penumbra range of 3-6 mm corresponding to clinical field sizes ($1 \times 1 \text{ cm}^2$ to $10 \times 10 \text{ cm}^2$) and depths (1.5 cm to 20 cm) and is valid for correction of penumbra in this range.
- iv. The non-linear penumbra equation was formulated and the ZE penumbra could be approximated by inputs of the measured penumbra and the detector diameter. The coefficients of the non-linear penumbra varied between the MLC crossplane data and the Jaw crossplane data. As shown in fig. 8.6, the correction involved with the non-linear penumbra equation involves a curvature that is dependent on the penumbra measured.
- v. The error involved in the non-linear penumbra equation was estimated by the comparison of the corrected penumbra with the ZE penumbra for the Jaws (see figs. 5.7, 5.8, and 5.9) and the MLC (see figs. 5.10, 5.11, and 5.12). There was a significant improvement of the penumbral estimation with the corrected non-

linear penumbras as compared to the measurement penumbras for both MLC and Jaw data.

8.4 CONCLUSIONS

The potential benefits and limitations of this technique includes:

- i. In essence, the determination of the coefficients for the non-linear penumbra equation is the reason for the possibility of correcting for the penumbra based on detector diameter without the data collection required for the extrapolation technique. After determination of the parameters in equation 8.3, the zero volume detector penumbra can be calculated from equations such as 8.5 and 8.6.
- ii. The limitation of the non-linear correction technique is that the correction only applies for the penumbra. There is no information on the effect on field size and dose differences (discussed in chapter 7).
- iii. The potential for this equation is large due to the constraints of clinical radiotherapy centres in performing work in upgrading the accuracy of their treatment planning systems to correct for detector volume. Once the parameters are determined, the non-linear correction is a quick and easy process. The lack of manpower, expertise, or equipment is the main limiting factor and an experimentally verified equation capable of correcting for the measured penumbra with the detector diameter would be of use to many users.
- iv. The value of the penumbra is critical as it influences the source size parameter in the treatment planning system (discussed in chapter 9).
- v. If the increase in penumbra due to the detector effect is not strongly dependent on the ZE penumbra (as in the case of the MLCs), then the non-linear correction technique is unnecessary. However, in the determination of the parameters, the calculation of a value of m_2 close to zero in equation 8.4 also serves as a verification tool to check that the dependency is not there.

Notes on future work regarding this investigation would include:

- i. Only 6 MV penumbra data was analysed and further work will be required for 10 MV and 18 MV energies.
- ii. In addition, the MLC and Jaw should be reanalysed in terms of the inplane direction.
- iii. The non-linear penumbra correction can be checked with attenuating material of different properties (e.g. the Siemens double-focused MLC leaves).
- iv. A larger set of field size and depths would increase the range of conditions to which the parameters in the equations of the form of equation 8.3 are applicable. By covering a larger set of penumbras, the relationship between the increase in penumbra due to the detector effect and the ZE penumbra will be further clarified.
- v. A sizeable amount of beam on time would be required to collect profiles for various detectors in order to collect a sufficient amount of data for sufficient analysis. However, once the parameters in equation 8.4 are determined, future determinations of zero volume penumbral data obviously more efficient.

Chapter 9: The Pinnacle Source Size model with respect to the detector effect

9.1 INTRODUCTION

The data measured with the IC, PP, and the DD were entered into the Pinnacle treatment planning system. Beam modelling was performed on the IC data initially, until a satisfactory match was achieved between the model and the measured data.

Modification of variables was made in the beam energy spectra for the depth dose component, in the electron contamination for the build-up region, and in the source size, scatter source, and transmission for the out of field component.

This model was used as a base and was loaded with the data associated with the PP and the DD. The source size was considered as the predominant parameter that would need adjustment to match the model to the new ZE penumbral profile data. It was the only variable optimised with respect to the data measured with different detector volumes.

In addition, the effects of dose calculation grid size was also found to be an important factor in the use of the Pinnacle treatment planning system algorithm, which affected the analysed isodose curves significantly.

The source size in the Pinnacle treatment planning system (TPS) is a strong determinant of the penumbra of modelled profiles. Since it is known that the detector volume affects the measured penumbra, the detector volume has a relationship to the source size in the TPS. After the relationship between the source size and the penumbra was quantified, the penumbral values from the IC, PP, DD, and ZE data were correlated directly with the Pinnacle TPS source size.

9.2 METHOD

As mentioned in Chapter 3 methods, modelling was performed in Pinnacle to match the data as much as possible. In the Pinnacle RTPS, the source size was analysed with the modelled profiles in terms of penumbra.

The shape of the source size can be elliptical, which models linacs with bending magnets; or circular, which models linacs with no bending magnets (Zhu, Bjarnsgard et al. 1995). Simulation of linear accelerator profiles tend towards circular source size geometries which may contribute to the difference between measured and simulated data (Vlamynck, Palmans et al. 1999), as can simulation of profiles with elliptical geometries with a linac with no bending magnet. The source size was modelled to be a circular source size due to evidence indicating the linac (Varian 600c) as corresponding to circular source sizes (Jaffray, Battista et al. 1993).

Small increments of source size were input into the Pinnacle RTPS and the output in terms of modelled profiles were analysed for their profiles. The crossplane profiles were analysed for the penumbra by the interpolation of the 80% and 20% dose points from the modelled data in the physics model. This was repeated for a selection of field sizes and depths, with the variation of penumbra with FWHM source size illustrated in table 9.1.

9.3 RESULTS

Table 9.1: The variation of the Pinnacle Source size and the Pinnacle modelled penumbra in mm
Cell values are the Pinnacle model penumbra (mm)

FS (cm ²)	Depth (mm)	FWHM source size (cm)					
		0.04	0.08	0.12	0.16	0.2	0.24
1	15	2.85	3.13	3.35	3.74	4.18	4.56
1	50	3.14	3.35	3.73	4.12	4.59	5.06
1	100	3.14	3.27	3.66	4.12	4.64	5.16
1	200	3.16	3.53	4.04	4.38	5.13	5.71
2	15	3.10	3.45	3.90	4.40	4.92	5.42
2	50	3.08	3.54	3.99	4.44	5.05	5.62
2	100	3.33	3.51	4.12	4.63	5.27	5.86
2	200	3.47	3.81	4.24	4.76	5.43	6.09
5	15	3.41	3.59	3.97	4.43	5.06	5.65
5	50	3.65	4.00	4.51	5.01	5.51	6.13
5	100	3.96	4.17	4.75	5.35	5.94	6.64
5	200	4.27	4.86	5.37	6.07	6.72	7.40
10	15	3.38	3.77	4.23	4.71	5.25	5.83
10	50	3.75	4.23	4.75	5.28	5.81	6.54
10	100	4.31	4.76	5.43	6.02	6.69	7.42
10	200	4.35	6.17	6.90	7.69	8.40	9.34

Data analysis was performed with the data found in table 9.1 to search for an optimum formula that correlated source size and modelled penumbra. A polynomial fit was found to satisfy a high R^2 value and was applied for penumbra and source size (see figure 6.1) in order to calculate the source size when given a certain penumbra. A fit was calculated for penumbra versus source size for each field size and depth. Figure 6.1 illustrates the fit for two curves.

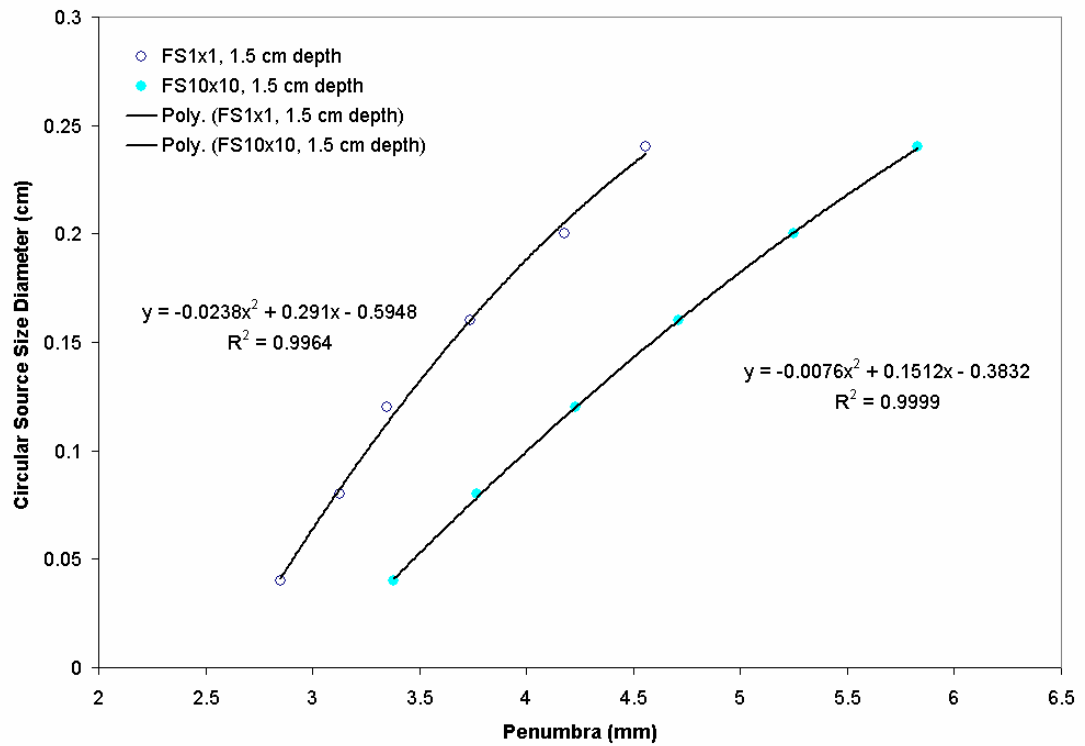


Figure 9.1: Plot illustrating the reliability of the relationship between the Pinnacle modelled penumbra and the Pinnacle source size.

Plots of penumbra versus source size indicated a solid relationship between the two variables. The relationship changed dependent on field size and depth. This was evident in the variation in coefficients for the polynomial curve form

$$y = ax^2 + bx + c \quad (9.1)$$

that satisfied the data points that were modelled. Tabulation was made of the source size and penumbra coefficients in table 9.2.

Table 9.2: Coefficients of the polynomial relationship between the Pinnacle source size and Pinnacle modelled penumbra at various field sizes and depths (for Jaw crossplane data)

Where Y is the source size in cm, x is the penumbra in mm, and a , b , c are coefficients fitted by the curve fit algorithm (see equation 9.1)

Field size (cm²)	Depth (mm)	a	b	c	r²
1	15	-0.0238	0.2910	-0.5948	0.9764
1	50	-0.0186	0.2525	-0.5644	0.9966
1	100	-0.0205	0.2616	-0.5680	0.9882
1	200	-0.0108	0.1731	-0.3982	0.9959
2	15	-0.0069	0.1432	-0.3349	0.9989
2	50	-0.0066	0.1361	-0.3177	0.9994
2	100	-0.0085	0.1518	-0.3612	0.9897
2	200	-0.0122	0.1911	-0.4733	0.9984
5	15	-0.0208	0.2724	-0.6377	0.9916
5	50	-0.0089	0.1649	-0.4641	0.9917
5	100	-0.0073	0.1512	-0.4120	0.9989
5	200	-0.0029	0.0975	-0.3235	0.9993
10	15	-0.0076	0.1512	-0.3832	0.9999
10	50	-0.0056	0.1300	-0.3696	0.9994
10	100	-0.0039	0.1091	-0.3556	0.9989
10	200	0.0039	-0.0117	0.0134	0.9911

The raw, measured penumbral measurements (with the IC, PP, and the DD) as well as the non-linear calculated penumbra (outlined in Chapter 6) were used in the equation 9.1 to calculate the Pinnacle RTPS modelled source size. Such a calculation was made for each combination of field size and depth.

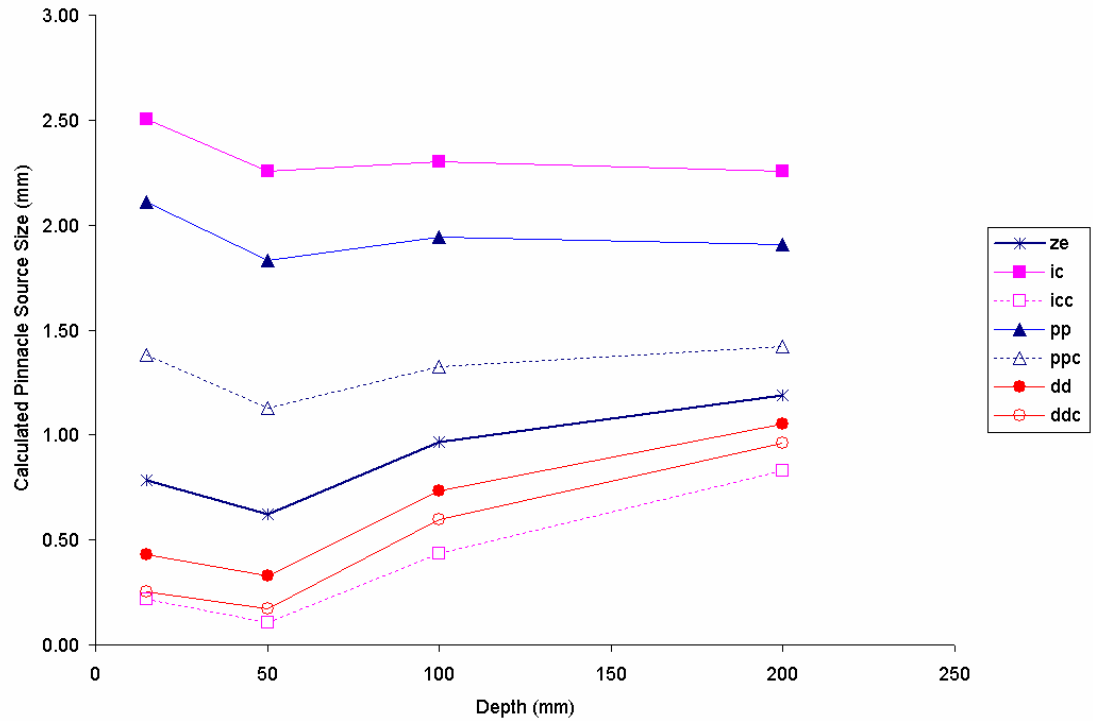


Figure 9.2: The calculated pinnacle source size (mm) with various datasets over depth at a field size of $1 \times 1 \text{ cm}^2$.

Figure 9.2 illustrates the results of the calculated source size from equation 9.1 with the parameters in table 9.2 at a field size of $1 \times 1 \text{ cm}^2$ with depth. For each combination of field size and depth required, the corresponding parameter in table 9.2 was combined with the corresponding penumbra of the data set (either measured or corrected for with the non-linear penumbra correction equation).

The results indicate (see table 9.3) that variations in the measured penumbra, which are affected by detector volume, strongly effect the modelled source size. In agreement with previous chapters on penumbra overestimation, the measured IC corresponded with the largest overestimation of the source size. The measured IC identified the source size as an average of 2.3 mm, while the PP with 2.0 mm, the DD with 0.6 mm, and the ZE at 0.9 mm. The non-linear penumbral correction, discussed in chapter 8, improved the measured results. The non-linear penumbra corrected IC data identified the source size as 0.4 mm, the corrected PP with 1.3 mm, and the corrected DD was slightly worse off at 0.5 mm.

Table 9.3: Averaged Pinnacle Source Sizes, variation of source size with depth, and deviation from the ZE source size for various datasets over depths at a field size of $1 \times 1 \text{ cm}^2$ (see figure 9.2)

Data	ZE	Measured IC	Non- lin. Corr. IC	Measured PP	Non- lin. Corr. PP	Measured DD	Non- lin. Corr. DD
Avg source size (mm)	0.9 mm	2.3 mm	0.4 mm	2.0 mm	1.3 mm	0.6 mm	0.5 mm
Variance in range	± 0.3 mm	± 0.1 mm	± 0.4 mm	± 0.1 mm	± 0.2 mm	± 0.4 mm	± 0.4 mm

Figure 9.3 illustrates the dependence of the RTPS source size with field size (at a depth of 1.5 cm). The variation in the calculated Pinnacle source size with field size at a depth of 1.5 cm was found to be similar to the variation of the source size with depth at a field size of $1 \times 1 \text{ cm}^2$. Note that while the parameters used for each combination of field size and depth are different (see table 9.2), the penumbra increases by only a slow function with field size at a depth of 1.5 cm (3.1 mm ZE penumbra at $1 \times 1 \text{ cm}^2$ vs. 4.3 mm ZE penumbra at $10 \times 10 \text{ cm}^2$).

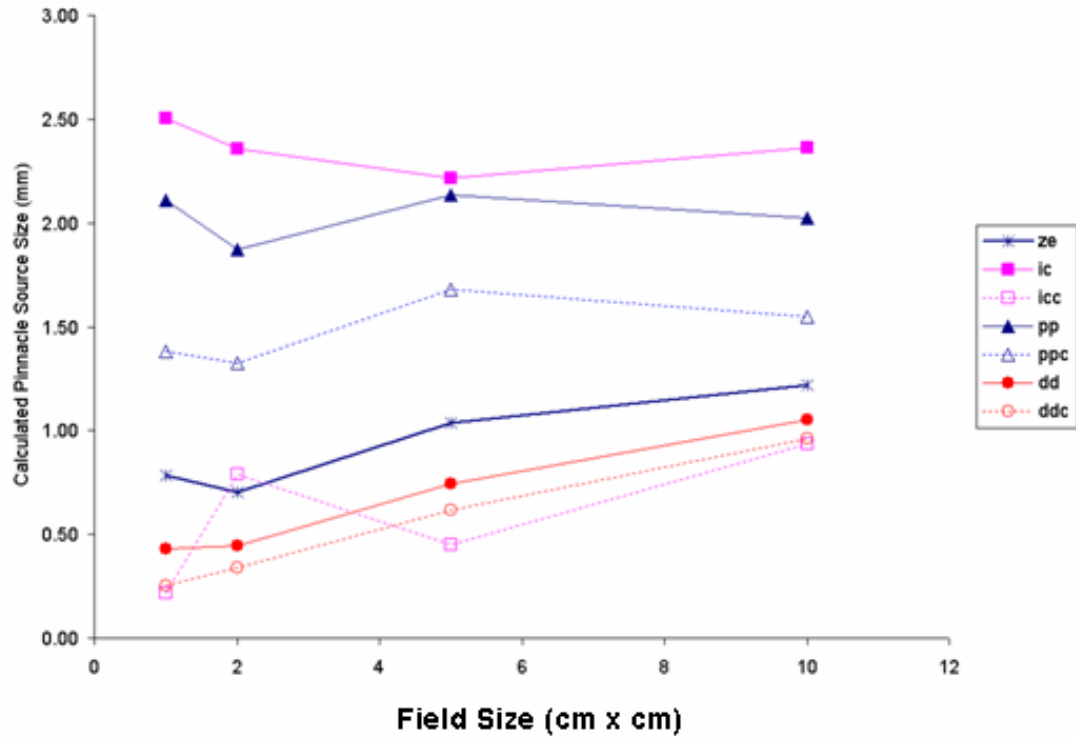


Figure 9.3: The calculated pinnacle source size (mm) with various datasets over various field sizes at a depth of 1.5 cm.

Table 9.4: Averaged Pinnacle Source Sizes, variation of source size with depth, and deviation from the ZE source size for various datasets over various field sizes at a depth of 1.5 cm (see figure 9.3)

Data	ZE	Measured IC	Non- lin. Corr. IC	Measured PP	Non- lin. Corr. PP	Measured DD	Non- lin. Corr. DD
Avg	0.9	2.4 mm	0.6 mm	2.0 mm	1.5 mm	0.7 mm	0.5 mm
source size (mm)	mm						
Variance	±0.3	±0.1 mm	±0.4	±0.1 mm	±0.7	±0.4 mm	±0.4
in range	mm		mm		mm		mm

The results in table 9.4 are similar to the ones in table 9.3. The measured IC identified the source size as an average of 2.4 mm, while the PP with 2.0 mm, the DD with 0.7 mm, and the ZE at 0.9 mm. The non-linear penumbra corrected IC data identified the source size as 0.6 mm, the corrected PP with 1.5 mm, and the corrected DD was 0.5 mm

which involved a larger difference when compared to the ZE than the measured DD data (0.7 mm).

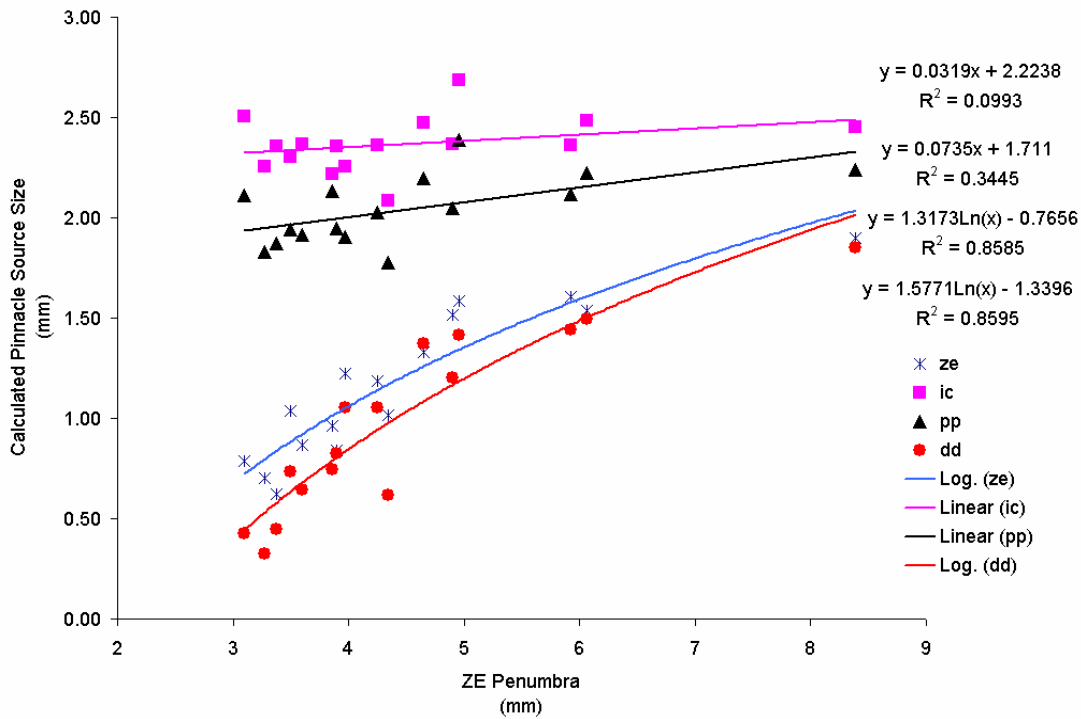


Figure 9.4: Figure illustrating the relationship between the ZE penumbra for the ZE and the measured detector dataset.

The combined analysis of all measured data was done by using the ZE penumbra as the x-axis (see fig. 9.4), which effectively included results corresponding to all combinations of field size and depth. It was observed that the largest penumbra increase was involved with a field size of $10 \times 10 \text{ cm}^2$ and a depth of 20 cm, where the ZE penumbra was measured at 8.4 mm (see the last data point in figure 9.4).

It can be observed in figure 9.4 that the measured IC and PP data involve curve fits that are nearly independent of ZE penumbra. The DD and the ZE, however, exhibit a non-linear dependence of source size with ZE penumbra. It was noted that the larger the detector the larger the source size and that the sublinearity of the extrapolation technique (discussed in Chapter 3) lead to an underestimation of the DD in terms of penumbra relative to the virtual zero detector volume data. Logarithmic functions were fitted to illustrate the trend of the data but the models were not analysed further in this study.

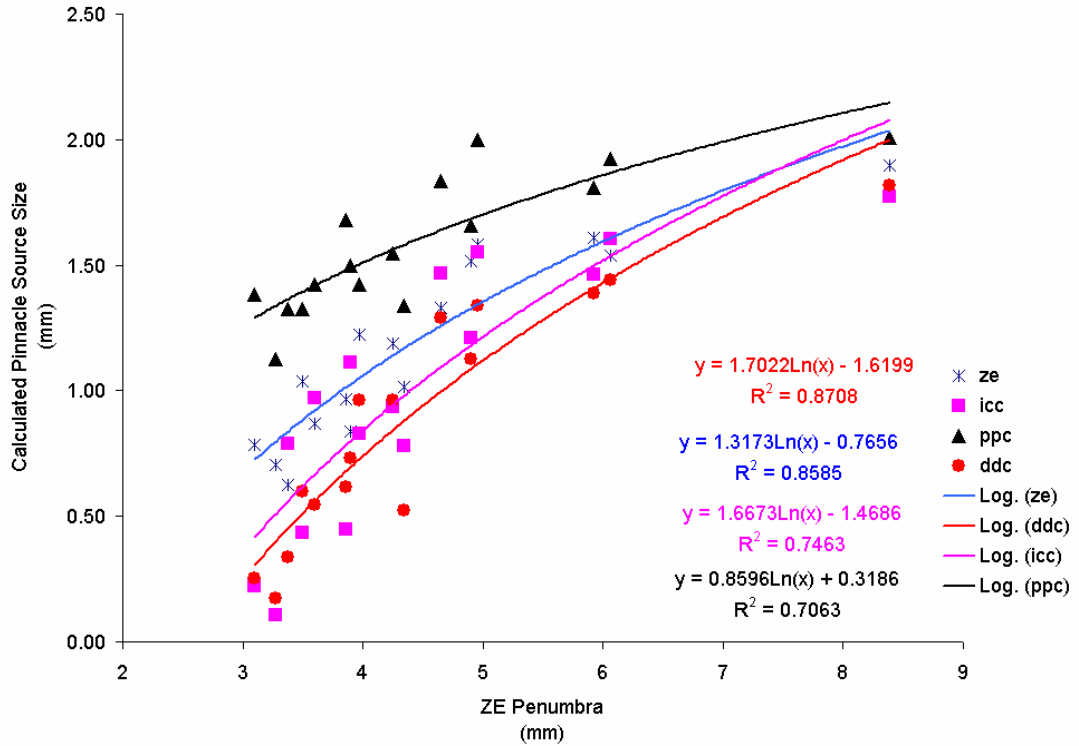


Figure 9.5: Figure illustrating the relationship between the ZE penumbra for the ZE and the non-linear penumbra corrected detector dataset.

Figure 9.5 follows the same procedure as figure 9.4 but the non-linear penumbra correction data was used instead of the original measured data for the IC, PP, and the DD datasets. It was observed that the corrected IC and PP datasets more closely matched the ZE data than the measured data. In addition, the corrected IC and PP datasets acquired the curve non-linearity of the ZE dataset as an effect of the non-linear penumbra correction.

It was noted that the corrected IC data, in figure 9.5, resulted in closer values to the ZE dataset than the DD dataset itself. This suggests that one of the applications of the non-linear penumbra correction involves its utility in modelling of the RTPS source size.

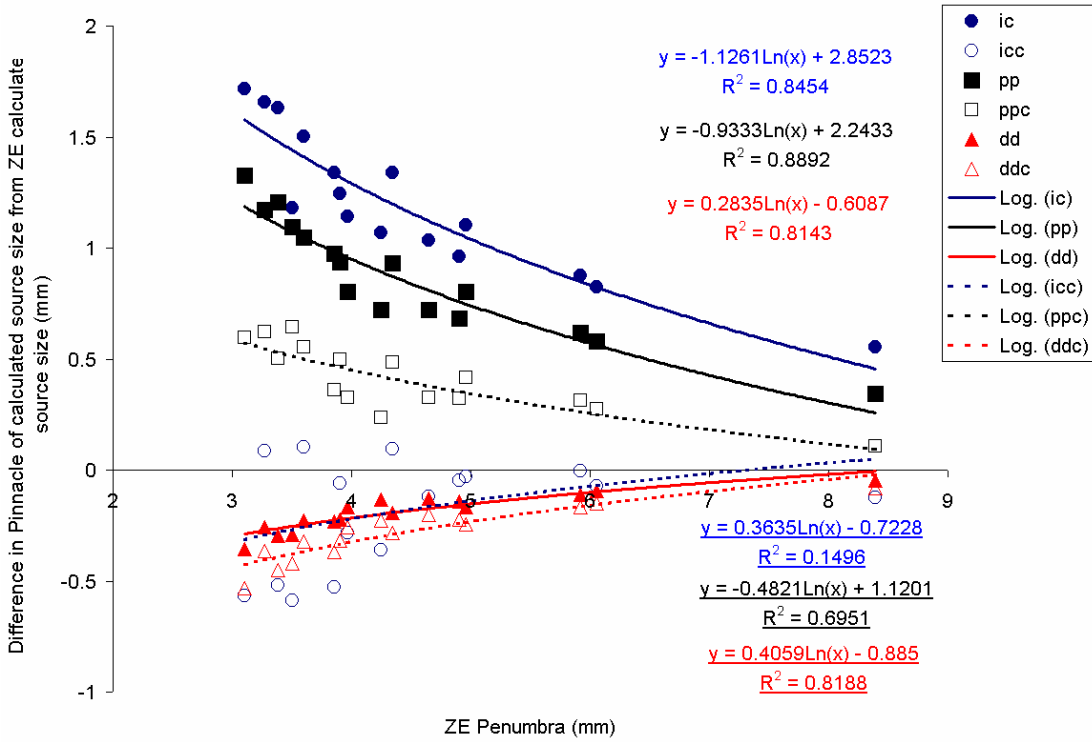


Figure 9.6: Figure showing the difference between the calculated Pinnacle source size using finite detectors and the ZE calculated Pinnacle source size modelled to match ZE penumbra profiles.

Figure 9.6 involved processing of the data in figures 9.4 and 9.5 with the following equation:

$$dS(data) = S(data) - S(ZE) \quad (2.11)$$

Where $dS(data)$ is the difference in Pinnacle of calculated source size $S(data)$ from the ZE calculated source size $S(ZE)$, which is the y-axis in figure 9.6. Equation 9.2 was applied for both the measured and the non-linear penumbra corrected datasets.

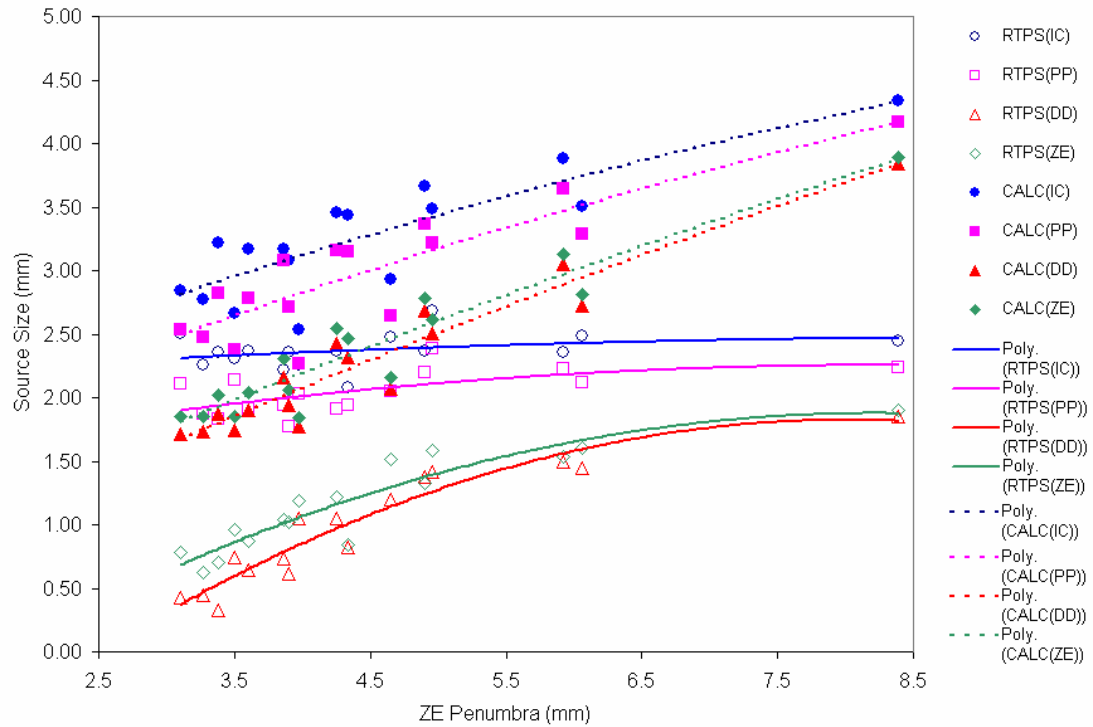


Figure 9.7: Comparison of calculated source size based on geometric penumbra and modelled source size based on RTPS model of penumbra

As an additional analysis, the source size calculation based on geometric penumbra (see equation 2.2 and the dotted line in figure 9.7) was also compared with the Pinnacle RTPS modelled source size with respect to measured data (solid lines in figure 9.4).

The source size calculation based on geometric penumbra overestimates the real source size. The equation correlates an increase in penumbra with an increase in source size linearly. There may be significant limitations for this calculation as it is based only on geometric penumbra (effective source size) whereas the measured penumbra includes the effects of radiological penumbra (lateral electron scatter) as well as the effects of detector volume and perturbation (see section 2.2.4).

The Pinnacle RTPS modelled source size involved polynomial functions, which fitted well with the data. This relationship, based on the composition of the Pinnacle RTPS code, illustrates a significant non-linearity of the penumbra with the optimum source size.

Ideally, the model of the RTPS should include variables that incorporate both the extra-focal and focal source contributions which vary with field size and depth in such a way that the source size parameter set is a constant over measured penumbras. It was observed that the IC data involved a minimal amount of variation in source size over the various penumbra values (based on field size and depth variations), which

could indicate that it was IC data which the Pinnacle RTPS was designed for (as this is the usual input data).

Another observation is that the Pinnacle RTPS shows more non-linearity for the DD and the ZE data, which suggests that the original Pinnacle RTPS code may have factored detector volume effects and detector perturbation effects into its source size modelling. Once the detector volume effect is reduced significantly, the Pinnacle RTPS treats the reduction in penumbra due to detector effects as genuine reduction in source size and reduces the optimal source size consequently.

Due to partial occlusion by the collimators of the extra-focal portion of the source, the x-ray source changes (Jaffray, Battista et al. 1993). Due to this, the calculated source size considered in this study was the source size calculated with the penumbra from $1 \times 1 \text{ cm}^2$ data. This is because Pinnacle models the source size and does not have a complete extrafocal multi-source model and because of the measurement of the source size can be more accurately measured with smaller field sizes (see table 9.5).

Table 9.5: Tabulated data showing the average difference from calculated source size with the ZE calculated source size over field size of $1 \times 1 \text{ cm}^2$ and depth 1.5 cm. The ZE source size was 0.9 mm.

Data	Measured IC	Non-lin. Corr. IC	Measured PP	Non-lin. Corr. PP	Measured DD	Non-lin. Corr. DD
Δ(source size) (mm)	+1.2	-0.2 mm	+1.0 mm	+0.3 mm	-0.2 mm	-0.3 mm
Variance in range	$\pm 0.6 \text{ mm}$	$\pm 0.3 \text{ mm}$	$\pm 0.5 \text{ mm}$	$\pm 0.3 \text{ mm}$	$\pm 0.2 \text{ mm}$	$\pm 0.2 \text{ mm}$

9.4 DISCUSSION

Comments on the methodology of correlating penumbra to source size

- The validity of the methodology of the derivation of the relationship between the penumbra was confirmed qualitatively by the close fits (see fig. 9.1) and the high R^2 values (table 9.2.). That a smaller source correlates with smaller penumbras is well documented theoretically and experimentally (Lydon 2005).
- The strong correlation between Pinnacle source size and penumbra created significant changes in the optimum source size in Pinnacle (see figure 9.1). The sensitivity of the source size to penumbral width increases the importance of correcting for, or accounting for, the detector effect in penumbral broadening.

- iii. This method is dependent on the structure of the model by the Pinnacle RTS. Factors that will influence this relationship include the modelling of the flattening filter (fluence and energy fluence away from the central axis), whether the extrafocal source is modelled or not (see fig. 9.8), and the lateral scattering calculated with the superposition and convolution algorithm that is dependent on the energy spectra of the beam.
- iv. In this study, the extrafocal source is not explicitly modelled in the Pinnacle RTPS and thus is a potential limitation. The current (2008) Pinnacle v0.8b does not implement the extrafocal component of the source and thus the modelling of the Pinnacle source size and the measured penumbra is an approximation limited by the Pinnacle model.
- v. Due to partial occlusion by the collimators of the extra-focal portion of the source, the x-ray source changes (Jaffray, Battista et al. 1993). It was also noted in the literature that to study the detector response in the primary x-ray beam, it is optimum to use a depth at dose maximum and to use small field size data, which is where the primary dose is the dominant contribution and provides the sharpest penumbra (van't.Veld, Lujik et al. 2001). In other words, with small fields a portion of the beam source is blocked from the detector (Das, Ding et al. 2007), namely the extrafocal region of the source size (at the edges). Due to this, the calculated source size considered in this study was the source size calculated with the penumbra from $1 \times 1 \text{ cm}^2$ data.

However, the choice of $1 \times 1 \text{ cm}^2$ source size to isolate the extrafocal component may not be the technique used by all, as some may choose to choose an intermediate source size value over field size to approximate the extrafocal component with an intermediate source size value.

- vi. The Pinnacle RTPS models the source size and not the extrafocal source and therefore the measurement of the source size can be more accurately measured with smaller field sizes. Results (table 9.5) indicate that, including the DD data, the non-linear penumbra correction (see chapter 8) of the measured IC, PP, and DD data was able to calculate the virtual zero detector volume source size (0.9 mm at $1 \times 1 \text{ cm}^2$) to within $\pm 0.3 \text{ mm}$.

Comments on the variation of penumbra to source size over field size and depth include:

- i. The calculated source size is also a function of source to collimator distance, source to surface distance, penumbra, and depth (Mould 1981; AAPM 2008).

The extrafocal component of the source size, first noted in 1993 (Jaffray, Battista et al. 1993), contributes to approximately 10% of the energy fluence and is dependent on field size (Sharpe, Miller et al. 2000).

- ii. The SCD, SSD, penumbra, and depth were taken into account in equation 2.2 and implemented in figure 9.7. In figure 9.7, the geometric penumbra equation calculated the source size (equation 2.2) and this was compared with the Pinnacle RTPS source size. Neither method considered the extrafocal component that was dependent on field size but the Pinnacle source size method involved scattering with the superposition/convolution method and therefore involved a smaller determined small size.
- iii. In comparing the Pinnacle RTPS source size to the source size calculated by the geometric penumbra equation (equation 2.2), the Pinnacle RTPS also more closely models the physical phenomena, which is observable in the smaller deviation in calculated source size with ZE penumbra (see figure 9.7).

9.5 CONCLUSIONS

Comparisons with other literature on source size compared to this study include”

- i. Although output factors are not considered in this study, it is noted that the output factors and the penumbra varies with field size (Munro, Rawlinson et al. 1988) due to the difference between having a focal source size and with the addition of the extrafocal source as well (Sharpe, Jaffray et al. 1995). The extrafocal component was measured with the data but was not modelled in this study.
- ii. In addition, as noted in Chapter 3, the output factor is not considered in this study.
- iii. It was noted that various RTPS cannot predict and account for penumbral degradation with an increase in field size (Patterson and Shragge 1981) due to the extrafocal component.
- iv. A 2x2 mm circular source size considered which was considered by researchers as a typical linac and a 0.1x0.1 mm considered the ideal source size (Topolnjak, Heide et al. 2007). For most linear accelerators, the source size is between approximately 1-2 mm (Sharpe, Jaffray et al. 1995).

In another study, measurements of the actual source size of linacs have been made by various authors. The source size was considered to be 0.2-0.3 cm

for a 6 MV beam (Dawson, Harper et al. 1984), with actual measurement of such a beam using pairs of tungsten copper blocks to create slits in a value of 0.15 cm for the FWHM of the source (Loewenthal and Loewinger 1992). With a CT reconstruction technique, the source size was measured to be 0.22 x 0.33 cm for a Therac 6 MV photon beam (Munro, Rawlinson et al. 1988), while using a technique involving thin sheets of lead sandwiched with cardboard found the source size to be 0.1 cm but for a 8 MV photon beam (Lutz, Maleki et al. 1988).

The results of the simulations in this study agree with predictions, with the ZE calculated source size at the low end the calculated source size range with ~0.8 mm and the IC calculated source size at the higher end with the calculated source size range of ~2.3 mm (see table 9.3).

The implications of this study can be summarised as follows:

- i. The Pinnacle RTPS source size parameter is sensitive to the penumbra and thus the detector effect on penumbra broadening has a significant effect on the source size.
- ii. It has been suggested in the literature (Topolnjak, Heide et al. 2007) that the characteristics of an ideal linac would involve a MLC leaf width of 2.5 mm, MLC transmission of 0%, and a source size of 0.1 mm. The real linac was evaluation with a real linac with MLC leaf width of 5 mm, MLC transmission of 0.75%, and a source size of 2 mm.
- iii. For radiotherapy treatments in the head and neck region, it was determined that increases in the MLC leaf width, MLC transmission, and source size increases the parotid dose. Also, by evaluating the effects of each individual component and also the effects of the combined components, it was found that the increase in dose to parotids from the real linac was smaller than the sum of the dose increase from each component but bigger than the square root of the sum of squared increases (Topolnjak, Heide et al. 2007).
- iv. Thus, the true clinical effect of source size variations needs to be weighed with the errors and limitations of MLC parameters such as the MLC leaf width and the MLC transmission.
- v. The correlation between detector diameter and penumbra (see Chapter 4-8) with the correlation between penumbra and source size (current chapter) enables the modelling of the likely effect of various detectors of different diameters (see table 9.6).

Table 9.6: Modelling of the sensitive diameter of PTW detectors with measured penumbra in column 3 (see equation 8.5) and the Pinnacle RTPS source size in column 4(see equation 9.1) at a field size of 1×1 cm² and depth 1.5 cm.

*Note: * Involved direct measurements and Δ Involved extrapolation of model*

PTW Detector	Sensitive diameter (mm)	Measured penumbra (mm)	Pinnacle RTPS source size (mm)
Diamond Detector Type 60003*	0.2	3.17	0.89
Dosimetry Diode P Type 60008^Δ	1.1	3.50	1.32
PinPoint Chambers Type 31014*	2.0	3.81	1.68
microLion Chamber Type 31018^Δ	2.5	3.99	1.87
0.1 cm3 Semiflex C Chamber Type 23322^Δ	3.3	4.26	2.13
0.3 cm3 Rigid Stem Chamber Type 31016^Δ	5.0	4.89	2.59
0.125 cm3 Semiflex Chamber Type 31010*	5.5	5.07	2.69
Farmer Chamber Type 30010^Δ	6.1	5.28	2.78
1.0 cm3 Rigid Stem Chamber Type 31015^Δ	7.9	5.92	2.94

Comments on future work on the relationship between source size and penumbra:

- i. The plots of the measured penumbra and the calculated source size revealed a pattern where large ZE penumbra corresponded to larger source sizes. It is currently unexplained why the IC and the PP exhibit measured source sizes independent on the measured field sizes. All other data sets, however, are well suited to a log fit (see fig. 9.5). It is currently insufficient data to make conclusive conclusions on this matter.
- ii. With respect to the effect on dose, the MLC transmission had the most dominant effect on dose when compared with source size and the MLC leaf width (Topolnjak, Heide et al. 2007). The source size predominantly changes the penumbral region, which is only a small portion of most clinical beams because most clinical beams are not of the order of $1 \times 1 \text{ cm}^2$, where the entire profile is composed of the penumbra. The effect of the source size can be compared with other errors of significant frequency and importance.
- iii. The same study can be implemented on other RTPS, especially ones where an extrafocal model is implemented (e.g. Monte Carlo based RTPS).

Comments on the source size determination techniques from a RTPS survey included as part of this study in 2008:

- i. With the source size being the primary parameter modified in this project, the issue of the dependence of the source size with machine, with the RTPS version, with the detector used to measure the data, and the beam energy was of interest.
- ii. 6 responses were recorded which amounted to a total of a 42 machines sample from survey data from Australia, Austria, Canada, the USA, the UK, and Spain. An email was sent to the Pinnacle email list asking for volunteer responses from radiotherapy centres to provide the machine model, beam energy, perpendicular source size, parallel source size, radiotherapy treatment planning model version, and the dosimeter used (see appendix H).
- iii. 46% of profile measurements were done with an ionisation chambers (IC10, IC15, IC13) over photon energies, while the remaining 54% using photon diodes. The average of parallel source size and perpendicular source size was considered as the main variable between these two groups.
- iv. The average source size used in the planning system for the linacs involved with the ionisation chamber was 1.66 mm while the average value for linacs involved with diodes was 0.47 mm. The trend towards overestimation of source size with

the IC of +1.19 mm is in agreement with the calculated overestimation in this study.

- v. This implies that there is a significant segment of the medical physics community that could implement a penumbral correction to improve the accuracy of their source size model in their RTPS.

vi.

Chapter 10: Effect of detector volume on isodose distributions

10.1 OVERVIEW

The detector effect on measured profiles was determined in chapter 4 and chapter 5 with both extrapolation and deconvolution techniques. In particular, the detector effect on penumbra, field size, and dose were investigated. In chapter 7, the effect of the source size parameter in the Pinnacle TPS was correlated with the modelled penumbra. The ZE penumbra was correlated with the optimum source size in Pinnacle. The change in source size relating to the detector effect is used to analyse the effect in isodose distributions in order to determine more accurately the clinical implications of the detector effect on radiation therapy dose distributions predicted by the computerised radiotherapy treatment planning system (RTPS).

The fundamental question was: would a ZE profile set alter the penumbra enough compared with an IC profile as indicated by isodose curves calculated from dose distributions.

10.2 METHOD

Modelling of the linac in Pinnacle with all parameters was initially performed (see Chapter 3). The creation of the modelled Pinnacle model with various source sizes was performed in Chapter 9. These machines were commissioned and used in the Pinnacle plans in this Chapter.

Four plans were used to highlight the effect of using the ZE profiles in the model to produce ZE isodose distributions. The plan 4FS1 (see table 7.1) involved two pairs of opposing fields (i.e. four field box) at gantry angles 0 and 180 and at 90 and 270 degrees with $1 \times 1 \text{ cm}^2$ fields. The isocentre was placed in the centre of a water phantom with a SAD setup. The plan 4FS10 (see table 7.3) was identical to plan 4FS1 but with field sizes set at $10 \times 10 \text{ cm}^2$. The plan 2FS1A (see table 7.2) involved two $1 \times 1 \text{ cm}^2$ fields that were adjacent to each other to form a $2 \times 1 \text{ cm}^2$ field when combined. Lastly, the plan 4 field box prostate plan (PROSTATE in table 7.4) involved clinical CT patient data with the use of MLC shaping as well. For each plan, the linacs of different source sizes were selected and used to calculate isodose distributions.

Table 10.1: Pinnacle parameters used in the plan 4 Field 1×1 cm² (4FS1)

<u>4FS1</u>	Image set:	Phantom		
	Beam 1	Beam 2	Beam 3	Beam 4
SAD (cm)	100.00	100.00	100.00	100.00
SSD (cm)	74.90	75.15	74.90	75.15
Gantry	0	180	90	270
Jaws	1×1	1×1	1×1	1×1
Beam	25	25	25	25
weighting (%)				
Points of Interest	Lateral (cm)	Ant-Post (cm)	Sup-Inf (cm)	Diameter (cm)
ISO	0	0	0	2.0

Table 10.2: Pinnacle parameters used in the plan 2 Field 1×1 cm² Abutted (2FSA)

<u>2FS1A</u>	Image set:	Phantom		
	Beam 1	Beam 2		
SAD (cm)	100.00	100.00		
SSD (cm)	74.90	74.90		
Gantry	0	0		
Jaws (L)	1.0	0		
Jaws (R)	0	1.0		
Jaws (T)	0.5	0.5		
Jaws (B)	0.5	0.5		
Beam	50	50		
weighting (%)				
Points of Interest	Lateral (cm)	Ant-Post (cm)	Sup-Inf (cm)	Diameter (cm)
ISO	0	0	0	2.0

Table 10.3: Pinnacle parameters used in the plan 4 Field 10×10 cm² (4FS10)

<u>4FS10</u>	Image set:	Phantom		
	Beam 1	Beam 2	Beam 3	Beam 4
SAD (cm)	100.00	100.00	100.00	100.00
SSD (cm)	74.90	75.15	74.90	75.15
Gantry	0	180	90	270
Jaws	10×10	10×10	10×10	10×10
Beam	25	25	25	25
weighting (%)				
Points of Interest	Lateral	Ant-Post	Sup-Inf	Diameter
	(cm)	(cm)	(cm)	(cm)
ISO	0	0	0	2.0

Table 10.4: Pinnacle parameters used in the plan PROSTATE

<u>PROSTATE</u>	Image set:	Patient CT		4 FIELD TREAT
	RAO	LAO	R Lateral	L Lateral
SAD (cm)	100.00	100.00	100.00	100.00
SSD (cm)	87.69	87.05	82.50	82.38
Gantry	315	45	270	90
Jaws (L)	3.0	3.5	2.7	3.0
Jaws (R)	3.5	3.4	3.0	2.7
Jaws (T)	3.5	3.5	3.5	3.5
Jaws (B)	4.0	4.0	4.0	4.0
Beam	15.11	16.31	27.34	27.82
weighting (%)				
Points of Interest	Lateral	Ant-Post	Sup-Inf	Diameter
	(cm)	(cm)	(cm)	(cm)
ISO	-0.31	2.11	-1.30	2.0

The isodoses were calculated in the Pinnacle plan for 4FS1 (see figure 10.1), 4FS10 (see figure 10.2), 2FS1A (see figure 10.3), and 4 field box prostate plan (see figure 10.4).

Note that the isodoses curves involve 98.0% as red, 80% as green, 60% as blue, 40% as yellow, and 20% as purple.

However, the dose grid was required to be exported into another format for dose difference analysis. Therefore, the planar dose utility was selected. This utility takes a user-coded planar dose point file and calculates the dose at each point. The user-coded planar dose point file contains the number of X points, the number of Y points, the spacing between points, and then the coordinates of the lateral, ant-post, and sup-inf for each point. After the dose plane maps were acquired for each beam, they were analysed in MATLAB. The 2 dimensional arrays of data were normalised before further analysis.

The CONTOUR function was used extensively to plot contours of combined fields (e.g. fig. 10.3), contour differences of single fields (e.g. fig. 10.2), and contour differences of combined fields (e.g. fig. 10.4). Profiles were also analysed across the ant-post direction across the isocentre plane (e.g. fig. 10.5).

10.3 RESULTS: PLAN 4FS1

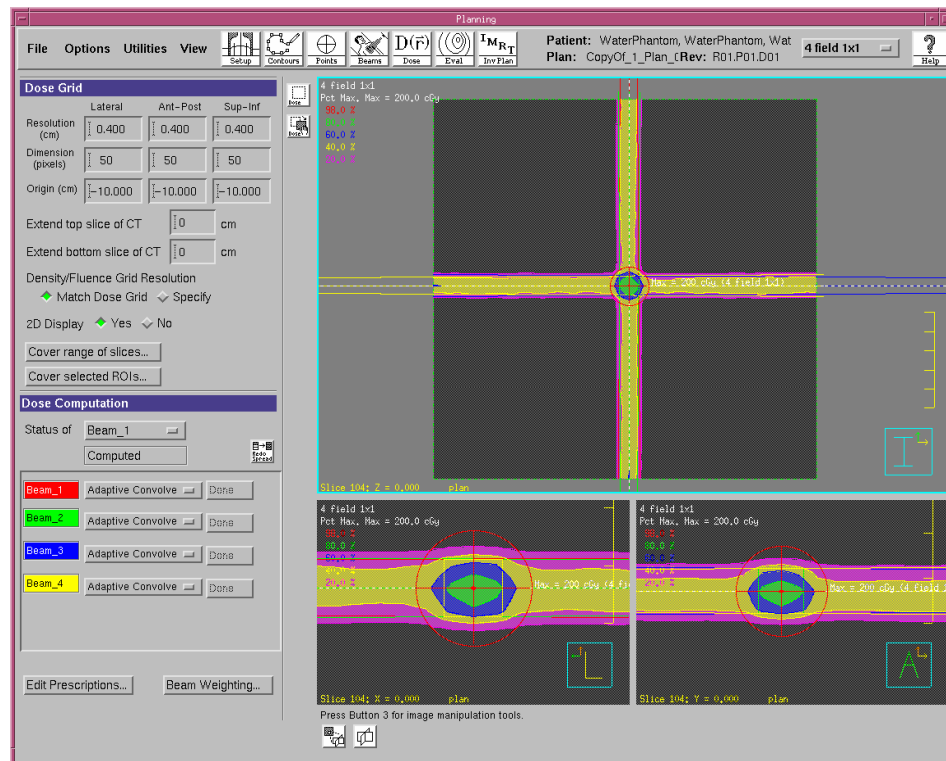


Figure 10.1: Pinnacle isodose distribution showing the beam geometry used in the plan 4FS1

Figure 10.1 shows a Pinnacle screen capture of plan 4FS1 (see table 10.1). There are four beams with field size $1 \times 1 \text{ cm}^2$ each. Each beam is at orthogonal angles to each other centred on a single point in the centre of a water phantom cube.

Figure 10.2 compares the contour map of a single $1 \times 1 \text{ cm}^2$ field with a 0.4 mm source (above in fig. 10.2) with a 2.4 mm source (below in fig. 10.2). The 0.4 mm source value (illustrative of the DD) was selected to maximise the contrast of the effect of the contour maps by the source size parameter. In figure 10.2, it can be observed that the ~ 0.7 values (orange) in the 0.4 mm data contour lines are larger than the 2.4 mm data contour lines while the ~ 0.2 values (blue) in the 2.4 mm are wider than the 0.4 mm data contour lines. The value of 2.4 mm was an approximate to the IC dataset and the value of 0.4 mm was an approximate to the lower ranges of the DD and the ZE dataset (see table 9.4).

The planar dose data extracted from the Pinnacle RTPS involved significant asymmetry that is highlighted in figure 10.3, which is the isodose difference plot for a single $1 \times 1 \text{ cm}^2$ field between a 2.4 mm model (illustrative of the IC data) and the 0.8 mm data (illustrative of the ZE data). It is hypothesised that the cause of the asymmetry is in the Pinnacle RTPS software due to the limited spatial resolution of the grid. The maximum value of the profile (in the central axis) must exist on a dose point in the dose grid, and has been forced to the left (shifted more for the 0.4 mm data).

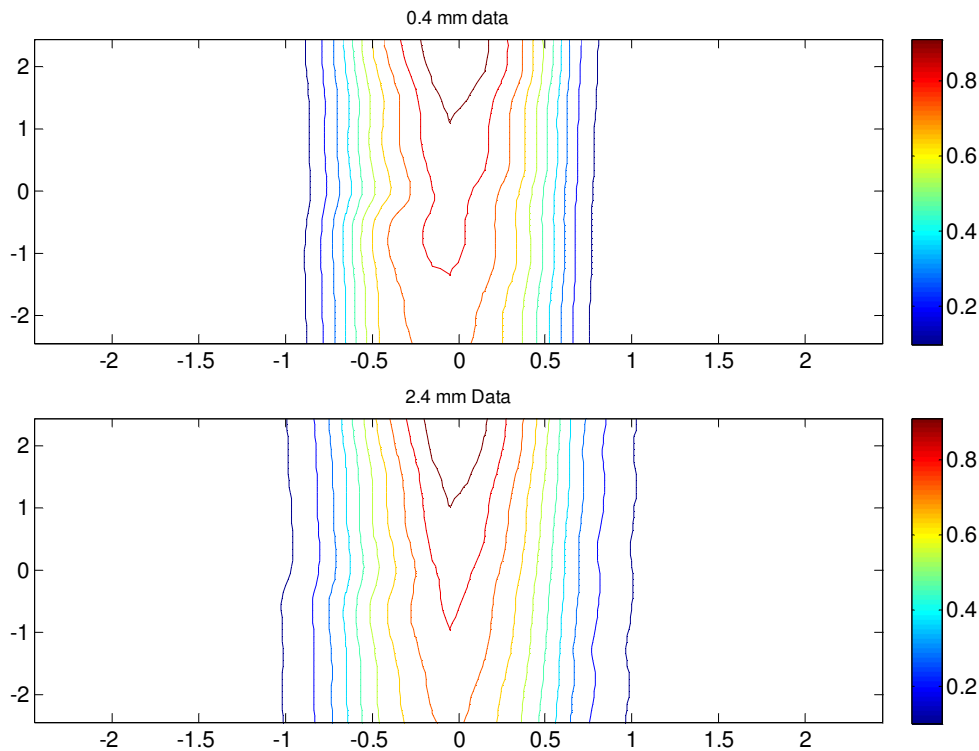


Figure 10.2: Plot showing the difference in isodose distribution for one $1 \times 1 \text{ cm}^2$ field between the 0.4 mm source size model (top) and the 2.4 mm source size model (bottom) used in the plan 4FS10

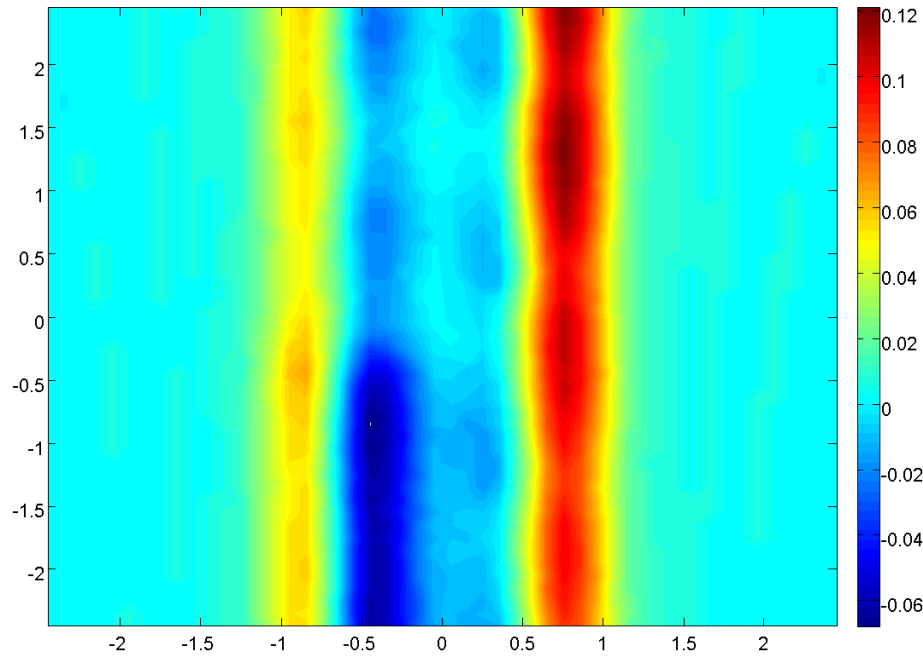


Figure 10.3 Plot showing the isodose difference plot for a single field (gantry 0), where each point was calculated by isodose point (2.4 mm model) minus isodose point (0.8 mm model)

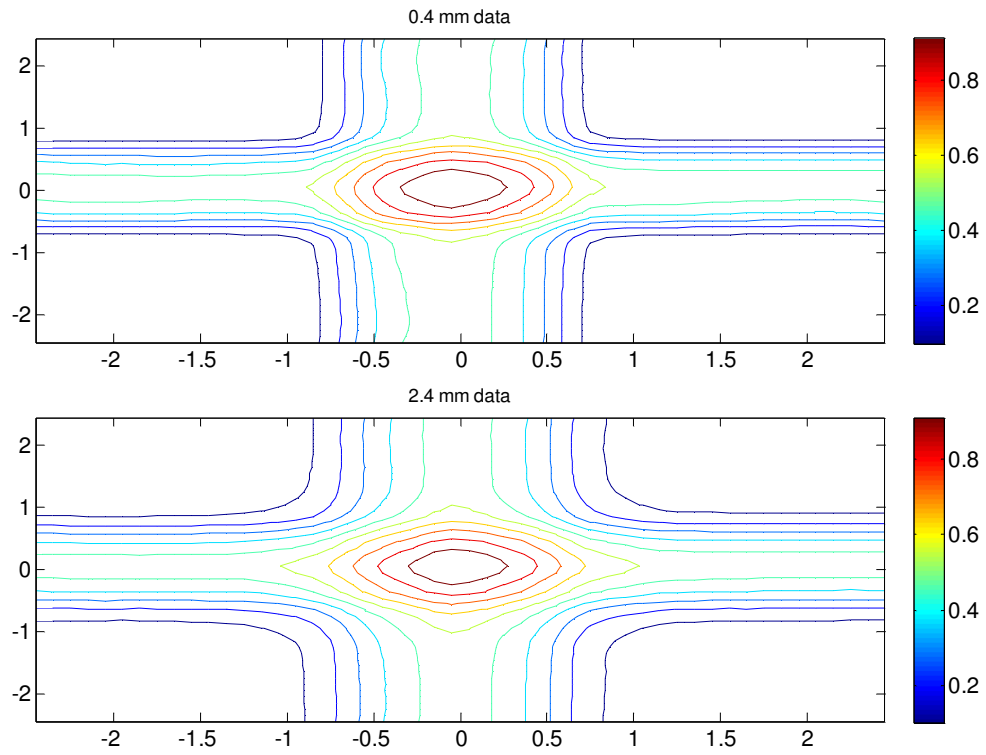


Figure 10.4: Plot showing the difference in isodose distribution for 4 \times 1 cm^2 fields between the 0.4 mm source size model (top) and the 2.4 mm source size model (bottom) used in the plan 4FS10

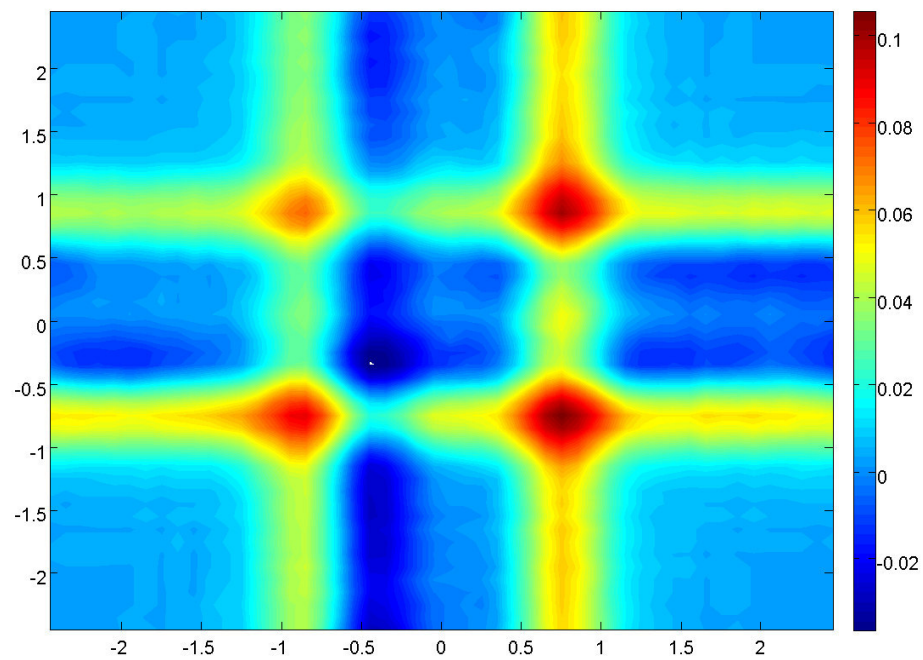


Figure 10.5: Plot showing the isodose difference plot for combined 4 fields, where each point was calculated by isodose point (2.4 mm model) minus isodose point (0.8 mm model)

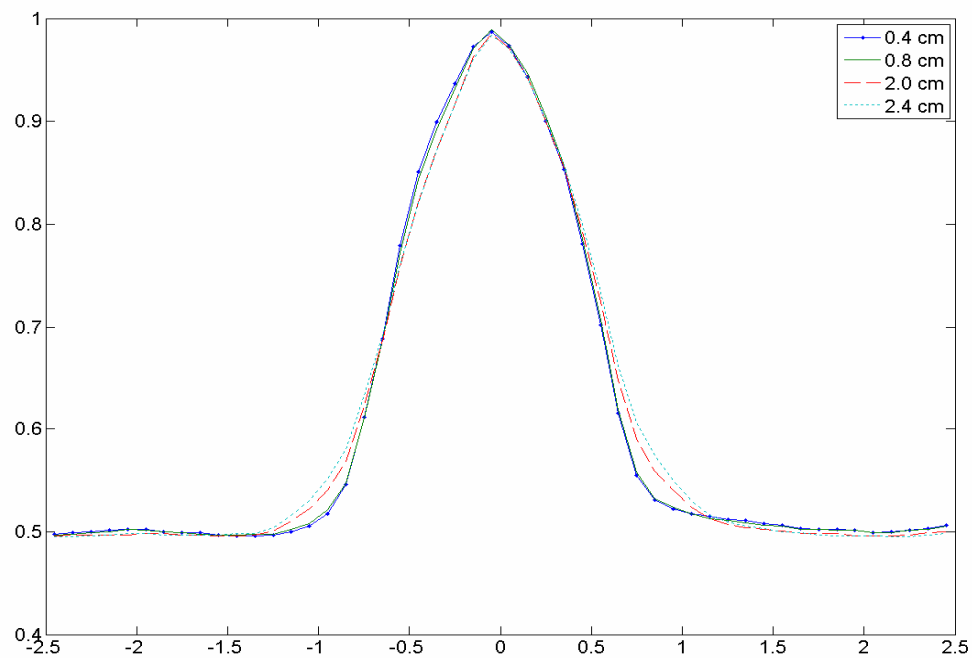


Figure 10.6: Profile across the rows in figure 10.5 at $y=0$ for combined beams

Figure 10.4 compares the isodose contour map of a four $1 \times 1 \text{ cm}^2$ field with a 0.4 mm source (above in fig. 10.4) with a 2.4 mm source (below in fig. 10.4). The isodose difference map is shown in figure 10.5 between the 2.4 mm source data and the 0.8 mm source data.

It is interesting to note that in figure 10.3, the maximum dose difference was +0.12 and -0.06 but for figure 10.5 the maximum dose difference was +0.10 and -0.02. This is due to the larger maximum dose in figure 10.5 which reduces the relative value of the maximum dose difference in a 4 field arrangement. Figure 10.5 also shows the concept of overlapping dose differences. In the coordinates (0.8, 1) in figure 10.5, the red region is the result of the dose difference overlap of the four beam edges to combine to form a higher dose difference region.

Figure 10.6 is a profile across the x-axis of figure 10.5 that crosses $y=0$. The plot shows plainly the quantisation of the dose points from the planar dose maps. The lack of data (and in other words the processing power to acquire the increased amount of data) contributes to the asymmetry that is noticeable. It can be seen that the 0.4 and 0.8 mm data requires a small shift to the right that is smaller than the resolution of the dose grid.

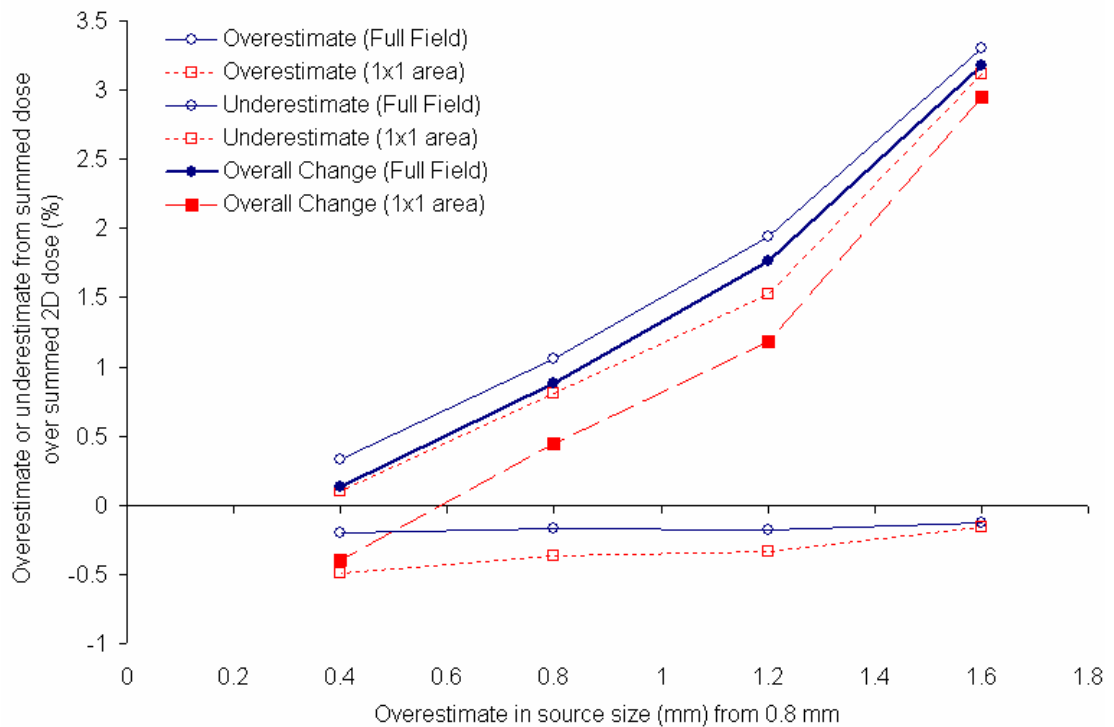


Figure 10.7: Dose analysis in terms of summation of 2D dose in a single $1 \times 1 \text{ cm}^2$ field

Figure 10.7 involves an analysis of the effect of the detector volume on the overestimate or underestimate of summed 2D dose. The mathematics used to calculate this is identical to the procedure and theory clarified in equations 7.2-7.7, however in this case the dataset is not a 1D dose profile but a 2D dose distribution. The 2D dose distribution corresponding to the 0.8 mm source data was used as the reference. The full field refers to a summation of the 2D dose over the entire dose grid extracted from the RTPS while the 1x1 area refers to the summation of the 2D dose in the treatment area only (the 1x1 cm² field centred on the isocentre). The x-axis of figure 10.7 refers to the overestimate of the source size from 0.8 mm –e.g. for the point corresponding to 0.4 overestimate in source size from 0.8 mm would involve the 1.2 mm source dataset.

The results indicate that the overall change for both the full field and the 1x1 cm² area in the isocentre involved overestimation of up to 3%, with increasing overestimation with an increasing overestimate in the source size.

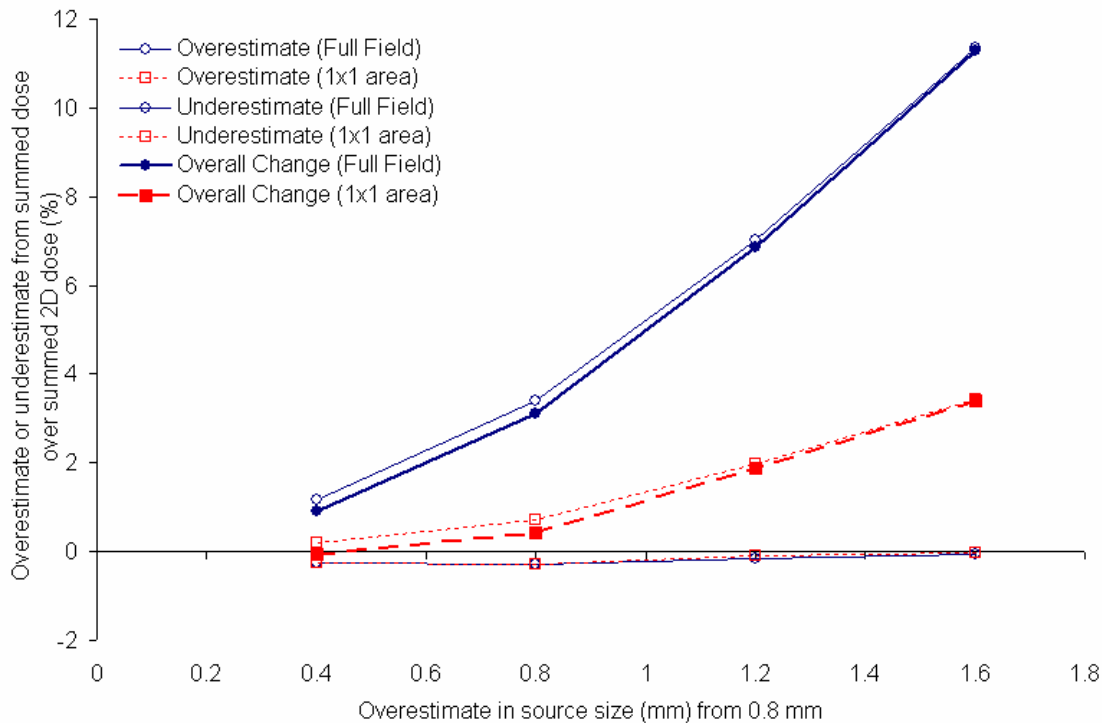


Figure 10.8: Dose analysis in terms of summation of 2D dose in a four 1x1 cm² field arrangement

Figure 10.8 involves the same procedure as figure 10.7 but instead of a single 1x1 cm² field, there are 4 1x1 cm² fields. The results indicate that the overall change increased dramatically for the full field to a maximum of 11%, with increasing overestimation with an increasing overestimate in the source size. For the 1x1 area, the maximum

overall change was 3%, also increasing overestimation with an increasing overestimate in the source size.

Results: Plan 2 Field Abutted $1 \times 1 \text{ cm}^2$

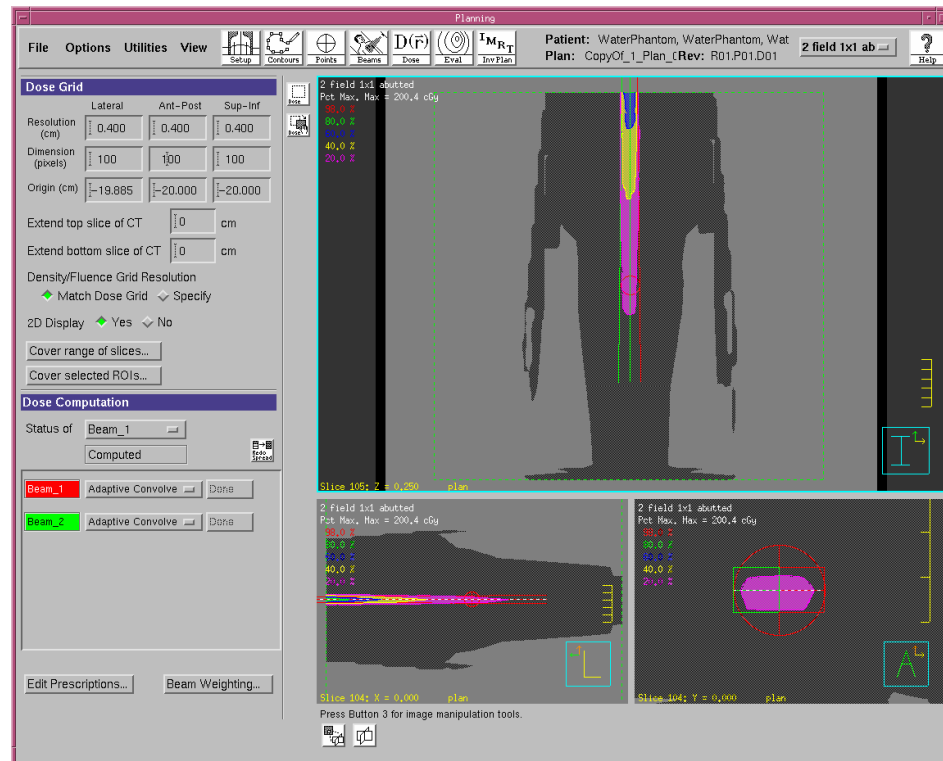


Figure 10.9: Pinnacle isodose distribution showing the beam geometry used in the plan 2FS1A

Figure 10.9 illustrates the plan containing two abutted $1 \times 1 \text{ cm}^2$ fields. This plan was designed to test the use of beam junctions where two fields are combined to create a larger one. This process is critical in IMRT as many beamlets are combined to create an intensity modulated 2D dose distribution.

Figure 10.10 shows the isodose difference map for each beam individually. The isodose difference shows similarities to figure 10.3, in that both involve overestimates on the right hand side. This suggests that with small $1 \times 1 \text{ cm}^2$ fields, the asymmetry issue corresponds to a shift towards the beam to the left. Figure 10.11 shows this more clearly. It seems that the 0.4 mm source data (top of figure 10.11) exhibits a clearer shift to the left than the 2.4 mm source data, by examining the ~ 0.7 line (orange).

However, the combination of the two fields was processed and an isodose distribution was made comparing the dose distributions from a 2.4 mm source and a 0.8 mm source in figure 10.12. The results indicated that the junction area was free from detector effects with minimal dose differences between different source parameters.

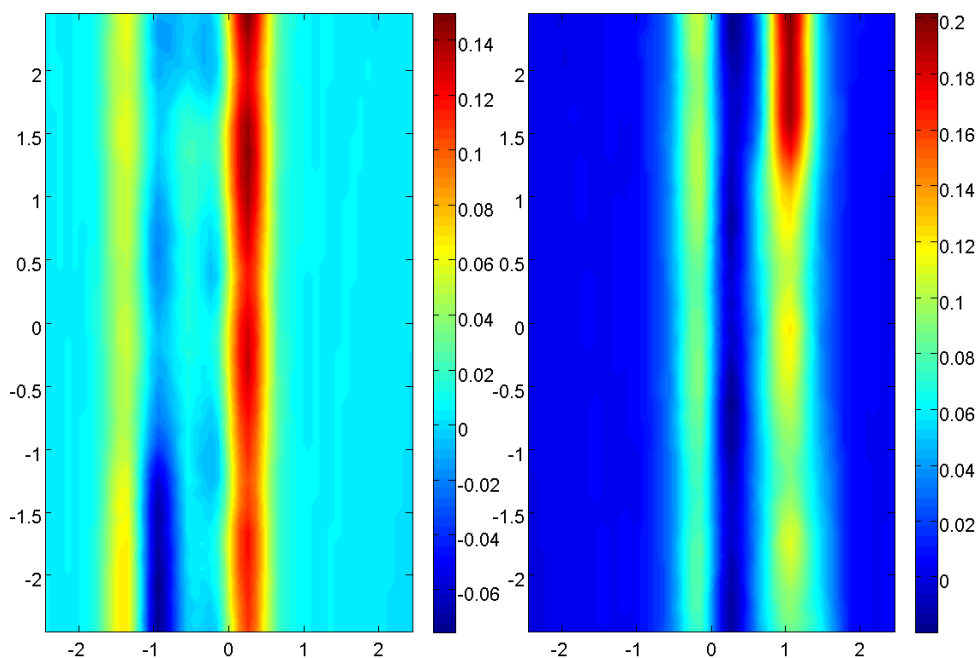


Figure 10.10: Plot showing the isodose difference plot, at gantry 0 for two single fields (gantry 0), where each point was calculated by isodose point (2.4 mm model) minus isodose point (0.8 mm model)

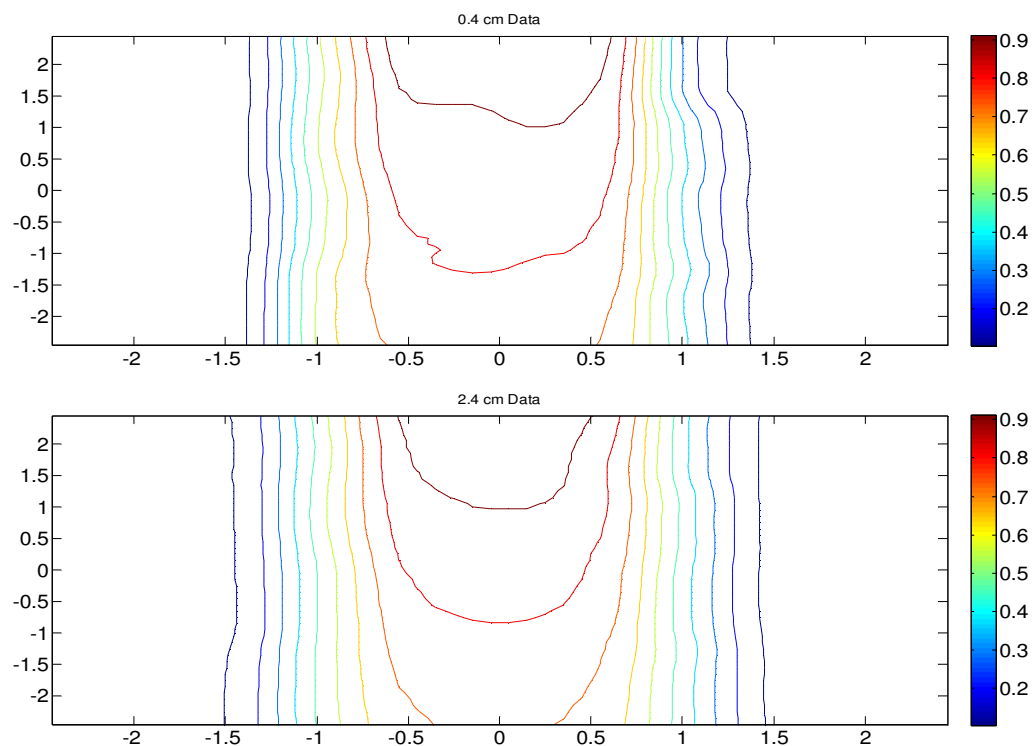


Figure 10.11: Plot showing the difference in isodose distribution for one 2x1 (abutted) cm² field between the 0.4 mm source size model (top) and the 2.4 mm source size model (bottom)

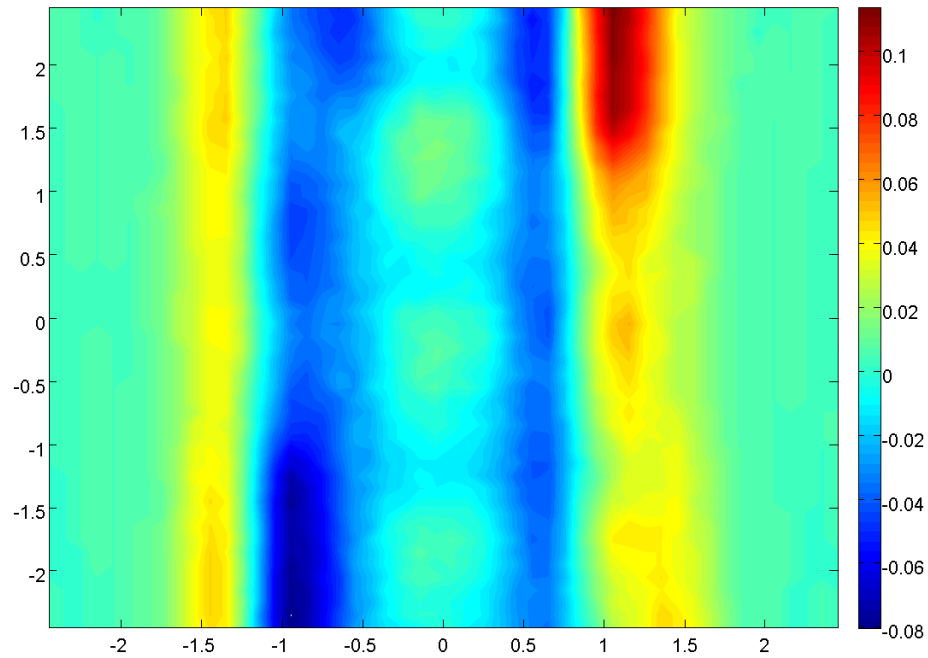


Figure 10.12 Isodose difference. Normalised isodoses 24 minus normalized isodoses 08, Combined Fields.

Figure 10.13 confirms this by a 1D plot of the dose profile across the top of the combined fields with various source parameter settings. Again, the asymmetry was visible which accentuated the overestimate and underestimate regions on the right penumbra but did not show the overestimate and underestimate on the left hand side.

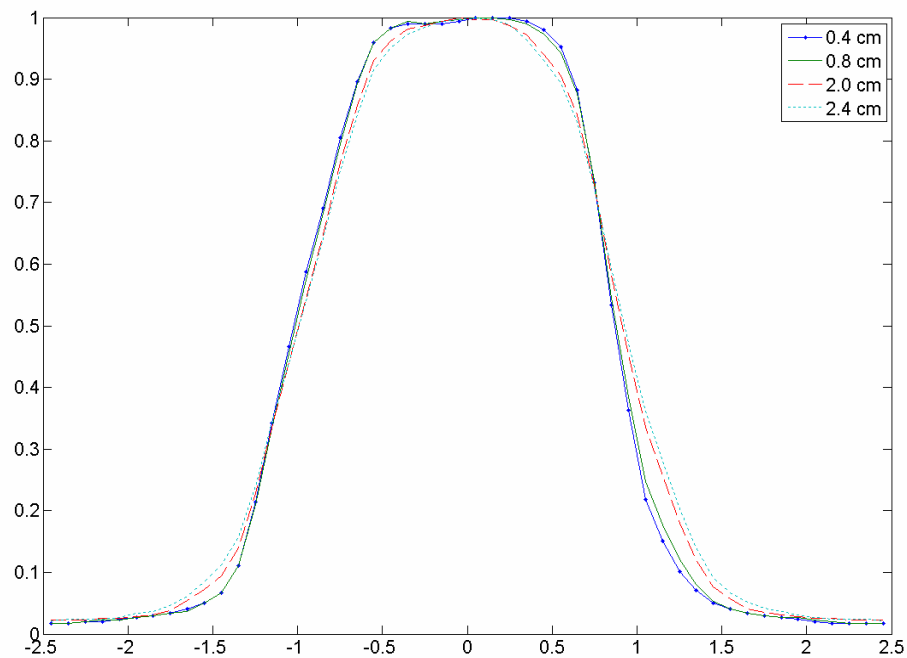


Figure 10.13 Profile with data from rows along $y=2.45$ cm (highest dose region) showing different source size for combined beams

RESULTS: 4 FIELD 10×10 CM2 PLAN

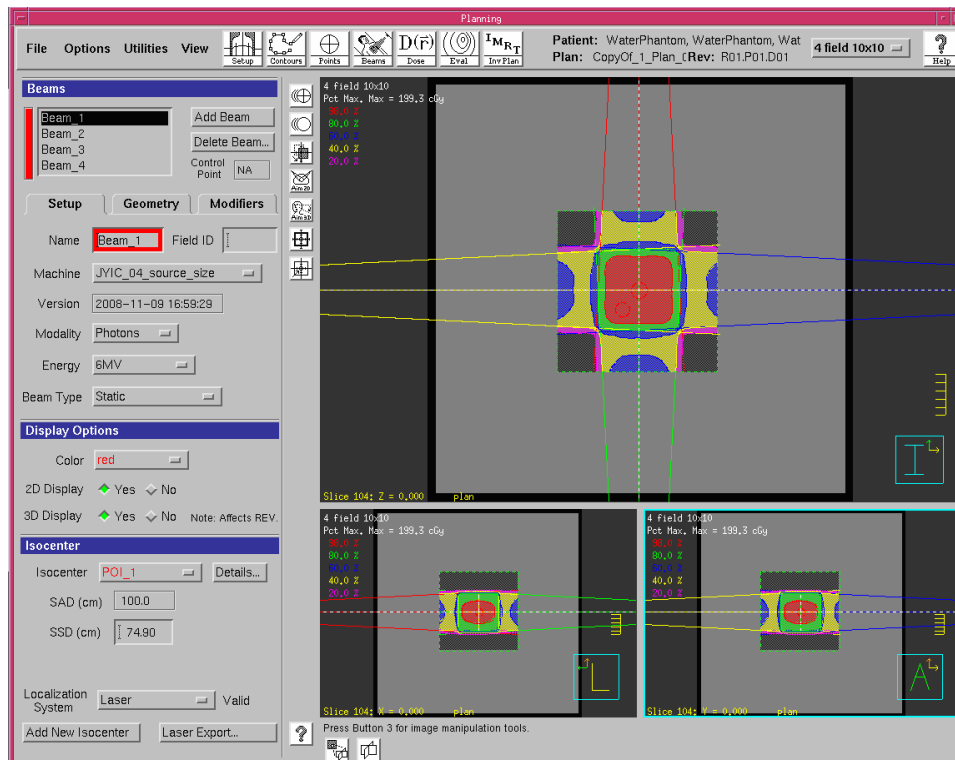


Figure 10.14: Pinnacle isodose distribution showing the beam geometry used in the plan 4FS10

Figure 10.14 illustrates the four field 10×10 cm² plan which corresponds closely to a 3DCRT plans, (with the exception that there is only jaws not MLC shapes). This is a more clinically realistic example than the compared to 1×1 cm² fields which are quite small even for stereotactic plans. Individual 10×10 cm² fields with 0.4 mm source data and 2.4 mm source data are plotted in figure 10.15. Unlike the 1×1 cm² fields, the asymmetry is not easily visible.

Figure 10.16 shows the dose difference of a single field between the 2.4 mm source data and the 0.8 mm source data. The dose difference is neatly isolated to the penumbra areas only, where the divergence of the penumbra with depth is also detectable. This is in contrast with the dose difference map in figure 10.3, where the central axis involved considerable dose difference values.

Figure 10.17 shows the dose difference of four 10×10 cm² fields and it is difficult to detect asymmetry. The difference in contours between the top figure in figure 10.17 (0.4 mm data) and the bottom figure (2.4 mm data) is small. This is confirmed by the dose difference map in figure 10.18 where the calculation shows that the maximum dose difference is +0.03 and -0.03.

Figure 10.19 shows a 1D dose profile along the central region of figure 10.17. It is confirmed that there is no dose difference in the inter-umbra region due to the source effect and that the penumbra is broadened with larger source sizes.

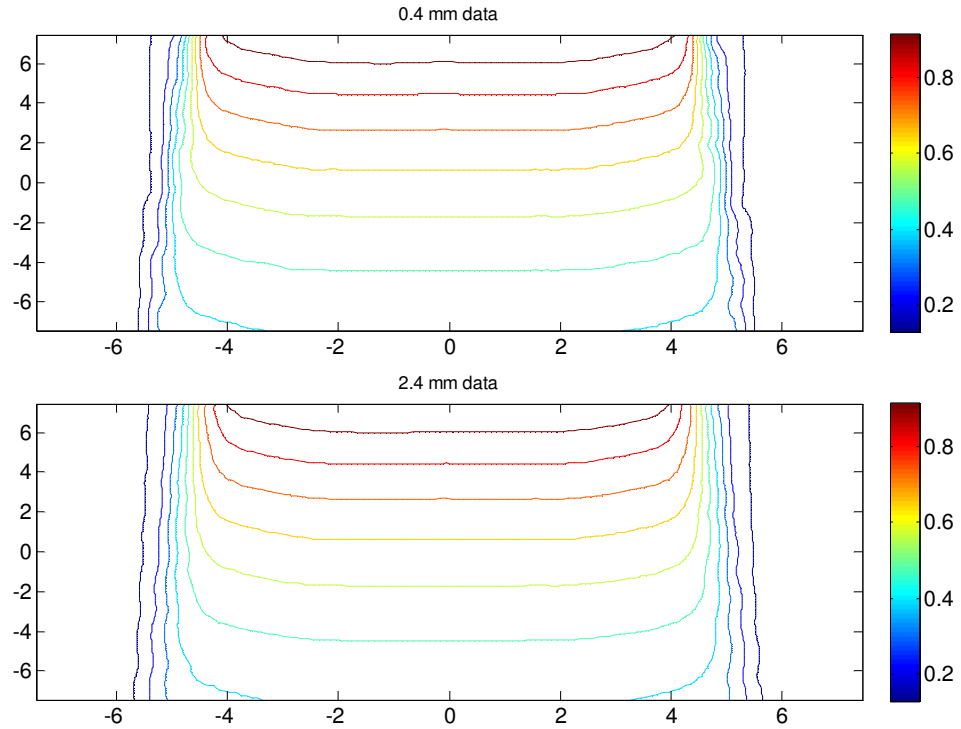


Figure 10.15: Plot showing the difference in isodose distribution for one 10×10 cm² field between the 0.4 mm source size model (top) and the 2.4 mm source size model (bottom) used in the plan 4FS10

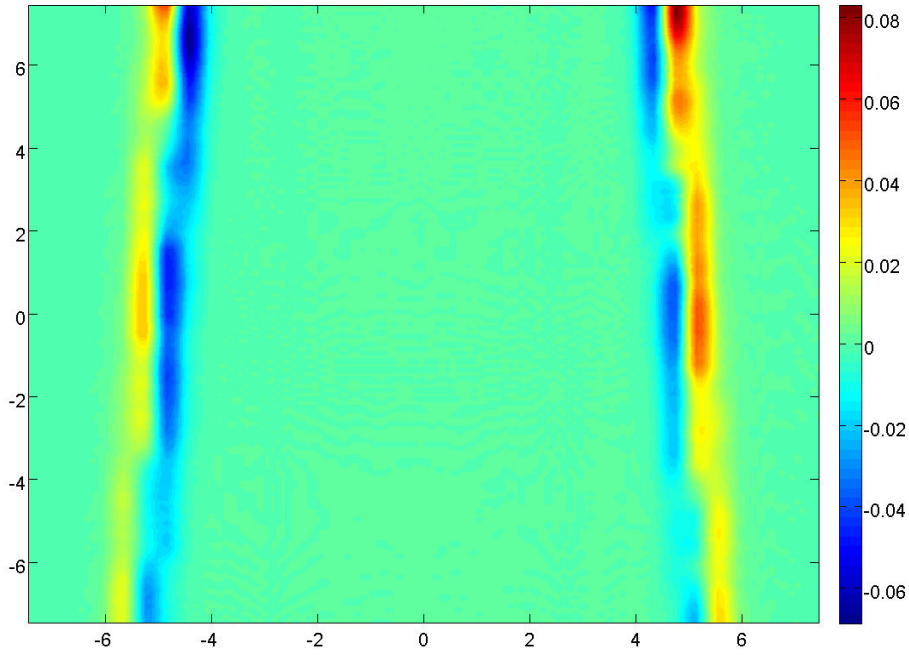


Figure 10.16: Plot showing the isodose difference plot, at gantry 0 for two single fields (gantry 0), where each point was calculated by isodose point (2.4 mm model) minus isodose point (0.8 mm model)

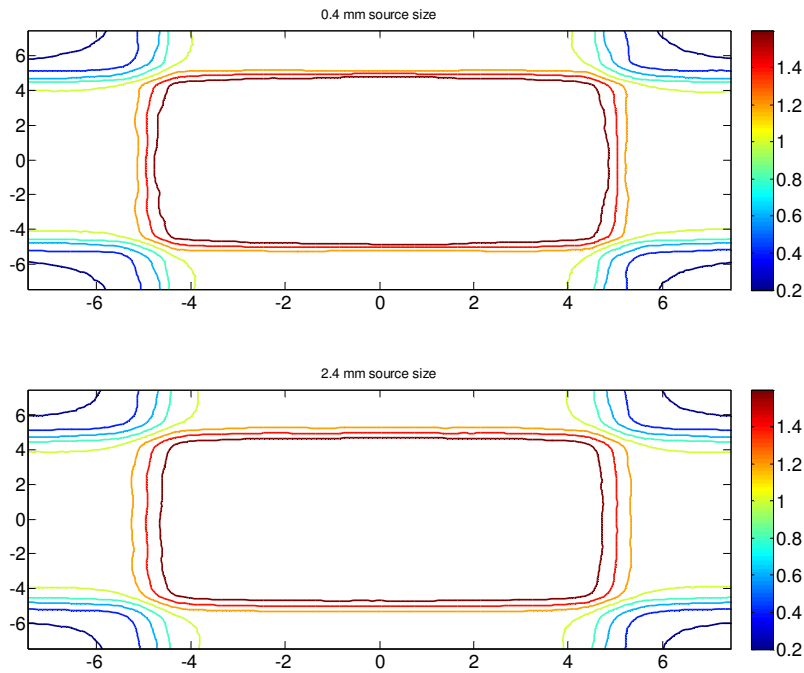


Figure 10.17: Plot showing the isodose difference plot, at gantry 0 for four single field that are $10 \times 10 \text{ cm}^2$, where each point was calculated by isodose point (2.4 mm model) minus isodose point (0.8 mm model)

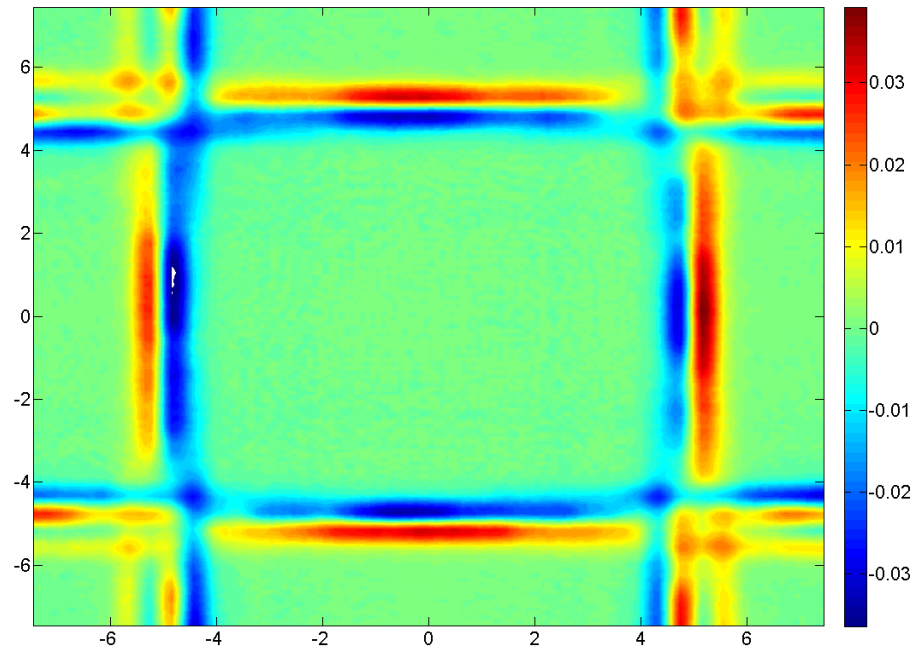


Figure 10.18: Plot showing the isodose difference plot, at gantry 0 for four single fields that are $10 \times 10 \text{ cm}^2$ (gantry 0), where each point was calculated by isodose point (2.4 mm model) minus isodose point (0.8 mm model)

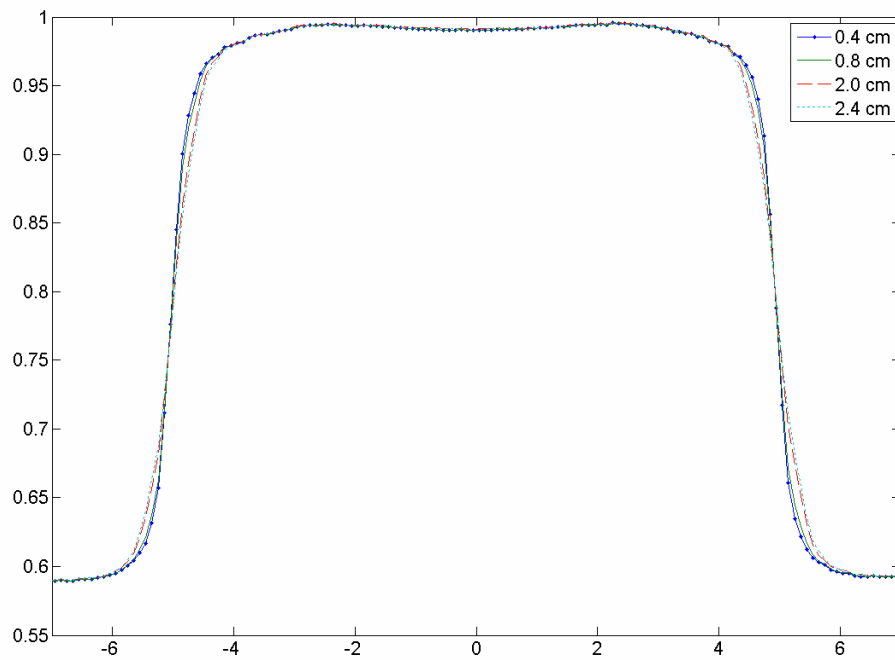


Figure 10.19: Profile from row data along $y=0$ (central region) showing different source size for combined beams

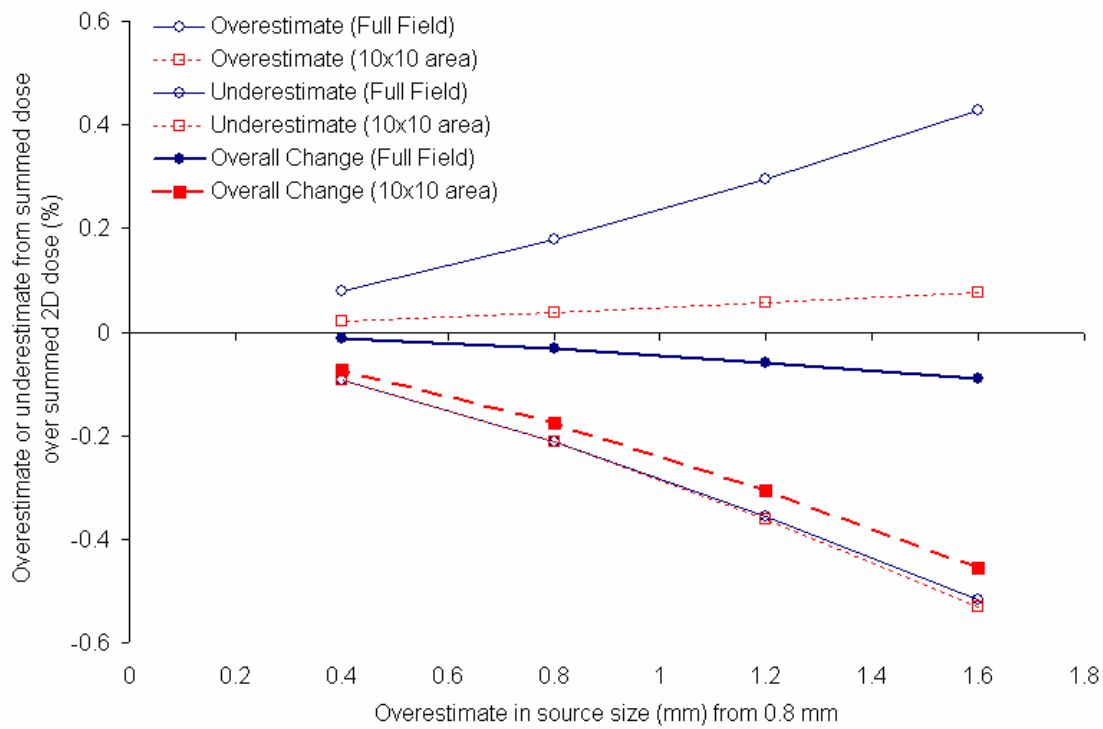


Figure 10.20: Dose analysis in terms of summation of 2D dose in a single 10×10 cm² field

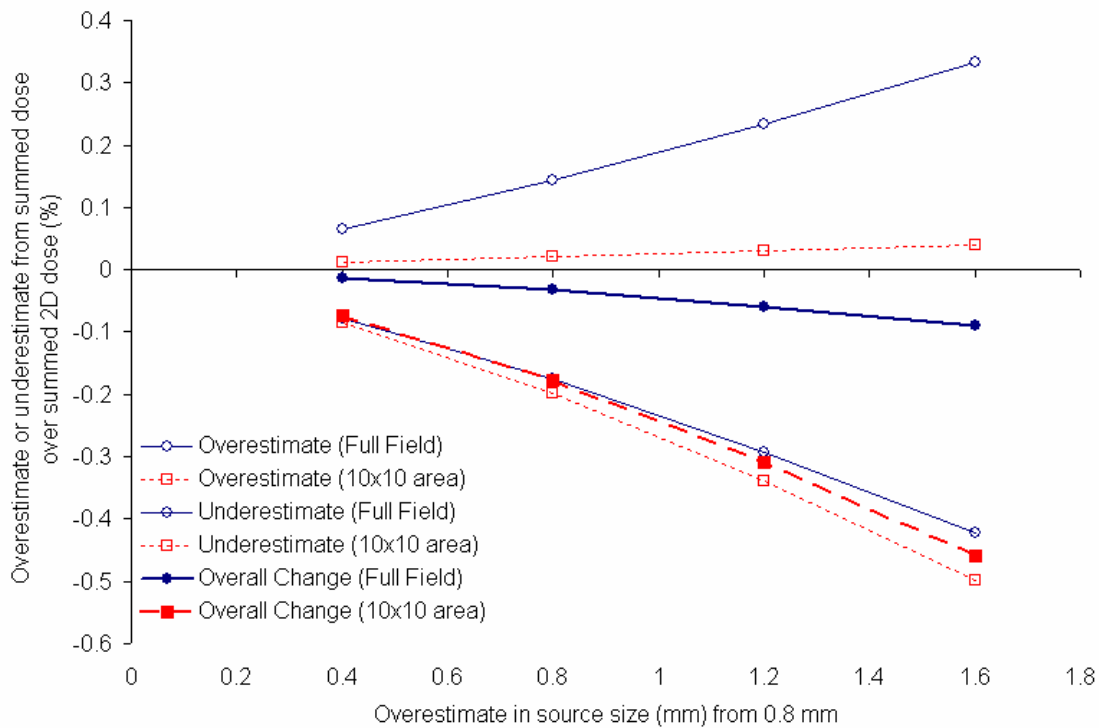


Figure 10.21: Dose analysis in terms of summation of 2D dose in a four 10×10 cm² field arrangement

Figure 10.20 shows the summation of the overestimate, underestimate, and overall change in dose distribution due to the source size effect. The results of the *full field* analysis agree with the results found in chapter 7 (see figure 7.6), namely that for larger field sizes, the change in summed dose is small. It is interesting to note that the overall change in dose is small (within -0.1%) but that the 10×10 area centred on the isocentre involved a maximum of -0.4% for the case of the IC (which is 1.6 mm more than the 0.8 mm that corresponds to the ZE data).

Figure 10.21 corresponds to the same analysis but for a four 10×10 cm² field arrangement. The results were similar compared to figure 10.20: for a full field, the overall change is within -0.1% and in the 10×10 area centred on the isocentre there was a maximum of -0.5% for the case of IC.

RESULTS: 4 FIELD PROSTATE PLAN

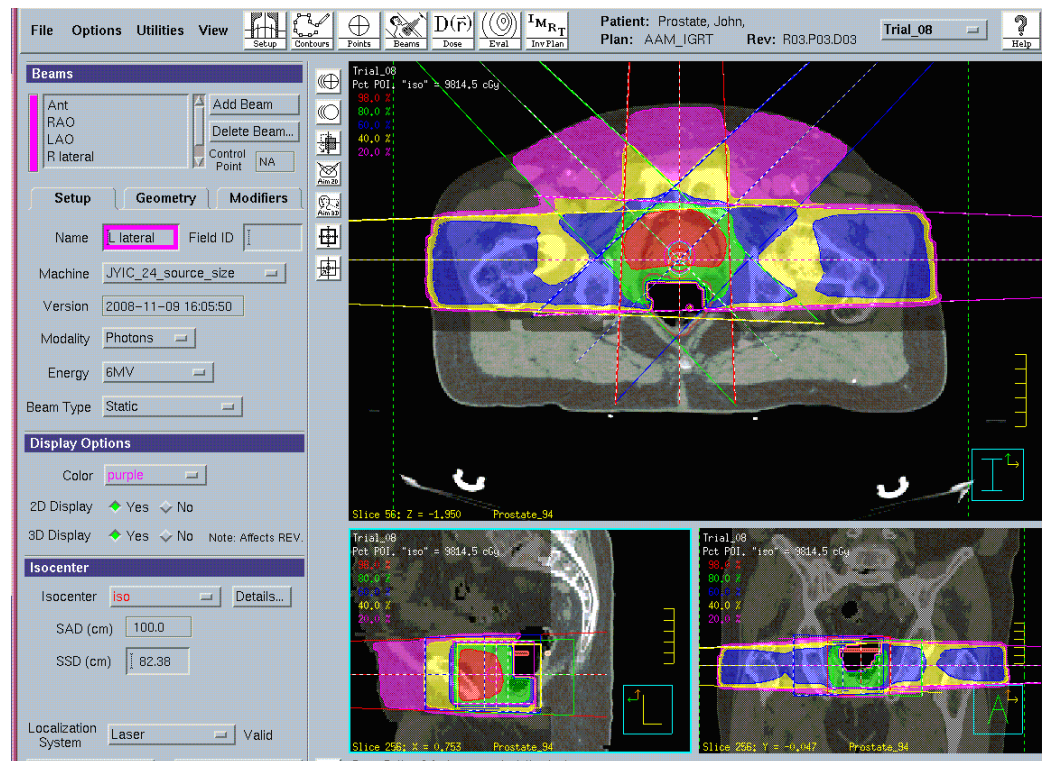


Figure 10.22: Pinnacle isodose distribution showing the beam geometry used in the plan PROST

Figure 10.22 shows the four field prostate plan which also involved a patient CT dataset. The plan features oblique beams, as well as inhomogeneous materials in the tissue such as bone and air. In figure 10.23, an oblique beam was compared with respect to source size variation. Similar to the 10×10 cm² field 10.16, the asymmetry was difficult to

detect (if any). The maximum dose difference of +0.04 and -0.05 in the isodose difference plot in figure 10.24 is also similar to the values in figure 10.16.

Figure 10.25 shows the contour plot of all field components with source size 0.8 mm (top) and 2.4 mm (bottom) while figure 10.26 shows the dose difference plot. The maximum dose differences of figure 10.26 are +0.03 and -0.03 (that is, $\pm 3\%$), again agreeing with the predictions made in chapter 7. It is noteworthy the spatial distribution of the dose difference map in figure 10.25 is relatively complex. This is of significance because the predictions of overestimate or underestimate will be more complicated in such circumstances (e.g. as compared to figure 10.20 and figure 10.21 where the underdose was easy to see from figure 10.18).

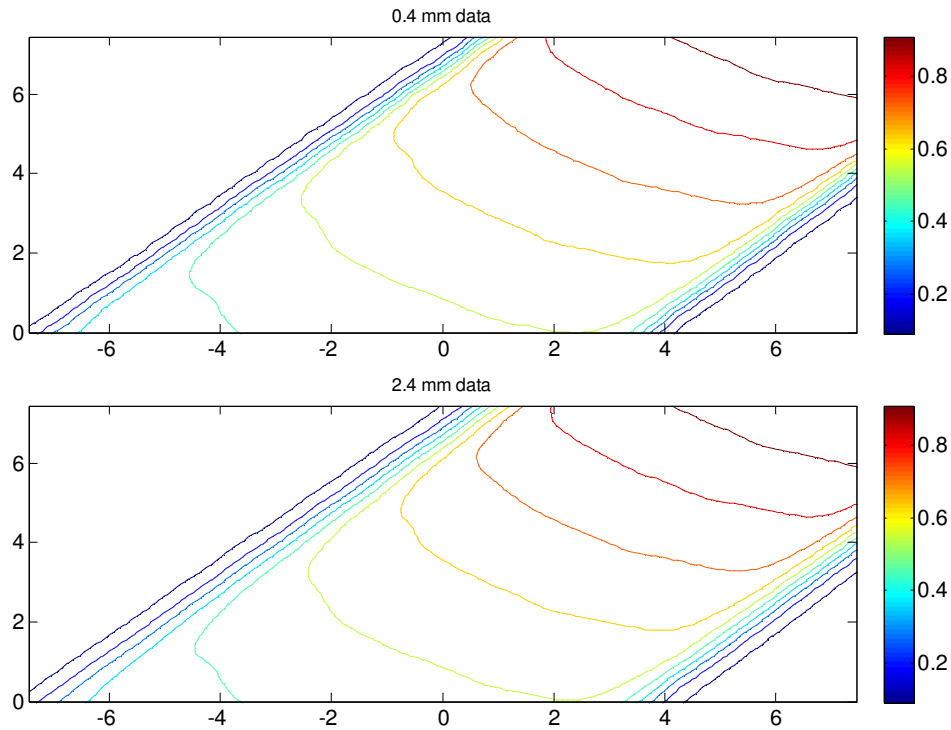


Figure 10.23: Plot showing the difference in isodose distribution for an oblique $10 \times 10 \text{ cm}^2$ field between the 0.4 mm source size model (top) and the 2.4 mm source size model (bottom) used in the plan 4FS10

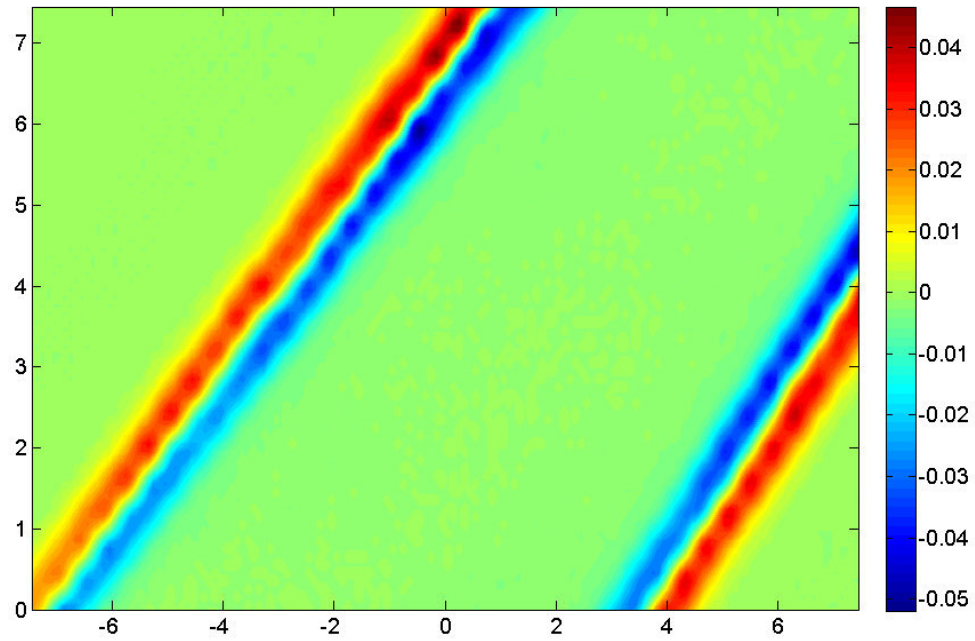


Figure 10.24: Plot showing the isodose difference plot, at gantry 0 for the oblique field, where each point was calculated by isodose point (2.4 mm model) minus isodose point (0.8 mm model)

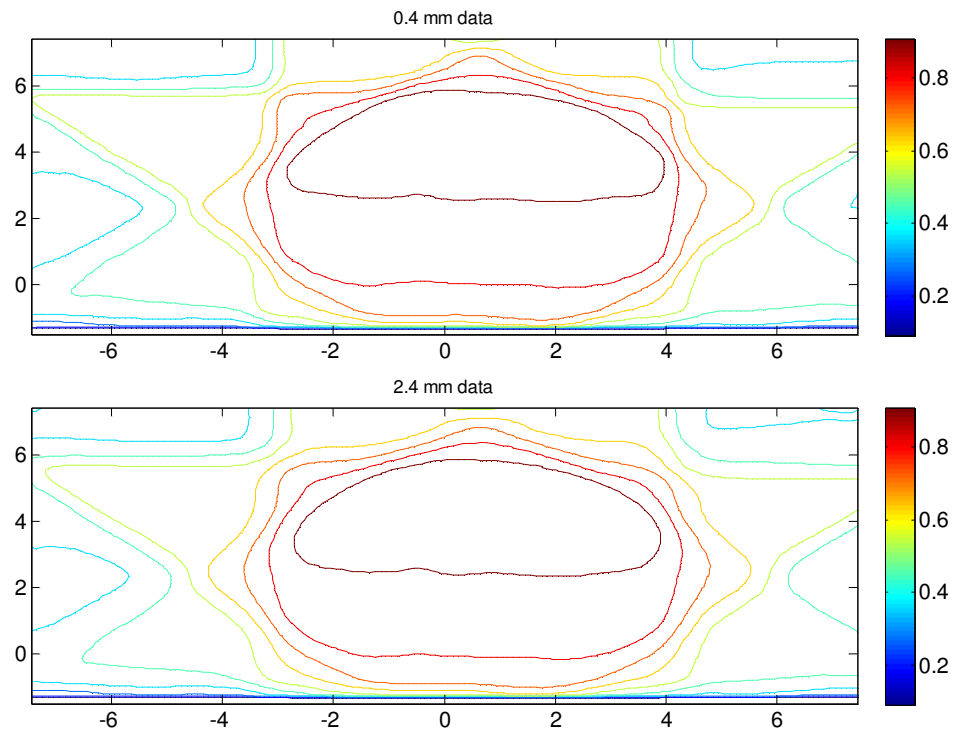


Figure 10.25: Plot showing the contour plots for the two source size setting in the prostate plan, where each point was calculated by isodose point (2.4 mm model) minus isodose point (0.8 mm model)

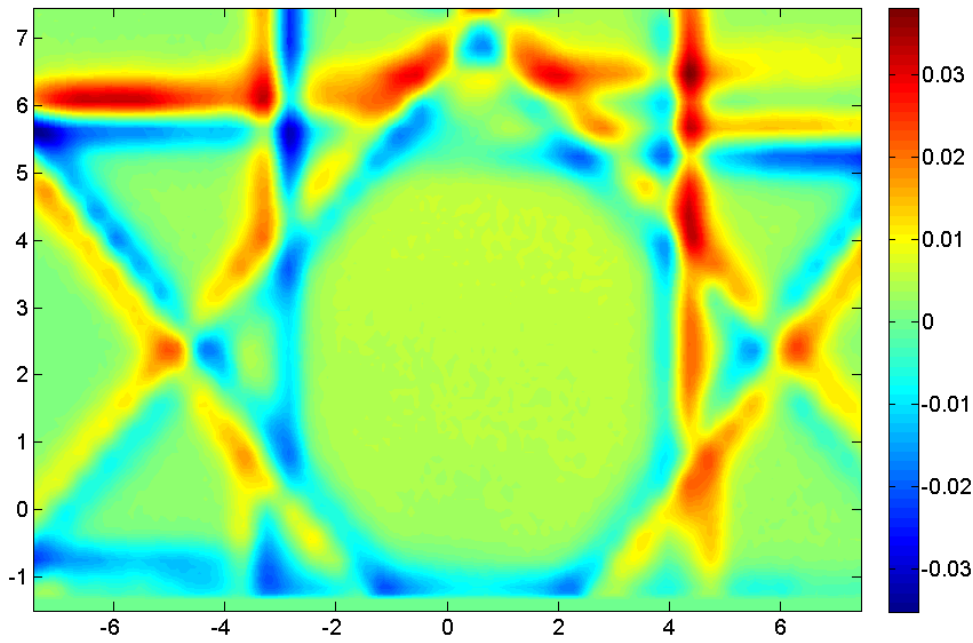


Figure 10.26: Plot showing the isodose difference plot, for four in the prostate plan, where each point was calculated by isodose point (2.4 mm model) minus isodose point (0.8 mm model)

Table 10.5: Dose volume histogram data showing the mean dose of various structures as a function of source size

	Source					
	size (mm)					
Mean dose	0.4	0.8	1.2	1.6	2	2.4
ctv	9232.5	9234.5	9218.9	9206.5	9183.4	9151.7
prostate1	9764.1	9763.7	9761.3	9759.6	9754.3	9746.6
bladder1	4584.4	4640.4	4706.6	4602	4612.7	4614
rectal volume	1925.5	1921.8	1914.9	1916.3	1910	1904.4
femur_r	4220.3	4227.4	4234.7	4214.8	4220.7	4203
femur_l	4120.6	4117.4	4107.4	4103.4	4091	4076.4
intestine	335.4	338.2	342.5	337.6	339.3	342.4
bowel	1379.2	1377.7	1374.6	1373.9	1370.3	1367.7

The mean values were calculated in the dose volume histogram window in the Pinnacle RTPS and these were correlated to volumes of interest and calculated with varying

source sizes (see table 10.5). A plot of the change in mean dose with source size (see figure 10.27) shows an unclear trend, due to the complicated distribution of dose differences and volumes of interest.

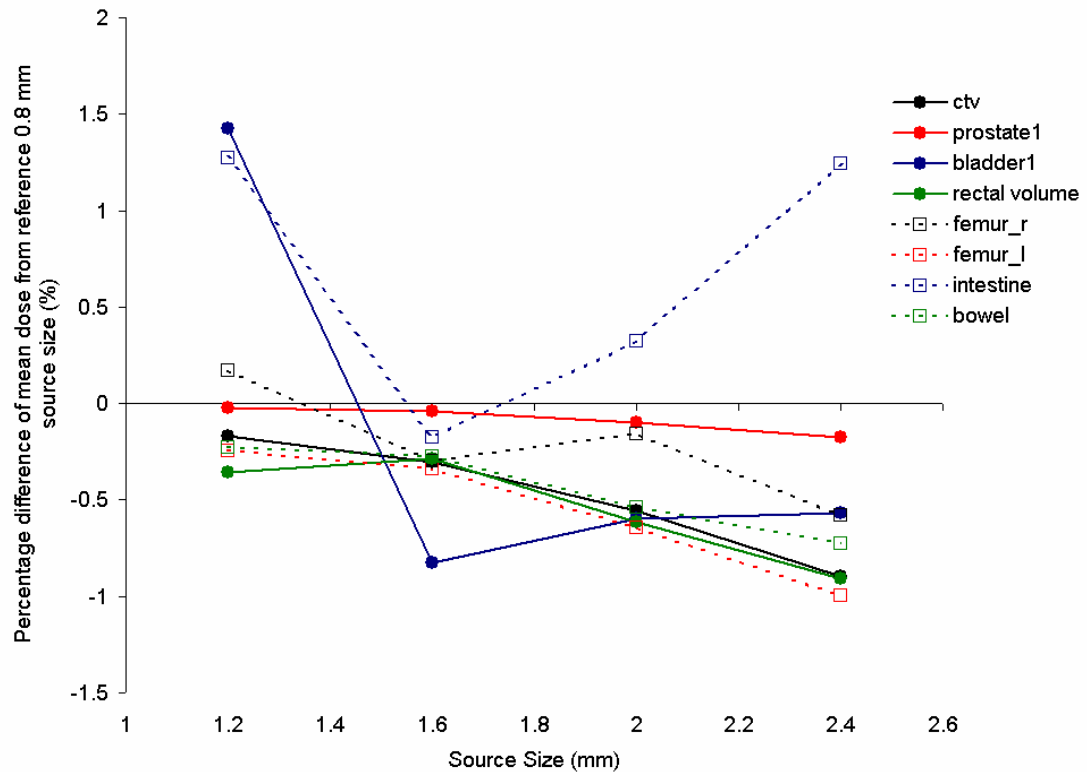


Figure 10.27: Plot of the dependence of change of the mean dose as a percentage of the mean dose of the source size 0.8 mm with source size

DISCUSSION

The study into the maximum dose differences involved the following observations:

- i. For $1 \times 1 \text{ cm}^2$ fields, the maximum dose difference between the 2.4 mm source size (IC data) and the 0.8 mm source size (ZE data) involved a typical overestimate of 12% (range 10% to 14%) and an underestimate of -6% (range -2% to -18%). This was worked out by the maximum and minimum values in the isodose difference maps, and was invariant of whether a single field was analysed or whether multiple fields were analysed because of the overlapping overestimate and underestimate regions.
- ii. For $10 \times 10 \text{ cm}^2$ fields, there was a difference in the maximum dose difference between single fields and multiple fields because while the central dose were additive, the dose difference regions did not add up due to the spatial distances between the corners of the $10 \times 10 \text{ cm}^2$ area at the isocentre. For a summation of

four $10 \times 10 \text{ cm}^2$ fields, the maximum dose difference involved an overestimate of 3% and underestimate of -3% was observed.

- iii. For a single $10 \times 10 \text{ cm}^2$ field, the data suggests that for a beam on central axis, the maximum dose difference involved a 8% overestimate and an underestimate of -8%.
- iv. This confirms the observation that for any field size, there are large overestimates for the IC data (see fig. 7.4). For a summation of small field sizes, the maximum overestimate regions can combine but for a summation of large field sizes, the maximum overestimate regions do not combine and are therefore smaller as a percentage of the maximum dose (which increases).

Investigations into the summation of 2D dose involved the same technique to the summation of 1D dose in chapter 7 and involved similar findings, which were that:

- i. For a single $1 \times 1 \text{ cm}^2$ field, the overall 2D dose (between a 2.4 mm source and a 0.8 mm source) involved an increase of 3% to the full dose map and 3% to the $1 \times 1 \text{ cm}^2$ area at the isocentre.
- ii. For a combination of four $1 \times 1 \text{ cm}^2$ fields, the overall 2D dose increased by 12% while the increase was only 3% to the $1 \times 1 \text{ cm}^2$ area at the isocentre.
- iii. For a single $10 \times 10 \text{ cm}^2$ field, the summation of the overall dose to the entire dose map involved a negligible change with source size (-0.1%). However, in the $10 \times 10 \text{ cm}^2$ area at the isocentre, there was a -0.5% decrease in summed 2D dose, which agreed with the predictions in figure 7.6. The same result was achieved with the summation of $10 \times 10 \text{ cm}^2$ fields, including the prostate four field plan.
- iv. As predicted in table 7.11, for field sizes under $2.3 \times 2.3 \text{ cm}^2$, there is a much larger component of overestimation with respect to underestimate due to the detector effect and this relationship has carried on to the radiation dosimetry calculations in the RTPS.

The observations as to the asymmetry of the RTPS dose distributions:

- i. In the literature it was found that if tuning was done on the Pinnacle³ treatment planning system for small fields, all fields except homogenous fields with field sizes less than or at $0.5 \times 0.5 \text{ cm}^2$ were reliable (Crop, Reynaert et al. 2007). Therefore, the use of $1 \times 1 \text{ cm}^2$ fields does not exceed the limitations of the Pinnacle RTPS.

- ii. The asymmetry effect was easily visible in dose difference maps and was only visible with $1 \times 1 \text{ cm}^2$ fields and not with $10 \times 10 \text{ cm}^2$ fields.
- iii. The asymmetry effect was due to a consistent shift in the beam always in the left direction (see fig. 10.2 and 10.11).
- iv. The observed asymmetry effect is linked to the grid resolution issue. The literature found that in Pinnacle³ (version 6.3b) compared to typical grid resolutions of 0.4 cm to 0.28 cm, a grid resolution of 0.1 cm produced dose distributions that agreed to typical grid resolutions to within 3% for field widths of 1 cm and above. At widths below 1 cm, the dose distribution from a grid resolution of 0.4 cm was up to 40% lower due to volume averaging. The grid placement also introduced variation of up to 30% for widths below 1 cm (Lydon 2005). In this study the dose maps were normalised so the lowered dose due to volume averaging is after normalisation could shift the dose distributions as the true maximal dose point would be lost due to volume averaging.
- v. The asymmetry effect did not affect the two $1 \times 1 \text{ cm}^2$ field junction region.
- vi. The junction region involved, to some degree, an underestimate region in the region around the junction (see figure 10.12).

CONCLUSION

The data from figures 10.3, 10.5, 10.7, 10.8, 10.16, 10.18, 10.20, and 10.21 were collected into table 10.6, which is illustrative of the maximum deviations from the ZE model because of the comparison made with the largest detector volume in the study, the IC.

Table 10.6: Tabulated results detailing the maximum point differences and summed overall change for the 1×1 cm² and 10×10 cm² field size beams over a single field and four field arrangement between the ZE model and the IC model

			Set field size	
			1×1 cm ²	10×10 cm ²
Maximum point difference (%)	Single field	Overestimate	12.0	8.0
	Single field	Underestimate	-6.0	-6.0
	4 field	Overestimate	10.0	3.0
	4 field	Underestimate	-2.0	-3.0
Summed overall change (%)		Central region		
	Single field	(1×1 cm ² , 10×10 cm ²)	3.00	-0.42
	Single field	Total region	3.20	-0.16
	4 field	Central region		
	4 field	(1×1 cm ² , 10×10 cm ²)	3.40	-0.47
	4 field	Total region	11.40	0.08

The potential implications of investigations into the effect of detector volume on isodose distributions include:

- The relationship between field size and the pattern of overestimation and underestimation of summed 1D dose and 2D dose agree –this was verified by comparing the 2D isodose distributions with the 1D dose distributions in Chapter 7. For the central region, the trend involved a significant increase (up to 3% for single fields) in the overall dose for small field sizes while for large field sizes the trend involves a minor decrease with the overall dose (approx. -0.5%).
- The summed overall change with regards to the total region involved a large overestimation (up to 11%) for small field sizes while for large field sizes this was minimal.
- The maximum point dose difference was larger for the single fields than the four field beams due to the higher maximum dose in the four field arrangements, which was used for normalisation. For smaller fields, the effect of source size on maximum dose difference is heightened.
- The spatial location of the maximum dose differences occurred in the intersection of the penumbral regions of two or more beams. It was noted that the maximum dose differences did not occur in the inter-umbra region of a beam, and because of this it

would be unlikely this would have any effect on the dose calculation point in treatment planning.

- v. The simulation of a clinical prostate plan with various source sizes revealed that, in general, the mean doses decreased with a range of 0-1%, which is in general agreement of the simulated overall dose of a 4 field beam with field size $10 \times 10 \text{ cm}^2$. The relationship between the change in mean dose and source size overestimation was not fully investigated and would require further investigation (this was also modelled briefly in Appendix E).

Chapter 11: Conclusion and future work

Note: This chapter involves a discussion that summarises the entire body of work. If more details are required, the reader is advised to open the specific chapter to find more numerical data and a more detailed discussion. Also note that the data and analysis in the appendices were not included in this chapter.

11.1 CONCLUSIONS

11.1.1 Intersection and Inflection points

To the author's knowledge, no previous literature has investigated the parameters of the intersection point (defined in this work as the intersection of two profiles measured with different detectors) and inflection points (defined in this work as the point where the second derivative is zero). The intersection and inflection points involved a strong dependence on field size. At large field sizes, the intersection and inflection points approximated 50%, which corresponds to the inflection point of a Gaussian curve. However, it is at small field sizes in the region of $1 \times 1 \text{ cm}^2$, that significant deviation in both intersection and inflection points occur. These results were relatively independent of the detector used.

11.1.2 Virtual zero detector volume profiles based on extrapolation

To the author's knowledge, no previous literature has investigated the validity of the extrapolation technique *quantitatively* with the analysis of R^2 , dose differences, cost function, field size, and with the value used for detector diameter. It was found that quantitative analysis techniques developed in this work was able to detect invalid extrapolation techniques –such as the use of incorrect sensitive diameters. The direction of profile measurement (in-plane or cross-plane) was important because it determined the direction of detector movement and hence determined the detector diameter (assuming that the detector was not rotated for measurement of each plane). The validated use of the extrapolation technique produced virtual zero detector profiles that agreed with the profiles measured with the diamond detector.

Conclusions include a recommendation of rotating the detectors with each plane to minimise the difference in detector perturbation due to the unstudied alteration in sensitive diameter values (the literature does not specify the sensitive diameter values of all detectors in both dimensions accurately). The work required for this technique was

tripled when compared with the data collection required from a single detector and while further academic investigations into the extrapolation technique would be warranted, clinical implementation of extrapolation is limited due to constraints in time and labour.

11.1.3 Virtual zero volume profile by deconvolution

The deconvolution technique used in this study involved restrictions on the technique to field sizes less than $2 \times 2 \text{ cm}^2$ due to the implementation of the Gaussian fit (larger field sizes involved a flat inter-umbra region extending across most of the inter-umbra field, which did not fit well with the Gaussian). The deconvolution technique suffered from uncertainty of the FWHM value used for the kernel not being well correlated to the sensitive diameters provided with the manufacturer. Direct measurements of the kernel FWHM noted in the literature were not performed in this study but would be useful in future studies. The potential value of the technique lies in the physical basis of the detector in convolving the true profile and of not having to perform any extra measurements –the virtual zero volume can be derived from the deconvolution of a valid kernel.

11.1.4 Detector volume effect on smearing dose profiles

The extrapolation technique was found to be more reliable than the deconvolution technique in this study due to the availability of the validation technique. For *micro* detectors such as the diamond detector, both the extrapolation technique and the deconvolution technique produced negligible differences with the virtual zero volume profile produced. The analysis of the smearing effect from detector volume found significant effects of the detector volume (see table 7.12 for more details) on penumbra broadening (up to ~2 mm for *standard* detectors), on field size overestimation (up to ~0.8 mm for *standard* detectors at *small* field sizes), on maximum point dose differences (up to ~8% overestimate for *standard* detectors), and on summed 1D dose differences (up to ~4% overall dose difference for *standard* detectors). The use of smaller detector volumes decreased the magnitude of each effect –in addition, it was noted that the penumbral overestimation and the maximum point dose difference was a significant factor across all field sizes whilst the field size overestimation and the summed 1D dose differences was dependent on field size, with small field sizes exhibiting a larger effect.

11.1.5 The non-linear extrapolation equation

The non-linear extrapolation equation was based on the hypothesis that the effect of the detector volume would be dependent on the dose gradient of the penumbral. The penumbral width was a function of dose gradient and this correlated with various combinations of depth and collimator field size. After correlation of the coefficients related to the equation formulated in this study, the virtual zero detector volume penumbra can be calculated based on the measured penumbra and the detector diameter. The method developed was able to reduce the penumbral deviation from the zero detector volume penumbras from up to ~2.0 mm (*standard* detectors) to within 0.5 mm (for all detectors studied) across all combinations of field sizes and depths studied. This model involves a large potential in penumbra modelling with the following caveats: (1) the model only provides a numerical value of the virtual zero penumbra and not the entire profile and (2) the model requires determined and verified coefficients (which would require further research).

11.1.6 Pinnacle RTP Source Size model matched to detector volume

The relationship between the penumbral width and the source size FWHM in the Pinnacle RTPS was investigated over a range of field sizes and depths. This relationship fitted well with a polynomial function, which allowed the calculation of the optimal source size parameter in the Pinnacle RTPS when given a particular penumbral width, field size, and depth. The deviation in optimal source size was up to ~1.8 mm (for *standard* detectors) from an extrapolated zero volume profile dataset. The use of the non-linear extrapolation equation formulated in this thesis was able to reduce the deviation in optimal source size to within ~0.3 mm (for all detectors).

However, this modelling depended on Pinnacle algorithms, which involved an imperfect model of the extrafocal source component discussed in the literature. In this study, the $1 \times 1 \text{ cm}^2$ data was considered in determining optimal source sizes (in order to minimise the extra-focal source component) for academic purposes but the caveat is that for clinical purposes, the optimal source size may be chosen as an average over clinically used field sizes.

The correlation of the measured penumbra and the detector volume to the virtual zero detector volume penumbral width in the non-linear extrapolation penumbral equation and the correlation of the penumbral width to the optimal source size parameter in the Pinnacle RTPS was combined (see table 9.6) to calculate the expected

measured penumbra as well as the expected optimal source size in Pinnacle for an arbitrary detector (given caveats that include the limitations of the coefficients in the equations which are dependent on factors such as beam energy, machine, and collimator type).

11.1.7 Effect of RTP virtual source size on isodose distributions

The effect of detector volume resulted in changes in the measured penumbral width and thereafter changes in the modelled source size parameter in the RTPS. The source size parameter was correlated with dose distributions and significant changes were observed in terms of summed dose and maximum dose point differences. It was noted that the change in dose distributions occurred in the penumbral regions of individual fields and was higher in areas where penumbral regions intersected with multiple beams. In comparison with the virtual zero volume detector, the IC involved minimal summed dose changes for large fields (within $\pm 0.5\%$). For small fields, the IC involved significant summed dose changes in the central region ($+3\%$) and in the entire region ($+3\%$). For the case of multiple small fields however, the summed dose change over the entire region was 11% (see table 10.6 for more details).

11.2 POTENTIAL CLINICAL SIGNIFICANCE

The effect of detector volume in the overestimation of the penumbral width in the measurement of dose profiles is well known in the literature and was reproduced in this study. The subsequent relationship of the penumbral width with the source size parameter in the Pinnacle RTPS was further investigated with respect to dose distributions. The changes measured in the 2D dose distributions produced from the Pinnacle RTPS matched the expected changes measured in the 1D dose profile datasets.

The clinical effect of the detector volume due to changes in the dose distribution was spatially located in the penumbral regions of the beam profile. The changes in dose distribution due to the detector volume effect were generally away from the centre of the fields and are therefore a negligible effect on dose calculations that is required for patient treatment. In other words, the amount of radiation output is independent on the detector volume effect.

However, there were significant effects modelled from the detector volume effect from maximum dose differences and the summation of overall dose. For a combination of large clinical fields typically used in 3DCRT (modelled with 4 fields of $10 \times 10 \text{ cm}^2$), the maximum point dose difference was approx. $\pm 3\%$ and the overall

summed dose change was -0.5% in the treatment area and negligible over the entire region. For a combination of small clinical fields characteristic of IMRT plans (modelled with 4 fields of $1 \times 1 \text{ cm}^2$), the maximum point dose difference was approx. +10% (to -2%) and the overall summed dose change was approx. +3% in the treatment region and approx. +11% over the whole region.

For 3DCRT plans, the clinical significance of the detector volume effect is minimal but not negligible. While the calculated and treatment MU would not be affected, there is a significant change in the summed dose in the treatment region as modelled by the source size parameter in the Pinnacle RTPS of approx. 0.5%. In view of the whole radiotherapy process which operates on an overall acceptable dose deviations of up to $\pm 5\%$, this deviation is small however this error is significant with respect to the national and international tolerances for dose calculations in radiotherapy which are set to 2% and 2 mm (Garcia et al, 2005). Optimisation of the source size parameter could be treated as an option to improve the precision of 3DCRT radiotherapy treatments.

For IMRT plans, the clinical significance of the detector volume effect was found to be substantial but the data used involved testing of the most extreme case ($1 \times 1 \text{ cm}^2$ fields with comparisons of the ZE with the largest detector, the 0.125 cc IC). The most extreme clinical effects that are possible for IMRT plans include acceptable, but large, deviations in summed dose to the treatment region (approx. +3%). For the total region, which would include normal tissues, the deviation in summed dose was approx. 10%, which substantiates further investigation. For IMRT plans that utilise field sizes larger than $1 \times 1 \text{ cm}^2$, the expected errors would be in a range from 10% to 0.5%, depending on field size. With further investigations, it is envisaged that recommendations could be made into an acceptable minimum field size to be used in IMRT plans. Preliminary findings are that the summed overall dose change due to the detector effect is minimal at the field size of $2.3 \times 2.3 \text{ cm}^2$ (see table 7.11), and hence the use of field sizes larger than $3 \times 3 \text{ cm}^2$ would be acceptable.

(In addition, a small change in radiation field size due to the detector volume effect was observed at field sizes of $1 \times 1 \text{ cm}^2$).

The links between detector volume, penumbral width, and source size parameter in this study produced preliminary parametric equations that linked the three parameters. Equation 8.3 linked detector volume, measured penumbral width, and the virtual zero detector volume penumbral width and equation 9.1 linked penumbral widths and the optimum source size in the Pinnacle RTPS. With due respect to the caveats involved,

one can use these equations to gauge the overestimation of penumbral width and source size parameter if the detector volume is used. The caveats involve the limitation due to the uncertainties in the coefficients derived in equations 8.3 and 9.1 which may vary between machine types, beam energies, and other factors.

The upgrade in accuracy by accounting for the detector volume effect can be approached from a few angles. Firstly, it is possible that if the uncertainties in equations 8.3 and 9.1 are answered with sufficient research, the effects of the detector volume on penumbral width and on the source size parameter in the Pinnacle RTPS could be corrected for parametrically. The potential advantage of this method is the efficiency at which this could be implemented as no comprehensive beam data acquisition would be required.

Secondly, measurement of profile data from a various detectors is possible but the time requirements of this technique make this unfeasible. Thirdly, deconvolution of the profiles with the FWHM of detector kernels can reduce the error but, in the authors opinion, the accuracy of the FWHM and the intricacies involved poses significant challenges to actual implementation.

Otherwise, until further research is available, the effects of the detector volume can be minimised by a clinical institution by conducting a set of profile measurements with detectors with detector volumes that approximate zero, preferentially with *micro* detectors (where the detector volume is of the order of 10^{-3}cm^3) such as film or diamond detectors. The potential disadvantage of this is the substantial work hours required for the collection and verification of beam data required, which would be in competition with other important work or research items demanded on a clinical physicist.

11.3 FUTURE WORK

11.3.1 Determination of the effective detector diameter

A large limitation encountered with the extrapolation technique was that the sensitive diameters for the detectors used were not specified in both measurement conditions in the literature. In this study, a verification algorithm was developed for the extrapolation technique which was able to detect an error involved with the use of the same sensitive diameter in measurement of dose profiles perpendicular to the axis of detector motion. For many measurements, rotation of the chamber, collimator, or the water tank are not performed to measure the two planes of the dose profiles and thus the absence of

sensitive diameter values for commonly used detectors involves the introduction of errors in penumbral measurement that are difficult to address.

A method of detector characterisation, as far as the author is aware of, that is not found in the literature, involves the collection of a number of *known* dose profiles (dose profiles measured with verified sensitive detector diameters) to calculate the *unknown* or *unspecified* detector diameter from dose profile measurements. The sensitive diameter can be measured for each detector, at each configuration (perpendicular laterally, perpendicular vertically, and parallel to the axis of detector motion) and at each energy.

Similarly, the deconvolution technique in this study encountered issues with the accuracy of the FWHM of the kernels associated. More detailed work investigating this issue would be required for an efficient implementation of the deconvolution technique over a sufficient amount of experimental conditions (such as over field sizes and beam energies).

11.3.2 Parametric non-linear extrapolation to virtual zero volume

The non-linear extrapolation method in calculating the virtual zero volume penumbra has substantial potential in clinical use, provided that the technique is properly verified and quantified. As far as the author is aware, the data and analysis in this study with regards to this technique has not been discussed in the literature and therefore this only represents a preliminary investigation of this technique.

Further investigation can be performed to employ the same technique with a wider and more comprehensive set of conditions, which may include:

- i. Different beam energies
- ii. Different types of linear accelerators
- iii. Different types of field-defining collimators (e.g. jaw-replacing MLCs)
- iv. A more comprehensive dataset with more field sizes and more depths
- v. Different types of detectors

Additional results will allow the investigator to re-evaluate equation 8.3 in terms of both the fit of the data with the curve-type and the variation of the coefficients with various datasets. Modifications of equation 8.3 may be justified if the correction to obtain the virtual zero detector volume penumbral width involves additional variables for more accuracy (e.g. beam energy). The link between the dose gradient, the penumbral width,

and the broadening of the penumbral width can be further understood with more investigation.

11.3.3 Relationship between source size in RTP model and penumbra

The relationship between the penumbral and the source size parameter described in equation 9.1 involved satisfactory fits ($R^2 > 0.99$) between data (the Pinnacle RTPS model) and model (equation 9.1). However, it was noted that the coefficients of the polynomial equation varied with field size and depth in this study.

Further investigations could reproduce the technique used in this study for:

- i. Different linear accelerators
- ii. Different beam energies
- iii. Different radiotherapy treatment systems
- iv. Monte Carlo models
- v. Different types of field-defining collimators (e.g. jaw-replacing MLCs)

Further investigation will determine whether the extent at which the individual institution will need to determine the relationship between the penumbral width and the source size parameter, if at all. Investigations into other mathematical expressions linking the penumbral width and the source size parameter may also be required if conditions such as different radiotherapy treatment systems (which have involve different dose calculation models) produce a substantially different dataset.

11.3.4 Detector volume effect on dose distributions

In this study, the following simulations were done to study the effect of the detector volume effect on dose distributions (as modelled by the Pinnacle RTPS):

- i. Single and four field beams of jaw-defined $1 \times 1 \text{ cm}^2$ field
- ii. Single and four field beams of jaw-defined $10 \times 10 \text{ cm}^2$ field
- iii. Two abutted beams of jaw-defined $1 \times 1 \text{ cm}^2$ field
- iv. Sample 3DCRT prostate plan

Further simulations can be done to model the likely effects on dose distributions from different source sizes (due to the detector volume effect), such as:

- i. Single and four field beams of jaw-defined with other field sizes
- ii. Clinical or experimental 3DCRT plans with various configurations such as:

- a. Abutted fields
 - b. Wedges
 - c. MLC shaped fields
- iii. Clinical or experimental IMRT plans with various configurations such as:
 - a. Variation of minimum field size
 - b. Variation of VOI margins
- iv. Clinical or experimental Stereotactic plans

Investigations could include an additional dimension by the study of a comprehensive list of source sizes in order to enable the transfer of the results to other institutions which may have used a different selection of detector. Lastly, in-house coding to enable dose-volume histogram would provide further analysis to clarify the possible clinical effects due to the detector volume.

11.3.5 Analytical fits of the dose profile function

Further investigation into the inflection point of dose profiles is warranted on one basis as the inflection point of a curve is a basic mathematical property. The change in the inflection point of a curve, which was observed in this study with a variation in field size, indicates a change in the curve properties of the dose profile. In this study, the inflection point at small field sizes was significantly different compared with the case for larger field sizes and this was theorized to be a result of the extent of lateral electron equilibrium in the profile.

A related analytical study of the dose profile involves an intersection analysis. Where two profiles intersect is the point where the same dose is measured (where both curves are normalised). The significance of this is that this defines where the underestimate and overestimate regions begin and end (see table 5.4). It is envisaged that it is the *symmetry of dose gradients* that determines the amount of dose deviation from the dose measured by a point detector.

Further studies of both these phenomena can be investigated with a variation of beam energy, machine, and collimator type –all of which would affect the lateral electron range due to a combination of conditions such as beam energy and the source of the scattered radiation. Monte Carlo simulations into the inflection properties of dose profiles would enable the researcher to distinguish whether the predominant influences to the inflection point were due to the conditions of the beam or to the perturbations by the detector. The intersection point can be further investigated by measurement with

different detectors, and if possible, comparison with the Monte Carlo data to isolate the detector effects.

Lastly, analysis into current analytical functions used in the literature in terms of inflection points allows comparison with the inflection points of measured and Monte Carlo data. The deviation of inflection points can be quantified and this would be an independent method in which analytical functions can be judged as a representation of the actual dose profile. Results may allow the researcher to modify existing analytic functions to better suit the inflection point requirements or to create new analytic functions that are of different form to existing ones.

11.3.6 Change in beam energy across beam profiles

A preliminary investigation was made into the change in beam energy over the beam profile with TPR_{20,10} calculations across the dose profile in appendix D. The known energy dependence of detectors that are available in the market would perturb the penumbral measurements due to fluctuations in the beam energy across the profile.

Monte Carlo simulations are recommended to fully investigate the extent of the change in beam energy across the profile and further investigations can study the influence of the detector beam dependence on the measurement of dose profile in the penumbral region.

The physics related to this is likely to be due to lateral electron disequilibrium (LED), However further investigation would be required to draw out useful physical interpretations in terms of electron range. It was not the objective of this work to describe LED in detail but rather to measure dose distributions and correct them using empirical correction methods. This would however represent potentially a very interesting avenue of future study.

Appendix A: The effect of jaw position for MLC fields in the central axis

Introduction

The recommended jaw position specified by Pinnacle³ for the collection of MLC data was 30x30 cm² (ADAC 2000b). The MLC field sizes varied from 1x1 cm² up to 20x20 cm², which involves varying distances between the MLC field edge and the jaw field edge with each MLC field size variation. It is believed that 30x30 cm was specified for jaws as they would be so far retracted that MLC effects dominate. One issue was this setting meant end leaf leakage would be a significant factor, and in this chapter measurements and analysis were done in the central axis with PDD data.

In clinical treatment mode, the jaw moves to shield the MLC out of field dose from a set distance from the largest rectangular field that the MLC defines. In IMRT, the jaw moves to a position from a set distance from the largest rectangular field amongst the segments in a particular field that the MLC defines. Some centres include a small jaw offset beyond this (typically 0.5 cm).

Since the MLC data acquisition and the treatment planning involve different Jaw-MLC conditions, a set of measurements were made to highlight the differences in the beam characteristics with various Jaw-MLC separations and ensure that the measurements made with the recommended jaw settings corresponded to jaw settings encountered in different clinical situations.

Method

The results were measured to suit the dosimetry of small fields. Thus, a setting of 1x1 cm² was set with the MLCs with the Jaw field size being the variable which allowed for different Jaw-MLC variations.

Table A.1: Settings used for the investigation of Jaw-MLC separation

Constant parameters		Variable parameters	
Collimator (degrees)	0	Jaw Square Field size (cm ²)	1, 2, 3, 4, 5, 10, 20
Gantry (degrees)	0	Depths (cm)	1.5, 5, 10
SSD (cm)	100	MLC end-leaf offset	0 cm
Energy	6 MV	Detector offset	0 cm
Dose Rate	250 MU/min		
MLC Square Field size (cm ²)	1		
Measurement resolution	0.1 cm (min) and 0.25 cm (max) (ADAC 2000b)		
Detector used:	Pinpoint Chamber		

Results: PDD dependence with Jaw-MLC distance

A comparison of the PDD between different Jaw-MLC distances shows firstly that there is a clear decrease in the nominal output with the Jaw set as the same field size as the MLC. Jaw positions larger than a field size of 2x2 cm² seem to have no further effect on the PDD (see figure A.1), in agreement with studies made with a MLC field size of 2x2 cm² (Chow, Seguin et al. 2005).

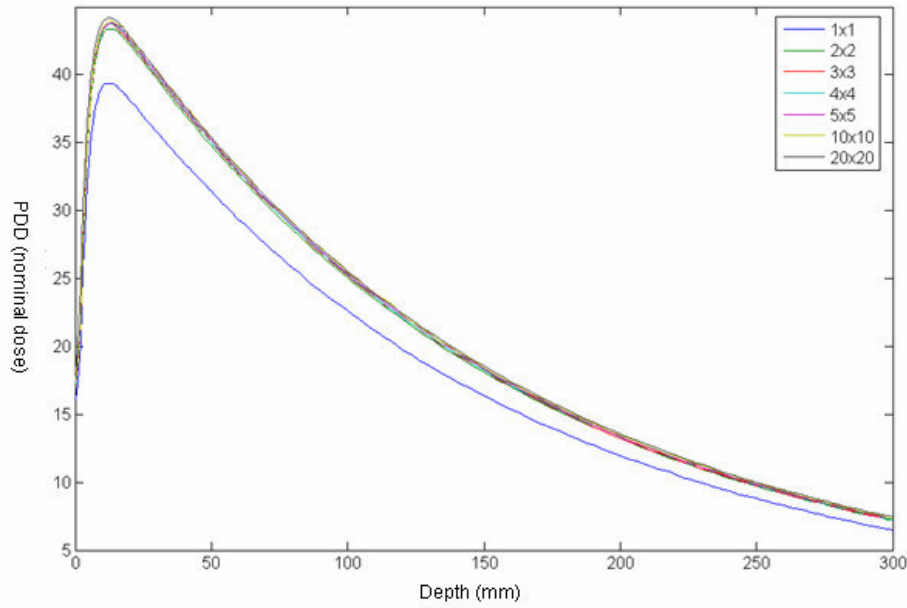
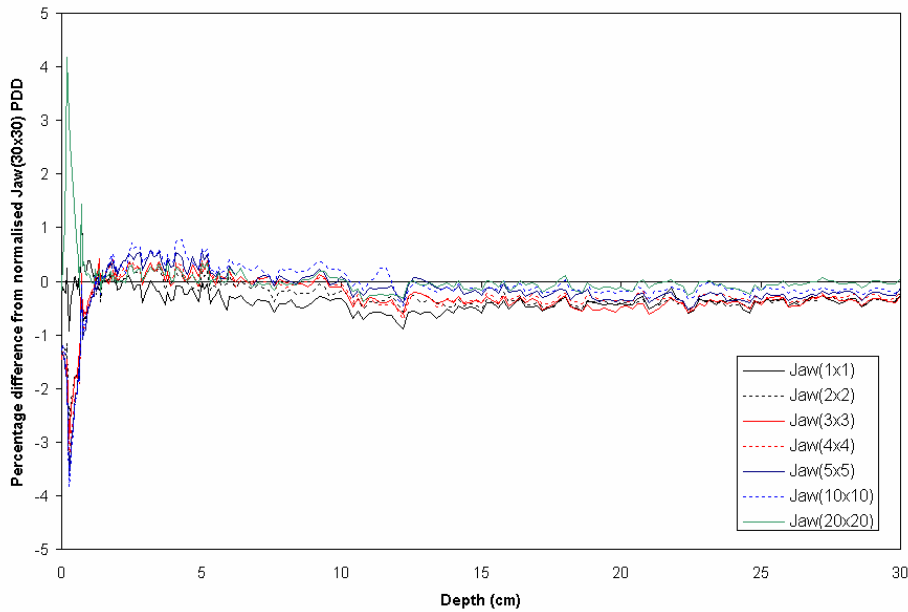


Figure A.1: PDD of MLC defined field of 1x1 cm² with various Jaw field sizes (not normalised)

The data was normalised at a d_{\max} of 1.5 cm and the percentage difference of the PDD from the PDD measured with the jaw setting at 30x30 cm² was plotted in figure A.2. The jaw position of 30x30 cm² was set as the standard with other PDD associated with other jaw settings compared with the standard.



FigureA.2: Diagram showing the percentage difference from a PDD associated with the MLC 1x1 cm² field with a jaw position of 30x30 cm² from other PDDs with different jaw positions.

Discussion

With the standard PDD being set at a Jaw position of $30 \times 30 \text{ cm}^2$, the MLC-Jaw distance of this was effectively 29 cm with a MLC position of $1 \times 1 \text{ cm}^2$. The percentage dose difference from the PDDs from other jaw positions from $1 \times 1 \text{ cm}^2$ to $20 \times 20 \text{ cm}^2$ show that after d_{max} (1.5 cm), dose differences are within $\pm 0.5\%$ from the PDD measured with a jaw position of $30 \times 30 \text{ cm}^2$.

Conclusion

The data suggests that the MLC-jaw distance as having a minimal effect on central axis dose measurements below d_{max} . The use of the jaw settings recommended by the Pinnacle measurement procedure, which involves different MLC-jaw distances with varying MLC field sizes and a fixed jaw field size of $30 \times 30 \text{ cm}^2$, does not affect dose measurements in the central axis significantly.

Appendix B: Profile measurements along leaf-end junction

Introduction

The effect of the dose through the leaf –end junction was investigated with measurement of the profile across the junction with different jaw positions at a MLC $1 \times 1 \text{ cm}^2$ field size. In the measurement procedure used in the main body of the thesis, this was not an issue as an offset was used in the leaf-end junction. The other method of avoiding this is to measure the profile with an offset in the chamber. The aim in this section was to obtain results in the case where neither of these options are undertaken.

Results: Profiles across the width of the MLC (leaf-end junction)

The profile measured across the leaf-end junction, shown below normalised, involves a large out-of-field dose of ~30% due to end leaf leakage of the central axis dose for a MLC $1 \times 1 \text{ cm}^2$ field. It can be seen that the jaw position can attenuate this junction dose very effectively. The leaf-end junction dose is sizeable enough to create a “second” penumbra, which is characterised by the attenuation of the leaf-end junction dose by the jaws.

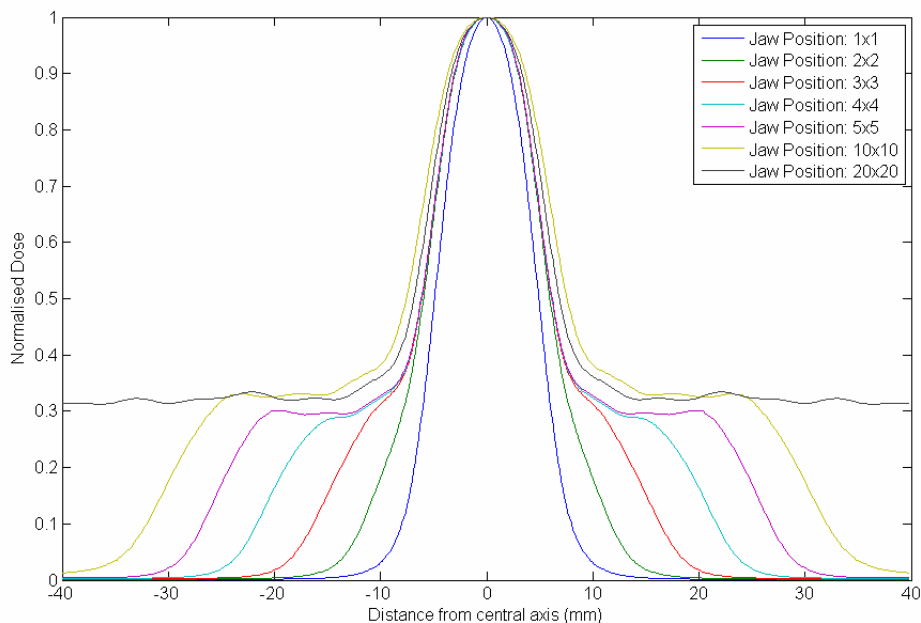


Figure B.1: A normalised perpendicular profile that measures the leaf-end junction introduces large doses out of the field area.

The figure above shows clearly why the leaf-end junction dose is avoided. It is unrepresentative of the dose distribution across the field as the leaf-end junction only covers a small cross-sectional area of the beam; it is up to 30% due to end leaf leakage (leaf end junction dose) of the central axis dose, which makes the 80-20 penumbra definition untenable; and it involves a heavy contribution of scattered dose to the patient which, as can be seen from the figure above, can be blocked by the secondary jaws.

Results: Profiles across the length of the MLC

The effect of the MLC-Jaw offset on profile parameters such as the field edge (defined as 50% of the central axis dose) and the penumbra was investigated. Figure B.2 shows the results of the measured profiles across the length of the MLC.

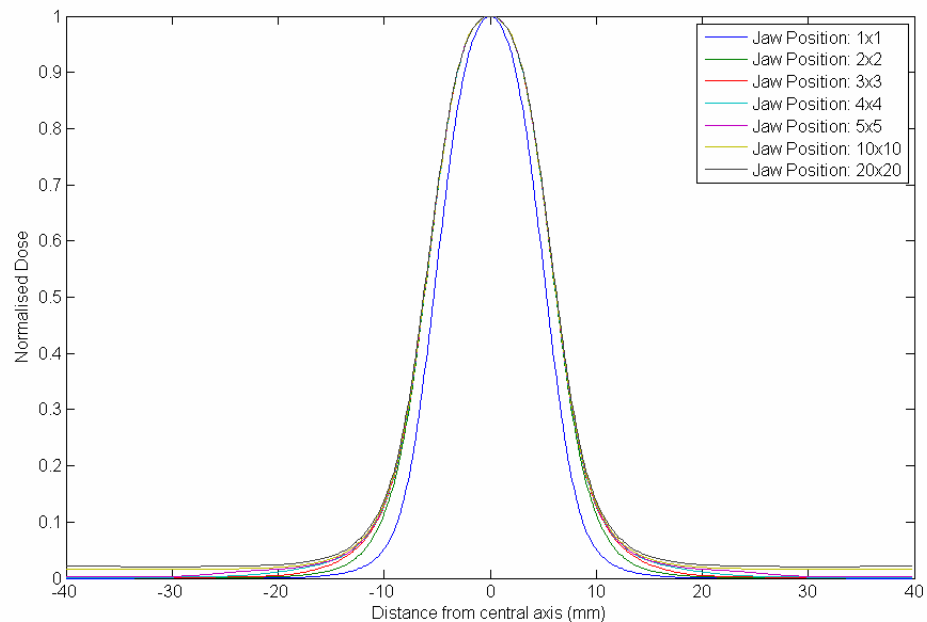


Figure B.2: A normalised parallel profile, depth 15 mm, MLC 1×1, with the pinpoint, that illustrates the effect of jaw position on profiles

A quantitative analysis of the effects of Jaw position, with a constant MLC field of 1×1 cm², on the field size (defined as the dose at 50%) is studied with respect with its dependence with depth. The full width half maximum (FWHM) is equivalent to the field size and was plotted with depth for each jaw setting. As expected, the jaw position of 1×1 cm² resulted in significant differences in FWHM with the other jaw positions by ~2.0 mm. Jaw positions which had a distance from the MLC of more than 2 cm (jaw positions larger than 3×3 cm²) agreed within each other by 0.3 mm at all depths and jaw

positions more than 1 cm from the MLC agreed within each other by 0.5 mm at all depths.

Table B.1: Tabulated analysis of the variation of penumbra and FWHM (in mm), for the profile measured across the length of the MLC

Depth (mm)	Jaw (cm)	Penumbra (mm)	FWHM (mm)
100	1	4.5	11.6
100	2	5.0	13.6
100	3	5.2	13.6
100	4	5.2	13.6
100	5	5.2	13.6
100	10	5.3	13.8
100	20	5.4	13.8

Discussion

The penumbra and FWHM measured changes with the jaw setting (see table B.1). This can be considered to be a function of the beam divergence of a beam with differences in the true effective field size. For a jaw size of $2 \times 2 \text{ cm}^2$ or more with a MLC field size of $1 \times 1 \text{ cm}^2$, the penumbra is within 0.4 mm and the FWHM is within 0.2 mm in the profile across the length of the MLC (see figure B.2). There are large changes in FWHM and penumbra in figure B.1.

Conclusion

The effect of the leaf-end junction on the profile across the length of the MLC are small with the penumbra and FWHM increasing by up to 0.4 mm when the jaw size is increased from $2 \times 2 \text{ cm}^2$ to $20 \times 20 \text{ cm}^2$. The leaf-end junction had large effects on the profile across the width of the MLC (that measures the leaf-end junction) and an offset in chamber of leaf-end junction are recommended to avoid this.

Appendix C: Investigation into the effect of End-leaf offset

Introduction

To avoid the leaf-end junction dose discussed in Appendix B, two methods can be used. Firstly, the chamber can be offset from the central axis away from the leaf-end junction. The potential disadvantage of this is that the profile measured would be away from the central axis and would rely on the flatness and symmetry of the beam in 2 dimensions. The second method involves an offset in the leaf-end junction. Before this method was used, investigation was done into the parameters involved with this method:

- i. To investigate the extent of the end-leaf junction dose.
- ii. To investigate the effect of the end-leaf offset on the end-leaf junction dose as well as other dosimetric parameters
- iii. To investigate the effect of the end-leaf offset on the end-leaf junction dose across the end-leaf junction profile

Method

The end-leaf offset in the MLC was varied from 0 cm (no end-leaf offset) to a value of 2.5 cm. Profiles and PDD were measured for each setting at a MLC setting of $1 \times 1 \text{ cm}^2$ and a jaw setting of $30 \times 30 \text{ cm}^2$. A schematic of the end-leaf technique, implemented using the shaper software (discussed in Chapter 3) is shown in figure C.1.

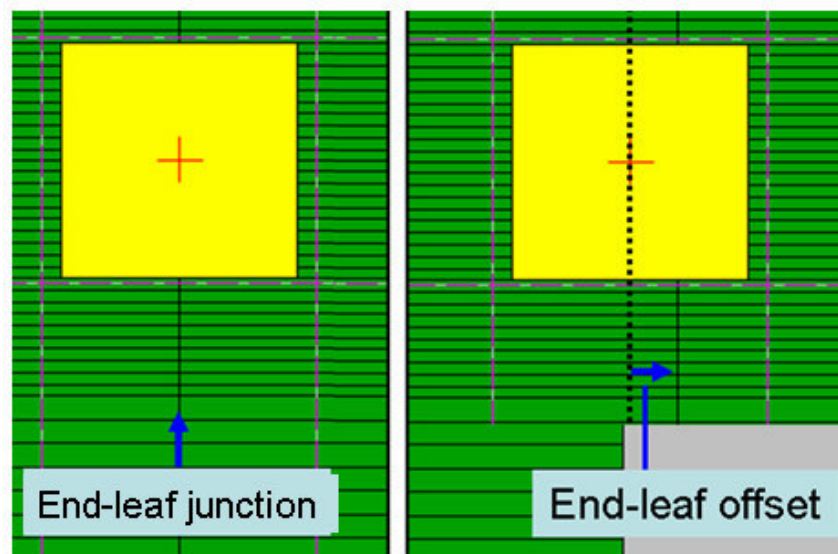


Figure C.1: The end-leaf offset contributes significant dose in the perpendicular profile (left) if measured without any offset. The end-leaf junction can be offset (right) so that the out-of-field perpendicular profile does not measure the end-leaf junction dose.

The variation of the MLC leaf-end junction is shown in figure C.2. The offset was varied from 0.5 cm to 2.5 cm away from the central axis.

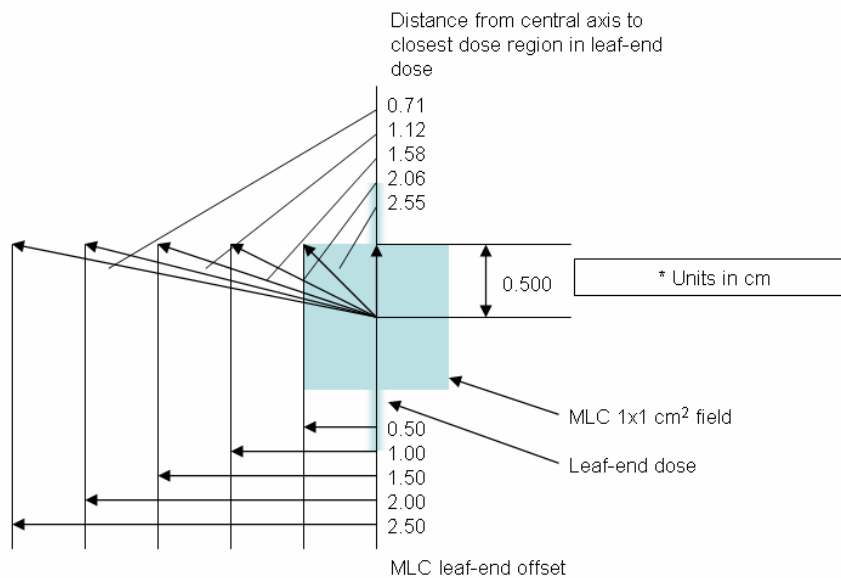


Figure C.2: Consideration of the effective distance of the central axis to the closest dose point in the leaf-end dose region with regards to phantom scatter at 100 cm SAD. The MLC leaf-end offset is also shown here.

Results: Effect of central axis dose with end-leaf offset

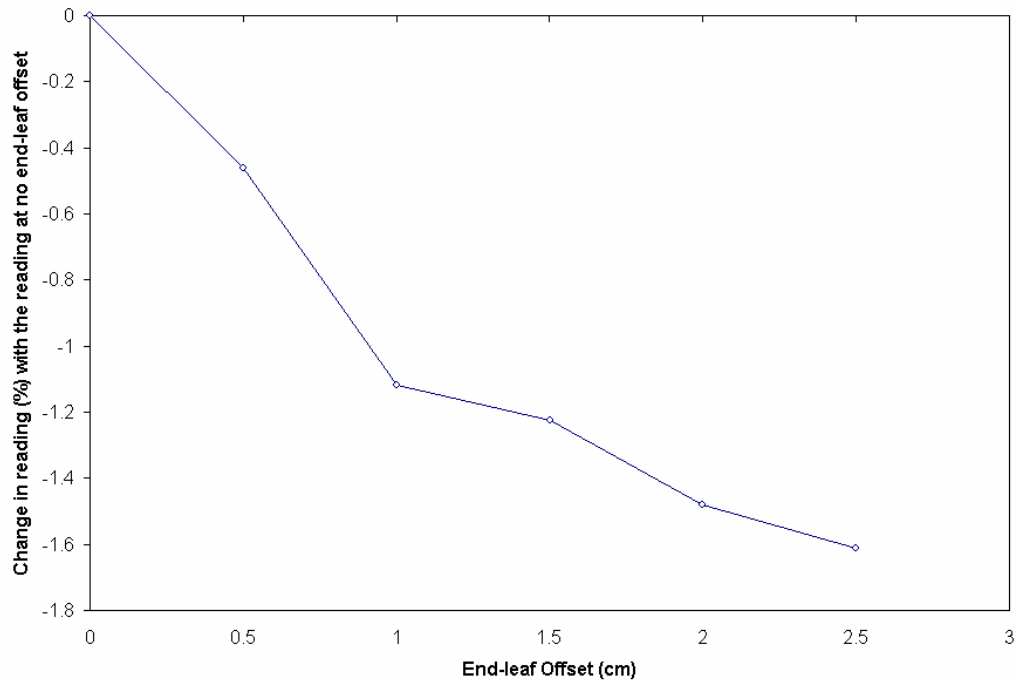


Figure C.3: Effect of end-leaf offset on the dose at dmax. The reading associated with an end-leaf offset of 0 cm was the highest and was used to compare with the other readings.

Results: Effect of profiles with leaf-end offset

The effect of the leaf-end offset on profiles is illustrated with the figure C.4. The curves show large changes in the normalised profiles from an offset of 0, 5, and 10 mm; the profiles with offsets 15 mm, 20 mm, and 25 mm converge to the same shape. With offsets smaller than 15 mm, the out of field dose increases dramatically with decreasing offset. The contribution from the leaf-end junction also clearly adds to the dose out of field to contribute in a larger effective FWHM (field size) with decreasing offset and also an increasing penumbra with decreasing offset.

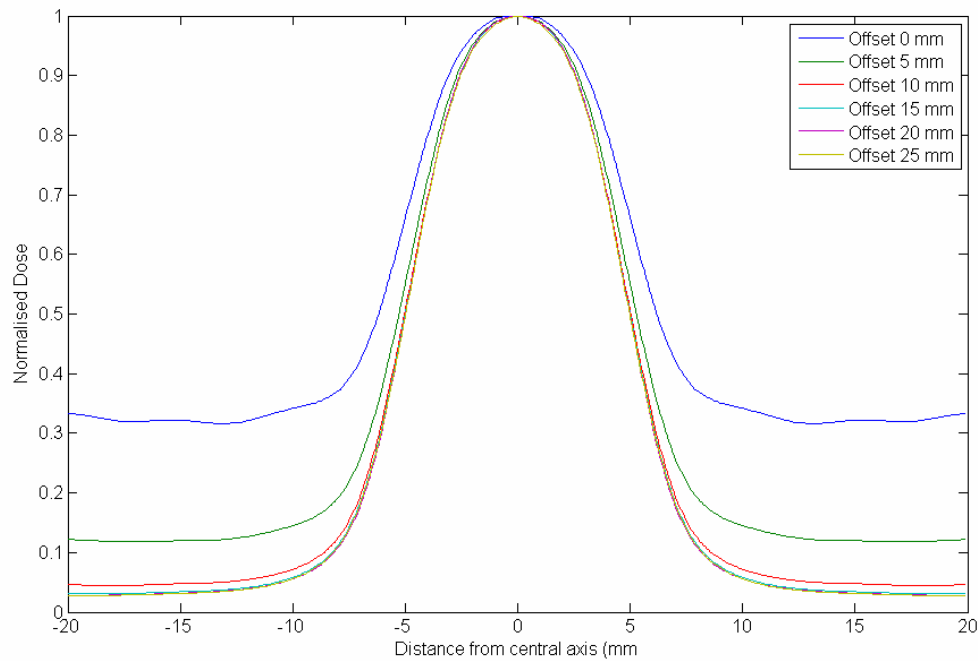


Figure C.4: A normalised perpendicular profile showing the effect of the leaf-end offset on the out of field dose, the field edge, and the penumbra

A quantitative analysis of the field size dependence on the leaf-end offset showed that there was a significant increase in the effective field size with the contribution of the dose from the leaf-end junction. With no offset and measurement on the central axis, the field size was 2.3 cm larger than 10 cm at a depth of 1.5 cm. Use of a leaf-end offset of 0.5 cm reduced the deviation from true field size to within 0.8 cm increase, while a 1.0 cm offset reduced the deviation further to within a 0.2 cm increase. Using a leaf-end offset of 2 cm or higher resulted in stable field sizes corresponding to the set field size (see table C.1).

Table C.1: Table showing the FWHM (field size) in cm with variation with depth and leaf-end offset for a MLC field size of $1 \times 1 \text{ cm}^2$, jaw setting of $30 \times 30 \text{ cm}^2$.

Depth (mm)	Leaf-end offset (cm)					
	0	0.5	1	1.5	2	2.5
15	12.3	10.6	10.0	10.0	10.0	10.0
50	13.0	11.1	10.5	10.5	10.3	10.3
100	13.8	11.6	11.1	10.9	10.9	10.9
200	15.5	12.8	12.2	12.0	12.0	12.0

Results: Effect of leaf-end junction dose with leaf-end offset

The effect of larger shifts of the leaf end was investigated with offsets ranging from 0 to 16 cm offsets investigated. Using the MLC *Shaper* software, the MLCs were programmed to be fully closed with shifts in the position of the closed MLC position also corresponding to measurements in the end leaf junction profile with a shift in the chamber measurement position. Note that the profiles measured in figure C.7 were measured with the chamber having an offset equal to the leaf-end junction offset.

The leaf end junction dose was expected to decrease with increasing offset due to the decrease of photon fluence with off axis distance. With the normalisation point being set at an offset of 0 cm, depth 1.5 cm, and at central axis, increasing offset distances were followed with decreasing leaf end doses across the profile. The jaws, set at $30 \times 30 \text{ cm}^2$, were effective in attenuating the beam to within 2% of the normalisation point.

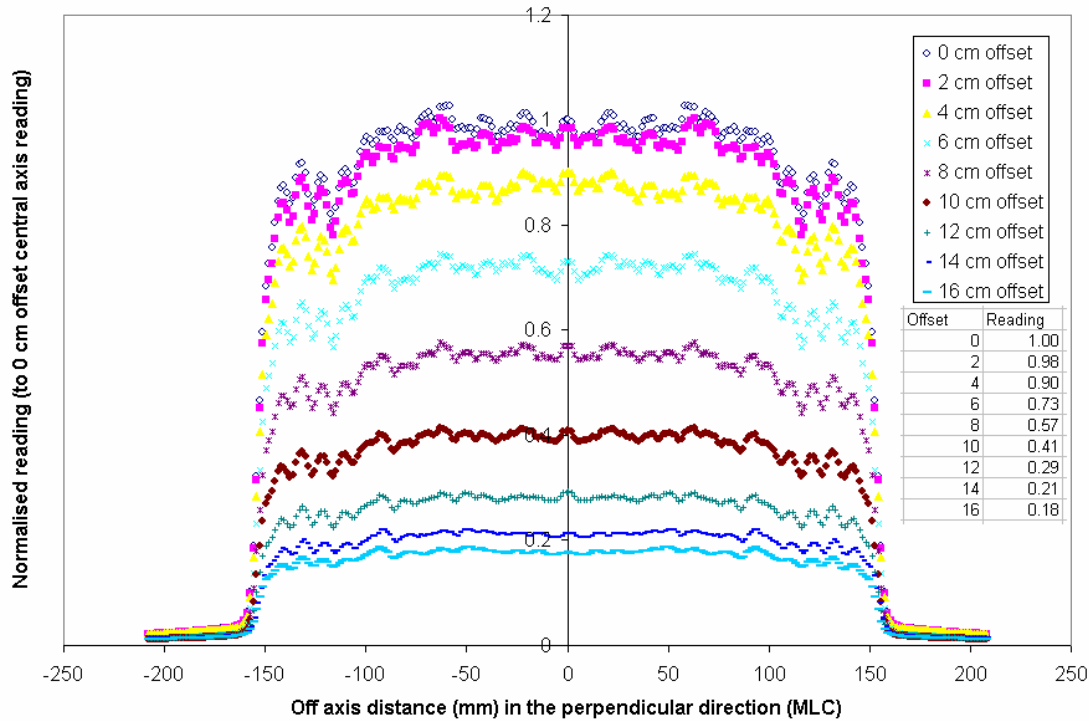


Figure C.5: Plot of the leaf end junction profile at a depth of 1.5 cm for a closed MLC field with various leaf end offsets

A leaf end offset shift of 2 cm reduces the dose at 1.5 cm by 2%. To reduce the leaf end junction dose by 10%, a 4 cm shift is required, for a 27% reduction a 6 cm shift is required, for a 43% reduction a 8 cm shift is required, and for a 59% reduction a 10 cm

shift is required. Further reductions were possible with shifts of 12 cm, 14 cm, and 16 cm (see the table in the figure above).

It is noted that there may be a limit in the offset possible due to the technical specifications of the MLC. The leafs have a set dimension in terms of the length of the lead and behind the leaf lies the electronics. If the leaf end offset is too high, the electronics will receive irradiation which could lead to radiation damage with large exposures.

Discussion

The contribution of scatter from the end-leaf offset may increase the dose to the central axis. The field size used in this case, a MLC field size of $1 \times 1 \text{ cm}^2$, was chosen to highlight this effect. For smaller field sizes, the distance between the central axis and the end-leaf junction outside the main field is smaller. Therefore, the contribution to the central axis from the end-leaf scatter component is relatively larger as the limited lateral electron range from the end-leaf scatter electrons has a larger probability of reaching the central axis point than for large fields. In fact, for MLC fields such as $10 \times 10 \text{ cm}^2$, the scatter from the end-leaf junction may not increase the central axis dose at all as the distance of 5 cm to the end-leaf junction from the central axis is larger than the electron range.

The variation of reading measured at the central axis point at d_{max} due to end-leaf junction may be significant as the reading could later be used to calculate the amount of dose required in treatment planning. With the reading associated with an end-leaf offset of 0 cm as the base, it was observed (see figure below) that the reading in the central axis at d_{max} decreases with increasing end-leaf offset.

The hypothesis that a shift in the leaf-end junction is more favourable than a shift in chamber position:

- i. The change in dose in the central axis due to dose contribution from the leaf-end junction changes with respect to the amount of shift in the leaf-end offset. Since the contribution from the collimator scatter does not decrease to a stable value, it is difficult to decide on a end-leaf offset to be used, with respect to the dose in the central axis.
- ii. If the Pinnacle data manual requires a chamber offset, an issue is whether Pinnacle models the issues raised above, mainly with regards to the issues of decreased dose due measurement of the central part of the profile being off the central axis;

as well as the issue of perturbation of the dose profile due to a lack of rectangular symmetry in the field. The documentation in the user manual and the physics section does not go into sufficient detail into this matter and these questions are left unanswered.

- iii. In clinical treatment, it is a matter of protocol and institution as to whether leaf-end offsets are employed. It may also be a matter of protocol in terms of the amount of leaf-end offsets used.

Conclusion

Within the technical limits with relations to preventing irradiation of the electronic circuitry connected to the MLC leaves, the leaf end offsets should be maximised in clinical treatment to reduce the out of field dose as much as possible. This is combined with movement of the jaw to reduce the leaf end junction dose, but with IMRT some MLC configurations would involve significant MLC-jaw distances. As a minimum, a leaf end offset of more than 2.0 cm or more is recommended to reduce any effect of the leaf end junction to the effective field size and the effective penumbra of the radiation profile.

Appendix D: Effect of Lateral electron equilibrium and beam quality estimates with field size

Introduction

The beam quality of the MLC and the jaw defined fields were analysed across field sizes and the minimum LEE equation (see equation 2.1) was invoked:

- i. To quantify the effect of field size on beam quality estimates with MLC and Jaw defined field sizes
- ii. To quantify the effect of lateral electron equilibrium with MLC and Jaw defined field sizes
- iii. To determine the minimum field size for lateral electron equilibrium

Method

The $\text{TPR}_{(20,10)}$ was calculated from the PDD with the formalism described in Chapter 3, which took into account the changes in phantom scatter, source to surface distance, and change in effective PDD used. The relationship between TPR and lateral electron equilibrium was also invoked (see equation 2.1).

Results: Variation of TPR with field size

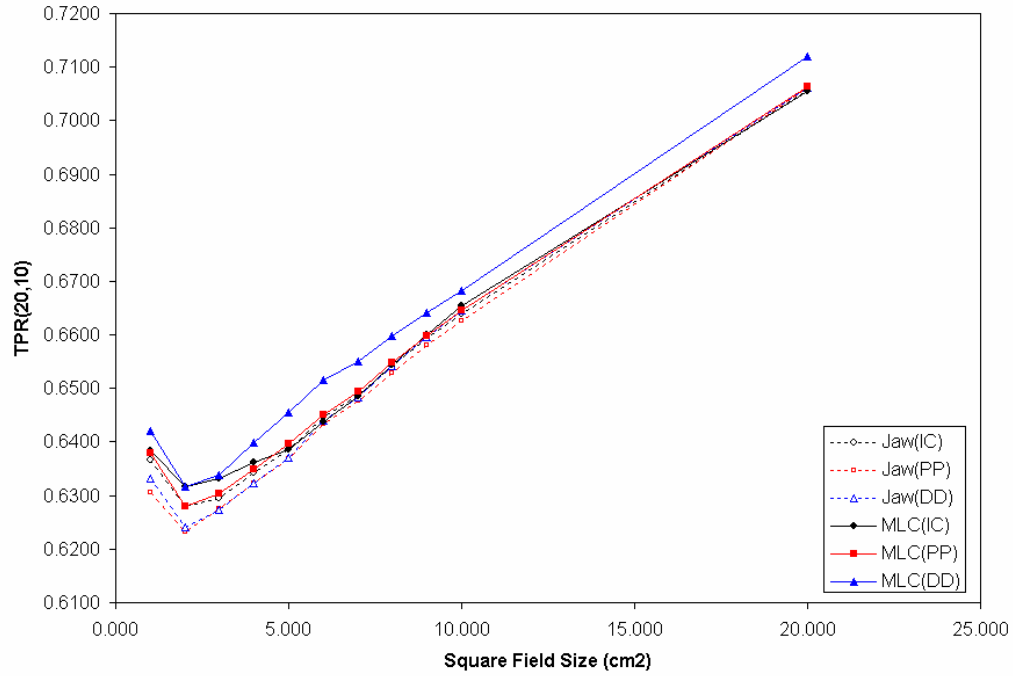


Figure D.1: Plot of TPR (20,10) with Square Field Size defined by the Jaw and MLC and measured with IC, PP, and DD.

Figure D.1 shows that the $TPR_{(20,10)}$ decreased with decreasing field size to a minimum $TPR_{(20,10)}$ of $2 \times 2 \text{ cm}^2$, with a slight upturn in $TPR_{(20,10)}$ with a field size of $1 \times 1 \text{ cm}^2$ for both MLC and Jaw defined square field sizes. Therefore, calculations indicate that the beam is less penetrating at lower field sizes.

For Jaw field sizes and with the pinpoint detector, the $TPR_{(20,10)}$ varied from 0.63 at $1 \times 1 \text{ cm}^2$, to 0.62 at $2 \times 2 \text{ cm}^2$, to 0.66 at $10 \times 10 \text{ cm}^2$, and 0.71 at $20 \times 20 \text{ cm}^2$. Similarly, for MLC field sizes, the $TPR_{(20,10)}$ varied from 0.64 at $1 \times 1 \text{ cm}^2$, to 0.63 at $2 \times 2 \text{ cm}^2$, to 0.66 at $10 \times 10 \text{ cm}^2$, and 0.71 at $20 \times 20 \text{ cm}^2$.

There were only minor differences in beam quality between the MLC and jaw fields, suggesting that the effect of scatter contribution in the collimator from the jaw and leaf edge and also the transmission through the jaw and leaf are only a weak factor in the determinant of the central axis beam quality factor $TPR_{(20,10)}$.

Results: Variation of lateral electron equilibrium with field size

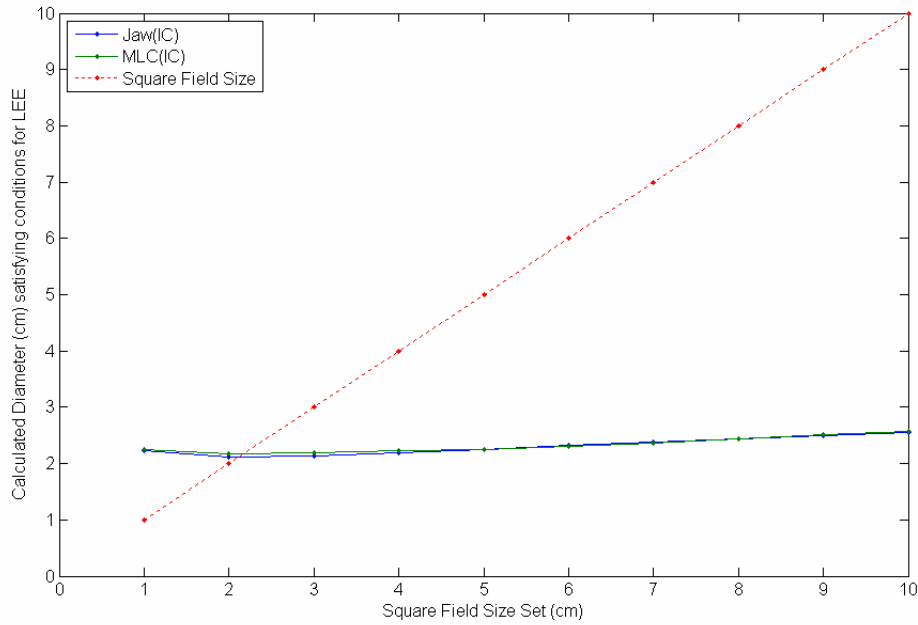


Figure D.2: Variation of the diameter associated with lateral electron equilibrium as calculated from $TPR_{(20,10)}$ compared with the increase of square field size (red). The intersection shows the minimum field size where there is LEE for the case of Jaws and MLCs.

The effect of a variation in $TPR_{(20,10)}$ affects electron equilibrium because the beam energy is related to lateral electron scattering. The relationship between the minimum radius required for lateral electron equilibrium (LEE) was correlated with $TPR_{(20,10)}$, and this was dependent on field size. The minimum diameter required for LEE was calculated and the variation with the field size was weak: for jaw field sizes, the diameter required for LEE was 2.23 cm at a field size of $1 \times 1 \text{ cm}^2$, 2.12 cm at a field size of $2 \times 2 \text{ cm}^2$, 2.56 cm at a field size of $10 \times 10 \text{ cm}^2$, and 3.05 cm at a field size of $20 \times 20 \text{ cm}^2$.

Discussion

The increase of the diameter required for LEE is significantly slower than the natural increase in irradiated field size with increasing jaw movement. The intersection of the two curves determines the point of transition of lateral electron equilibrium. Based on such an analysis, the transition for lateral electron equilibrium occurs at a field size of $2.13 \times 2.13 \text{ cm}^2$ for Jaws and $2.17 \times 2.17 \text{ cm}^2$ for MLC.

For MLCs, however, the resolution is limited in the direction perpendicular to jaw motion (for Varian MLCs) and thus the clinically effective transition point is $2.5 \times 2.5 \text{ cm}^2$.

It was found that the beam quality did not differ strongly between the use of jaws or MLCs. The analysis of the beam quality with field size indicates that the beam quality decreases (beam softens) to a minimum at a field size of $2 \times 2 \text{ cm}^2$ from large field sizes and then increases slightly at a field size of $1 \times 1 \text{ cm}^2$. The beam quality at a field size of $10 \times 10 \text{ cm}^2$ for our linac was 0.66, and varied from 0.63 with small fields to 0.71 for large fields.

The minimum field size for lateral electron equilibrium is dependent on the field size set on the linac itself. This dependence is weak and was calculated to vary between 2.12 ($2 \times 2 \text{ cm}^2$) and 3.05 cm ($20 \times 20 \text{ cm}^2$). For lateral electron equilibrium, the irradiated field size needs to be larger than the minimum diameter for LEE. The variance in this diameter with field size was not previously investigated in the literature; the intersection of the increase in irradiated field size with the LEE diameter determined that the transition to *small field* where there is a lack of electron equilibrium occurred at a field size of $2.17 \times 2.17 \text{ cm}^2$.

Conclusion

The transition to *small field* measured in this study represents a lower value than with other results that have generally evaluated this value at $3 \times 3 \text{ cm}^2$ (Heydarian, Hoban et al. 1996; Crop, Reynaert et al. 2007). The results agree with the value of 2-2.6 diameter field size (Björngard, Tsai et al. 1990). To avoid small field dosimetry in the past, some centres have limited their measurements to $4 \times 4 \text{ cm}^2$ in the past but our results indicate that measurements can be made up to $3 \times 3 \text{ cm}^2$ that satisfy the condition for lateral electron equilibrium.

Appendix E: Basic mathematical modelling of the Central Axis dose versus the Out of Field Dose

Introduction

A basic mathematical model was formulated to:

- i. Investigate the out of field (transmission) dose as compared to the central axis dose as a function of field size for Jaws and MLC
- ii. Use a simple model to investigate the effects of out of field doses clinically

Method

Profile measurements were made at a depth of 10 cm at various field sizes ranging from $1 \times 1 \text{ cm}^2$ to $20 \times 20 \text{ cm}^2$ with both the jaw and the MLC. The reading was taken at the outermost region of the profile and divided with the reading at the central axis. This ratio was calculated as a percentage and analysed into a simple model to investigate the variation of this ratio clinically with field size.

This data was used to create a simplified model to estimate the effect of field size on the out of field dose. A central square field sizes that would give dose to a theoretical tumour was considered, with a larger square field size outside that gives out-of-field dose to theoretical normal tissue. The end leaf leakage due to the finite distance between two sets of rounded leaf ends can be moved off axis and also be blocked by the jaw. The interleaf transmission, which is along the perpendicular to leaf motion axis, is reduced by the tongue-and-groove design. Both these effects are not considered in this simplified model.

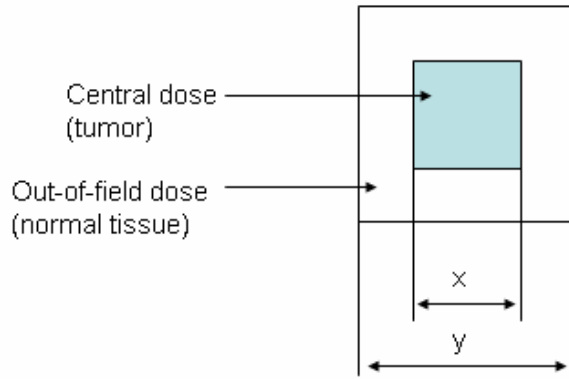


Figure E.1: Figure showing the dimensions of the model used

The radiation profile was considered to be step functions, which involve equations that multiply the area by the dose at a representative region. Furthermore, the estimation of the dose to normal tissue over the dose to the tumour dose is represented in one slice at a depth of 10 cm only.

$$\begin{aligned}
 Dose(tumor) &= d_f x^2 \\
 Dose(normal) &= d_{out} (y^2 - x^2) \\
 \frac{Dose(normal)}{Dose(tumor)} &= \frac{d_{out}}{d_f} \frac{(y^2 - x^2)}{x^2} \\
 &= \frac{d_{out}}{d_f} \frac{((x+z)^2 - x^2)}{x^2} \\
 &= \frac{d_{out}}{d_f} \frac{(2xz + z^2)}{x^2}
 \end{aligned}$$

(E.1)

For y (see equation E.1), various values were tested. y was made equal to x plus z, where z was a unit in cm that represented the area around the tumour cell considered. z, for a MLC field, could also represent the position of the jaws –for large segments, the jaws do not follow each configuration but is subtended by the maximum MLC configuration for the entire segment.

Results: The ratio of out of field to central axis dose in the profile

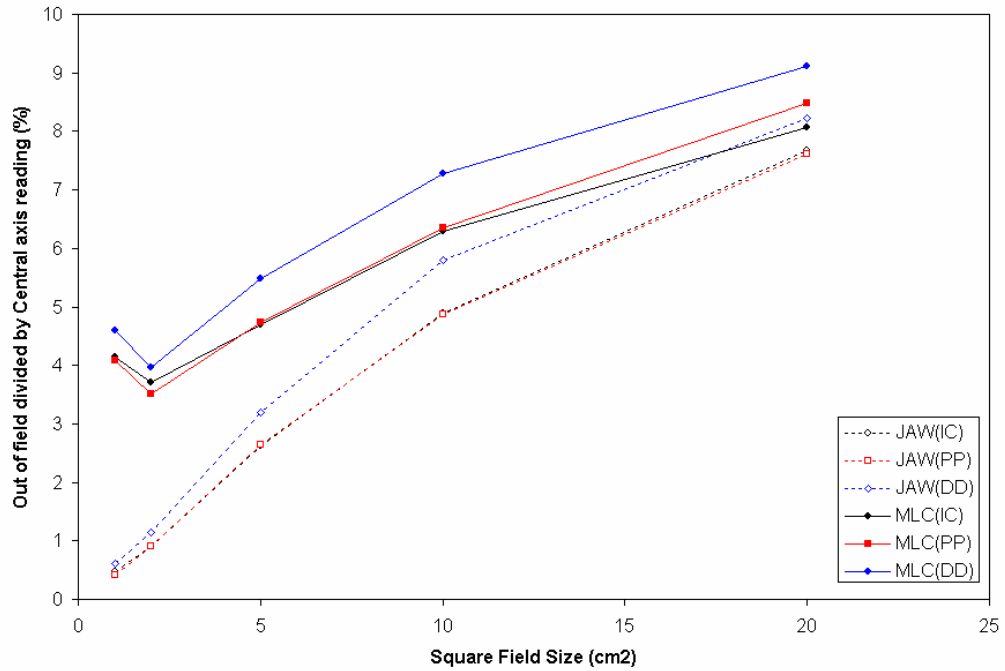


Figure E.2: Illustration of the out of field relative to the central axis reading as a % with increasing square field size for the case of MLC and Jaw with different detector readings. Data analysed with a depth of 10 cm.

Figure E.2 illustrates that it may be more beneficial to use smaller field sizes as the scattered dose from the out of field component is smaller as a ratio of central axis dose with smaller field sizes for both jaw and MLC fields.

Results: Simple modelling of the integral normal tissue and tumour dose

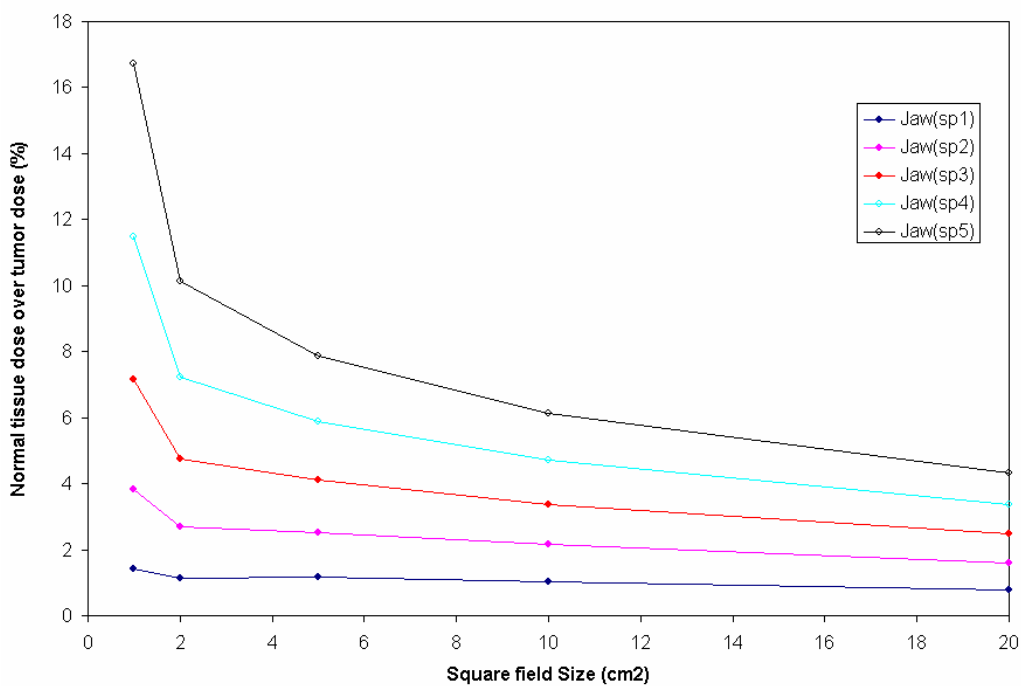


Figure E.3: Results of modelled normal dose over tumour dose for jaw settings. Sp1 considers a normal tissue volume 1 cm around the tumour volume.

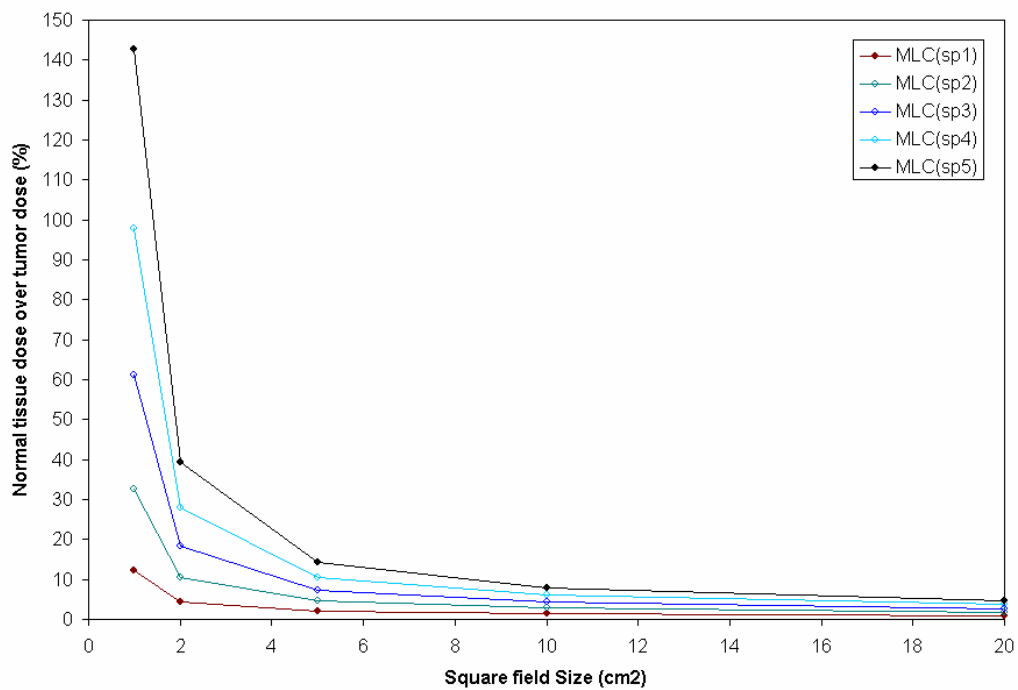


Figure E.4: Results of modelled normal dose over tumour dose for MLC settings. Sp1 considers a normal tissue volume 1 cm around the tumour volume.

The results (see figure E.3 and E.4) show that the normal tissue dose over tumour dose (which one hopes to minimise), decreases with field size and with decreasing normal tissue, and is also lower with jaws than with MLC. Furthermore, the increase in the normal tissue dose over tumour dose is more significant at the small field sizes of $1 \times 1 \text{ cm}^2$ and $2 \times 2 \text{ cm}^2$, with the effect of the amount of normal tissue also becoming more significant in this region. For a $1 \times 1 \text{ cm}^2$ MLC field, the integral dose to normal tissue approaches the tumour dose with a $5 \times 5 \text{ cm}^2$ field exposed normal tissue area.

Discussion

It is interesting to note that the out of field dose as a ratio to the central field dose decreases with increasing field size, for both MLC and jaw. With jaw defined field sizes, the out of field dose is $\sim 0.5 \%$ of the central axis dose for a $1 \times 1 \text{ cm}^2$ field, increasing to $\sim 7.0\%$ with a $20 \times 20 \text{ cm}^2$ field. With MLC defined field sizes, the out of field dose is $\sim 4.0 \%$ of the central axis dose for a $1 \times 1 \text{ cm}^2$ field, increasing to $\sim 8.0\%$ with a $20 \times 20 \text{ cm}^2$ field. In terms of dose to a point, the data suggests that it is advantageous to clinically treat with lower field sizes due to this effect.

However, a simplified model illustrated the effects of dose with integration in two dimensions. The integral dose to the irradiated field was compared to the integral dose to an area outside the irradiated field that represented the dose to normal tissue. The larger the area of the normal tissue outside the irradiated field, the larger the ratio was for normal tissue dose with respect to tumour dose. In addition, the larger the field size, the smaller the ratio became. It is desirable to have a small ratio, as the smaller the ratios of normal tissue dose to tumour dose, the larger the tumour to normal tissue dose.

For small field sizes, especially below $2 \times 2 \text{ cm}^2$, the normal tissue dose to tumour dose ratio showed a large dependence on the amount of normal tissue irradiated in the field. The relative area was a significant factor in this: for larger fields, the ratio of the area irradiated by the normal tissue versus normal tissue decreases.

Conclusions

Small MLC field sizes where the jaw does not provide adequate coverage should be avoided where possible. In terms of reducing integral dose to normal tissue, larger field sizes are desirable. The size of the field size may, however, be determined by the end point of conformality to the PTV with 3DCRT. For minimisation of integral normal tissue dose in IMRT, however, the minimum field size is a variable that can be

controlled, and since the jaw does not adjoin to each MLC configuration, the minimum field size set should be preferably $>3 \times 3 \text{ cm}^2$.

Appendix F: MCC File format

The data from the beam data acquisition system was produced in the MCC2 format. The format was used to separate the many profiles measured into fields such as

- i. Field size
- ii. Depth
- iii. Profile plane (crossplane or inplane) or PDD
- iv. Detector used

Other parameters that can be analysed, which were not modified in this study include:

- i. SSD
- ii. Off-axis parameter

Table F.1 and table F.2 illustrates important features of the MCC2 file format, with the left column showing the raw data and the right column showing comments on the properties of the data.

Table F.1: File format of the mcc format used with MEPHYSTO mc² (Part 1/2)

BEGIN_SCAN_DATA	Identifier for start of file
FORMAT=CC-Export V1.60	File header
FILE_CREATION_DATE=23-Jun-2005 10:58	
LAST_MODIFIED=23-Jun-2005 10:58	
BEGIN_SCAN 1	Identifier for start of first scan
TASK_NAME=tba	PDD Profiles Task designation
PROGRAM=tbaScan	Name of measuring module
COMMENT=Test-Messung / Test Measurement	Comment on scan
MEAS_DATE=23-Jun-2005 10:57	Date and time of measurement
LINAC=LINAC C	Radiation device data
MODALITY=EL	
ISOCENTER=1000.00	
INPLANE_AXIS=Inplane	
CROSSPLANE_AXIS=Crossplane	
DEPTH_AXIS=Depth	
INPLANE_AXIS_DIR=GUN_TARGET	
CROSSPLANE_AXIS_DIR=LEFT_RIGHT	
DEPTH_AXIS_DIR=UP_DOWN	Radiation device settings
ENERGY=4.00	
SSD=950.00	
SCD=450.00	
BLOCK=0	
WEDGE=App10×10	
FIELD_INPLANE=100.00	
FIELD_CROSSPLANE=100.00	
FIELD_TYPE=RECTANGULAR	
GANTRY=0.00	
GANTRY_UPRIGHT_POSITION=0	
GANTRY_ROTATION=CW	
COLL_ANGLE=0.00	
COLL_OFFSET_INPLANE=0.00	
COLL_OFFSET_CROSSPLANE=0.00	
SCAN_DEVICE=MP3	Measuring device and detector
SCAN_DEVICE_SETUP=BARA_RIGHT_LEFT	
ELECTROMETER=TANDEM	
RANGE_FIELD=AUTO	
RANGE_REFERENCE=AUTO	
DETECTOR=PLANE_PARALLEL_CHAMBER	
DETECTOR_RADIUS=0.00	
DETECTOR_NAME=PTW 34001 Roos	
DETECTOR_SN=0000	
DETECTOR_CALIBRATION=84810000.00	
DETECTOR_IS_CALIBRATED=1	
REF_FIELD_DEPTH=0.00	Measurement reference parameters
REF_FIELD_DEFINED=WATER_SURFACE	
REF_FIELD_INPLANE=100.00	
REF_FIELD_CROSSPLANE=100.00	

Table F.2 format of the mcc format used with MEPHYSTO mc² (Part 2/2)

SCAN_CURVETYPE=PDD	Measurement parameters
SCAN_OFFAXIS_INPLANE=0.00	
SCAN_OFFAXIS_CROSSPLANE=0.00	
SCAN_ANGLE=0.00	
SCAN_DIAGONAL=NOT_DIAGONAL	
SCAN_DIRECTION=NEGATIVE	
MEAS_PRESET=REFERENCE_DOSEMETER	
MEAS_TIME=0.500 Preset mode	
MEAS_UNIT=A.U.	
SCAN_SPEEDS=20.00; 5.00;40.00; 40.00;400.00; 50.00;	Advanced measurement parameters
DELAY_TIMES=20.00; 0.000;150.00; 0.000;400.00; 0.000;	
PRESSURE=1013.20	Miscellaneous
TEMPERATURE=20.00	
NORM_TEMPERATURE=20.00	
CORRECTION_FACTOR=1.0000	
BEGIN_DATA	Identifier for start of measuring data
0.001.4096E+00	Measuring data
1.001.4180E+00	
2.001.4338E+00	
3.001.4839E+00	
4.001.5391E+00	
5.001.6168E+00	
6.001.6523E+00	
7.001.6772E+00	
8.001.6600E+00	
9.001.5993E+00	
10.001.5081E+00	
11.001.3641E+00	
12.001.2253E+00	
13.001.0029E+00	
14.00819.66E-03	
15.00613.47E-03	
17.00291.78E-03	
19.0092.467E-03	
21.0022.923E-03	
23.007.4504E-03	
25.006.0302E-03	
27.005.9090E-03	
29.005.7898E-03	
31.005.6626E-03	
33.005.6183E-03	
35.005.5320E-03	
40.005.2793E-03	
45.005.1116E-03	
50.004.9190E-03	
END_DATA	Identifier for end of measuring data
END_SCAN 1	Identifier for end of first scan
END_SCAN_DATA	Identifier for end of file

Appendix G: Beam quality across the profile

Introduction

In theory, the measure of beam quality involves the $PDD_{20,10}$, which is defined as the division of the dose at a depth of 20 cm by the dose at a depth at 10 cm. The PDD is measured and calculated on the central axis normally. This chapter aims to calculate a value of beam quality across the profile.

Method

The Mephysto software acquires the profile data with respect to depth with the same amount of spatial data points. The number of data points remains the same but the spacing between the data points are increased with depth to account for the divergence of the beam with depth. The division of two data points at a depth of 20 cm and 10 cm was performed across the data points to determine how the beam quality changes with the profile (see figures G.1, G.2, G.3).

Results

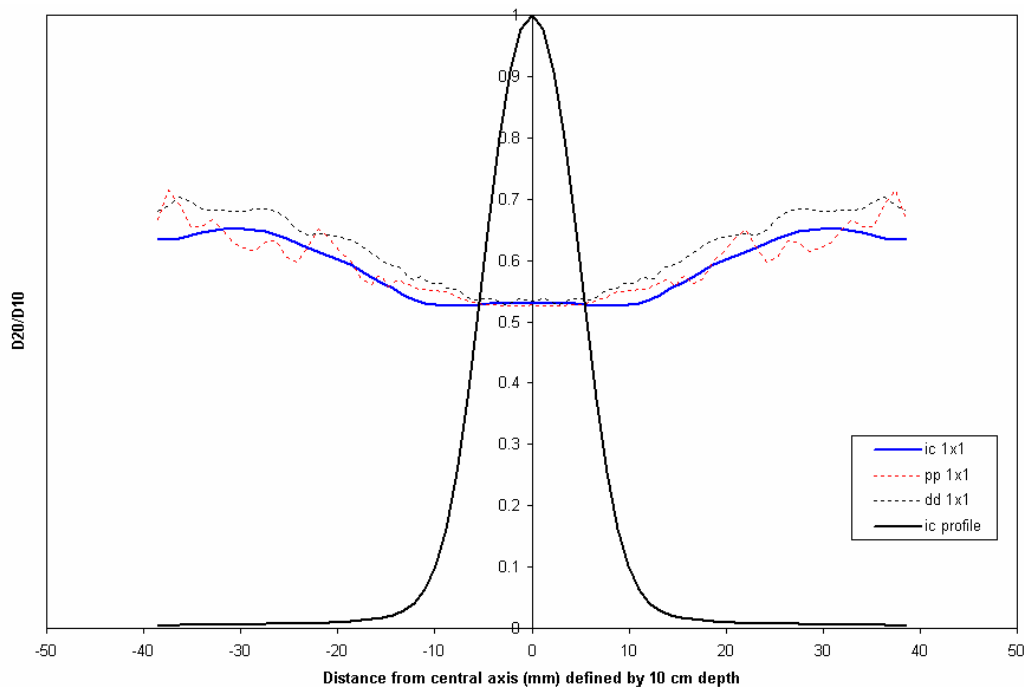


Figure G.1: Variation of beam quality across the profile for a 1x1 cm² field

For a 1×1 field, the penumbral region exhibits minimal beam quality change, based on the measurement of the beam quality by the 0.125 cc ionisation chamber (see figure G.1). Based on the measurement of beam quality by the PP and the DD, the penumbra region exhibits small but non-zero beam quality change. A similar pattern is seen across the penumbra for the 5×5 and 10×10 cm² field size (see figures G.2 and G.3).

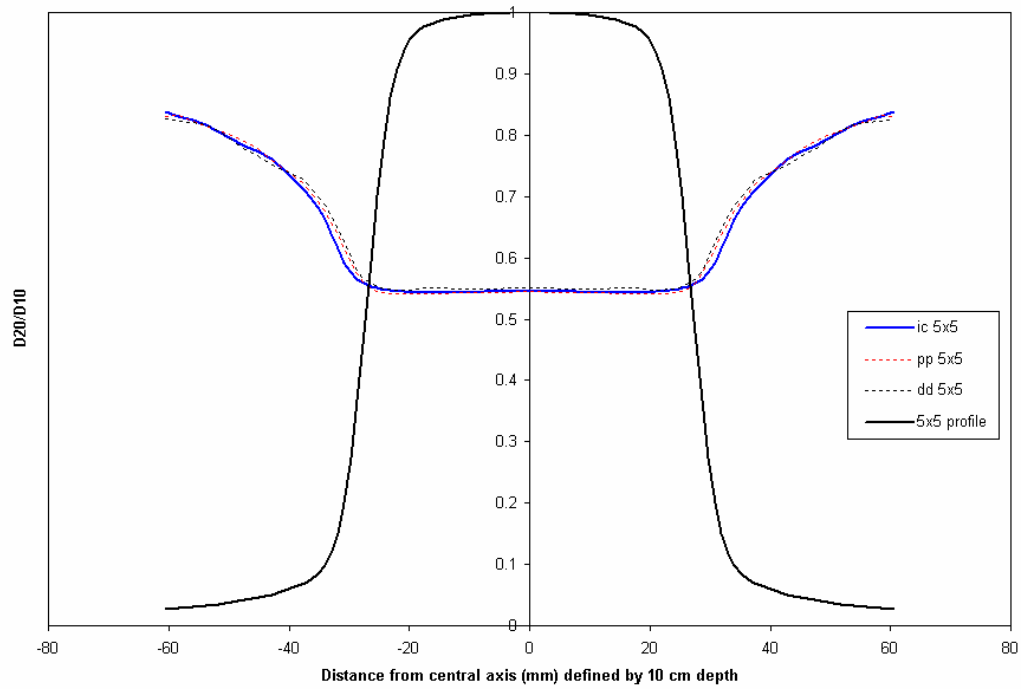


Figure G.2: Variation of beam quality across the profile for a 5×5 cm² field

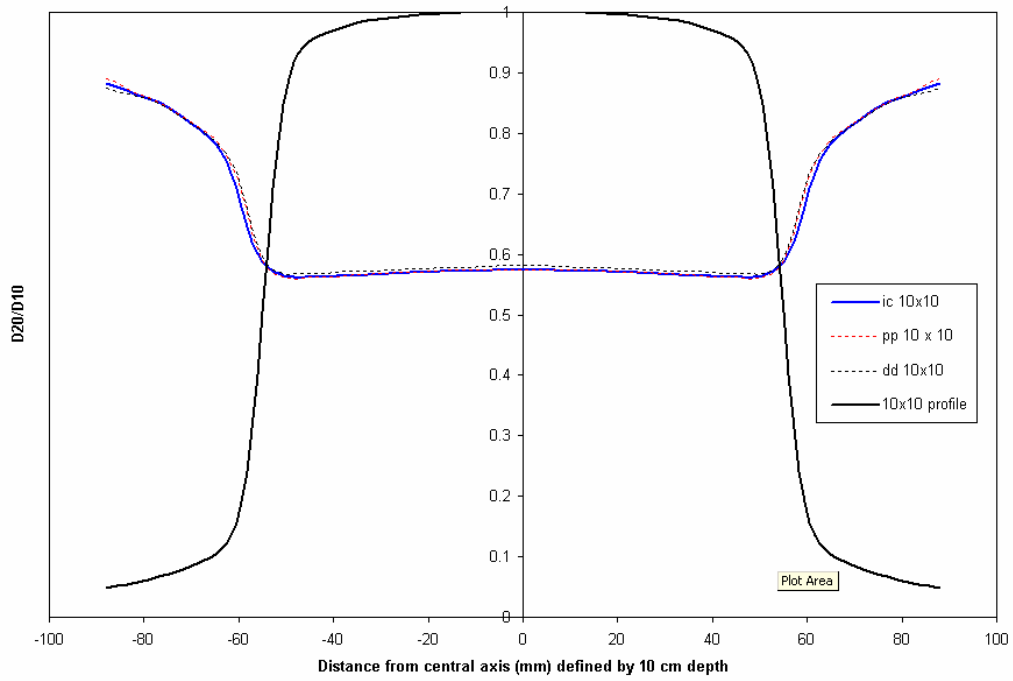


Figure G.3: Variation of beam quality across the profile for a 10×10 cm² field

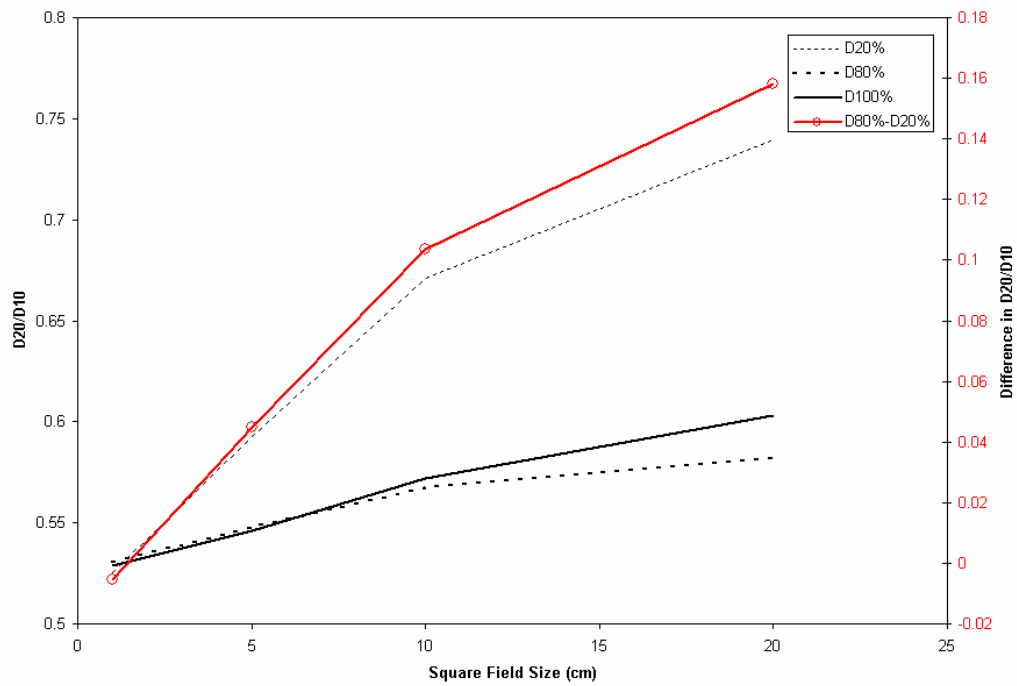


Figure G.4: The beam quality variation with field size (black). The change in beam quality across the profile is also plotted (red) with field size.

Figure G.4 indicate that the change in beam quality in the penumbra corresponding to the dose level at 80% and at 20% increase with square field size. The red line

(corresponding to the axis on the right hand side) denotes the change in beam quality in the region of the penumbra.

Discussion

With small field sizes, the change in beam quality in the penumbra is minimal, but the beam quality increases from the dose at 80% to the dose at 20% by ~ 0.1 at a field size of $10 \times 10 \text{ cm}^2$ and by ~ 0.16 at a field size of $20 \times 20 \text{ cm}^2$. The change in beam quality in the penumbral region is larger with larger field sizes.

Results also indicate that the beam quality on the central axis matches the penumbra at small field sizes of $1 \times 1 \text{ cm}^2$, but the penumbra at the dose level 20% increase strongly while the beam quality at the dose level of 80% decreases weakly.

Conclusion

More investigations are required to fully investigate the effects of the change in beam quality over the profile. However, it is clear that (1) the beam is softer out of the field as compared to in the central axis, (2) the change in beam quality in the penumbral region is significant, (3) the change in beam quality in the penumbral region is larger with increasing field size.

Appendix H: Results of source size survey

Note that

- In centres where multiple linacs were submitted, each linac was treated as a separate entry. Thus, the statistics are based on the number of linacs (and not the number of centres).
- Note that the source size survey was sent on the *Pinnacle List Server* and thus only Pinnacle RTPS were studied.
- The institution and contact person have been omitted from the tabulated data.
- The survey results incorporated data from the 5/10/08 to the 1/1/09.

Table H.1: Anonymous results from the source size survey for the Pinnacle RTPS (PTO)

Machine	Date	Photon Energy (MV)	Source size cross plane (cm)	Source size gun-target (cm)	RTPS	Dosimeter
Varian 21iX	2001-2006	18x	0.17	0.14	Pinn 8.0m	IC15 chamber (0.13 cc sensitive volume)
Varian 21iX	2001-2006	18x	0.17	0.14	Pinn 8.0m	IC15 chamber (0.13 cc sensitive volume)
Varian 21EX	2001-2006	18x	0.17	0.14	Pinn 8.0m	IC15 chamber (0.13 cc sensitive volume)
Varian 21EX	2001-2006	18x	0.17	0.14	Pinn 8.0m	IC15 chamber (0.13 cc sensitive volume)
Varian 21EX	2001-2006	18x	0.17	0.14	Pinn 8.0m	IC15 chamber (0.13 cc sensitive volume)
Varian 21EX	2001-2006	18x	0.17	0.14	Pinn 8.0m	IC15 chamber (0.13 cc sensitive volume)
Varian Trilogy	2001-2006	18x	0.17	0.14	Pinn 8.0m	IC15 chamber (0.13 cc sensitive volume)
Varian 2100 C	1998	18x	0.1947	0.0964	Pinn 8.0m	IC15 chamber (0.13 cc sensitive volume)
Varian	2001-2006	6x	0.1	0.1	Pinn 8.0m	IC15 chamber

21iX						(0.13 cc sensitive volume)
Varian 21iX	2001-2006	6x	0.1	0.1	Pinn 8.0m	IC15 chamber (0.13 cc sensitive volume)
Varian 21EX	2001-2006	6x	0.1	0.1	Pinn 8.0m	IC15 chamber (0.13 cc sensitive volume)
Varian 21EX	2001-2006	6x	0.1	0.1	Pinn 8.0m	IC15 chamber (0.13 cc sensitive volume)
Varian 21EX	2001-2006	6x	0.1	0.1	Pinn 8.0m	IC15 chamber (0.13 cc sensitive volume)
Varian 21EX	2001-2006	6x	0.1	0.1	Pinn 8.0m	IC15 chamber (0.13 cc sensitive volume)
Varian 21EX	2001-2006	6x	0.1	0.1	Pinn 8.0m	IC15 chamber (0.13 cc sensitive volume)
Varian Trilogy	2001-2006	6x	0.1	0.1	Pinn 8.0m	IC15 chamber (0.13 cc sensitive volume)
Varian 2100 C	1998	6x	0.1109	0.0964	Pinn 8.0m	IC15 chamber (0.13 cc sensitive volume)
Varian 21EX	1999	6x	0.1	0.077	Pinn 8.0m	IC15 chamber (0.13 cc sensitive volume)
Varian 2100 CD	2001	10x	0.028	0.028	Pinn 6.2b	Scanitronix shielded photon diode p-type effect detector diameter 2.5 mm
Varian 2100 CD	2005	10x	0.01	0.02	Pinn 7.4f	Scanitronix shielded photon diode p-type effect detector diameter 2.5 mm
Varian 2100 CD	2005	10x	0.01	0.02	Pinn 7.4f	Scanitronix shielded photon diode p-type effect detector diameter 2.5 mm
Varian	2006	10x	0.02	0.02	Pinn 7.4f	Scanitronix

2100 CD						shielded photon diode p-type effect detector diameter 2.5 mm
Varian Clinac 2100CD	1996	10x	0.0843	0.0587	Pinn 4.2	Solid state diode detector, diameter 2 mm
Varian Clinac iX	1996	10x	0.0106	0.0218	Pinn 8.0m	Solid state diode detector, diameter 2 mm
Siemens Primus with klystron	1998	15x	0.0121	0.0103	Pinn 7.6c	Scanitronix shielded photon diode
Siemens Primus with klystron	1998	15x	0.0671	0.0703	Pinn 7.6c	Scanitronix shielded photon diode
Siemens Primus with klystron	1998	15x	0.01	0.015	Pinn 7.6c	Scanitronix shielded photon diode
Varian IX	2008	18x	0.0218	0.0214	Pinn 8.0m	Scanditronix/Wel lhofer photon field diode PFD s/n 3743, diameter of active area 2 mm
Varian IX	2008	6x	0.1098	0.1372	Pinn 8.0m	Scanditronix/Wel lhofer photon field diode PFD s/n 3743, diameter of active area 2 mm
Siemens Primus with klystron	2002	6x	0.0255	0.0618	Pinn 7.6c	Scanitronix shielded photon diode
Siemens Primus	2004	6x	0.0255	0.105	Pinn 7.6c	Scanitronix shielded photon

with klystron						diode
Siemens Primus with klystron	1998	6x	0.035	0.12	Pinn 7.6c	Scanitronix shielded photon diode
Varian 2100 CD	2001	6x	0.04	0.04	Pinn 6.2b	Scanitronix shielded photon diode p-type effect detector diameter 2.5 mm
Varian 2100 CD	2005	6x	0.01	0.02	Pinn 7.4f	Scanitronix shielded photon diode p-type effect detector diameter 2.5 mm
Varian 2100 CD	2005	6x	0.01	0.02	Pinn 7.4f	Scanitronix shielded photon diode p-type effect detector diameter 2.5 mm
Varian 2100 CD	2006	6x	0.01	0.02	Pinn 7.4f	Scanitronix shielded photon diode p-type effect detector diameter 2.5 mm
Varian 600 C	2007	6x	0.12	0.12	Pinn 7.4f	Scanitronix shielded photon diode p-type effect detector diameter 2.5 mm
Varian 600 C	2004	6x	0.09	0.09	Pinn 6.2b	Scanitronix shielded photon diode p-type effect detector diameter 2.5 mm
Varian Clinac 2100CD	1996	6x	0.0842	0.0774	Pinn 4.2	Solid state diode detector, diameter 2 mm
Varian	1996	6x	0.0842	0.0587	Pinn 8.0m	Solid state diode

Clinac 600CD						detector, diameter 2 mm
Varian Clinac iX	1996	6x	0.0587	0.0218	Pinn 8.0m	Solid state diode detector, diameter 2 mm
Varian 21EX	2001	6x	0.4	0.4	Pinn 8.0d	Scanitronix PFD diode
Varian 21EX	2003	6x	0.4	0.4	Pinn 8.0d	Scanitronix PFD diode
Varian 21EX	2006	6x	0.4	0.4	Pinn 8.0d	Scanitronix PFD diode

Appendix I: Code for deconvolution

MATLAB code was used for the deconvolution algorithm and is included here as a rough guide. Code was required in MATLAB before the deconvolution code, e.g. finding the best Gaussian fit for the measured data in cftool.

Table I.1: Deconvolution code used in MATLAB for the thesis (PTO)

Code	Notes
<pre> display('require xln') display('prof1=profile not needed, entered in with gaussian') display('prof2=kernel not needed, calculated directly.') display('prof3=deconvolved') display('prof4=comparison') display('radius dd=0.15,pp=1.0,ic=2.75') modelname1=input('type in name of model>'); k1f=input('type in radius of detector in mm>'); for i=1:512 prof1(i)=modelname1(xln(i)); end %Calculating the kernel.... prof2=1; for i=1:length(xln) prof2(i)=(1/2.51)*(1/k1f)*exp((- 0.5)*(1/k1f)*(1/k1f)*(xln(i)*xln(i))); end prof2=prof2'; %putting the profile to be deconvolved in the middle, filling the rest with empty data from the out of field dose prof1=prof1/max(prof1); for i=1:1511 prof1b(i)=prof1(1); end prof1b(257:768)=prof1(1:512); %getting the kernel, finding the maximum and the point where it is less %than 1%, and then... extracting the right side of the kernel for i=1:512 prof2b(i)=prof2(1); end prof2c=find(prof2==max(prof2)); w1=find(prof2(prof2c:size(prof2,1))<0.001); prof2d=prof2(prof2c:prof2c+w1(1)); </pre>	<p>xln is a 1D array of spatial coordinates</p> <p>prof2 is the 1D array of the Gaussian calculated with the FWHM of the kernel</p> <p>k1f is the radius of the Gaussian kernel (input)</p> <p>prof1 is calculated from a Gaussian model (earlier fitted with cftool on the measured data)</p> <p>prof1b is prof1 with padding</p> <p>prof2b is half of the prof2 profile</p> <p>prof3 is the deconvolution of prof1b with prof2b</p> <p>prof3b is the normalized version of prof3</p> <p>prof3c finds the location of the maximum point in prof3b</p> <p>prof3d performs steps to undo the padding performed earlier from prof3b</p>

```
%deconvolution of the EDITED input profile and the EDITED
profile... into
prof3=deconv(prof1b,prof2d);

prof3b=prof3/max(prof3(10:size(prof3,2)-10));
prof3c=find(prof3b==1);
prof3d=prof3b(prof3c-256:prof3c+255);
if prof3c<size(prof3,1)-512
    plot(xln,prof3d,'--',xln,prof1,'-')
else
    plot(prof3);
end

prof3d=prof3d';
size(prof3)
prof3c
```

Appendix J: Code for planar dose

The MATLAB code used for creating the data format required by the Pinnacle RTPS for planar dose maps (see sections 3.3.3 and 3.5.2) are illustrated in Table J.1.

Table J.1: Code for creation of the planar dose file for the Pinnacle RTPS

```
display('write planar dose grid for pinnacle axial dose')

IMG_X=input('How many points in X for image>');
IMG_Y=input('How many points in Y for image>');
IMG_R=input('what resolution (in cm) for image, typ 0.1-0.5>');

%consider case for symmetrical field of view
ArrayX=-(0.5*(IMG_X*IMG_R)):IMG_R:(0.5*(IMG_X*IMG_R));
ArrayZ=-(0.5*(IMG_Y*IMG_R)):IMG_R:(0.5*(IMG_Y*IMG_R));

Out1=0;
Out1(1,1)=IMG_X;
Out1(1,2)=IMG_Y;
Out1(1,3)=IMG_R;

p=1;
for j=1:length(ArrayX)-1
    for i=1:length(ArrayZ)-1
        Out2(p,1)=ArrayX(j);
        Out2(p,2)=ArrayZ(i);
        Out2(p,3)=0;
        p=p+1;
    end
end

OFF_X=input('offset for x>');
OFF_Y=input('offset for y>');
OFF_Z=input('offset for z>');

Out2b=Out2;
for i=1:size(Out2b,1)
    Out2b(i,1)=Out2(i,1)+OFF_X;
    Out2b(i,2)=Out2(i,2)+OFF_Y;
    Out2b(i,3)=Out2(i,3)+OFF_Z;
end

inputFILENAME1=input('3>typeinfilename including the .pts at the end>','s');
dlmwrite(inputFILENAME1,Out1,'delimiter',' ');
dlmwrite(inputFILENAME1,Out2b,'delimiter',' ','precision','%1f','-append');
```

References

- AAPM-TG50 (2001). AAPM Report No. 72: Basic Applications of Multileaf Collimators.
- AAPM (1994). "American Association of Physicists (AAPM) Task Group 40: Comprehensive QA for radiation oncology: Report of AAPM radiation therapy committee Task Group 40." *Med Phys* **21**: 582-618.
- AAPM (2008). Web-based Dosimetry Training Tool.
- AAPM_TG_50 (2001). "AAPM Report No. 72: Basic Applications of Multileaf Applicators."
- ADAC (2000b). "Pinnacle³ Physics Guide: External Beam and Brachytherapy Physics."
- AIHW (2005). Mortality FAQs, Australian Institute of Health and Welfare, <http://www.aihw.gov.au/mortality/data/faqs.cfm> (Accessed May 2008).
- AIHW (2008). Latest mortality data, Australian Institute of Health and Welfare, http://www.aihw.gov.au/mortality/data/current_data.cfm (Accessed May 2008).
- AIHW (2008). Life expectancy, Australian Institute of Health and Welfare, http://www.aihw.gov.au/mortality/data/life_expectancy.cfm (Accessed May 2008).
- Andreo, P., D. T. Burns, et al. (2004). "IAEA TRS-398 Absorbed Dose Determination in External Beam Radiotherapy: An International Code of Practice for Dosimetry based on Standards of Absorbed Dose to Water."
- Angelis, C. D., S. Onori, et al. (2002). "An investigation of the operating characteristics of two PTW diamond detectors in photon and electron beams." *Med. Phys.* **29**(2): 248.
- Arnfield, M. R., K. Otto, et al. (2005). "The use of film dosimetry of the penumbra region to improve the accuracy of intensity modulated radiotherapy." *Med. Phys.* **32**(1): 12.
- Arnfield, M. R., J. V. Siebers, et al. (2000). "A method for determining multileaf collimator transmission and scatter for dynamic intensity modulated radiotherapy." *Med. Phys.* **27**(10): 2231.
- Arnfield, M. R., Q. Wu, et al. (2001). "Dosimetric Validation for Multileaf Collimator-Based Intensity-Modulated Radiotherapy: A Review." *Medical Dosimetry* **26**(2): 179-188.
- ARPANSA (1990). What is Background Radiation, Australian Radiation Protection and Nuclear Safety Agency.
- ARPANSA (2008). Radiation Protection in the Medical Applications of Ionizing Radiation, Radiation Protection Series Publication No. 14, Australian Radiation Protection and Nuclear Safety Agency.
- Azcona, J. D., R. A. C. Siochi, et al. (2002). "Quality assurance in IMRT: Importance of the transmission through the jaws for an accurate calculation of absolute doses and relative distributions." *Med. Phys.* **29**(3): 269.
- Babel, B., E. Bomsdorf, et al. (2007). "Future life expectancy in Australia, Europe, Japan, and North America." *Journal of Population Research* **24**(1): 119.
- Bednarz, G., M. S. Huq, et al. (2002). "Deconvolution of detector size effect for output factor measurement for narrow Gamma Knife radiosurgery beams." *Phys. Med. Biol.* **47**: 3643.
- Biggs, P., J. Capalucci, et al. (1991). "Comparison of the penumbra between focused and nondivergent blocks- Implications for multileaf collimators." *Med. Phys.* **18**(4): 753.
- Björngård, B. E., J.-S. Tsai, et al. (1990). "Doses on the central axes of narrow 6-MV x-ray beams." *Med. Phys.* **5**: 794-799.

- Bjork, P., T. Knoos, et al. (2000). "Comparative dosimetry of diode and diamond detectors in electron beams for intraoperative radiation therapy." Med. Phys. **27**(11): 2580-2588.
- Bortfield, T. (2006). "IMRT: a review and preview." Phys. Med. Biol. **51**: R363-R379.
- Bortfield, T., U. Oelfke, et al. (2000). "What is the optimum leaf width of a multileaf collimator?" Med. Phys. **27**(11): 2494.
- Boyer, A. L., T. G. Ochran, et al. (1992). "Clinical dosimetry for implementation of a multileaf collimator." Med. Phys. **19**(5): 1255-1261.
- Brahme, A. (1984). "Dosimetric precision requirements in radiation therapy." Acta Radiol. Oncol. **23**: 379-391.
- Brahme, A. (1988). "Optimization of stationary and moving beam radiation therapy techniques." Radiotherapy and Oncology **12**: 129-140.
- Bruch, P. M. and W. Zhen (2000). "Viewpoints to consider in the development of MLC and IMRT programs." Medical Dosimetry, **26**(1): 91-94.
- Bucciolini, M., E. Borchi, et al. (2005). "Diamond dosimetry: Outcomes of the CANDIDO and CONRADINFN projects." Nuclear Instruments and Methods in Physics Research A **552**(189-196): 189-196.
- Bucciolini, M., F. B. Buonamici, et al. (2003). "Diamond detector versus silicon diode and ion chamber in photon beams of different energy and field size." Med. Phys. **30**(8): 2149.
- Burch, S. E., K. J. Kearfott, et al. (1997). "A new approach to film dosimetry for high energy photon beams: Lateral scatter filtering." Med. Phys. **24**(5): 775.
- Butson, M. J., P. K. N. Yu, et al. (2003). "Rounded end multi-leaf penumbral measurements with radiochromic film." Phys. Med. Biol. **48**: N247-N252.
- Carlson, D. (2001). "Intensity Modulation using Multileaf Collimators: Current Status." Medical Dosimetry **26**(2): 151-156.
- Chang, K.-S., F.-F. Yin, et al. (1996). "The effect of detector size to the broadening of the penumbra—a computer simulated study." Med. Phys. **23**(8): 1407-1411.
- Charland, P., E. El-khatib, et al. (1998). "The use of deconvolution and total least squares in recovering a radiation detector line spread function." Med Phys **25**(2): 152-160.
- Cheng, C.-W., S. H. Cho, et al. (2007). "Determination of zero-field size percent depth doses and tissue maximum ratios for stereotactic radiosurgery and IMRT dosimetry: Comparison between experimental measurements and Monte Carlo simulation." Med. Phys. **34**(8): 3149-3157.
- Cheung, K. Y., P. H. Choi, et al. (1999). "The roles of multileaf collimators and micro-multileaf collimators in conformal and conventional nasopharyngeal carcinoma radiotherapy treatments." Med. Phys. **26**: 2077-85.
- Cheung, T., M. J. Butson, et al. (2006). "Measurement of high energy x-ray beam penumbra with Gafchromic™ EBT radiochromic film." Med. Phys. **33**(8): 2912.
- Chow, J. C. L., M. Seguin, et al. (2005). "Dosimetric effect of collimating jaws for small multileaf collimated fields." Med. Phys. **23**(3): 759.
- Chow, J. C. L., B. Wettlaufer, et al. (2006). "Dosimetric effects on the penumbra region of irregular multi-leaf collimated fields." Phys. Med. Biol. **51**: N31-N38.
- Chui, C.-S. and R. Mohan (1987). "Extraction of pencil beam kernels by the deconvolution method." Med Phys **15**(2): 138.
- Clark, B. G., T. Teke, et al. (2006). "Penumbra evaluation of the Varian Millennium and BrainLAB M3 Multileaf Collimator." Int. J. Radiation Oncology Biol. Phys. **66**(4): S71-S75.
- Crop, F., N. Reynaert, et al. (2007). "Monte Carlo modelling of the ModuLeaf miniature MLC for small field dosimetry and quality assurance of the clinical treatment planning system." Phys. Med. Biol. **52**: 3275-3290.

- Das, I. J., G. X. Ding, et al. (2007). "Small fields: Nonequilibrium radiation dosimetry." Med. Phys. **35**(1): 206-215.
- Dawson, D. J., J. M. Harper, et al. (1984). "Analysis of physical parameters associated with the measurement of high-energy x-ray penumbra." Med. Phys. **11**(4): 491.
- Dawson, D. J., N. J. Schroeder, et al. (1985). "Penumbra measurements in water for high-energy x rays." Med. Phys. **13**(1): 101.
- Ding, G. X., D. M. Duggan, et al. (2006). "Commissioning stereotactic radiosurgery beams using both experimental and theoretical methods." Phys. Med. Biol. **51**: 2549-2566.
- Dogan, N. and G. P. Glasgow (2003). "Surface and build-up region dosimetry for obliquely incident intensity modulated radiotherapy 6 MV x rays." Med. Phys. **30**(12): 3091.
- Dollinger, M., E. Rosenbaum, et al. (2002). Everyone's Guide to Cancer Therapy: How Cancer is Diagnosed, Treated, and Managed Day to Day.
- Fidanzio, A., L. Azario, et al. (2002). "A correction method for diamond detector signal dependence with proton energy." Med. Phys. **29**(5): 669.
- Fidanzio, A., L. Azario, et al. (2000). "PTW-diamond detector: Dose rate and particle type dependence." Med. Phys. **27**(11): 2589.
- Fiveash, J. B., H. Murshed, et al. (2002). "Effect of multileaf collimator leaf width on physical dose distributions in the treatment of CNS and head and neck neoplasms with intensity modulated radiation therapy." Med. Phys. **29**(6): 1116.
- Fowler, J. F. (1966). Solid state electrical conductivity dosimeters, Radiation Dosimetry, New York: Academic.
- Garcia-Vicente, F., M. J. Bejar, et al. (2004). "Clinical impact of the detector size effect in 3D-CRT." Radiotherapy and Oncology **74**: 315-322.
- Garcia-Vicente, F., J. M. Delgado, et al. (1997). "Experimental determination of the convolution kernel for the study of the spatial response of a detector." Med. Phys. **25**(2): 202.
- Graves, M. N., A. V. Thompson, et al. (2001). "Calibration and quality assurance for rounded leaf-end MLC systems." Med. Phys. **28**(11): 2227-2233.
- Hansen, E. K. and M. Roach (2007). "Handbook of Evidence-based Radiation Oncology."
- Hardcastle, N., P. Metcalfe, et al. (2007). "Multileaf collimator end leaf leakage: implications for wide-field IMRT." Phys. Med. Biol. **52**: N493-N504.
- Heath, E. and J. Seuntjens (2003). "Development and validation of a BEAMnrc component module for accurate Monte Carlo modelling of the Varian dynamic Millennium multileaf collimator." Phys. Med. Biol. **48**(4045-4063).
- Hendry, J., B. Jeremic, et al. (2006). "Normal tissue complications after radiation therapy." Pan Am J Public Health **20**(2/3): 151-160.
- Heydarian, M., P. Hoban, et al. (1996). "A comparison of dosimetry techniques in stereotactic radiosurgery." Phys. Med. Biol. **41**: 93-110.
- Higgins, P. D., C. H. Sibata, et al. (1995). "Deconvolution of detector size effect for small field measurement." Medical Physics **22**(10): 1663-1666.
- Hoban, P. W., M. Heydarian, et al. (1994). "Dose rate dependence of a PTW diamond detector in the dosimetry of a 6 MV photon beam." Phys. Med. Biol. **39**: 1219-1229.
- Hugtenburg, R. P., K. Johnston, et al. (2001). "Application of diamond detectors to the dosimetry of 45 and 100 kVp therapy beams: comparison with a parallel-plate ionization chamber and Monte Carlo." Phys. Med. Biol. **46**: 2489-2501.
- IAEA (2005). "Radiation Oncology Physics: A Handbook for Teachers and Students."

- IAEA (2004), "Technical Report Series No. 430: Commissioning and Quality Assurance of Computerized Planning Systems for Radiation Treatment of Cancer."
- ICRU29 (1978). "Dose specifications for reporting external beam therapy with photons and electrons, ICRU: Report 29, International Committee on Radiation Units and Measurements."
- ICRU (1993). "International Commission on Radiation Units and Measurements. ICRU Report 50. Prescribing, Recording, and Reporting Photon Beam Therapy. ."
- IMRT-CWG (2001). "Intensity-modulated radiotherapy: current status and issues of interest." Int. J. Radiation Oncology Biol. Phys. **51**: 880-914.
- IPEM (1999). "Physics Aspects of Quality Control in Radiotherapy."
- Jaffray, D. A., J. J. Battista, et al. (1993). "X-ray sources of medical linear accelerators: Focal and extra-focal radiation." Med. Phys. **20**(5): 1417.
- Jang, S. Y., O. N. Vassiliev, et al. (2006). "Development and commissioning of a multileaf collimator model in Monte Carlo dose calculations for intensity-modulated radiation therapy." Med. Phys. **33**(3): 770.
- Ju, S. G., Y. C. Ahn, et al. (2002). "Film dosimetry for intensity modulated radiation therapy: Dosimetric evaluation." Med. Phys. **29**(3): 351.
- Kaisary, A. V. (1999). Textbook of Prostate Cancer: Pathology, Diagnosis and Treatment.
- Karzmark, C. J. and R. J. Morton (1997). A Primer on Theory and Operation of Linear Accelerators in Radiation Therapy, Second Edition, Medical Physics Publishing.
- Killoran, J. H., J. Y. Giraud, et al. (2002). "A dosimetric comparison of two multileaf collimator designs." Med. Phys. **29**(8): 1752.
- Kim, J. O., J. V. Siebers, et al. (2001). "A Monte Carlo study of radiation transport through multileaf collimators." Med. Phys. **28**(12): 2497-2506.
- Kron, T., A. Elliot, et al. (1993). "The penumbra of a 6-MV x-ray beam as measured by thermoluminescent dosimetry and evaluated using an inverse square root function." Med. Phys. **20**(5): 1429.
- Kubo, H. D., R. B. Wilder, et al. (1999). "Impact of collimator leaf width on stereotactic radiosurgery and 3D conformal radiotherapy treatment plans." Int. J. Radiat. Oncol. Biol. Phys. **44**: 937-45.
- Laub, W. U. (2002). "Comparison of TG-43 dose calculations to pinpoint ion chamber and diamond detector measurements." Phys. Med. Biol. **47**: N315-N318.
- Laub, W. U., T. W. Kaulich, et al. (1997). "Energy and dose rate dependence of a diamond detector in the dosimetry of 4–25 MV photon beams." Med. Phys. **24**(4): 535.
- Laub, W. U., T. W. Kaulich, et al. (1999). "A diamond detector in the dosimetry of high-energy electron and photon beams." Phys. Med. Biol. **44**: 2183-2192.
- Laub, W. U. and T. Wong (2003). "The volume effect of detectors in the dosimetry of small fields used in IMRT." Med. Phys. **30**(3): 341-347.
- Lee, H.-R., M. Pankuch, et al. (2002). "Evaluation and characterization of parallel plate microchamber's functionalities in small beam dosimetry." Med. Phys. **29**(11): 2489-2496.
- Li, X. A., M. Soubra, et al. (1995). "Lateral electron equilibrium and electron contamination in measurements of head-scatter factors using miniphantoms and brass caps." Med. Phys. **22**(7): 1167-1170.
- Loewenthal, E. and E. Loewinger (1992). "Measurement of the source size of a 6- and 18-MV radiotherapy linac." Med. Phys. **19**(3): 687.
- LoSasso, T., C.-S. Chui, et al. (2001). "Comprehensive quality assurance for the delivery of intensity modulated radiotherapy with a multileaf collimator used in the dynamic mode." Med. Phys. **28**(11): 2209-2219.

- Low, D. A., J. W. Sohn, et al. (2001). "Characterization of a commercial multileaf collimator used for intensity modulated radiation therapy." Med. Phys. **28**(5): 752-756.
- Lutz, W. R., N. Maleki, et al. (1988). "Evaluation of a beam-spot camera for megavoltage x rays." Med. Phys. **15**(4): 614.
- Lydon, J. M. (2005). "Theoretical and experimental validation of treatment planning for narrow MLC defined photon fields." Phys. Med. Biol. **50**: 2701-2714.
- Martens, C., C. D. Wagter, et al. (2000). "The value of the PinPoint ion chamber for characterization of small field segments used in intensity-modulated radiotherapy." Physics in Medicine and Biology **45**(9): 2519.
- Mayles, P., A. E. Nahum, et al. (2007). Handbook of Radiotherapy Physics: Theory and Practice, CRC Press.
- McKerracher, C. and D. I. Thwaites (2006). "Notes on the construction of solid-state detectors." Radiotherapy and Oncology **79**: 348-351.
- McNutt, T. and M. Gehring (1997). The ADAC Pinnacle³ Convolution Superposition Dose Model, ADAC.
- Metcalfe, P., T. Kron, et al. (1993). "Dosimetry of 6-MV x-ray beam penumbra." Med. Phys. **20**(5): 1439-1445.
- Metcalfe, P., T. Kron, et al. (2007). The Physics of Radiotherapy X-Rays and Electrons, Medical Physics Publishing.
- Millar, M., C. J, et al. (1997). "ACPSEM Position Paper: Recommendations for the safe use of external beams and sealed brachytherapy sources in radiation oncology." Aust. Phys. Eng. Sci. Med. **20**: 1-35.
- Mobit, P. N. and G. A. Sandison (1999). "A Monte Carlo comparison of the response of the PTW-diamond and the TL-diamond detectors in megavoltage photon beams." Med Phys. **26**(11): 2503.
- Mohan, R., C. Chui, et al. (1985). "Energy and angular distributions of photons from medical linear accelerators." Med Phys **12**(5): 592.
- Mould, R. F. (1981). Radiotherapy Treatment Planning Second Edition, Adam Hilger Ltd.
- Munro, P., J. A. Rawlinson, et al. (1988). "Therapy imaging: Source sizes of radiotherapy beams." Med. Phys. **15**(4): 517.
- NCI (2008). Cancer -An Overview, National Cancer Institute (U.S. National Institutes of Health) <http://www.cancer.gov/cancertopics/wyntk/overview/page4> (Accessed May 2008).
- Nill, S., T. Tucking, et al. (2005). "Intensity modulated radiation therapy with multileaf collimators of different leaf widths: a comparison of achievable dose distributions." Radiotherapy and Oncology **75**(106-111).
- O'Malley, L., J.-P. Pignol, et al. (2006). "Improvement of radiological penumbra using intermediate energy photons (IEP) for stereotactic radiosurgery." Phys. Med. Biol. **51**: 2537-2548.
- Olshansky, S. J., B. A. Carnes, et al. (1990). "In Search of Methuselah: Estimating the Upper Limits to Human Longevity." Science **250**: 634-40.
- Pappas, E., T. G. Maris, et al. (2006). "Experimental determination of the effect of detector size on profile measurements in narrow photon beams." Medical Physics **33**(10): 3700-3710.
- Pappas, E., L. Petrokokkinos, et al. (2005). "Relative output factor measurements of a 5 mm diameter radiosurgical photon beam using polymer gel dosimetry." Med. Phys. **32**(6): 1513-1520.
- Parent, L., J. Seco, et al. (2005). "Evaluation of two methods of predicting MLC leaf positions using EPID measurements." Med. Phys. **33**(9): 3174.

- Patterson, M. S. and P. C. Shragge (1981). "Characteristics of an 18 MV photon beam from a Therac 20 Medical Linear Accelerator." Med. Phys. **8**(3): 312.
- Pawlicki, T. and C.-M. C. Ma (2001). "Monte carlo simulation for MLC-based intensity-modulated radiotherapy." Medical Dosimetry **26**(2): 157-168.
- PTW-Freiburg (2008). Ionisation Detectors.
- PTW (2006). MEPHYSTO mcc 1.3 Help File.
- Renner, W. D., K. Norton, et al. (2005). "A method for deconvolution of integrated electronic portal images to obtain incident fluence for dose reconstruction." Journal of Applied Clinical Medical Physics **6**(4): 22-39.
- Riley, J. C. (2001). Rising Life Expectancy: A Global History, Cambridge University Press.
- Sanchez-doblado, F., G. H. Hartmann, et al. (2007). "Uncertainty estimation in intensity-modulated radiotherapy absolute dosimetry verification." Int. J. Radiation Oncology Biol. Phys. **68**(1): 301-310.
- Saw, C. B., K. M. Ayyangar, et al. (2001). "Commissioning and quality assurance for MLC-based IMRT." Medical Dosimetry, **26**(2): 125–133.
- Saw, C. B., R. A. C. Siochi, et al. (2001). "Leaf sequencing techniques for MLC-based IMRT." Medical Dosimetry **26**(2): 199-204.
- Sharpe, M. B., D. A. Jaffray, et al. (1995). "Extrafocal radiation: A unified approach to the prediction of beam penumbra and output factors for megavoltage x-ray beams." Med. Phys. **22**(12): 2065.
- Sharpe, M. B., B. M. Miller, et al. (2000). "Compensation of x-ray beam penumbra in conformal radiotherapy." Med Phys. **27**(8): 1739-1745.
- Tannock, I., R. P. Hill, et al. (2005). The Basic Science of Oncology, Mc-Graw-Hill Professional.
- Topolnjak, R., U. A. v. d. Heide, et al. (2007). "Influence of the linac design on intensity-modulated radiotherapy of head-and-neck plans." Phys. Med. Biol. **52**: 169-182.
- Tracey, E., D. Baker, et al. (2005). Cancer in New South Wales: Incidence, Mortality and Prevalence Report 2005, Cancer Institute NSW.
- Tsai, J. S., M. J. Rivard, et al. (2003). "Determination of the 4 mm gamma knife helmet relative output factor using a variety of detectors." Med. Phys. **30**: 986-92.
- van't.Veld, A. A., P. v. Lujik, et al. (2001). "Detector linear spread functions determined analytically by transport of Compton recoil electrons." Med Phys. **28**(5): 738.
- van't.Veld, A. A., P. v. Lujik, et al. (2001). "Detector linear spread functions determined analytically by transport of Compton recoil electrons." Med Phys. **28**(5): 738.
- Van-Dyk, J. (1999). The Modern Technology of Radiation Oncology, Medical Physics Publishing.
- Venencia, C. D. and P. Besa (2004). "Commissioning and quality assurance for intensity modulated radiotherapy with dynamic multileaf collimator: Experience of the Pontificia Universidad Católica de Chile." Journal of Applied Clinical Medical Physics **5**(3): 37-54.
- Vlamynck, K. D., H. Palmans, et al. (1999). "Dose measurements compared with Monte Carlo simulations of narrow 6 MV multileaf collimator shaped photon beams." Med. Phys. **26**(9): 1874.
- Webb, S. (1993). The Physics of Three-dimensional Radiation Therapy: Conformal radiotherapy, radiosurgery and treatment planning, CRC Press.
- Westermarck, M., J. Arndt, et al. (1999). "Comparative dosimetry in narrow high-energy photon beams." Phys. Med. Biol. **45**: 685-702.
- Westermarck, M., J. Arndt, et al. (2000). "Comparative dosimetry in narrow high-energy photon beams." Phys. Med. Biol. **45**: 685-702.

- Wieslander, E. and T. Knoos (2007). "A virtual-accelerator-based verification of a Monte Carlo dose calculation algorithm for electron beam treatment planning in clinical situations." Radiotherapy and Oncology **82**: 208-217.
- Wiki (2008). Life expectancy, Wikipedia, http://en.wikipedia.org/wiki/Life_expectancy (Accessed May 2008).
- Wu, V. W. C. (2007). "Effects of multileaf collimator parameters on treatment planning of intensity-modulated radiotherapy." Medical Dosimetry **32**(1): 38-43.
- Xue, J., P. Zhang, et al. (2002). "Implementation of the isocenter-shift technique for smoothing MLC field edge on a 3D treatment planning system." Med. Phys. **29**(7): 1413.
- Zhu, T. C. and B. E. Bjarngard (1994). "The head-scatter factor for small field sizes." Med. Phys. **21**: 65-8.
- Zhu, T. C., B. E. Bjarngard, et al. (1995). "X-ray source and the output factor." Med. Phys. **22**(6): 793.
- Zhu, X. R., J. J. Allen, et al. (2000). "Total scatter factors and tissue maximum ratios for small radiosurgery fields: comparison of diode detectors, a parallel-plate ion chamber, and radiographic film." Med. Phys. **27**: 472-7.
- Zygmanski, P. and J. H. Kung (2001). "Method of identifying dynamic multileaf collimator irradiation that is highly sensitive to a systematic MLC calibration error." Med. Phys. **28**(11): 2220-2226.

End